Exploration of applications of photon-counting detector computed tomography (CT) using a table-top CT system

by

Devon Richtsmeier
BS, Boise State University, 2018

A Dissertation Submitted in Partial Fulfillment of the
Requirements for the Degree of

DOCTOR OF PHILOSOPHY

in the Department of Physics and Astronomy

Exploration of applications of photon-counting detector computed tomography (CT) using a table-top CT system

by

Devon Richtsmeier
BS, Boise State University, 2018

Supervisory Committee

Dr. Magdalena Bazalova-Carter, Co-Supervisor
(Department of Physics and Astronomy)

Dr. Matthew Moffitt, Co-Supervisor
(Department of Chemistry)

Dr. Derek Wells, Departmental Member
(Department of Physics and Astronomy)

Abstract

Computed Tomography (CT) is an essential diagnostic tool in healthcare, widely used for various applications including cancer detection, vascular disease evaluations, and radiation therapy planning. Recent advancements in photon-counting detector (PCD) technology have led to the development of photon-counting detector CT (PCD-CT), a promising innovation offering high spatial resolution and superior contrast-to-noise ratios compared to traditional CT. PCD-CT excels in detecting and characterizing small structures in various body parts, enhancing tissue differentiation, and material decomposition, thus potentially improving disease diagnosis and radiotherapy treatment planning. This research explores the applications of PCD-CT using a bench-top system, offering insights into its potential benefits over conventional CT systems. Despite its limitations in fully representing a clinical CT system, the bench-top model provides flexibility in assessing clinically useful features. This dissertation investigates four key applications of PCD-CT: material decomposition, multi-contrast imaging, metal artifact reduction, and high-resolution imaging.

We investigated the material decomposition capabilities of our bench-top PCD-CT scanner using a dual-energy CT (DECT) method for extracting effective atomic number (Z_{eff}) and relative electron density (ρ_e) of tissues. We demonstrated that the method with PCD-CT was more accurate in extracting Z_{eff} and ρ_e for a set of electron density phantom materials with known Z_{eff} and ρ_e than the method with DECT. In addition, four tissue types were correctly identified in an *ex-vivo* tissue sample and an injected gold contrast agent was separated from the other four tissue types using K-edge subtraction imaging.

Multi-contrast imaging was demonstrated in a phantom model with four contrast agents: gadolinium, dysprosium, lutetium, and gold. The four contrast agents were inserted into the same cylindrical phantom and imaged in one scan. Using K-edge subtraction, we were able to demonstrate complete separation and accurate quantification of the four contrast agents, even of gadolinium and dysprosium, which have K-edge energies of 50.2 keV and 53.8 keV, respectively. Additionally, we optimized the acquisition parameters for the various contrast agents.

We also developed a novel metal artifact reduction (MAR) method using PCD-CT. As metal attenuates fewer higher energy x-rays than low energy x-rays, we showed that the high-energy range of 100–110 keV demonstrated fewer metal artifacts. The high energy range is separable from the other x-ray data with the PCD. With this in mind, we developed trace replacement metal artifact reduction (TRMAR). The metal traces in the corrupted conventional CT sinogram space are replaced with the high-energy trace data from the 100–

110 keV range. With this, we maintained the contrast and image quality of the full spectrum conventional CT image and also kept the reduced metal artifacts from the high energy data.

Finally, we demonstrated the high spatial resolution of our PCD-CT system by imaging coronary artery stents and comparing the same stents imaged with two conventional CT scanners. PCD-CT demonstrated more accurate measurement of the stent strut, or wire, width, stent lumen diameter, and lumen CT number compared to conventional CT. In addition, this led to more accurate 3D representations of the stents. The higher accuracy of strut width and stent visualization is due to the higher spatial resolution of the PCD-CT system and the reduced metal and blooming artifacts it offers over conventional CT.

Each of these applications demonstrates the significant potential of PCD-CT in enhancing medical diagnostics and treatment, particularly in cardiovascular imaging, highlighting its diverse contributions to the field of medical imaging.

Table of Contents

List of Tables

List of Figures

Acknowledgements

First of all I would like to thank **Dr. Magdalena Bazalova-Carter** for her amazing support throughout all of my graduate work, I wholeheartedly believe it would not have been as enjoyable under any other supervisor. Getting a PhD is a stressful undertaking at times and a good supervisor makes all the difference, which I can confidently say she is. She'll even let you live in her house when she goes on sabbatical. Ok, now on to the cons....this will be a lot longer.....nope I got nothing.

I would also like to thank **Dr. Daniel Fologea**, who was my undergraduate mentor, for his encouragement and support throughout my undergraduate career and afterwards, I would not have considered graduate school otherwise.

There are many from the XCITE lab I would also like to thank for contributing to a community of support and just being great to be around in general: **Dr. Chelsea A.S. Dunning**, **Dr. Nolan Esplen**, **Dr. Pierre-Antoine Rodesch**, **Dr. Jericho O'Connell**, **Alex Hart**, **Jade Fischer**, **Olivia Masella**, and many, many others. You all made conferences, lab meetings, and grad school a blast. Thanks for all your help.

Also thanks to my collaborators **Dr. Kris Iniewski** and Redlen Technologies for their support of my research and career.

And finally, thanks to my family for supporting me as well as all the great friends I've made over the last few years: **Alex Hart**, **Kirsten Aasen**, **Liam McDougall**, **Hayley Smith**, and **Jericho O'Connell**, along with all the other swimmers out there, you guys are the best.

Thanks to putting up with me as a roommate as well, **Alex Hart**.

Dedication

I'd like to thank:

Sandy, for giving me an excuse to not work.

the UVIC Decision Desk (Alex, Matt, and Kyle), for bagels and support through classes, research, and life.

the Salish Sea Swimmers, for the swims, the late nights, and the best group of friends I've ever had.

I'm in there like swimwear.
- Spy Fox

Chapter 1

Introduction

Computed Tomography (CT) is a widely used diagnostic tool in modern healthcare, offering detailed cross-sectional images of the body. It is commonly employed for a broad range of applications, including detecting various cancers, studying vascular diseases, and radiation therapy treatment planning [1, 2]. CT scans are instrumental in planning and guiding medical treatments and surgeries, assessing the effectiveness of therapies, and guiding diagnostic procedures such as biopsies.

With advancements in high-flux photon-counting detector (PCD) technology, photon-counting detector CT (PCD-CT) is becoming clinically viable, with one PCD-CT scanner currently on the market [3] and several others in development [4, 5, 6, 7, 8]. PCD-CT represents a significant step forward, providing high spatial resolution and superior contrast-to-noise ratios (CNRs) compared to conventional CT, among other potential benefits. The enhanced spatial resolution enables more precise detection and characterization of small structures across various body parts, such as the coronary arteries, brain, lungs, and intricate bone structures and implants such as stents [9, 10]. PCD-CT's energy discrimination capabilities can improve tissue differentiation and material decomposition, potentially enhancing disease diagnosis and radiotherapy treatment planning [11]. However, the integration of PCD-CT into routine clinical practice faces challenges, including the management of the large data volumes it generates and inherent properties of PCDs such as charge-sharing and pulse pileup [11, 10]. Despite these hurdles, the potential of PCD-CT to revolutionize medical imaging remains considerable, promising further advancements and broader applications in healthcare.

In this work we have developed and utilized a bench-top PCD-CT system in order to study various applications of PCD-CT in order to determine the benefits it could offer over current, conventional CT systems. Although our bench-top system may not provide a fully representative comparison to a full clinical CT system, it offers much more flexibility in

the available parameter space in order to assess what features might be useful clinically whereas others may be of less use. Several of the applications for PCD-CT demonstrate significant potential for future clinical use. The first application we investigated was multi-contrast imaging, demonstrating PCD-CT's capacity to distinguish between various contrast agents, a crucial aspect for detailed medical diagnostics. The second application delves into metal artifact reduction, addressing a common issue in imaging patients with metal implants. The third application highlights material decomposition, showcasing PCD-CT's ability to identify and differentiate between diverse tissues and materials. Finally, the fourth application focuses on stent visualization, emphasizing the enhanced cardiovascular imaging capabilities offered by PCD-CT. Each application underscores the diverse and significant contributions of PCD-CT to medical imaging.

Chapter 2

From the Basics to CT Imaging

2.1 Radiation and matter

An understanding of x-rays and their interactions with matter are the key to CT at a fundamental level. The measurement of the differences in the attenuation of x-rays within matter, as they travel through a subject, are the basis of CT imaging. There are a number of mechanisms through which x-rays can be attenuated including Rayleigh scattering, Compton scattering, the photoelectric effect, and pair production. The extent to which x-rays go through any of these processes depends on the type of material they are passing through as well as the energy of the x-ray itself. CT is conducted within the diagnostic x-ray energy range between 30–150 keV [1], so the main processes of concern are Compton and the photoelectric effect, and to lesser extent, Rayleigh scattering. Pair production only occurs with photons above 1.022 MeV, so it is irrelevant in CT imaging. In addition to the fundamental x-ray-matter interactions, electron interactions also play a part. These interactions include *bremsstrahlung* and Meitner-Auger electrons.

2.1.1 Structure of an atom

Atoms are the basic unit that makes up all matter. At the center of each atom (Fig. 2.1) is the nucleus, made up of two basic particles, protons and neutrons, which are positively- and neutrally-charged, respectively. Elements are defined by their atomic number (Z), which refers to the number of protons which are contained in the nucleus. The number of neutrons determines the isotope of the element. Surrounding the nucleus are the third particles, the electrons, which are negatively charged. A neutral atom will have an equal number of protons and electrons. If not, the atom is said to be an ion, or ionized. Electrons occupy orbits, or shells, around the nucleus, each of which has an associated binding energy, which is greater the closer the shell is to the nucleus. The binding energy depends on the particular element.

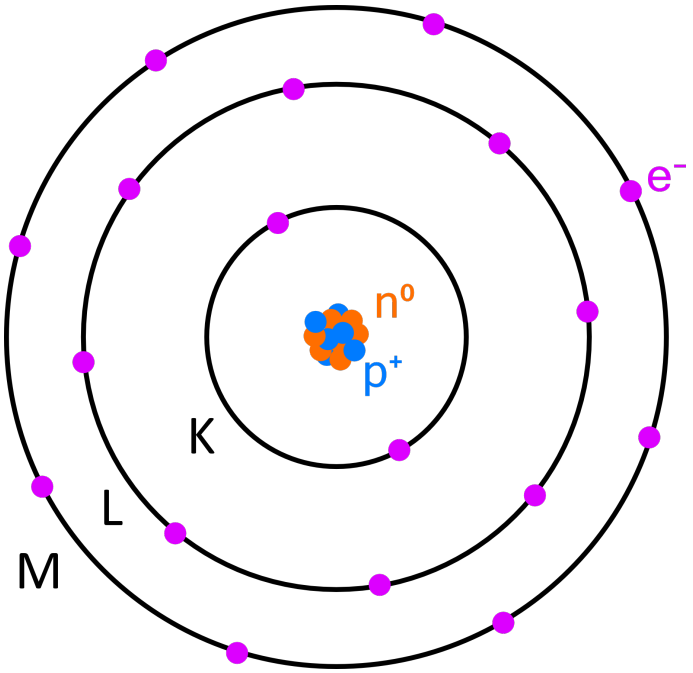

Figure 2.1: A simple diagram of an atom showing the nucleus, composed of protons (blue, p^+) and neutrons (orange, n^0), as well as electrons (magenta, e^-) in the K, L, and M shells.

The first orbit, or K-shell, has the highest binding energy and can hold two electrons. The second, or L-shell, can hold eight. As Z increases, the M-shell will be filled, followed by the N-shell.

2.1.2 X-ray absorption

The absorption of x-rays within a material is governed by the type of material and the energy of the x-rays. First, to simplify, consider an number of monochromatic x-rays (N_0) which are incident on a uniform material of thickness (x). The number of x-rays (N) that are left after the beam has passed through the material can be found using the exponential decay formula:

$$N = N_0 e^{-\mu x} \tag{2.1}$$

where μ is the linear attenuation coefficient of the material. μ is defined by the properties of the material and varies with x-ray energy. It can be thought of as "the fraction of x-rays that interact per unit thickness of attenuator," or material [12]. Of the x-rays that were absorbed in the material, there are four processes by which that could take place, mentioned above: Rayleigh scattering, the photoelectric effect, Compton scattering, and

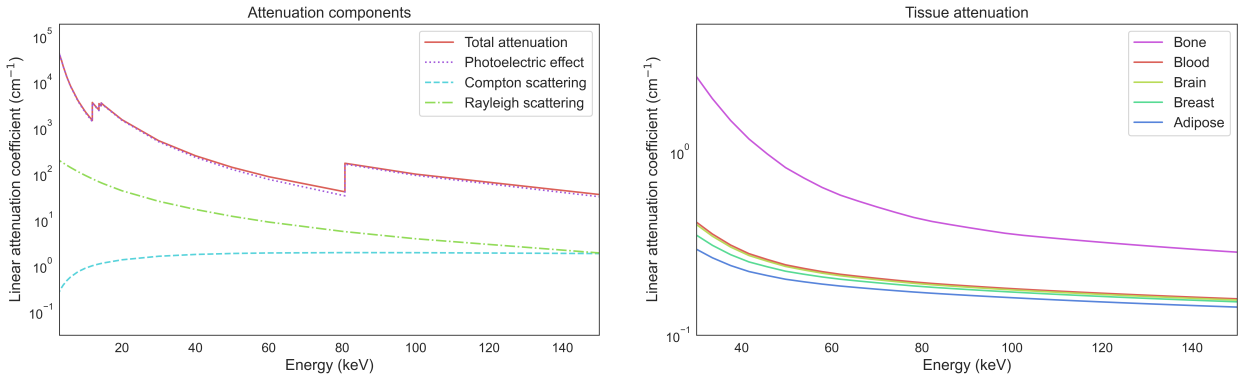

(a) (b)

Figure 2.2: (a) A plot of the linear attenuation coefficient for gold and its constituent components: the photoelectric effect, Rayleigh scattering, and Compton scattering over the diagnostic energy range. (b) A plot of the linear attenuation coefficients for several tissues: bone, blood, brain, breast, and adipose over the diagnostic energy range.

pair production. Each of the processes has a probability of that interaction occurring, each of which are a component in the total attenuation. Thus, μ can be described as the sum of the four process components:

$$\mu = \tau + \sigma_{ray} + \sigma_{comp} + \kappa \tag{2.2}$$

where τ is the photoelectric component, σ_{ray} is the Rayleigh component, σ_{comp} is the Compton component, and κ is the pair production component (Fig. 2.2a). Excluding pair production, the individual processes will be discussed further below.

2.1.3 Rayleigh scattering

The effect of Rayleigh scattering mainly serves to broaden the size of the original x-ray beam, or divert individual x-rays slightly in the forward direction. The incoming x-rays interacts with the bound electrons of the atom, but imparts no kinetic energy to any of the electrons. The incoming x-ray has an oscillating electric field which momentarily imparts a slight vibration to the electrons of the atom, which emit radiation at the same energy and frequency. The effect is for the incoming x-ray to be scattered at a slight angle relative to the incident path, usually in the forward direction. However, given that no energy is transferred to the medium during this process and the fact that Rayleigh scattering makes up less than 13% of the total attenuation in water at x-ray energies above 30 keV, it is generally disregarded for CT imaging[12].

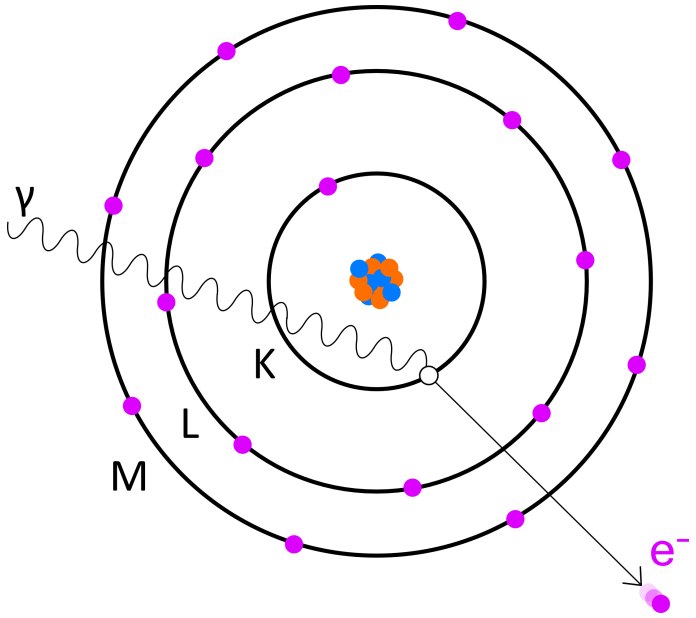

Figure 2.3: A diagram of the process of the photoelectric effect, in which a K-shell electron (e^-) is ejected from its shell by an x-ray (γ).

2.1.4 The photoelectric effect

The photoelectric effect occurs when an x-ray interacts with a tightly bound electron in the K, L, M, or N shells of an atom. The x-ray is completely absorbed and the electron is ejected from the atom with a kinetic energy (KE) equal to the energy of the incoming x-ray ($h\nu$) minus the binding energy of the particular electron shell (E_b). The ejected electron is known as the photoelectron, and it leaves behind a vacancy in the shell it was ejected from. The process is illustrated in Fig. 2.3. As an example, consider a photoelectron which is ejected from the K-shell of an atom. The atom is left in an excited state and thus an electron from a higher shell will transition to fill the vacancy in the K-shell. This transition requires a change in energy, which is the difference in binding energy between the K-shell and the higher shell. This excess energy is then irradiated away from the atom as characteristic radiation or Meitner-Auger electrons, which will both be described in detail below [13, 14]. The probability of an x-ray undergoing the photoelectric effect varies with both Z and energy (E). For low Z materials, the cross section varies as a function of approximately $Z^{3.8}$, and for higher Z materials it behaves as Z^3. For all atomic numbers the coefficient drops off as E^{-3}, as E increases.

2.1.5 Meitner-Auger electrons and fluorescence

In the photoelectric effect, the ejection of an electron leaves behind a vacancy in the shell in which the electron was originally bound. This hole leaves the atom in an excited state. The lowest energy state for the atom is to have the lowest energy shells filled, so an electron from a higher shell will drop down to fill the vacancy in the lower shell. However, the difference binding energy between the higher and lower shells must be irradiated away from the atom in some manner, which can occur either through fluorescence or Meitner-Auger electrons [13, 14]. Consider an example in which a K-shell electron is ejected through the photoelectric effect and an electron from the M-shell fills the vacancy in the K-shell, as in Fig. 2.4a. If the difference in energy is accounted for as fluorescence, the atom will release an x-ray with energy $h\nu = E_K - E_M$. Fluorescence is also referred to as characteristic radiation due to the fact that the x-rays resulting from this process can only take on specific energies which correspond to the difference in binding energy between the various electron shells. These shells have specific energies which depend on Z, so elements can be readily identified based on the energy of their characteristic radiation. The second method by which the energy difference can be accounted for is with the release of an Meitner-Auger electron. Consider an example in which an L-shell electron has filled the K-shell vacancy, an M-shell electron could be released with kinetic energy $E = E_K - E_L - E_M$ (Fig 2.4b). Subsequent vacancies within the lower shells would be filled with higher-shell electrons until the atom achieved the lowest energy state. Lower Z values tend towards releasing energy via Meitner-Auger electrons, while higher Z materials have a higher probability of characteristic radiation.

2.1.6 Compton scattering

Compton scattering is the most important process for soft tissue in the x-ray energy range used for diagnostic purposes. The process occurs when an x-ray of energy $h\nu$ collides with a free electron in the material as seen in Fig. 2.5. The electron is set in motion with energy E at an angle ϕ, while the incoming x-ray is scattered at an angle θ with energy $h\nu'$, which can be found using:

$$h\nu' = h\nu \frac{1}{1 + \alpha(1 - \cos\theta)} \tag{2.3}$$

where $\alpha = \frac{h\nu}{m_0 c^2}$ and $m_0 c^2$ is 511 keV, or the rest energy of the electron. The energy the electron gains as kinetic energy is the difference between the x-ray's energy before and after the collision. The lowest energy that can be imparted to the electron is ~0, when the x-ray

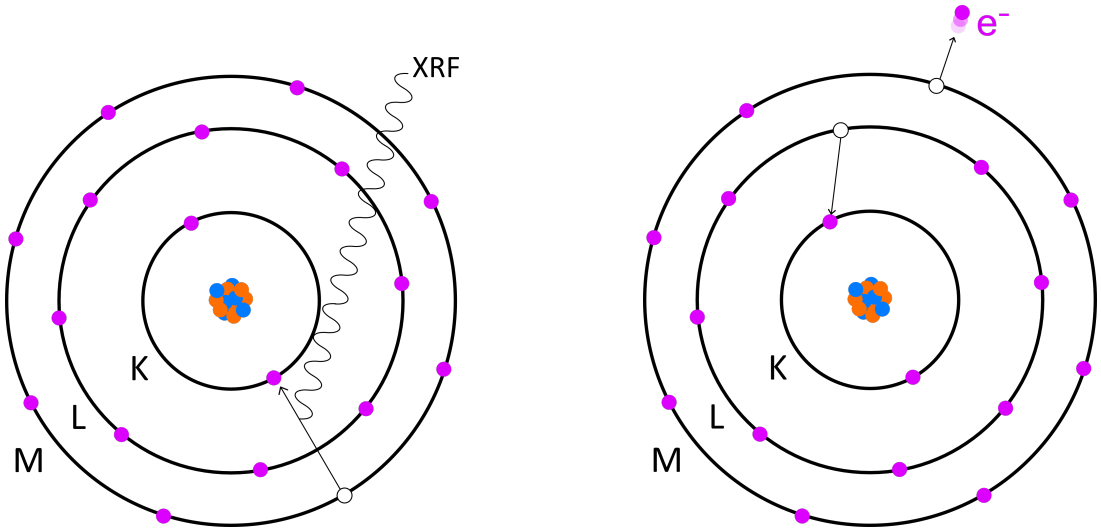

Figure 2.4: (a) A diagram of the process of fluorescence after a K-shell space has been filled by an M-shell electron. A fluorescent x-ray is released with energy $h\nu = E_K - E_M$. (b) A diagram of the release of a Meitner-Auger electron after a K-shell space has been filled by an L-shell electron. An M-shell electron (e^-) is released with kinetic energy $E = E_K - E_L - E_M$.

strikes only a glancing blow to the electron and continues with essentially no deviation and no loss in energy. In this case the electron is ejected at a 90° angle. The maximum energy that can be imparted to the electron occurs when the x-ray strikes the electron directly and rebounds at an angle 180° to its initial path. The electron is set in motion in the original direction of the x-ray. Thus, over all possible Compton interaction angles, the photon can be scattered at any angle between 0 and 180 degrees and the electron can be set in motion at angles between 0 and 90 degrees, both relative to the incident x-ray's direction. The relationship between the two angles can be defined by the equation below:

$$\cot\phi = (1+\alpha)\tan\left(\frac{\theta}{2}\right) \tag{2.4}$$

The differential cross section per unit solid angle ($\frac{d\sigma}{d\Phi}$) is given by Klein-Nishina equation [15], which describes the probability of the process happening as a function of initial x-ray energy and x-ray scattering angle. This equation is seen below:

$$\frac{d\sigma}{d\Phi} = \frac{r_0^2}{2}(1+\cos^2\theta)\left(\frac{1}{1+\alpha(1-\cos\theta)}\right)^2\left(1+\frac{\alpha^2(1-\cos\theta)^2}{[1+\alpha(1-\cos\theta)](1+\cos^2\theta)}\right) \tag{2.5}$$

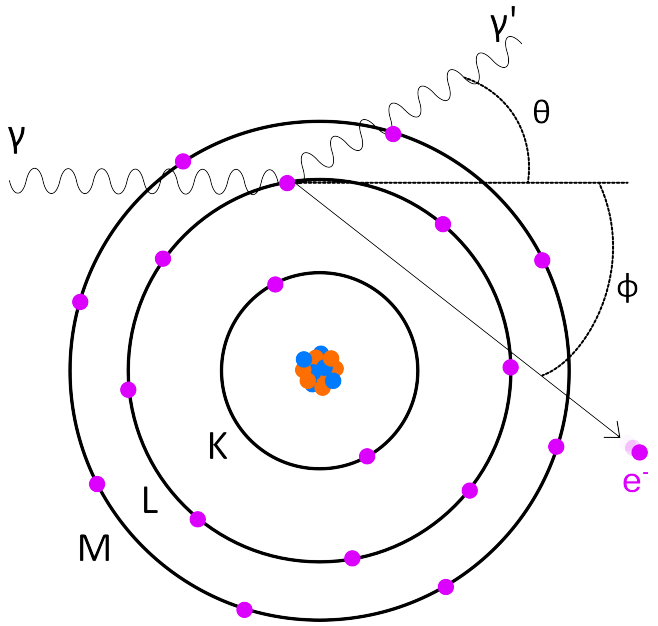

Figure 2.5: A diagram of the process of Compton scattering. The initial x-ray (γ) ejects an electron (e^-) at an angle ϕ and is itself scattered (γ') at an angle θ with a reduction in energy.

where $r_0 = 2.818 * 10^{-15}$ m is the classical electron radius. The Klein-Nishina equation is only valid for truly free electrons, which is not usually the case for electrons within the medium. A slight modification is necessary for bound electrons, which is dependent on $h\nu$, θ, and the atomic number of the medium. The probability of Compton scattering depends linearly on Z and inversely on the incident energy of the x-ray.

2.1.7 *Bremsstrahlung*

A number of these processes have ejected electrons from atoms within the medium, but what happens to those electrons after leaving the atom? The first type of interaction are collisional, in which the initial electron collides with other atomic electrons, transferring kinetic energy to the medium. Depending on the energy transferred to these atomic electrons, they may also be ejected and go on to collide with additional electrons. These types of collisions transfer energy to the medium which largely ends up as heat.

The second type of interaction is *bremsstrahlung*, or braking radiation. This occurs when an electron passes close to the nucleus an atom. The attraction due to the polar charges of the nucleus of the atom cause the electron to decelerate and change direction, which necessitates a loss of energy. The release of energy takes the form of a *bremsstrahlung* x-ray

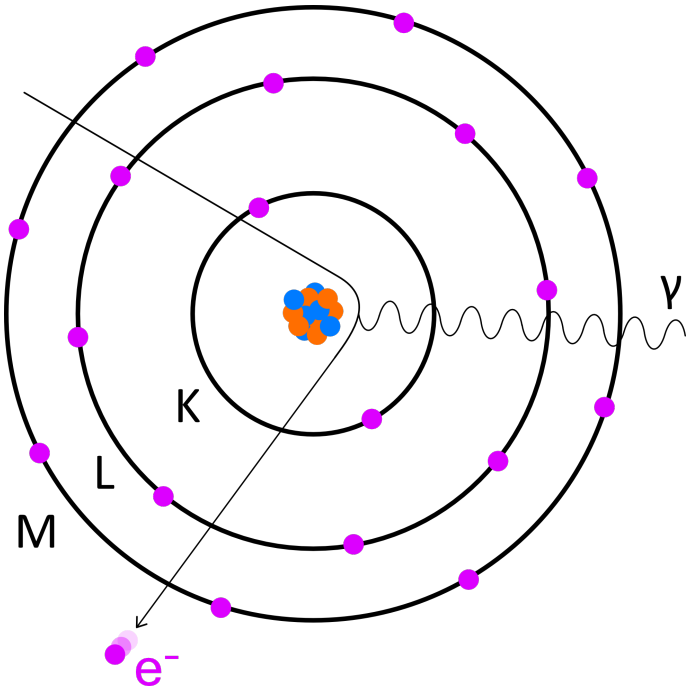

Figure 2.6: A diagram of the *bremsstrahlung* process. A free electron (e^-) interacts closely with the nucleus of an atom, causing deceleration including a change in direction. A *bremsstrahlung* x-ray (γ) is released due to the loss of energy caused by the deceleration.

(Fig. 2.6). The degree of deceleration the electron experiences dictates the energy lost. An impact with the nucleus of the atom results in a complete loss of kinetic energy and the resulting *bremsstrahlung* x-ray acquires the full energy of the electron. Interactions that occur farther from the nucleus result is less energy lost, and a less energetic *bremsstrahlung* x-ray.

2.2 X-ray Sources

The first step in any x-ray imaging, including CT, is the generation of x-rays. X-rays are generated by first producing electrons and then converting them to x-ray radiation by accelerating them into a target material. X-rays are then produced through *bremsstrahlung* and characteristic emission as described above, when the electrons interact with the target material. The equipment that generates x-rays in this manner is called an x-ray tube, a simplified diagram of which can be seen in Fig. 2.7 [16]. For x-ray imaging a large voltage (the tube voltage) is applied across the two electrodes: the cathode and the anode which are encased within a vacuum. The cathode is made up of a helical, tungsten filament which is heated via the filament circuit. The heated cathode emits electrons through thermionic

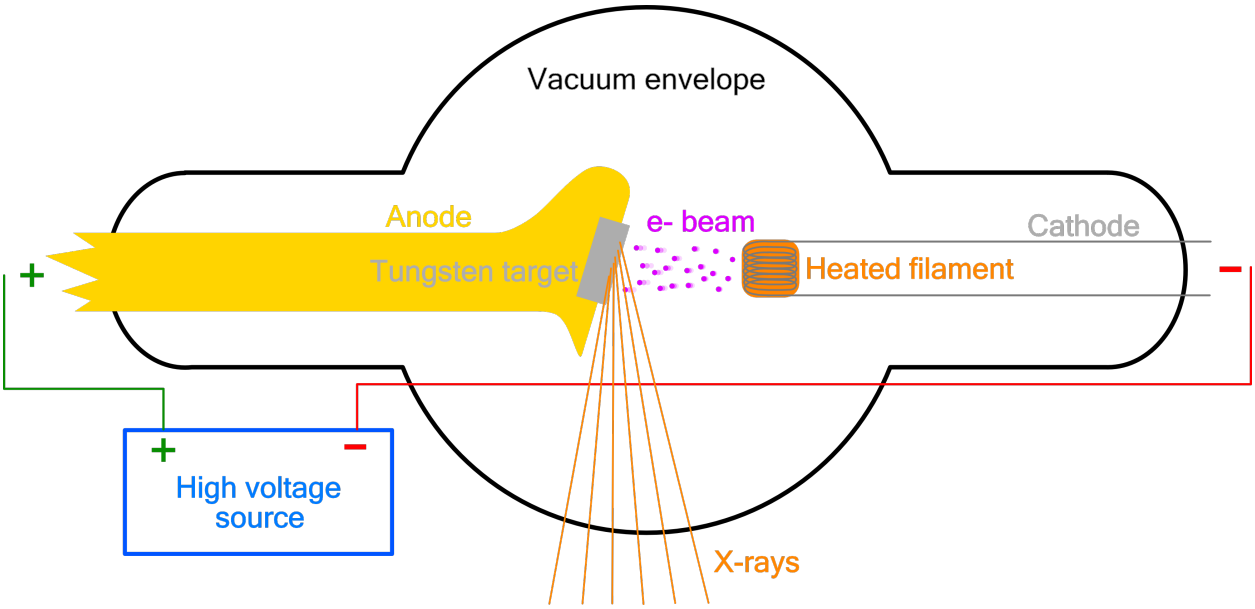

Figure 2.7: Diagram of an x-ray tube, adapted from Bushberg *et al* (2011) [16].

emission, with the rate of emission determined by the filament current. The electrons are then accelerated from the cathode to the anode due to the applied tube voltage, which determines the energy the electrons acquire before impinging the target anode. A tube voltage of 100 kV means the electrons will gain an energy of 100 keV, as the definition of eV is the energy gained by an electron accelerated through a potential of 1 V. The anode is made up of a target, usually a high-Z material, such as tungsten, embedded within the greater copper anode, which allows for heat dissipation. Most of the energy of the electrons is deposited in the target as heat through collisional interactions, but a portion produces *bremsstrahlung* or results in characteristic radiation. *Bremsstrahlung* is produced isotropically, so the x-ray tube is also shielded to prevent x-rays from escaping the tube except through x-ray window, positioned 90° parallel to the path between the cathode and the anode. The anode is also tilted towards the window in order to have the least amount of target material for the x-rays to travel through.

All the electrons are accelerated to their peak energy by the tube voltage, but the x-ray spectrum produced ranges from 0 keV to the peak electron energy. In an unfiltered x-ray spectrum produced through *bremsstrahlung*, the most x-rays are produced close to 0 keV, and decreases linearly with energy, until it reaches 0 and the maximum x-ray energy dictated by the tube voltage (Fig. 2.8a). Filtration is almost always added to an x-ray beam, in the form of thin sheets of metals such as aluminum, copper, titanium, and tin to achieve the desired mean x-ray energy and spectrum shape. Generally, with filtration

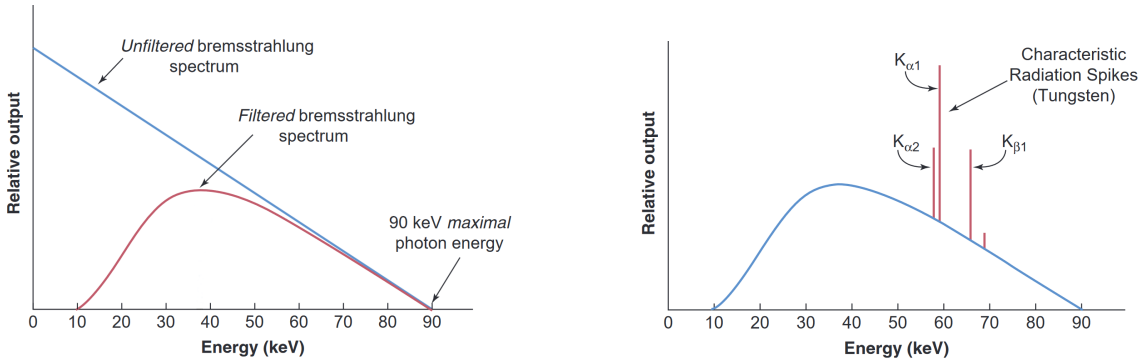

Figure 2.8: (a) Plot showing the unfiltered *bremsstrahlung* spectrum decreasing linearly from a maximum at 0 keV to zero at the peak x-ray energy. Additionally a filtered spectrum is also shown. (b) The same 90 kVp filtered spectrum from (a) is shown along with the characteristic peaks from the tungsten target of the x-ray tube. Adapted from Bushberg *et al* (2011) [16].

there are no x-rays with energy below at most 10 keV in filtered x-ray beams. In addition to the *bremsstrahlung* spectrum, there is also the characteristic radiation spectrum, which is defined by the target material (Fig. 2.8b). The x-ray energies seen in the characteristic x-ray spectrum are determined by the difference in binding energies between the material's electron shells. Generally, only the transitions that result with an electron filling a vacancy in the K-shell are of sufficient energy to be of practical use in x-ray imaging. These appear as spikes at the characteristic energies in the total x-ray spectrum, which is the sum of the characteristic and *bremsstrahlung* spectra. One of the most common x-ray target materials is tungsten, which has characteristic energies of 59.32 keV, 57.98 keV and 67.24 keV.

2.3 X-ray Detectors

Perhaps the most important aspect of CT is the detection of x-rays, which forms the basis for the resulting images. The vast majority of current CT systems utilize energy-integrating detectors (EIDs). However, high-flux photon-counting detectors (PCDs) have been researched for their potential in CT imaging for the past 20 years and are being integrated into the next generation of CT systems. In this section, both EIDs and PCDs will be introduced along with the advantages and disadvantages of both.

2.3.1 Energy-Integrating Detectors

Current EIDs are indirect detectors, meaning there is an intermediate step between x-ray absorption and the conversion to electrical signal. The first component of an EID module is the ceramic scintillator crystal in which x-rays are absorbed and light photons are produced. The material used for the scintillator varies depending on the imaging requirements, but generally depends mostly on the energy of x-rays being used for imaging. For current conventional CT systems, detector scintillators are usually composed of Gd_2O_2S (GOS), $CdWO_4$, or CsI [17, 2, 18]. Regardless of the crystal type, when an x-ray is absorbed within the scintillator light photons are promptly produced, the number of which is proportional to the energy of the x-ray, or the energy deposited in the interaction within the scintillator (Fig. 2.9a). For a single detector module, the crystal will be scored or cut with a saw or laser to divide the crystal into individual pixels to allow for spatial information to be recorded. An opaque filler is introduced to the scored areas to prevent cross-talk, or the spread of light photons between individual pixels [16]. The light photons propagate isotropically from the point of the x-ray interaction, so spatial resolution would be degraded without such filler. Photodiodes are connected to the bottom of the scintillator to collect and quantify the light signal produced in each pixel. A cross section view of an EID can be seen in Fig. 2.9a. The detector module, made up of the photodiodes and the scintillator crystal are then placed on top of a larger stack of electronic devices which amplify the signal from the photodiode as well as convert the signal to a digital number. The electronics integrate the total signal for individual pixels over the acquisition time window, which is usually on the order of 0.2 to 0.5 ms [16].

2.3.2 Photon-Counting Detectors

PCDs, unlike EIDs, are direct conversion detectors; there is no intermediate step of converting x-rays to light photons. As the name implies, PCDs operate by counting individual x-rays as they interact with the detector crystal. Most current PCD technology utilizes CdTe or CdZnTe (CZT) semiconductor crystals, though silicon is also used in some systems [11, 9, 2, 17]. A solid cathode layer is usually deposited on the top of the crystal and pixellated anodes are attached to the bottom, which are electrically isolated from one another. A high voltage is applied across the crystal and as x-rays pass through the cathode they enter the semiconductor. As the x-rays interact within the crystal, electron-hole pairs are created, the number of which is proportional to the energy deposited by the x-ray. A cross section view of an PCD can be seen in Fig. 2.9b. Due to the high voltage applied across the crystal,

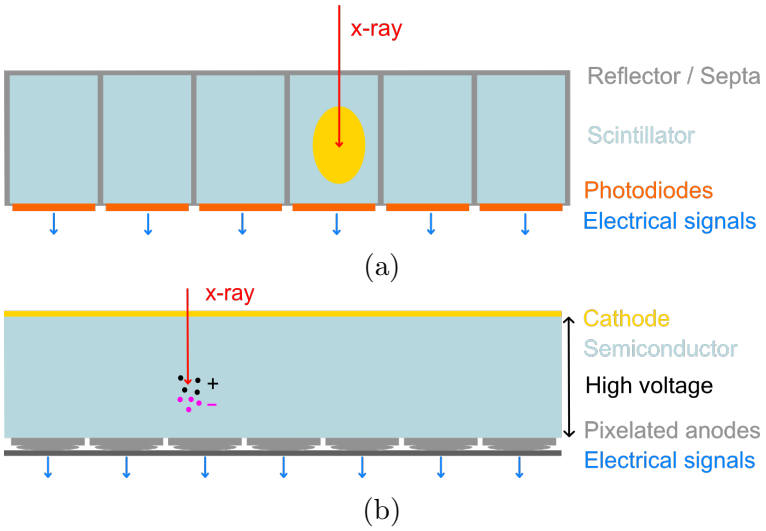

Figure 2.9: (a) Energy-integrating detector. And x-ray is first attenuated in the scintillator layer, which produces light. The light is then detected by the photodiodes and converted into electrical signals. (b) Photon-counting detector. An x-ray is attenuated in the semiconductor and electron/hole pairs are produced directly. Due to the high voltage applied across the semiconductor, the electrons are accelerated to the anodes where they are converted to electrical signals.

the electrons are accelerated towards the anode closest to the location of the interaction. Because the anodes are pixellated, no additional material is needed to subdivide the crystal into individual pixels. The anodes are also connected to an application specific integrated circuit (ASIC) which processes the signal collected by the anodes. As the electron-charge clouds are collected by the anode, the ASIC reads an electrical spike, which is proportional to the number of electrons and thus the energy of the x-ray. Depending on the type of ASIC, 2–8 programmable thresholds are generally available [11]. Based on the electric pulse height, the ASIC will increment the counter between the appropriate thresholds by one, indicating that the x-ray's energy was between the energies corresponding to the two thresholds. Unlike EIDs, where the total signal is integrated together for each pixel, pixels within PCDs have multiple counters defining the number of x-rays within specific energy ranges that were detected.

2.3.3 Advantages and Disadvantages of EIDs and PCDs

PCDs offer a number of advantages over EIDs, hence the interest in building the next generation of CT scanners with PCDs. However, the advantages also come with drawbacks which have yet to be fully resolved or compensated for. The following section will detail the

properties of EIDs and PCDs and the benefits and drawbacks of each.

Energy Information

The first feature offered by PCDs is, of course, the preservation of the energy information of individual x-rays. As described above, PCD signal is a direct measure of the number of x-rays detected within a specific energy range while EID signal is a measure of the total energy deposited. PCDs sort the detections according to their electrical magnitude, preserving the energy information of the x-rays, while the same information is lost with EIDs because it is integrated into the total.

Spatial Resolution

One important parameter of both detectors is the spatial resolution. For CT systems the system spatial resolution in reconstructed images depends on a varied set of system parameters and components which will be described in subsequent sections. The most important feature the detector contributes to the spatial resolution is the size of individual pixels. Detector pixels can be manufactured to a specified size in both detector types, however smaller pixels are possible with PCDs compared to EIDs. With EIDs, pixels become more dose-inefficient as they become smaller since the septa between pixels are limited to a finite width. As the pixel size is reduced, more of the detector area will be covered with septa versus detector crystal, rendering a large proportion of the x-ray beam useless. So while smaller pixels in EIDs become dose-inefficient, PCD pixels retain their efficiency. However, a smaller pixel size in PCDs has a drawback not seen in EIDs: charge-sharing.

Where EIDs have septa to prevent light photons from propagating to adjacent pixels, there are no such structures in PCDs. This leads to a phenomena referred to as charge-sharing. The charge-cloud created by an x-ray interaction is not finite in size and the charge-cloud spreads out slightly as it travels to the anode. If an x-ray interacts near the border between pixels (Fig. 2.10) the full charge may be split between multiple pixels. Depending on the pulse height registered in the pixels, the x-ray may be counted more than once and the energy of the interaction will be reduced accordingly. This serves to reduce the spatial resolution, by causing x-rays to be registered over a larger area, and to reduce the accuracy of the energy information. The magnitude of the charge-sharing effect depends on the pixel size as well. As pixel size is reduced the distance between pixels becomes smaller, increasing the likelihood that the electrons will collected by multiple pixels.

Both PCDs and EIDs experience crosstalk, which occurs when a fluorescent x-ray or

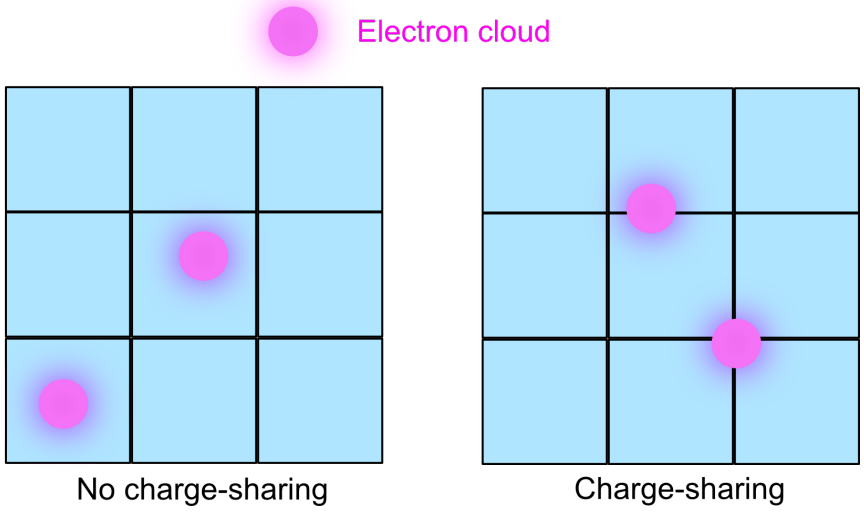

Figure 2.10: Charge-sharing. The left 3×3 pixel array shows electron clouds generated from x-ray detections in which no charge-sharing would occur between pixels. The right 3×3 pixel array shows the resulting electron clouds from detections that occurred on or near a border between pixels, causing the charge to be spread over multiple pixels.

Compton scattered x-ray deposit a portion of the energy of the incident x-ray outside of the initial pixel.

Image Noise

Image noise affects both EIDs and PCDs and can be traced back to two sources: quantum noise and electronic noise. Quantum noise is dependent on the inherent randomness of x-ray interactions and relies on the number of detected x-rays. Electronic noise is the umbrella under which all other noise falls under and originates from the electronic circuits within the detector module and the larger system. Electronic noise is not dependent on the number of detected x-rays. Thus, the relative effect of quantum and electronic noise depends on the incident x-ray flux. Electronic noise is generally only dominant under conditions in which there are lower numbers of detected x-rays, such as with low-dose scans or with large patients in which a greater proportion of the incident spectrum is attenuated before hitting the detector. Given such a situation, EIDs suffer more from electronic noise when compared with PCDs because the signal generated from the electronic noise is integrated into the total, which due to the low flux is relatively small. Thus the electronic noise has a greater effect. For PCDs, the low level signal from electronic noise can be completely mitigated by setting the trigger threshold above it. As seen in Fig. 2.11a, the lowest, or trigger, threshold can

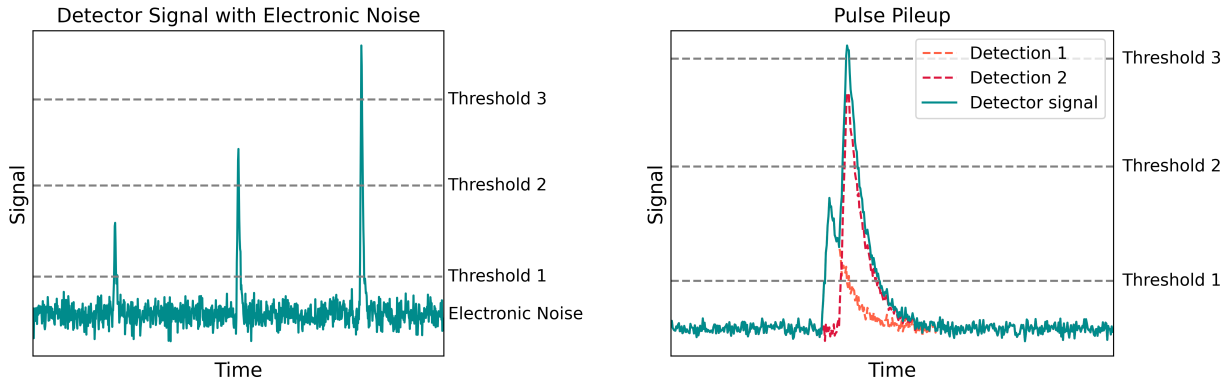

(a) (b)

Figure 2.11: (a) X-ray detections with electronic noise. One detection would be counted in each energy bin defined between the thresholds. The electronic noise all occurs below the first threshold so would not contribute to the final signal. (b) Pulse pileup. Two x-rays are detected within the same pixel within a short time. The resulting pulses overlap creating one large pulse which is counted in the highest energy bin.

be set such that the highest spikes generated from electronic noise are below it and thus completely neglected from the resulting signal.

While the individual counting nature of PCDs lends benefits in terms of reducing noise under low flux conditions especially, it can also be a detriment for high-flux situations. For an individual x-ray to be counted by the PCD, its pulse within the electronics must be distinguishable from the pulses received immediately before and after. Under high-flux conditions, two or more x-rays can interact within the same pixel at a time interval close enough that the pulses are not separable (Fig. 2.11)b. The system then records the multiple x-rays as a single event at an energy that is higher than that of any of the x-rays individually. This effect is called pileup and it has the effect of reducing the reliability of the energy information from the PCD. As with charge-sharing, the pileup can be mitigated by selecting an appropriate flux for the pixel size of the PCD. However, reducing the pixel size reduces pileup, but increases charge-sharing, so a balance must be struck between the two effects. EIDs offer a benefit in this case, as they are not effected by pileup; more x-ray interactions result in more light photons, which all is measured as more signal, regardless of how close together the events occurred.

PCDs can also suffer from non-conforming pixels, which is a catch-all term for pixels that do not behave as other adjacent pixels in response to the same input. Each pixel has its own threshold calibrations which can be defective and there are other issues such as the individual contact points with the ASIC or crystal abnormalities which affect the counting response.

Sometimes the direct cause is not known and can only be compensated for. However, it does add noise to the system.

2.3.4 Anti-Scatter Grids

Scatter is a phenomena inherent in all x-ray imaging and refers to all x-rays which interact within or are produced within the subject due to x-ray interactions. Ideally, x-ray imaging, including CT would only measure x-rays which are produced by the source and do not interact within the subject. However, scatter is always present and also reaches the detector which reduces image quality. Clinical CT scanners usually employ anti-scatter grids (ASGs), which are either one or two dimensional metal grids which are placed just in of the detector array so that the beam passes through the grid before hitting the detector. The grid septa align with the septa within the EID crystal or with the "streets" between the pixelated anodes of PCDs and extend above the detector. The ASG is also manufactured to match the beam divergence so x-rays produced by the source have a straight path to the detector pixels. This means that x-rays not matching the beam divergence are more likely to be attenuated by the ASG and restricted from being detected and reducing image quality.

2.4 CT Image Acquisition and Reconstruction

2.4.1 Projection images

Projection images refer to the two-dimensional (2D) data acquired by a computed tomography (CT) scanner. These images are obtained by acquiring 2D x-ray images at various angles around the subject. Thus, a single projection image is a measurement of the x-ray attenuation through the subject at a single angle. The attenuation is calculated using the following equation:

$$P = -ln\left(\frac{I}{I_0}\right) \tag{2.6}$$

where P is the resulting 2D projection image, which is a measure of the attenuation, I is the signal in the 2D x-ray images, and I_0 is the signal in a flat-field or air scan acquisition, which is acquired with the same parameters as the 2D x-ray image, but with no subject in the path of the beam.

In a conventional clinical scanner, the image acquisition is performed by rotating the x-ray source and detector around the subject, capturing a series of projected images from multiple angles. A sinogram is a graphical representation of the raw data, where each row

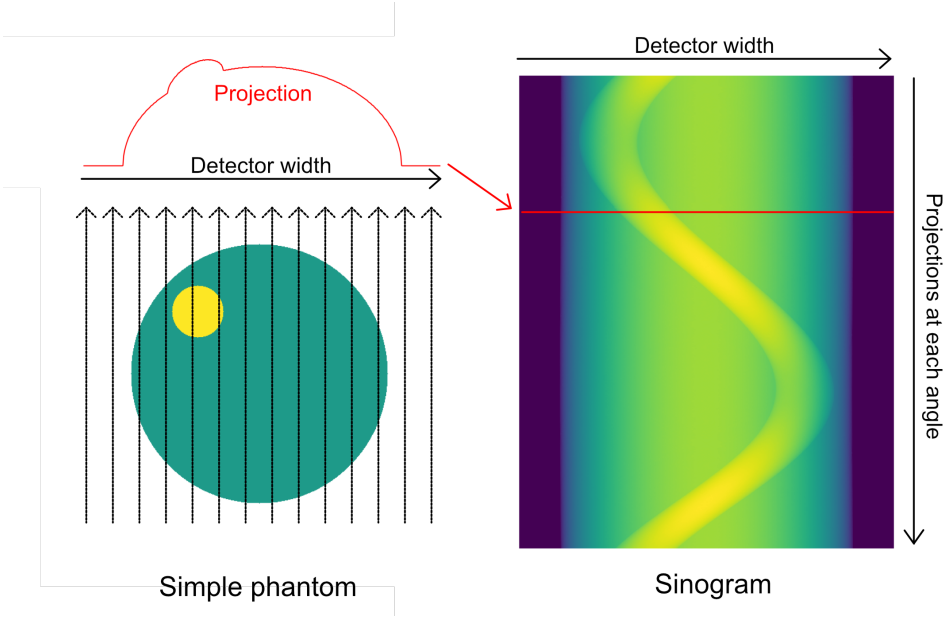

Figure 2.12: On the right is a simple phantom, with the projection for one row of pixels of a detector shown in red. On the left is the resulting sinogram for that row of pixels at each each angle around the simple phantom. The red line shows the location of the projection shown on the right.

corresponds to a single projection image, and the columns represent the detectors (Fig. 2.12). The intensity at each point in the sinogram indicates the attenuation of X-rays at specific angles, providing a comprehensive dataset for image reconstruction.

The projection data plays a crucial role in the reconstruction of CT images. It contains all the raw data necessary to reconstruct cross-sectional images of the scanned subject. The conversion of the projection data into actual CT images is achieved through computational algorithms, such as filtered backprojection or iterative reconstruction.

Moreover, the quality and completeness of the projection data directly impact the quality of the reconstructed CT images. Any artifacts or missing data in the sinogram can lead to corresponding inaccuracies or artifacts in the final CT images. Therefore, ensuring the integrity of the projection data is essential for obtaining high-quality diagnostic images.

2.4.2 CT Geometries

There are different CT geometries used for image acquisition, including parallel-beam, fan-beam, and cone-beam geometries. Parallel-beam geometry refers to the configuration in which the x-ray source emits a parallel beam of x-rays, and the detector array is perpendicular to the emitted beam. In practice, parallel-beam geometry it is simulated by moving a pencil

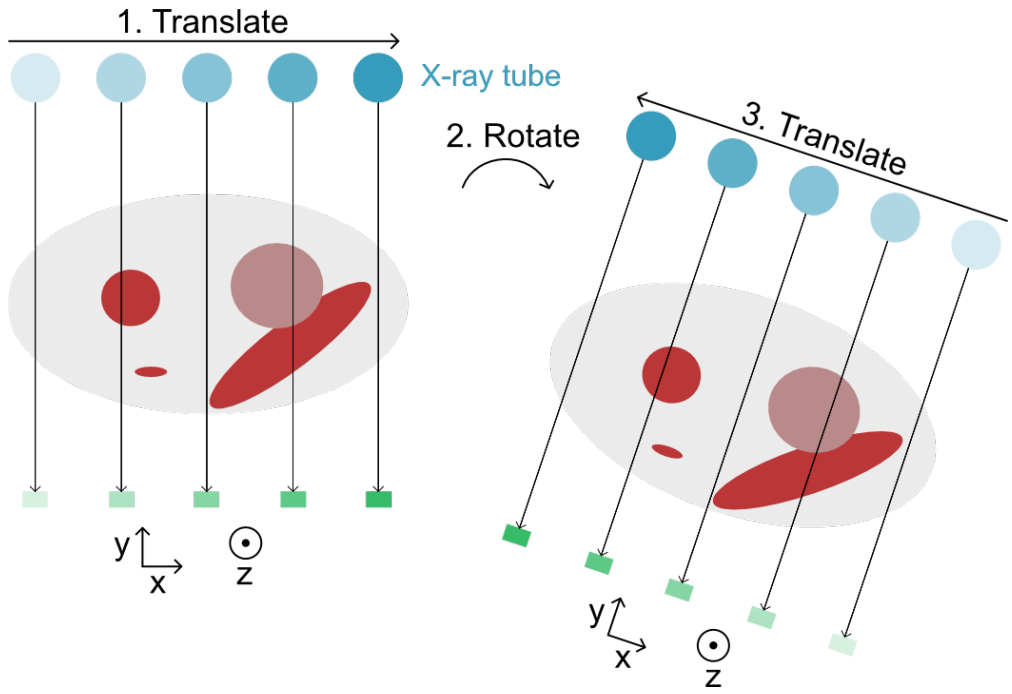

Figure 2.13: Parallel beam geometry. A single detector element and the x-ray tube are translated parallel to another to capture the full subject. The x-ray tube and detector are then rotated around the subject by a specific angle and the process is repeated until the x-ray tube and detector have rotated fully around the subject.

beam across the object in a controlled pattern for each projection image (Fig. 2.13). Parallel-beam geometry was the original CT configuration and serves as the basis for algorithms used in fan-beam and cone-beam geometries.

Fan-beam geometry involves the x-ray source emitting a diverging beam of x-rays in a fan shape onto a row of distinct detector pixels (Fig. 2.14). The detector pixels offer spatial discrimination in the image plane, negating the need for detector translation. The angle of the fan beam is determined by the width of the detector and the desired field of view (FOV) of the scanner. The FOV is the circle within the x-y plane defined by the edges of the x-ray beam as it rotates around the subject (Fig. 2.14). Unlike the detector depicted in Fig. 2.14, most modern CT scanners offer a curved detector array. The curved detector array maintains the distance from the source to each of the detector elements voiding the need for correction methods due to the inverse square law and heel effect–based differences in fluence. For the most basic fan-beam projection, the detector consists of only a single row of pixels which captures a single slice per 360° rotation, and the source and detector must still be translated in the z-direction (Fig. 2.14) relative to the subject to obtain more slices.

Cone-beam geometry, on the other hand, refers to the configuration in which the x-ray

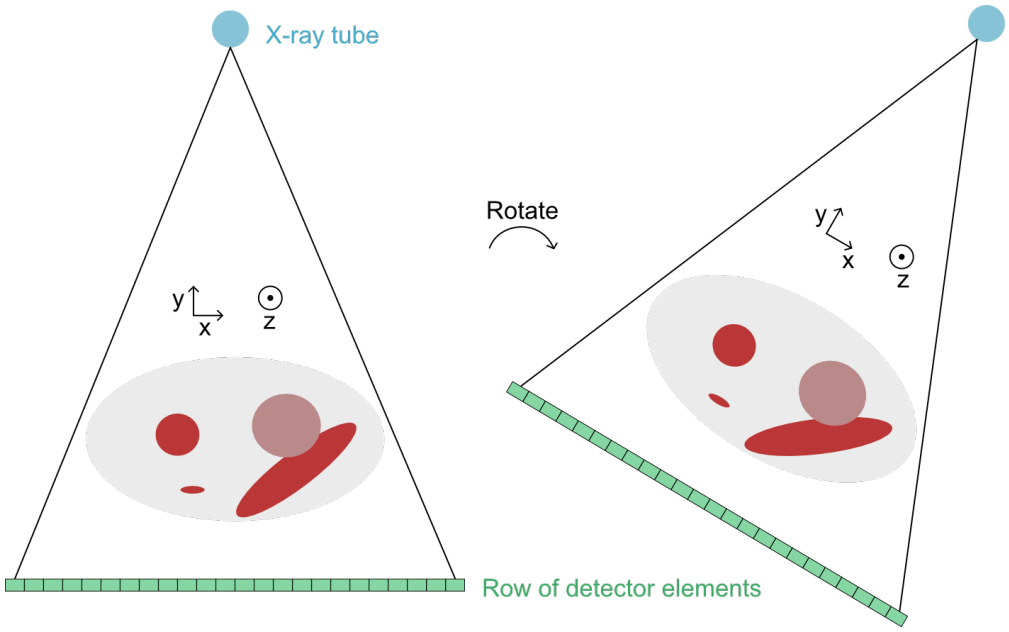

Figure 2.14: Fan beam geometry. The x-ray beam is fan-shaped and the row of detector elements provide the spatial information given by the translation in parallel-beam geometry. The x-ray ray tube and detector are rotated around the subject to cover the full 2π geometry.

source emits a conical beam of x-rays, and the detector array is a two-dimensional panel (Fig. 2.15). The difference in x-ray path length to the different areas of the detector requires additional mathematical compensation in the reconstruction algorithms as well. Again, in most modern CT scanners, the detector array is curved to match the divergence of the x-ray beam, though not in the z-direction (Fig. 2.15). Flat panel detectors are also used in specialized systems and on radiation therapy treatment machines. Curved detectors have multiple rows of pixels in the z-direction, and only requires corrections in that direction, while for flat-panel detectors, both the directions require correction.

2.4.3 Imaging Dose

One of the most important factors to consider in any CT scan is the radiation dose to the patient. Dose is defined as the mean energy deposited per unit mass to a medium and is measured in Gray (Gy) or joules per kilogram (J/kg). In x-ray imaging, dose is deposited by the electrons emitted within in the medium due to x-ray interactions. As radiation dose does have a carcinogenic effect, it is important to keep the dose to patients as low as reasonably achievable to conduct the required scans. Typically, for CT, a single scan can range from 0.1 to 100 mGy [16].

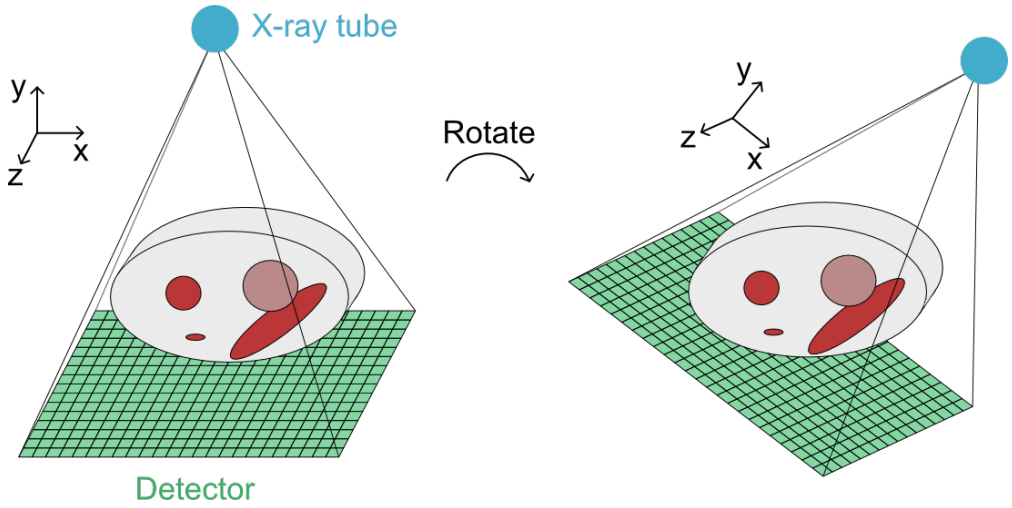

Figure 2.15: Cone-beam geometry. The x-ray beam is cone-shaped and the multiple rows of detector elements provide the spatial information in the z-direction, enabling the capture of multiple slices simultaneously. The x-ray ray tube and detector are rotated around the subject to cover the full 2π geometry.

2.4.4 X-ray Beam Shaping

In addition to the x-ray beam filtration mentioned above in section 2.2 (Fig. **??**) in which metal is added to the path of an x-ray beam in order to adjust its quality before reaching the patient, the x-ray beam is also shaped in CT. This beam shaping is accomplished by using a bow tie filter. If no beam shaping is used, the periphery of the imaging subject would receive slightly more dose at every beam angle. This is due to the divergent nature of the x-ray beam (Fig. 2.14). The beam at the periphery and the beam at the center of the subject would supply similar entrance doses. However, the beam at the center of the subject would be much more highly attenuated due to the traveling through the full thickness of the subject. The beam on the periphery gives a much higher dose at the exit point. As the full beam rotates around the subject, more dose is accumulated at the edges of the subject, meaning the subject is receives more dose than is necessary for the scan. A bow tie filter preferentially attenuates the edges of the beam compared to the central portion of the beam, shaping it to supply as uniform as dose to the subject as possible.

2.4.5 Filtered Backprojection

Filtered backprojection (FBP) is a fundamental step in CT reconstruction. First, the acquired sinogram data is passed through a filter to suppress or enhance specific features of the data. The filtering is done in the frequency, or Fourier, domain using a convolution oper-

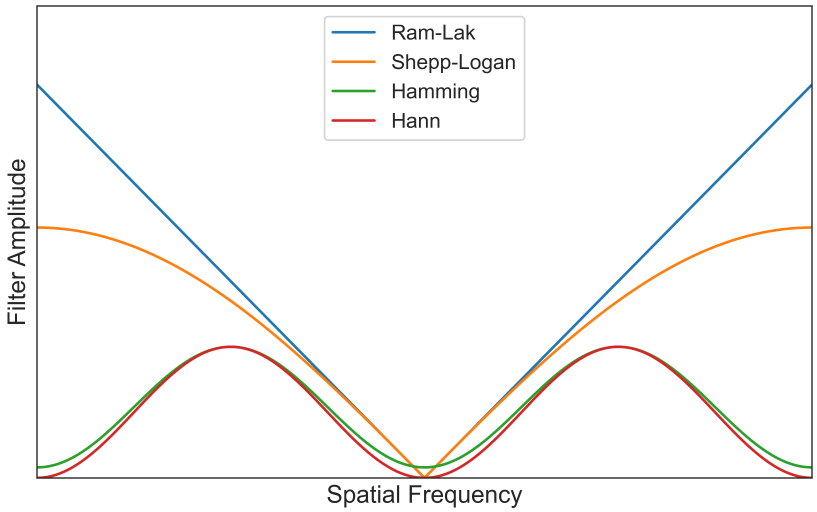

Figure 2.16: Reconstruction filters. Amplitude as a function of spatial frequency for several reconstruction filters.

ation. While there are many different filters a few common ones include the Ram-Lak filter, Shepp-Logan filter, and Hann or Hamming window filters (Fig. 2.16). Once the sinogram data has been filtered it is then backprojected to obtain the corresponding two-dimensional section. Backprojection involves integrating the pixel values from the sinogram back into the image space using the inverse Radon Transform [19]. This reconstructs a 2D or 3D image of the scanned object depending on the dimensions of the detector.

2.4.6 Cone-beam Algorithms

Cone-beam algorithms are specifically designed for cone-beam CT geometry. The most basic cone-beam algorithm is the Feldkamp-Davis-Kress, or FDK, algorithm [20] and it reconstructs the entire volume of the data set as defined by the source and detector geometry. This algorithm is an adaptation of the 2D fan-beam FBP algorithm to the 3D cone-beam geometry and corrects from beam divergence and the source to detector differences over the full detector array. It has been widely used in circular cone-beam CT and produces good results for even moderate cone-angles, the authors demonstrated its effectiveness for cone angles up to 53°.

2.4.7 Iterative Reconstruction

In addition to FBP, iterative reconstruction techniques are also used in CT reconstruction. These techniques utilize iterative algorithms to obtain a more accurate reconstruction by repeatedly updating the image estimate after starting from an initial guess, such as a simple FBP image. Iterative reconstruction algorithms have the advantage of modeling the system geometry more accurately and incorporating physical effects such as beam spectrum, noise, beam hardening effects.

2.5 Image Quality

At the heart of CT's usefulness in the clinic, and other industries, lies the quality of its images. High-quality CT images ensure precise detail, enabling clinicians to detect subtle abnormalities, differentiate between tissue types, and accurately assess pathological conditions. This precision is not only critical for diagnosis but also plays a vital role in other areas such as radiotherapy treatment planning. In radiation oncology, CT images of each patient are used to develop the specific delivery plan, ensuring that the correct dose is administered precisely to the targeted area while sparing surrounding healthy tissue. Conversely, poor image quality can lead to diagnostic errors and sub-optimal radiation planning, potentially impacting patient outcomes adversely. Therefore, maintaining and improving image quality in CT scans is not just a technical necessity, but a critical responsibility. It marries technology with patient care to drive informed medical decisions, enhance the efficacy of treatments, and optimize the safety and success of radiation therapy. There are a number of metrics that are used to benchmark image quality, which will be described here.

2.5.1 CT Image Signal

Signal in CT images is referred to as CT number and is measured in Hounsfield units (HU). CT number is a measure of the linear attenuation coefficient of the material at each point in the image and is described by the equation:

$$HU = 1000 \cdot \frac{\mu - \mu_{water}}{\mu_{water}} \tag{2.7}$$

where μ_{water} is the linear attenuation coefficient for water and μ is the linear attenuation coefficient of the material at the specific voxel in the image. The Hounsfield scale is defined such that air is -1000 HU and water is 0 HU.

2.5.2 Spatial Resolution

Spatial resolution is a critical metric in CT imaging, determining the ability of the system to distinguish between small structures and detail in the acquired images. It is fundamentally influenced by various CT acquisition parameters and can be quantitatively assessed using specific measurement methods.

There are a number of CT acquisition parameters which influence the resulting system spatial resolution. The first is the x-ray tube focal spot size. A smaller focal spot allows for finer detail to be resolved, but it may be limited by increased heat production at higher resolutions. The size of the individual pixels within the detector array also impacts spatial resolution. Smaller detector elements can capture finer details, leading to higher spatial resolution. Additionally, thicker slices can reduce spatial resolution in the z-dimension (along the subject's longitudinal axis) (Fig. 2.15). Thinner slices improve resolution but increase radiation dose and scanning time. Slices are also generally determined the height of the rows of detector pixels in the detector array. The effect of the focal spot size and detector pixel size is also dependent on the geometry of the CT system (Fig. 2.17), i.e. the distance from the x-ray source to isocentre (a) and the distance from the isocentre to the detector (b) [16]. The combination of these two parameters determines the magnification (M) of the system:

$$M = \frac{a+b}{a} \tag{2.8}$$

The size of the subject in reconstructed CT images will appear to magnified by the factor determined by Eq. 2.8. The further the total distance ($a+b$) is within the system, the larger the focal spot will appear on the detector. Finally, in helical CT scanning, the pitch (the table feed per rotation relative to the slice thickness) can affect resolution as well. A lower pitch tends to improve resolution but increases the radiation dose.

In addition to the physical parameters of the CT system and acquisition, the reconstruction algorithm and parameters will also affect the spatial resolution in the final CT images. FBP, as mentioned above, is the standard method, but the filter kernel applied will also affect the resolution, with some filters emphasizing edges and others softening them. Iterative reconstruction techniques are also becoming more prevalent, as they can improve image quality and reduce noise [16].

The measurement of the spatial resolution in reconstructed images is especially important for benchmarking CT systems, comparing images across different platforms, and monitoring changes to a single system over time. The main method for measuring spatial resolution is the Modulation Transfer Function (MTF). It describes the system's ability to reproduce

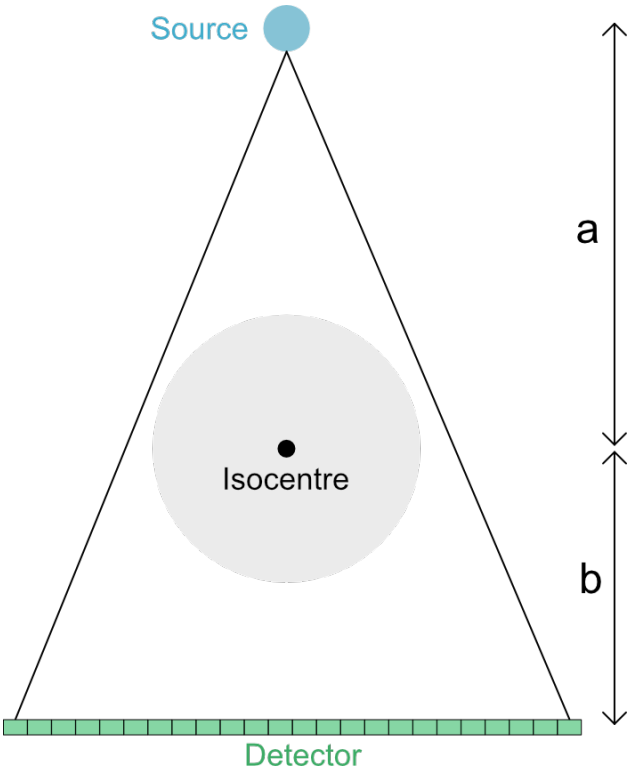

Figure 2.17: CT system geometry showing the x-ray source to isocentre distance (a) and the distance from the isocentre to the detector (b).

different levels of detail in an object, typically represented as a function of spatial frequency. The MTF curve is derived from the Line Spread Function (LSF) or the Edge Spread Function (ESF) and decreases with increasing spatial frequency. The MTF is normalized to its value at a spatial frequency of 0, and the limiting spatial frequency of the system is usually measured at 10 or 20% of the maximum MTF. Slice Sensitivity Profile (SSP) is also relevant for assessing the spatial resolution in the z-dimension of CT images. It measures the system's response to a point-like object and is defined as the shape of the system response to a point input along the z-axis. The SSP provides information about the effective thickness of the imaging slice and its impact on z-axis resolution [16]. Images of the same *ex-vivo* tissue sample with different resolution can be seen in Fig. 2.18.

Current CT applications require different spatial resolutions. Standard CT scans for routine diagnosis and radiation therapy treatment planning generally utilize a spatial resolution of 0.5–1.0 mm. However, for other applications such as lung imaging, cardiac imaging, CT angiography, and others, higher resolution is necessary, namely 0.1–0.2 mm [21], in order to resolve small structures.

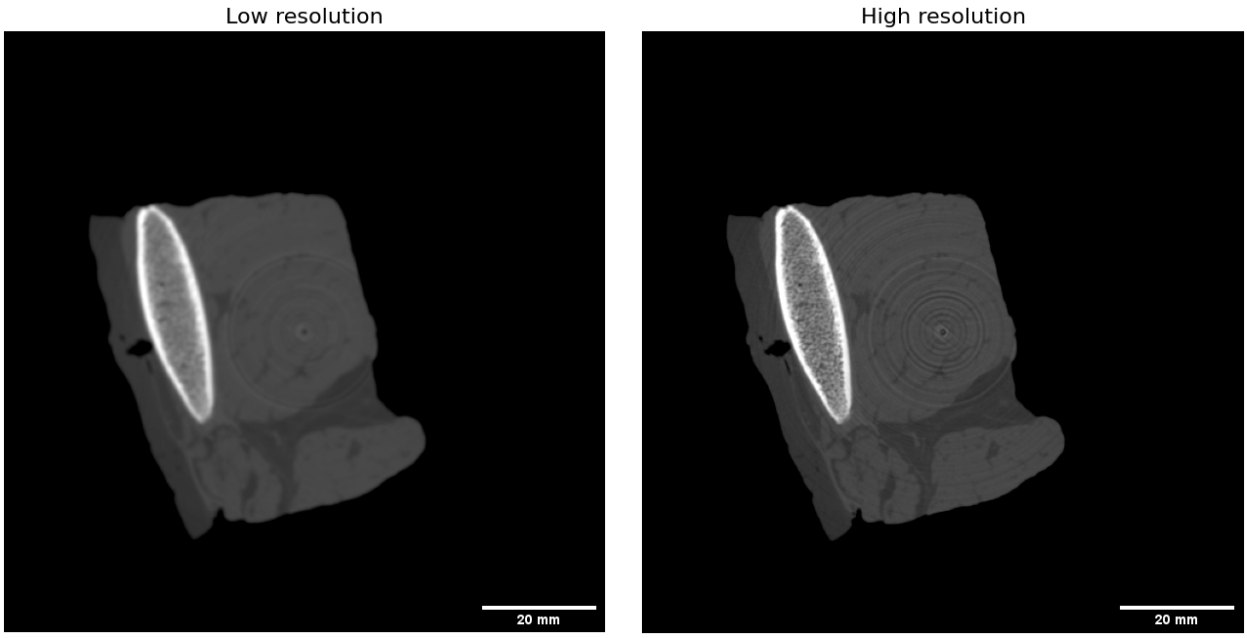

(a) (b)

Figure 2.18: Spatial resolution. CT slice of an *ex-vivo* tissue sample with (a) low resolution (b) high resolution.

2.5.3 Noise

Noise in CT images is an unavoidable byproduct of the imaging process, significantly influencing image quality. It affects the clarity and sharpness of the images, thereby impacting their usefulness. The first system parameters affecting image noise are the x-ray tube current and exposure time, which are often combined as a product into the current-time product (measured in mAs). Each is directly proportional to the number of x-rays generated. Thus, increasing the current-time product reduces noise by increasing the x-ray flux, but it also increases the patient's radiation exposure. The x-ray tube voltage influences the energy of x-rays; higher tube voltage settings increase x-ray penetration, reducing noise but potentially decreasing image contrast. Lower tube voltage settings can enhance contrast between soft tissues (Fig. 2.2b) due to the larger differences in attenuation at lower energies. However, a lower tube voltage may increase noise due to reduced x-ray penetration.

The efficiency of the CT detector in capturing x-rays also influences noise. Higher detector efficiency results in better signal capture and lower image noise. The detector efficiency can be affected by the detector crystal and electronics, whether there are septa and how large they are, and whether an anti-scatter grid is included. Thicker slices in the z-dimension also increases the signal by accumulating more x-rays, thus reducing noise. However, this comes

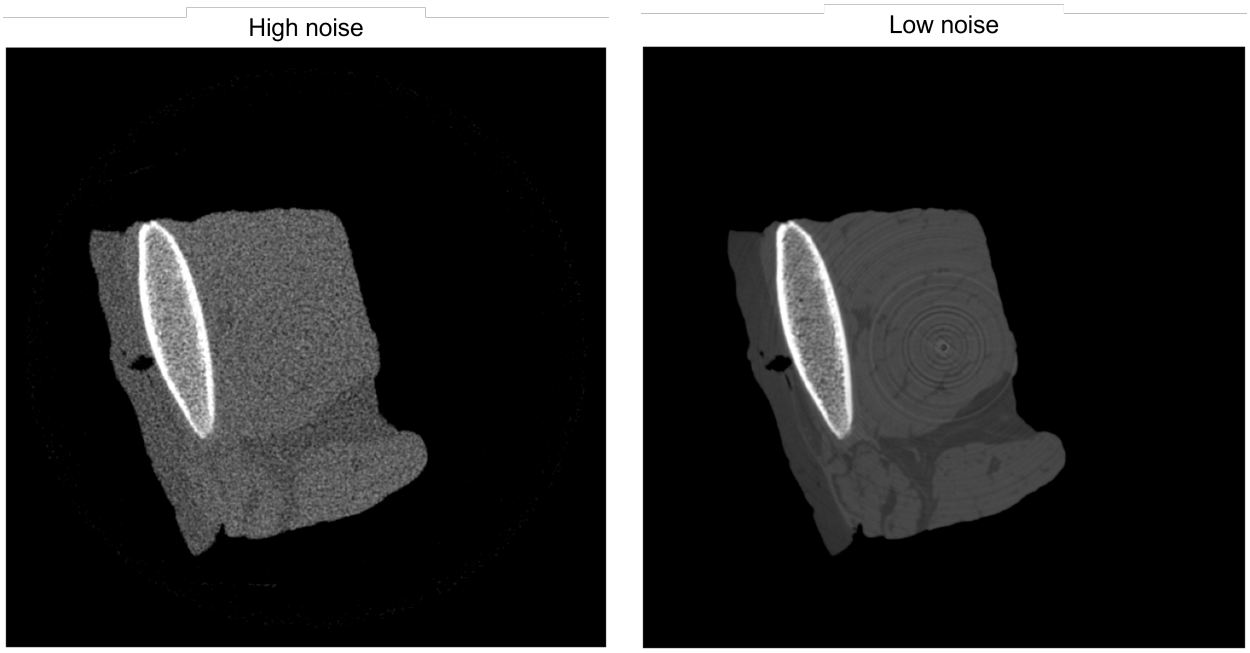

(a) (b)

Figure 2.19: Image noise. CT slice of an *ex-vivo* tissue sample with (a) high image noise (b) low image noise.

at the cost of reduced spatial resolution. And finally, the reconstruction algorithms and reconstruction filters will also affect the image noise. Iterative reconstruction techniques can significantly reduce noise compared to traditional FBP methods, even with reduced radiation doses.

The first and most common measurement of noise is to calculate the standard deviation of pixel values within a uniform region of the image. This region is typically chosen in an area without anatomical structures, like a region of uniform soft tissue or a homogeneous part of a phantom. The noise power spectrum (NPS) provides a more detailed characterization of noise, describing how noise varies across different spatial frequencies. It gives insights into the texture of the noise in the image, which can be important for image interpretation and patient diagnosis. And finally, while the signal-to-noise ratio (SNR) is often considered a measure of detectability, it is also a critical metric for assessing noise. SNR compares the level of a desired signal to the level of background noise, and a higher SNR indicates less noise relative to the signal [16]. Examples of low and high image noise can be seen in Fig. 2.19.

2.5.4 Contrast Detection

Contrast detection in CT imaging refers to the ability of the system to distinguish between differences in x-ray attenuation of various materials or tissues that make up the subject. It is a crucial factor in identifying and characterizing different anatomical structures and pathologies. The effectiveness of contrast detection is influenced by several CT acquisition parameters and can be measured using specific methods. The first is the x-ray tube voltage. The tube voltage setting affects the contrast in CT images because different tissues generally have higher differences in attenuation at lower energies. Therefore a lower tube voltage results in higher contrast between tissues. However, this may lead to an increase in noise due to the higher attenuation of the beam as it passes through the subject. As the beam passes through a subject it naturally hardens, or lower energy x-rays are more highly attenuated, raising the average energy of the beam. Beam hardening and other image artifacts can affect contrast detection, and will be discussed in the next section. Like spatial resolution and noise, the reconstruction algorithm and filter type can also enhance contrast detection. Iterative reconstruction techniques can improve the visibility of low-contrast structures and reduce noise. And finally, the use of various types of contrast agents can enhance the differences between tissue types. These agents operate by increasing the attenuation of specific structures, such as blood vessels or the gastrointestinal tract, making them more visible compared to the surrounding tissue. Contrast agents can be given intravenously or orally depending on the specific agent or application and will be in more detail in later sections.

Various methods exist to measure contrast, but perhaps the most common are the contrast-to-noise ratio (CNR) and SNR. CNR measuring the contrast between a region of interest (ROI) and the background relative to the amount of noise. It provides a quantitative assessment of the ability to detect specific structures within the image and is calculated as follows:

$$CNR = \frac{\bar{x}_{ROI} - \bar{x}_{BG}}{\sigma_{BG}} \tag{2.9}$$

where $\bar{x}_{ROI}$ and $\bar{x}_{BG}$ are the mean signal in the ROI and background, respectively, and σ_{ROI} is the noise in the background. SNR is measured by the ratio of the signal within an ROI ($\bar{x}_{ROI}$) and the background noise (σ_{ROI}). For the purposes of measuring system performance, phantoms are often used as objects with known materials and arrangement to assess contrast and detail both visually and using metrics such as CNR and SNR. The visibility of these objects in phantom images by eye provides a practical measure of the system's contrast

resolution capabilities. An SNR or CNR of 4 is considered the lower limit in order for the object to be discernible by eye as defined by the Rose criterion [22]. Finally, the detective quantum efficiency (DQE) can also be used to indirectly assess contrast detection. DQE is primarily associated with noise and detectability and assesses how efficiently an imaging system converts the incoming x-ray signal into image contrast, considering both the signal and noise characteristics.

In CT imaging, optimizing contrast detection is essential for accurate diagnosis and characterization of diseases. The balance between adequate contrast in the images and factors such as patient dose and image quality is a key consideration. Understanding and measuring contrast detection help in optimizing CT protocols for various clinical applications and ensuring the highest possible efficacy.

2.6 Image Artifacts

Image artifacts are any structure or effect that can appear in CT images which do not correspond to the anatomy or makeup of the imaging subject. They reduce the usefulness of CT images for both diagnosis or radiotherapy treatment planning as they can obscure structures or anomalies or cause tissues to be mis-identified.

2.6.1 Beam Hardening and Scatter

Beam hardening and scatter are two significant artifacts in CT imaging. Beam hardening occurs due to the polychromatic nature of x-ray beams used in CT scanners. As the beam passes through an object, lower-energy x-rays are absorbed more than the higher-energy ones. This results in an alteration of the energy spectrum of the beam, causing areas with dense objects (like bones or metal) to appear darker. The effect is compounded in regions with multiple dense objects, leading to characteristic dark streaks or bands between these objects. Beam hardening can also contribute to other phenomena like cupping artifacts and pseudoenhancement [23].

Scatter artifacts arise when x-rays deviate from their original paths after interacting with the tissue, primarily through processes like Compton scattering. This scattering results in x-rays reaching detectors at angles different from the original beam, causing misregistration in the reconstructed image. Scatter can contribute to a decrease in image contrast and may lead to artifacts resembling streaks or shading. Scatter artifacts become more pronounced with an increased number of detector rows and larger scan fields, as more tissue volume contributes to scattering. Scatter can be reduced with the addition of anti-scatter grids,

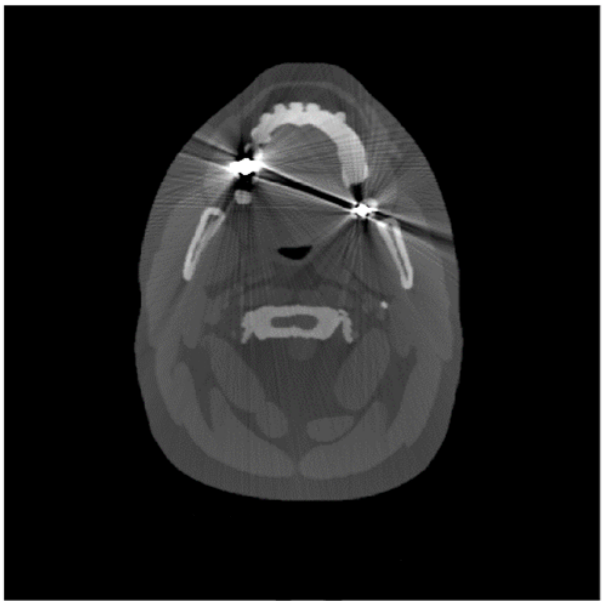

Figure 2.20: Metal artifacts from dental implants in the XCAT head phantom [24]. Adapted from Richtsmeier *et al* (2022) [25].

which are metal grids which are placed in front of the detector that restrict the angles from which x-rays can interact in the detector [23].

2.6.2 Metal Artifacts

Metal artifacts in CT scans are common, occurring when high Z, dense objects are imaged, such as metal implants. These artifacts can be attributed to several mechanisms related to the metal itself and its edges. Metals like iron or platinum cause beam hardening and scatter effects, leading to dark streaks between the metal and surrounding bright streaks (Fig. 2.20). This happens as metals with high Z values significantly attenuate the x-rays, causing beam hardening and scatter. Metal edges can create artifacts due to undersampling, motion, cone beam, and windmill effects. These issues lead to large discontinuities in detector measurements, which are exaggerated by the FBP process. As a result, thin bright and dark streaks can emanate from the metal. Artifacts are more pronounced with metals of higher Z values, such as platinum; low Z metals like titanium typically produce fewer artifacts. Additionally, patient positioning or gantry tilt so the x-ray beam does not shoot through the metal can reduce metal artifacts, especially in cases like dental fillings in head CT scans [23].

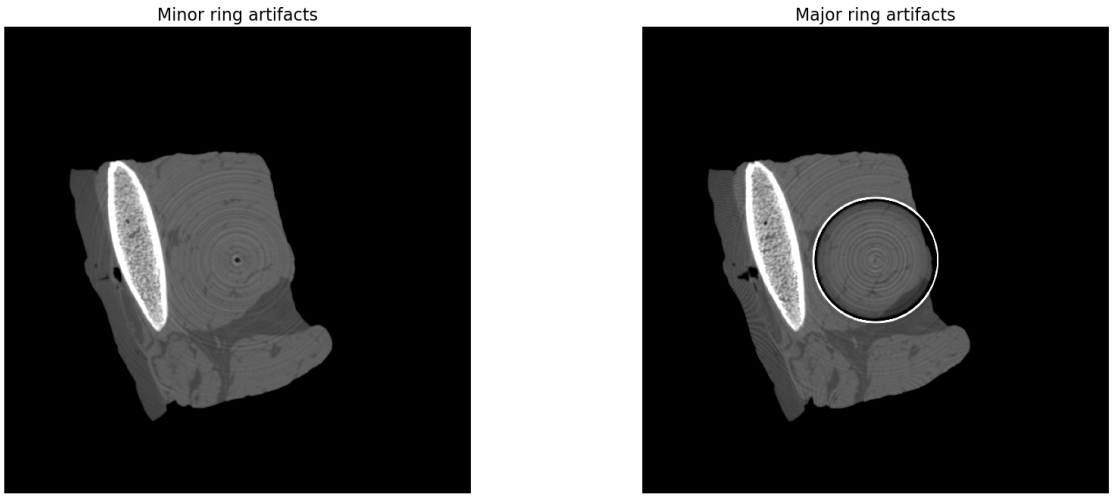

(a) (b)

Figure 2.21: Ring Artifacts. CT slice of an *ex-vivo* tissue sample with (a) several minor ring artifacts and (b) a major ring artifact.

2.6.3 Ring Artifacts

The primary characteristic of ring artifacts is the appearance of bright or dark rings centered on the axis of rotation within the CT image. Ring artifacts in CT imaging are directly related to miscalibration or pixels defects within the detector array. Each detector row in a CT scanner is responsible for capturing a specific slice of the scanned volume. When one of the pixels within the row is miscalibrated or suffers from a defect, the non-conforming pixel produces inconsistent data compared to adjacent, properly functioning elements. As the CT scanner rotates around the patient, these inconsistencies manifest as circular artifacts as they appear in the same location in each projection image relative to the axis of rotation. The visibility of ring artifacts can vary from subtle to prominent, depending on the extent of detector miscalibration or defect (Fig. 2.21). In some cases, these artifacts can be so pronounced or numerous that they can significantly obscure the images or even simulate pathology, misleading the diagnostic process. For instance, a subtle ring artifact might be mistaken for a lesion or abnormality in the brain or other critical organs [23].

Regular calibration and maintenance of CT scanners can often mitigate or remove most ring artifacts. However, some detectors can still suffer from these artifacts even after calibration and require correction methods to be applied.

2.6.4 Motion Artifacts

Motion artifacts can manifest as blurring, double images, and long-range streaks, which significantly impair the image quality. They are usually only prevalent in CT scans of patients as they are caused by any involuntary or voluntary patient movement during the scanning process. This includes movements related to breathing, cardiac motion, bowel movements, or patient repositioning. Blurring occurs when the patient moves during the scan, causing a loss of detail and sharpness in the images. For example, respiratory or cardiac motion can blur the thoracic and abdominal anatomy. Double images, or ghosting, happen if the movement is abrupt or large in magnitude. This is particularly noticeable in areas of high contrast, such as the boundaries between soft tissue and air. Long-range streaks can also appear during motion and typically extend from high contrast edges towards the position of the x-ray tube during the motion occurs. These streaks are artifacts created by the misalignment of data due to motion.

Faster scanners can significantly reduce motion artifacts as the data can be captured over a shorter period of time, reducing the chance of involuntary patient motion. Additionally, both respiratory or cardiac gating can be implemented for scans in which accurate data of the chest cavity or heart is especially necessary. These types of gating require specialized equipment and monitor the motion of the lungs or heart, respectively, and only capture data during specific phases of the breathing or cardiac cycle in which the the anatomy of the patient is in the same location [23].

2.6.5 Noise

The noise in CT scans is primarily attributed to Poisson noise, which arises from the statistical error of low x-ray counts. This type of noise is characterized by random thin bright and dark streaks that appear along the direction of greatest attenuation, such as through both shoulders of patient. Poisson noise is inherent to the process of x-ray detection and is influenced by the number of x-rays that reach the detector. As such it can be mitigated by increasing the exposure, or current-time product, of the scan, but at the cost of a increased radiation dose. However, iterative reconstruction algorithms can also help in reducing noise, but often come at a cost of a higher reconstruction time. There are also methods to reduce noise such as increasing slice thickness or using softer reconstruction kernels. However, these can lead to a decrease in spatial resolution.

While high contrast objects like bones may be visible under high noise conditions, low contrast structures, particularly soft tissue boundaries, can be obscured. This differential

visibility is due to the varying degrees of x-ray attenuation by different tissues and the resultant variance in x-ray counts [23].

2.6.6 Cone-beam Artifacts

Cone-beam artifacts occur in CT scanners with detectors with multiple rows of detector elements and they primarily arise from the misalignment of projection planes with the axial plane. In these scanners, the projection planes defined by the x-ray source and each detector row are not exactly parallel to the axial plane. This misalignment is especially pronounced for detector rows further from the center, as they deviate more significantly from the axial plane. The misalignment can create streaks in the reconstructed image, particularly noticeable when there is a high contrast edge in the z-direction (Fig. 2.15) between the axial plane and the projection plane. These streaks are the direct result of the reconstruction algorithm inaccurately interpolating high-contrast edges due to the geometric misalignment. Stair-step artifacts are a specific instance of this misalignment, often observed in multiplanar reconstructions, such as coronal or sagittal views. They appear as serrated or stepped edges, especially along structures that should have smooth, linear boundaries. This artifact is most noticeable when viewing structures that run obliquely to the axial plane, where the jagged appearance can reduce the diagnostic usefulness of the images. The severity of these artifacts is influenced by the scanner's geometry, specifically the number of detector rows and their alignment relative to the axial plane [23].

2.6.7 Helical Scanning Artifacts

Helical or windmill artifacts are artifacts which are observed in helical multidetector row CT scans. In helical CT, where the table moves continuously while the x-ray tube rotates around the patient, the reconstruction process alternates between using data from a single detector row and interpolating between two rows. When high-contrast edges exist between these rows, interpolation inaccuracies can lead to artifacts. These inaccuracies manifest as smooth, periodic dark and light streaks originating from high-contrast edges, termed windmill artifacts. They are more prominent in thin slices, and the orientation of these streaks (the 'vanes' of the windmill) changes as one scrolls through axial slices. Similar mechanisms also cause stair-step artifacts, seen as serrations on coronal or sagittal images, and zebra artifacts, which are periodic stripes of varying noise levels seen at the image periphery on coronal or sagittal images [23].

2.6.8 Out-of-Field Artifacts

Out of field artifacts in CT imaging occur when the object being scanned extends outside the FOV of the scanner, and the interaction of the scanned object with the existing reconstruction algorithm leads to artifacts. This is because the filter used in FBP is highly localized. A characteristic appearance of out of field artifacts is the presence of bright pixels at the edge of the FOV. These bright edges might be mistaken for pathological findings or lead to misinterpretation of the actual boundaries of an object. These artifacts highlight the importance of appropriate patient positioning and scan planning to ensure that the entire region of interest is within the scanner's FOV. However, in some cases, especially with larger patients or when scanning large body parts, it may be challenging to keep the entire area of interest within the FOV [23].

Chapter 3

Photon-counting detector CT

3.1 Photon-Counting Detector CT Principles

Photon-counting detector computed tomography represents a significant advancement in medical imaging technology, though the majority of CT principles still apply to PCD-CT. Despite their differences in detector technology, the basic design, operational workflow, and clinical objectives are very much aligned between the two types of CT systems. The current applications for conventional CT will remain the same or be improved with PCD-CT, and PCD-CT will offer additional new applications, improving the versatility of CT as a whole.

The advantages that PCD-CT offers over conventional CT stem from photon-counting detectors as they are the difference between conventional and PCD-CT. An exploration of PCDs was covered in an earlier section (Section 2.3.2), but the principles, characteristics, and applications of PCD-CT will be explored further here. There are two main principles of PCD-CT which distinguish it from conventional CT: individual x-ray detection and energy resolution. The benefits and new applications for PCD-CT all stem from these two characteristics.

3.1.1 Photon-counting

As the name implies, photon-counting detectors operate by counting individual photons (see Section 2.3.2). X-rays are individually detected if their electronic pulse height is above a specific threshold (Fig. 2.11), which reduces electronic noise, which is especially helpful in low-dose scans where noise has a higher relative effect Even disregarding the energy-resolving capabilities counting individual photons offers, there is still benefits. If we think about identical polychromatic x-ray beams, one measured with a PCD and one with an EID, the PCD will weigh each detected x-ray equally, while an EID will naturally give more weight to x-rays with a higher energy. An uniform x-ray weighting scheme will offer better

contrast between soft tissues because soft tissues have larger differences in attenuation at lower energies in the diagnostic energy range. Additionally, equal weighting in terms of signal also increases the dose efficiency of low-energy x-rays as they contribute an equal amount to the resulting signal in PCDs while they do not in EIDs.

3.1.2 Energy-resolution

The second principle of energy resolution offers more benefits than photon-counting itself, but would not be possible without it. If individual x-rays were not distinguishable in the first place, measuring their energy would be impossible. When the electronic pulse from an x-ray rises above the triggering threshold of the detector, PCDs have higher thresholds which define the boundaries of 2–8 energy bins [11]. As described in section 2.3.2 however, this is not the case; effects such as charge-sharing and pileup distort the counts. While the data of real PCDs may not be perfect, charge-sharing and other effects usually do not completely obscure the energy information, it is still largely preserved.

The data from the energy bins can be utilized separately or combined for applications such as material decomposition, which will be discussed more comprehensively below. Additionally, on top of the higher contrast provided by the uniform energy weighting, the low energy bins can provide even higher contrast than the full energy range as they are composed of exclusively low energy x-rays. High energy bins can provide a reduction in certain artifacts such as beam hardening and metal artifacts. The energy information can be used to assign more or less weight to the separate bins as well and then combine them to optimize image quality [26, 27, 28, 29, 30].

A benefit of the energy resolution capabilities of PCD-CT is that the spectral information, or energy bins, are always available. Dual-energy CT (DECT) systems are currently clinically available, and they are able to provide spectral information through a variety of mechanisms including various iterations of conducting two scans with differing beam energies or through a dual-layer detector, in which the low energy x-rays are captured by the first layer and the higher energies by the second layer. However, in most cases these systems are utilized to confirm a diagnosis after a patient has exhibited other symptoms or had a routine scan. With PCD-CT, that information is always available, meaning that many uses for DECT could be done using only the patient's PCD-CT scan, with the energy information already gathered, negating the need for a second scan.

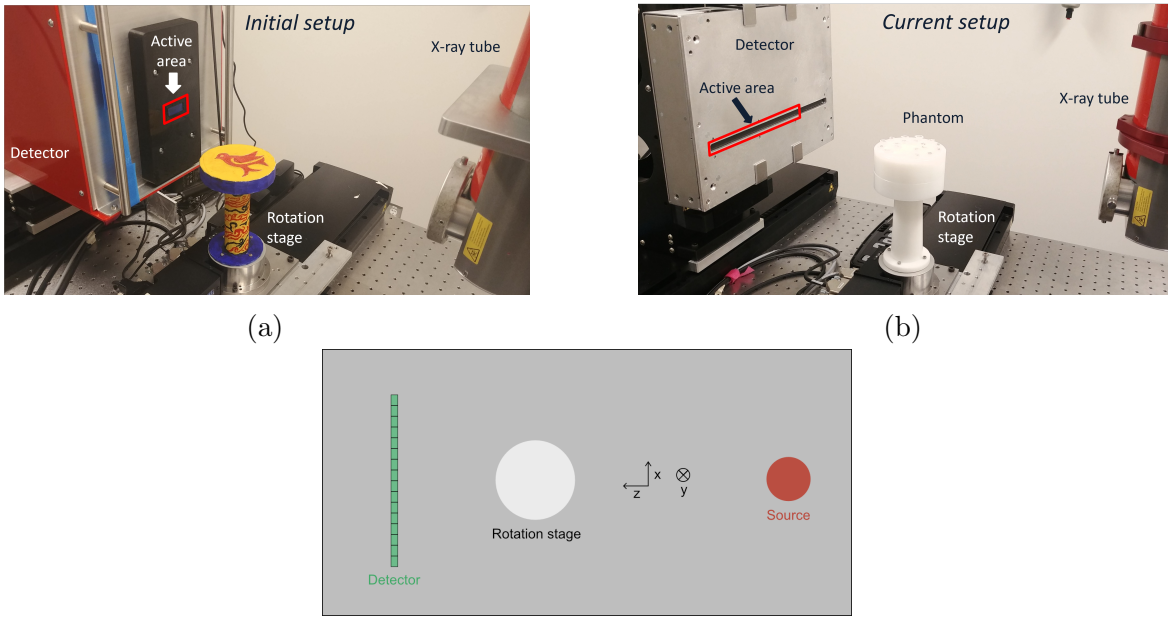

(a) (b)

(c)

Figure 3.1: XCITE lab PCD-CT bench-top system. (a) The initial setup with a 0.8×24 mm^2 photon-counting detector (PCD). (b) The current setup with a 0.8×190 mm^2 PCD. (c) Schematic of the bench-top system with directions shown.

3.2 PCD-CT Applications

This section covers the potential clinical applications of PCD-CT we investigated with our bench-top system. We were interested in studying the applications of PCD-CT with a bench-top system because, while it is not a clinical imaging system, we had more control over the system parameters than most other PCD-CT systems.

3.2.1 XCITE Lab Bench-Top PCD-CT system

All of the studies conducted in this dissertation were carried out on the bench-top PCD-CT system in the XCITE Lab at the University of Victoria. The system (Fig. 3.1) consisted of an x-ray tube (MRX-160/22, Comet Technologies, Flamatt, Switzerland) and PCD mounted on M-IMS300V and M-IMS600LM motion stages (Newport Corporation, Irvine, CA, USA) which allowed for movement in the y-direction (Fig. 3.1c) for both, movement in the z-direction for the x-ray tube, and in the x-direction for the PCD. A sample stage was mounted on an RVS80CC rotation stage (Newport Corporation, Irvine, CA, USA) allowing for rotation of scanned objects.

Two iterations of the system were utilized for this work: the initial setup with a PCD with

an active detector area of 8×24 mm^2 and the current setup with a PCD with an active area of 8×190 mm^2 (both Redlen Technologies, Saanichton, BC, Canada). The only difference between the physical properties of the detectors was the active area. Both detectors were made up of a 2-mm-thick cadmium zinc telluride (CZT) crystal mounted on an ASIC which supplied the photon-counting capabilities. The pixel pitch of both detectors was 0.33×0.33 mm^2 and both detectors had six energy thresholds. In addition to the energy thresholds we were able to control the triggering threshold (the energy below which x-rays are not counted), the dead time window, and we could apply our own energy calibration if desired [31, 32].

3.2.2 Material Decomposition

In addition to reconstructing separate energy images for each energy bin, PCD-CT opens the door to material decomposition in a single scan. DECT was proposed shortly after SECT, citing the need for multiple energy scans to be acquired for material decomposition. This required specific hardware to be developed to acquire two scans to minimize patient movement, such as fast kVp switching or dual-layer detectors. Material decomposition relies on determining the full attenuation curve at all energies at all points in the image [33, 34, 35, 36, 37]. However, it is not usually required to have a large number of energy bins to determine this [34]. Within the diagnostic energy range (30–150 keV) [1], tissue attenuation can be essentially described by the photoelectric effect and Compton scattering.

$$\mu(E) = \rho \cdot \left(\left(\frac{\mu}{\rho}\right)_{photo}(E,Z) + \left(\frac{\mu}{\rho}\right)_{Compton}(E,Z) \right) \approx \rho \cdot \left(\alpha \frac{Z_{eff}^k}{E^n} + \beta \cdot f_{KN}(E) \right) \tag{3.1}$$

Here, $\alpha \frac{Z_{eff}^k}{E^n}$ is the photoelectric attenuation, where Z_{eff} is the effective atomic number, $k \sim 3-4$, and $n \sim 3-3.5$. ρ is the mass density, $f_{KN}(E)$ is the Klein-Nishina Compton attenuation and α and β are constants [1]. If at least two measurements at different energies are known, two basis materials can be separated based on a linear combination of the components in the approximation f Eq. 3.1. Common basis materials include water and calcium or water and iodine. Of course, tissue is not made up of only water and calcium (or water and iodine), but the attenuation of various tissues can be represented as a combination of the two.

Decomposition into more than two basis materials requires both an additional energy measurement and the addition of a high-Z material with a K-edge within the diagnostic energy range, such as a contrast agent. The attenuation of a high-Z material requires an

addition term to Eq. 3.1:

$$\mu(E) \approx \rho \cdot \left(\alpha \frac{Z_{eff}^{k}}{E^{n}} + \beta \cdot f_{KN}(E) + a_{K-edge} f_{K-edge}(E) \right) \tag{3.2}$$

where f_{K-edge} is the energy-dependent component of the K-edge material and a_{K-edge} is a constant. This allows for a three-material decomposition. If more high-Z materials are introduced and more energy measurements are taken, material decomposition of for than three materials is possible [1].

DECT can currently used for a numerous applications in the clinic, as detailed in a number of review articles [38, 39, 40, 41]. DECT can, for example,differentiate and quantify materials like iodine, uric acid, and calcium, which is useful in applications such as tumor staging, assessing organ perfusion, identifying uric acid in gout, and characterizing kidney stones [39]. DECT offers the advantage of higher contrast-to-noise ratio, reduced beam-hardening artifacts, and the ability to create material-specific images, virtual monoenergetic images (VMIs), and virtual noncontrast images [38, 39]. These advantages lead to better diagnostic performance compared to single-energy CT due to higher image quality. The technology allows for injections of lower concentrations of contrast agents and potential reduction in radiation dose, thanks to its capability to generate virtual non-contrast images and optimize image quality. As discussed above, material decomposition would always be possible with PCD-CT as the energy information is always collected.

In Chapter 4 we studied whether an existing DECT method could be adapted to PCD-CT on our bench-top system. The method we investigated by Bourque *et al* (2014) [42] decomposes scanned materials into effective atomic number Z_{eff} and electron density relative to water ρ_e by calibrating a polynomial expansion model with materials of known Z_{eff} and ρ_e. This information enhances the accuracy of dose calculation in radiation therapy, since accurate tissue identification is critical to predict dose deposition. In place of using two separate energy measurements, we utilized the energy information from two energy bins of the PCD. We then compared the two energy bin method with the two energy scan method. Both methods were evaluated using tissue-equivalent materials from the RMI Gammex electron density phantom, which provided known Z_{eff} and ρ_e values. We also decomposed an *ex-vivo* tissue sample, which will be discussed in Ch. 4.

3.2.3 High Atomic Number Contrast Agents and Multi-Contrast Imaging

The use contrast agents is key for many of the uses of conventional CT in the clinic and is referred to as contrast-enhanced CT. The vast majority of contrast-enhanced CT scans

where contrast is injected intraveneosly are conducted with iodinated contrast agents. Iodine has a K-edge energy of 33.2 keV, which is near the low end of the diagnostic energy range for CT. However, due to the effect of increased photoelectric absorption of iodine, the average attenuation of iodine over the diagnostic energy range is higher than that of soft tissue. Different structures can be enhanced based on the time at which the CT scan is taken post-injection, such as during the early- or late-arterial phase [43]. This requires multiple scans if a scan with and without contrast are needed as well. Though iodine-based contrast agents are the primary contrast agent used in CT, gadolinium-based agents can be utilized if the patient has an allergy to the iodine-based agent. Additionally, barium sulphate is an oral contrast agent that can be used to study the gastrointestinal tract [44]. Table 3.1 shows the most common elements which are either used or under development for use in CT and PCD-CT.

Table 3.1: Elements used contrast agents for CT and PCD-CT. Adapted from [21].

Element	**Atomic Number**	**K-edge (keV)**	**Density (g/cm^3)**	**Development Status**
Iodine	53	33.2	4.9	Clinically available for CT
Barium	56	37.4	3.59	Clinically available for CT [44]
Gadolinium	64	50.2	7.9	Clinically available for MRI and CT
Ytterbium	70	61.3	6.9	Small animal preclinical CT and PCD-CT
Hafnium	72	65.4	13.3	Small animal preclinical CT and PCD-CT
Tantalum	73	67.4	16.4	Small animal preclinical CT and PCD-CT
Gold	79	80.7	19.3	Small animal preclinical CT and PCD-CT
Bismuth	83	90.5	9.8	Small animal preclinical CT and PCD-CT

One of the most well studied preclinical contrast agents for CT and PCD-CT is gold, specifically in the form of gold nanoparticles (AuNPs). AuNPs have been extensively studied [45, 46, 47] for drug delivery [48, 49, 50], as facilitators for other therapeutics [51, 52, 53], and as CT contrast agents [54, 55], including in PCD-CT where they have been studied in small animals[56, 57, 58].

As discussed in the introduction to material decomposition (section 3.2.2), DECT for material decomposition was described almost as soon as single-energy CT [33, 35, 34]. Now with PCD-CT, where three or more energy data sets can be acquired simultaneously, three material decomposition is possible with addition of a high-Z contrast agent with a K-edge

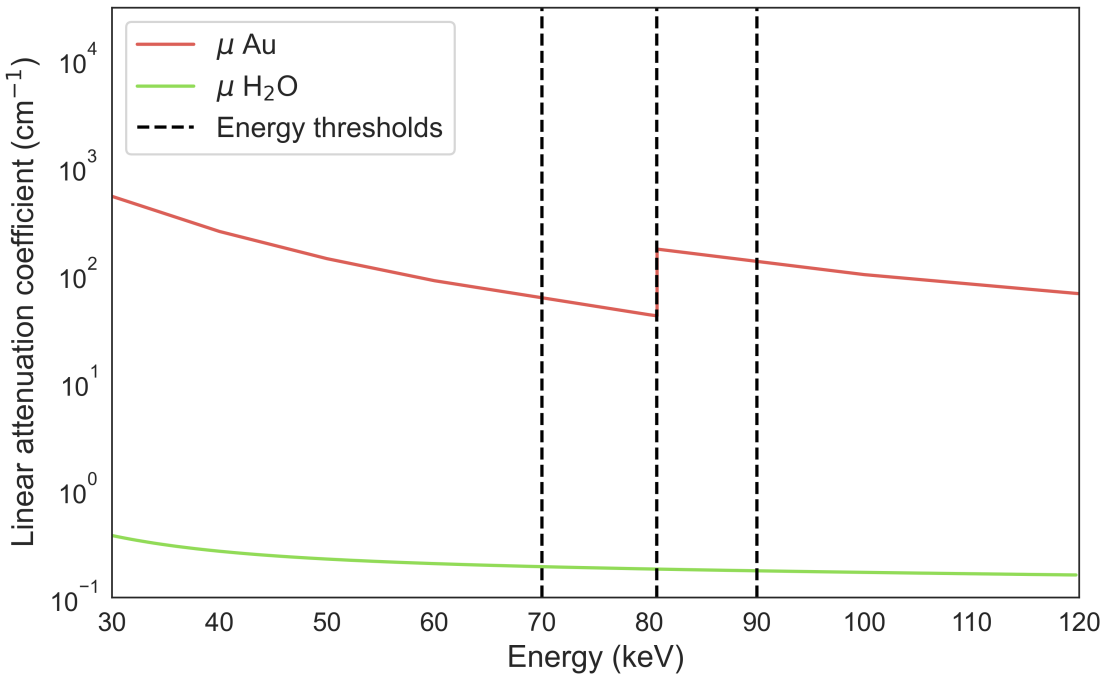

Figure 3.2: Linear attenuation for K-edge subtraction. The plot shows the total linear attenuation coefficient for gold and water between 30 and 120 keV as well three energy thresholds at 70, 80.7, and 90 keV. 80.7 is the K-edge energy for gold.

in the energy range of 40–100 keV. If multiple high-Z materials are introduced four or more material decomposition is possible as well. An alternative method for separating and quantifying high-Z contrast agents is K-edge subtraction imaging. A detailed explanation of the K-edge subtraction is described by Sarnelli *et al* (2004) [59] and a similar decomposition method by Zhang *et al* (2020) [60]. However, a simplified explanation can be offered based on the linear attenuation coefficients for water and gold presented in Fig. 3.2 for gold, which has a K-edge energy of 80.7 keV. Two CT images could be reconstructed using the two energy ranges shown by the dashed lines, one on either side of the K-edge. For water, the difference in average attenuation for the two energy bins is close to zero, while gold has a relatively large difference between the high and low energy bins. If a CT image reconstructed from the low energy bin was subtracted from the high energy bin, what would remain is signal from the gold only, resulting in a K-edge image of gold. Depending on the number of available thresholds, multiple high-Z contrast agents could be separated using this method.

Recent developments in contrast agents for CT have shown a number of alternatives to

traditional iodine-based agents. New agents aim to enhance x-ray attenuation, thus minimizing radiation and contrast dose and improving contrast compared to iodinated agents. Research has focused on high-Z elements with and high K-edge energies, such as hafnium, tungsten, gold, and bismuth [61]. Additionally, advancements in nanoparticle technology have introduced high-density nanoparticles, including gold and tantalum oxide nanoparticles, as potential contrast agents. These nanoparticles offer high x-ray attenuation and the possibility for targeted imaging, although challenges remain in ensuring their safe and efficient renal elimination [62]. One possibility opened by the continued development of novel contrast agents is the use of multiple agents within a single scan, which could have uses such as multiphase perfusion imaging [63, 64]. Additionally, gold nanoparticles (AuNPs) have also been investigated for radiosensitization of tumors [47] AuNPs offer benefits as contrast agents due to their biocompatiblity and their ability to accumulate in tumors through the enhanced permeability and retention effect, when injected intravenously, if they are within 50-200 nm in diameter [65]. AuNPs can also be easily functionalized, with molecules targeting specific cancers attached to their surface [58]. This opens the path for dual-use AuNPs for targeted cancer therapy and imaging contrast.

In Chapter 5, we present a study on the possibility of imaging four high-Z contrast agents, two with K-edges within 4 keV of one another, and investigated acquisition parameters which would improve the detectability of those agents. The system parameters we investigated were beam filter type and thickness, projection acquisition time, and energy bin width. These parameters are evaluated based on PCD-CT signal, contrast to noise ratio (CNR), and noise in K-edge images.

3.2.4 Metal Artifact Reduction

Metal artifacts are a significant problem in modern CT as many patients have prostheses, surgical materials, and/or dental fillings. As detailed in section 2.6.2, metal artifacts are the result of one or a combination of beam hardening, scatter, noise, and other factors [66, 23]. To combat this, there have been many metal artifact reduction (MAR) methods developed over the years [67, 68] and they fall into three broad categories. The first is projection completion or inpainting. These methods seek to correct for metal artifacts in the projection space before reconstruction. The metal traces can either be correction through the use of models predicting beam hardening, noise, and other causes of metal artifacts or through complete replacement of the data using mechanisms like interpolation. The second type of MAR methods are iterative reconstruction methods that suppress metal artifacts

during reconstruction [67]. And the final type of MAR methods that have been developed more recently are deep learning algorithms which can learn to mitigate the artifacts [68]. Additionally since PCD-CT has been shown to naturally reduce beam hardening and noise, and thus metal artifacts, it has been a source of new MAR methods.

There are a number of reasons why PCD-CT is able to reduce metal artifacts compared with conventional CT [11, 9, 69]. PCD-CT has been shown in numerous studies to reduce beam hardening in high-energy bins, as higher energy x-rays are less likely to be attenuated by high-density objects like metal implants [70, 71]. Additionally, the reduction of electronic noise is especially important in areas where no photons reach the detector, which is called photon-starvation. A reduction in noise in those areas reduces metal artifacts since no signal is expected in those locations due to the complete attenuation of the beam. PCD-CT can also easily be used to create VMIs through material decomposition, which suffer from very few artifacts since they are replicating images created using a single energy [72, 73].

In Chapter 6 we developed an inpainting method for PCD-CT which relies on capturing high- and low-energy information simultaneously in order to correct the metal traces in the sinogram space. We titled the method trace replacement metal artifact reduction (TRMAR). We conducted a phantom study and compared image quality without TRMAR and with TRMAR to a ground truth phantom without metal artifacts. Additionally, we compared the method to a standard in-painting method, normalized metal artifact reduction (NMAR).

3.2.5 High Spatial Resolution Imaging

Due to the smaller pixel sizes of PCDs compared to EIDs, PCD-CT features higher spatial resolution compared with conventional CT, offering numerous benefits. PCD-CT also often outperforms conventional CT for high-resolution imaging at the same resolution in terms of dose. Conventional ultra-high resolution CT employs a comb or grid filter to restrict the x-rays incident on each pixel to an even smaller area, which is dose inefficient [9, 21]. PCD-CT can achieve the higher spatial resolution without the filter because PCD pixels do not require septa and thus may be smaller than EID pixels. There are gaps between the pixelated anodes of PCDs, but they are generally on the order of only a few tens of micrometers.

There are a number of current clinical applications for high-resolution CT for which PCD-CT could offer improvements. The first is for dedicated breast CT, as the lesions that are small and not easily detected [74, 75]. The high spatial resolution and improved contrast detectability could offer benefits in terms of lesion detection. High-resolution lung imaging is another area in which PCD-CT could offer significant benefits, especially in the

detection of lung diseases and cancer [21]. Studies have been conducted showing that PCD-CT could be beneficial for visualizing lung nodules, demonstrated in images of phantoms and cadavers [76, 77]. Cardiovascular imaging could also greatly gain from PCD-CT in clinical practice. Many preventative and post-treatment cardiovascular diseases require imaging of the small structures of the system such as the coronary artery both with and without contrast agents [21]. Benefits with PCD-CT over conventional CT have also been shown in the imaging of stents [78, 25, 79, 80, 81, 82] and the evaluation of calcifications via calcium scoring [83, 84, 85, 21]. Additionally, imaging of kidney stones and determining their makeup [86, 21], imaging bone microstructures for osteoarthritis and osteoporosis [21], temporal bone imaging [21, 11], and many other potential uses [2, 11, 10, 21, 9] would also see benefits due to the improvements in spatial resolution as well as spectral information information of PCDs.

In Chapter 7 we investigated the resolving capabilities of our bench-top system we explored imaging of stents and compared the results to two conventional CT systems. We replicated the spatial resolution of the clinical systems as closely as possible with our bench-top setup and separately demonstrated the highest resolution possible with our system. The study examined three different stents and compared the apparent strut thickness, lumen diameter, and lumen attenuation in the reconstructed images. Additionally, K-edge images were reconstructed to demonstrate how metal artifacts can be reduced for metals with a K-edge in PCD-CT.

Chapter 4

Material decomposition with a prototype photon-counting detector CT system: expanding a stoichiometric dual-energy CT method via energy bin optimization and K-edge imaging

The following work was published in *Physics in Medicine and Biology* in 2024 and can be found at the following DOI: 10.1088/1361-6560/ad25c8.

4.1 Summary

Objective: Computed tomography (CT) has advanced since its inception, with breakthroughs such as dual-energy CT (DECT), which extracts additional information by acquiring two sets of data at different energies. As high-flux photon-counting detectors (PCDs) become available, PCD-CT is also becoming a reality. PCD-CT can acquire multi-energy data sets in a single scan by spectrally binning the incident x-ray beam. With this, K-edge imaging becomes possible, allowing high atomic number (high-Z) contrast materials to be distinguished and quantified. In this study, we demonstrated that DECT methods can be converted to PCD-CT systems by extending the method of Bourque *et al* (2014). We optimized the energy bins of the PCD for this purpose and expanded the capabilities by employing K-edge subtraction imaging to separate a high-atomic number contrast material.

Approach: The method decomposes materials into their effective atomic number (Z_{eff}) and electron density relative to water (ρ_e). The model was calibrated and evaluated using tissue-equivalent materials from the RMI Gammex electron density phantom with known ρ_e values and elemental compositions. Theoretical Z_{eff} values were found for the appropriate energy ranges using the elemental composition of the materials. Z_{eff} varied slightly with

energy but was considered a systematic error. An *ex-vivo* bovine tissue sample was decomposed to evaluate the model further and was injected with gold chloride to demonstrate the separation of a K-edge contrast agent.

Main results: The mean root mean squared percent errors on the extracted Z_{eff} and ρ_e for PCD-CT were 0.76% and 0.72%, respectively and 1.77% and 1.98% for DECT. The tissue types in the *ex-vivo* bovine tissue sample were also correctly identified after decomposition. Additionally, gold chloride was separated from the *ex-vivo* tissue sample with K-edge imaging.

Significance: PCD-CT offers the ability to employ DECT material decomposition methods, along with providing additional capabilities such as K-edge imaging.

4.2 Introduction

Computed Tomography (CT) is a widely used medical imaging technology, and since its inception in the early 1970s [33], it has evolved dramatically. One of the most significant breakthroughs in CT technology has been the development of dual- and multi-energy CT. Dual-energy CT (DECT) and multi-energy CT (MECT) refer to techniques in which two or more sets of CT data are acquired at different energy levels. This allows for the extraction of additional information, which is not possible with conventional, single-energy CT (SECT), which only consists of data acquired at one effective energy using an energy-integrating detector (EID). EIDs generate signal by first converting x-rays to light photons within a scintillating crystal, which are then integrated for the final output.

Dual-energy CT for material decomposition was first hypothesized [34] and demonstrated [35] in the 1970s, shortly after SECT was first implemented. Unfortunately, the use of DECT was limited clinically due to technological constraints. However, with the advancement of CT technology, DECT has become more widely available and is used in a wide range of clinical applications [87, 88, 89]. DECT also utilizes EIDs, but captures two data acquisitions at different effective energies. With the two sets of linear attenuation information given by the two sets of energy data, two subsequent sets of data can be decomposed or extracted, usually referred to as the basis functions in the decomposition formula. For example, as shown in the seminal DECT paper by Alvarez et al [34], the photoelectric and Compton scattering components of the linear attenuation coefficient can be determined with DECT material decomposition. Though there are many decomposition algorithms and basis functions, one of the most well-studied sets of basis functions is the effective atomic number (Z_{eff}) and electron density relative to that of water (ρ_e), first demonstrated by Rutherford *et al* (1976) [35].

Since then, many algorithms have been developed to extract these values, including using monochromatic x-rays [90, 91]. The decomposition of data into Z_{eff} and ρ_e has a number of uses, including increased diagnostic capabilities by distinguishing between materials with similar attenuation curves. However, one of the most well-studied uses is for its use in improving material segmentation and identification for radiation therapy treatment planning [92, 93, 94, 95, 96], especially in the fields of low dose rate brachytherapy [97, 98, 99] and proton therapy [100, 101, 102, 42, 103].

Now, with the advent of high-flux photon-counting detector (PCD) technology [104, 105, 106] which offers energy windowing, the ability to distinguish the energy of incident x-rays and bin each one into a set of discrete energy ranges, MECT is becoming a clinical possibility as well. In fact, clinical PCD-CT scanners are currently available [3], with several others close behind [107, 7, 4]. PCD-CT typically offers up to eight energy bins [11], which significantly increases the options for material decomposition. Additionally, each energy range is captured simultaneously, mitigating any issues with co-registration between the different energy data sets. In DECT and MECT, co-registration refers to matching the multiple energy data sets to one another so that the various structures of the subject match up in the same location in each set. Any mechanism which shifts the subject so that it appears in a slightly different location in each data set will lead to decomposition errors.

PCD-CT systems offer benefits over the current clinical CT systems, even when excluding PCD-CT's energy discrimination abilities. Current clinical systems utilize EIDs, over which PCDs have several potential benefits. The first benefit is higher spatial resolution. EIDs first convert x-rays to light photons, which requires septa to be placed between individual pixels within the detector crystal to mitigate the spread of light photons outside of the pixel the x-ray was incident upon. PCDs are direct conversion detectors, requiring no septa within the detector crystal. The exclusion of the septa in PCDs allows for a higher possible inherent spatial resolution than EIDs, since EIDs suffer from increased dose inefficiency as the pixel size is reduced, as the the septa take up more area [108, 9, 11, 69]. PCDs also can reduce electronic noise because they function by counting individual photons rather than integrating the detected light signal from individual x-rays [11, 9, 1]. PCDs determine each count by measuring whether the charge detection peak is higher than a minimum threshold. Signal below the threshold is discarded as noise, while signal spikes above the threshold are counted as x-ray detections. EIDs integrate all signal, including electronic noise, though the noise has largely been mitigated at clinical acquisition parameters [109]. However, PCD-CT systems have still demonstrated lower image noise compared with state-of-the-art EID-CT systems [110, 111, 2]. PCDs' counting behavior also inherently allows for uniform energy weighting, as

each x-ray is counted individually without regard to how far over the threshold the detection spike is, other than to bin the x-ray in the appropriate energy range [108, 9, 11, 1]. However, as EIDs integrate the signal generated from the detected x-rays, higher energy photons are weighted more highly as they produce a proportionally higher signal. The inherent uniform energy weighting of PCDs allows lower-energy x-rays to contribute equally to the detected signal, which offers better CT image contrast as most soft tissues have larger differences in attenuation at lower energies. Additionally, energy weighting can be applied to PCD data to further improve contrast [27, 112, 30].

However, PCDs do offer challenges as well; the two main drawbacks being charge-sharing and pulse pileup. Charge-sharing occurs when an x-ray is incident near the border of two or more pixels, and the resulting charge cloud is partially collected by multiple pixels. Thus, the full charge is split, and multiple pixels record a count at a lower energy than the pixel with the incident x-ray. This degrades both the spatial and energy resolution. Pulse pileup occurs when two x-rays are nearly simultaneously incident on a pixel. The resulting signal pulses are summed up and recorded as a single event at a higher energy than either of the two incoming x-rays alone. Pulse pileup degrades the spatial resolution as well as increases the noise within the image [11]. A trade-off exists in the physical detector itself: smaller pixels will lead to more charge-sharing [113], but less pileup. Thus, a balance must be struck between the two. Methods are being developed to compensate for both effects [114] including coincidence counters which are implemented within the detector architecture to monitor and compensate for charge-sharing events [115, 116].

Much focus has also been devoted to material extraction of high-atomic number (high-Z) contrast agents via K-edge imaging [36, 37, 57, 117, 118]. K-edge imaging can refer to methods that utilize the K-edge discontinuities in the attenuation curves of high-Z materials to extract a third (or higher) material map [36], on top of the two material maps possible with DECT, or that utilize K-edge subtraction to separate high-Z materials from conventional CT images, which was first demonstrated using monoenergetic x-ray beams [119, 120, 121] and later using photon-counting detectors and polyenergetic beams [117, 118]. Interest has also been shown in using PCD-CT for material decomposition in a variety of fashions. For example, there are methods that extend DECT methods of Z_{eff} and ρ_e decomposition, such as those for predicting properties like tissue stopping power ratios for particle therapies [122, 123].

In this study, we demonstrate that DECT methods can be adapted to PCD-CT systems by applying the method outlined by Bourque *et al* (2014) [42] on a bench-top PCD-CT setup, with the added benefit of acquiring the data with a single scan. We optimized the

ideal energy ranges with which to perform the decomposition by adjusting the energy bins of the PCD through an extensive set of threshold options. We also expanded the material decomposition capabilities of this method by employing K-edge subtraction imaging to separate a high-atomic number contrast material, i.e., gold. From the perspective of a dual-energy measurement, unless the peak energy of the lower energy scan could be set to the K-edge energy of the contrast material, at least three energy bins would be needed to produce Z_{eff} and ρ_e images, along with a separate K-edge contrast image. Gold is currently under investigation as a CT contrast agent in the form of gold nanoparticles [57, 124, 54]. The decomposition method was calibrated and evaluated using a number of tissue equivalent materials with known Z_{eff} and ρ_e as well as tested on a *ex-vivo* bovine tissue sample which were compared to tabulated tissue values. In addition, the adapted method was compared against the same method used as it was originally intended, with DECT data.

4.3 Materials and methods

4.3.1 Bench-top photon-counting CT system

The bench-top PCD-CT system used in this work to evaluate the material decomposition method described above consisted of an x-ray tube (MXR 160/22, Comet Technologies, San Jose, CA, USA) and a PCD (Redlen Technologies, Saanichton, BC, Canada) with a rotating sample stage (Newport Corporation, Irving, CA, USA) mounted between the two (Figure 4.1). The source to isocenter distance was set to 322 mm with a source to detector distance of 578 mm. The PCD has two 8×95 mm^2 modules which together create an 8×190 mm^2 detector active area. This yielded a 106 mm field of view with 4.5 mm Z-coverage at isocenter. The detector crystal is 2-mm thick cadmium zinc telluride (CZT) which is connected to an Application Specific Integrated Circuit (ASIC). The detector offers a pixel pitch of 330 μm and six energy thresholds which can be set by the user. The six thresholds define five specific energy ranges into which incident x-rays are binned. A sixth bin is in place to record for events over the highest threshold setting, and a seventh bin counts every event above the noise threshold of 24 keV. The PCD operates at up to 650 Mcps/mm^2 without polarization and is linear up 6 Mcps/mm^2 (deviation from output count rate vs input count rate linearity is less than 1%) [115, 125]. The maximum count rate in this study was 12.6 Mcps/mm^2 with a deviation from linearity of less than 2%, causing negligible errors in our estimates [118, 126, 25, 31]. The ASIC includes a coincidence circuit, which accounts for some amount of charge-sharing by monitoring pixels immediately adjacent to incident pixel after an x-ray detection. If any charge less than that collected in the incident pixel is

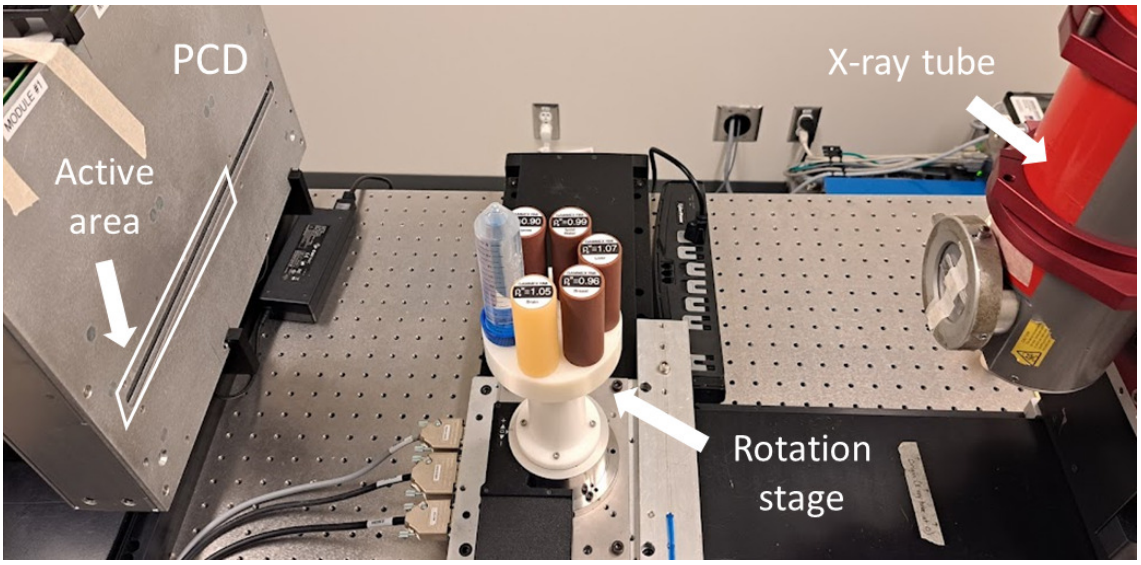

Figure 4.1: The bench-top imaging setup.

measured in the adjacent pixels during a specified time window, those counts in both the incident and adjacent pixel are considered to be charge-shared. The ASIC can operate in two modes; one mode discards all charge-shared counts, and the other mode includes all counts, regardless of charge sharing. We utilized the total counts mode as there was little difference between the two modes at the low flux rates used in this study. Other non-idealities within the PCD system do still exist, such as differences in ASIC dead times and inconsistencies in gain between pixels and variations in the CZT crystal itself. Calibration was conducted on the detector to minimize the inconsistencies in pixel dead time to less than 100 ps. Energy calibration was also performed on a per pixel basis using either an Americium-241 or a Cobalt-57 source. Instabilities between pixels in the time domain were tested for using both 1-second and 1-minute stability tests. If a detector failed any of the above tests it was not utilized in this study.

4.3.2 CT acquisitions

For all CT acquisitions, the beam was collimated to 172.5 mm horizontal and 17.25 mm vertical coverage at isocenter. The sample stage was rotated at 2 deg/s for a total of 180 s over which 720 projection images were acquired for 0.25 s each.

PCD-CT data sets were acquired at a tube voltage of 120 kVp, with a tube current of 2 mA, the small focal spot (∼0.4 mm), and 6 mm Al filtration in order to replicate the filtration of a clinical head protocol.

DECT data sets were acquired at 80 kVp and 120 kVp. DECT scans were still acquired with the PCD as our lab does not have access to an EID capable of CT acquisitions. The 120 kVp acquisitions were acquired at the same time as the PCD-CT scans (at 2 mA with 6 mm Al), but only utilized the bin which counts every x-ray above 24 keV. The 80 kVp scans were obtained with a tube current of 2.5 mA, the small focal spot, and 3 mm Al filtration. The parameters for the 80 kVp scans were chosen to replicate the same dose as the 120 kVp scans, calculated in SpekPy [127]. For the 80 kVp scans, the sixth energy bin was used, containing energies from 24-80 keV.

4.3.3 Image reconstruction and normalization

The projection images from each CT acquisition, along with flat field and water phantom projection first had dead pixels corrected for using nearest neighbor's interpolation. The flat field and water phantom projection were acquired with the same parameters as the CT projections. The projection images were then corrected for air in each bin using the equation:

$$p_n = -ln(\frac{I_n}{I_{0,n}}); n = 1, 2, 3, 4, 5, 6 \tag{4.1}$$

in which p is the corrected sinogram image, I is the number of counts in the projection image, and I_0 is the number of counts in the flat field scan. n refers to the energy bin number; bins 1-5 are the individual energy bins and bin 6 is the total counts bin. Additionally, an in-house ring artifact correction method was applied to the sinograms using the water phantom scan [25]. The water phantom was chosen to cover the full field-of-view (FOV) of the detector, leaving no air showing at the edges of the detector after the scan. The water phantom data was corrected for air using Eq. 4.1. Then, each row of the corrected water phantom data was filtered with a median filter to smooth out any large spikes in the data, as the water phantom should appear a smooth curve when a single row is plotted. Each median-smoothed row was fit with an 8-degree polynomial and the ratio between the polynomial fit and the air-corrected data was found. This created a gain-matrix for each pixel which was multiplied to each projection image to correct for small pixel response variations. Finally, all of the gain-corrected projections were summed together to create a single summed projection. Each row of the summed projection was smoothed with a median filter and linearly interpolated to find the "ideal" summed projection. The difference between the "ideal" and the original summed projection was found and any pixels still displaying large deviations were corrected for using nearest-neighbor interpolation.

CT images for each energy bin were reconstructed separately using the Feldkamp-Davis-

Kress (FDK) algorithm [20] with a Hamming filter, as implemented in the TIGRE package [128] in Python. Images were reconstructed with 24 slices, each containing 512×512 pixels. The reconstructed image slices were 105×105 mm^2 with a slice thickness of 0.184 mm. The images were then converted to CT number (HU) using the equation:

$$HU = 1000 * \left(\frac{\mu - \mu_w}{\mu_w} \right) \tag{4.2}$$

where μ is the un-normalized image signal and μ_w is the mean signal within the water vials. For the *ex-vivo* acquisitions, the water vial signal from the calibration insert scans was used for μ_w.

4.3.4 Effective atomic number

For mixtures composed of multiple elements, an effective atomic number (Z_{eff}) can be defined which in theory takes into account the atomic numbers of each of the consituent elements. Here, Z_{eff} was calculated based on the method detailed in [42]. Briefly, for elements, we can define CT number in the following manner:

$$HU = 1000(\rho_e f(Z) - 1) \tag{4.3}$$

where, $f(Z)$ is the electronic cross section relative to water; therefore, CT number is a function of ρ_e and σ_e. We seek to define Z_{eff} for mixtures based on the electronic cross section so that CT data can be used to tissue characterization [42]. Thus, we parameterize the electronic cross section ($\hat{\sigma_e}(Z)$) such that it is a bijective function over the Z domain that covers human tissues. For a given photon spectrum, the parametric electronic cross section at Z_{eff} would be the electronic cross section for the mixture averaged over the spectrum ($\sigma_{e,mix}$). This gives

$$\hat{\sigma_e}(Z_{eff}) = \sigma_{e,mix} \tag{4.4}$$

and

$$Z_{eff} = \hat{\sigma_e}^{-1}(\sigma_{e,mix}) \tag{4.5}$$

Thus, Z_{eff} can be defined for a material at a specific energy.

4.3.5 Material decomposition methodology

The material decomposition method used in this study is an adaptation of the DECT stoichiometric calibration method detailed by Bourque *et al* (2014) [42], which is based on the method by Schneider *et al* (1996) [129]. In the method laid out in [42], a DECT scan of a set of calibration materials with known Z_{eff} and ρ_e values is performed. The average CT numbers in both of the energy scans are calculated for each of the various calibration materials and paired with their known Z_{eff} and ρ_e values. A pair of calibration coefficient vectors are then estimated via least-squares which define the relationship between the CT numbers and the physical material properties, Z_{eff} and ρ_e. In subsequent scans under the same conditions, the calibration coefficients can then be used to determine Z_{eff} and ρ_e for unknown materials. In this study, the method remains the same, but the information from two PCD energy bins collected from a single CT acquisition are used in place of two different energy scans from a DECT acquisition. The following is a short explanation of the method as detailed in [42].

CT numbers in both the low and high data sets can be converted to reduced CT numbers, u_r, in which r is defined as either L or H for either the low and high energy ranges, respectively. The reduced CT number is calculated as follows and is the ratio of the average linear attenuation coefficient of the material (μ_r) to that of water ($\mu_{w,r}$) within that energy range:

$$u_r = \frac{\mu_r}{\mu_{w,r}} = \frac{HU_r + 1000}{1000} \tag{4.6}$$

[130] stated that some have argued, to some degree of accuracy, that the linear attenuation coefficient can be parameterized into the photoelectric, Compton scattering, and Rayleigh scattering cross sections:

$$\mu(Z) = n_e \sigma_e(Z) = n_e(k_{ph}\tilde{z}^{3.62} + k_{ray}\hat{z}^{1.86} + k_{KN}) \tag{4.7}$$

where n_e is the electron density, σ_e is the electronic cross section, the k values are coefficients associated with the three cross sections, and the values $\tilde{z}$ and $\hat{z}$ are given by the power law additivity rule [131, 132]:

$$z_j = \Big[\sum_i \gamma_i Z_i^j\Big]^{1/j} \tag{4.8}$$

so $\tilde{z} = z_{3.62}$ and $\hat{z} = z_{1.86}$. γ_i are the fractional weights of the elements in the mixture.

Dividing Eq. 4.7 by μ_w leads to the reduced CT number or relative linear attenuation coefficient (u), and n_e becomes the relative electron density, ρ_e. However, [133] and [130] state that such a model is not sufficient as the power law additivity rule varies with photon energy and with samples containing elements with a large range of atomic numbers. [130] also state that empirical formula have been explored by polynomial or exponential functions that are valid over a specific range of Z and energy. [42] develop such a model. They show that the electronic cross section (σ_e) can be parameterized for any Z:

$$\sigma_e = \sum_{m=1}^{M} a_m Z^{m-1} \tag{4.9}$$

a_m are coefficients which can be estimated through a least-squares fit of the electronic cross section from the NIST database [134]. The behavior of the electronic cross section with respect to Z can be seen in [42]. Thus, for u, a relationship can be defined for one of the two energy scans:

$$u_r = \rho_{e,r} \sum_{m=1}^{M} b_{m,r} Z_{eff}^{m-1} \tag{4.10}$$

Here, $b_{m,r}$ are the first sets of coefficients which are estimated through calibration with a set of known materials. One set of coefficients corresponds to the low energy data set and the other corresponds to the high energy data set. It should be noted that the polynomial expansion in Eq. 4.10 [135, 136] offers more degrees of freedom compared to Eq 4.7. Additionally, for integer values of Z_{eff} in Eq. 4.10, corresponding to elements, the b_m values would be equal to the a_m values from Eq. 4.9 divided by the linear attenuation coefficient for water at the effective energy of the spectra. However, when looking at mixtures, the b_m values for said mixtures differ from the elemental a_m values.

Next, we define a variable (Γ) called the dual-energy index [137], which incorporates both CT numbers for a specific material or voxel, which is independent of ρ_e.

$$\Gamma = \frac{u_L - u_H}{u_L + u_H} \tag{4.11}$$

Γ is independent of ρ_e, and we can assume Z_{eff} is independent of the photon spectrum over the range of energies used [42]. Thus, we can say $\Gamma \equiv \Gamma(Z)$ within the domain $Z \in [Z_{min}, Z_{max}]$, where both Γ and Z are bijective. Z_{min} and Z_{max} refer to the lowest effective atomic numbers of the calibration materials. So, we can then define Z_{eff} as a polynomial sum of the Γ of order K.

$$Z_{eff} = \sum_{k=1}^{K} c_k \Gamma^{k-1} \tag{4.12}$$

Here, c_k is the second set of coefficients which are found through a least squares solution given known Z_{eff} and Γ values.

Once the $b_{m,r}$ and c_k coefficients have been found, Γ can be defined per voxel for subsequent scans and Z_{eff} can be estimated using Eq. 4.12 and ρ_e found using:

$$\rho_e = \frac{1}{2}[\rho_{e,L} + \rho_{e,H}] \tag{4.13}$$

in which

$$\rho_{e,r} = \frac{u_r}{\sum_{m=1}^{M} b_{m,r} Z_{eff}^{m-1}} \tag{4.14}$$

The only other modification made to the method from [42] occurs if the CT number of a voxel in either of the bins is below -900 HU, that voxel is automatically assigned to air with a Z_{eff} value of 7.66 and ρ_e value of 0.0011. Excluding air, the material with the lowest CT number is the LN-300 Lung insert, which averages approximately -710 HU over multiple imaging modalities, with the lowest CT number being -805 HU [138]. Alternatively, they demonstrated air had a maximum CT number of -960 HU. A threshold of -900 HU straddles the difference between the two, erring towards considering values as not air. Our system does suffer from ring artifacts which occur in regions of air as well, so utilizing a slightly higher threshold mitigates those artifacts from propagating into the Z_{eff} and ρ_e maps.

4.3.6 Tissue equivalent materials

Twelve inserts from an RMI electron density phantom (Gammex, Middleton, WI, USA) were used for the stoichiometric calibration for both PCD-CT and DECT, as well as for method evaluation. The insert information can be seen in Table 4.1 including their ρ_e and elemental compositions. The inserts' relative electron densities were provided with the phantom, and the elemental compositions were requested and obtained from the manufacturer. However, the phantom model was older than the manufacturer's records so a number of relative electron densities of the materials from the requested data did not match with the original data sheet provided with the phantom. The elemental composition of these materials was then found in other publications. Specifically, the elemental compositions of LN-450 Lung and IB Inner Bone were obtained from [139] and the two $CaCO_3$ cylinders were obtained from [96]. The materials covered most tissue types, with soft-tissue like materials ($Z_{eff} < 8$)

Table 4.1: Relative electron density (ρ_e), effective atomic number (Z_{eff}) for PCD-CT and DECT, and elemental composition for the tissue equivalent materials used in this study.

Material	ρ_e	$\mathbf{Z_{eff}}$ **PCD-CT**	$\mathbf{Z_{eff}}$ **DECT**	H	O	C	N	Cl	Ca	P	Mg	Si
Lung (LN-300)	0.280	7.782 ± 0.020	7.796 ± 0.000	7.43	20.71	57.86	1.96	0.08			11.19	0.77
Lung (LN-450)	0.465	7.704 ± 0.020	7.719 ± 0.000	8.47	18.11	59.56	1.97	0.1			11.21	0.58
AP6 Adipose	0.937	6.339 ± 0.024	6.362 ± 0.004	9.44	14.86	73.5	2.07	0.13				
BR-12 Breast	0.957	6.994 ± 0.023	7.011 ± 0.000	8.97	16.45	71.36	2.14	0.13	0.93			
Water	1.000	7.687 ± 0.006	7.693 ± 0.001	11.19	88.81							
Solid Water	0.987	7.763 ± 0.029	7.777 ± 0.003	8.39	18.40	68.59	2.19	0.14	2.26		0.03	
BRN-SR2 Brain	1.049	6.338 ± 0.024	6.362 ± 0.005	9.97	16.34	72.13	1.69	0.07				
LV1 Liver	1.077	7.755 ± 0.033	7.773 ± 0.003	8.40	18.50	68.41	2.25	0.14	2.26			
IB Inner Bone	1.106	10.638 ± 0.055	10.666 ± 0.003	6.67	23.52	55.65	1.96	0.11	8.86	3.23		
B-200 Bone	1.105	10.482 ± 0.058	10.515 ± 0.001	6.94	19.82	56.62	1.81	0.11	6.39	8.31		
CB2-30% $CaCO_3$	1.274	11.076 ± 0.046	11.095 ± 0.004	6.68	25.61	53.48	2.12	0.11	12.01			
CB2-50% $CaCO_3$	1.467	12.513 ± 0.012	12.499 ± 0.011	4.47	32.00	41.63	1.52	0.08	20.02			
SB3 Cortical Bone	1.691	13.582 ± 0.008	13.562 ± 0.013	2.26	39.08	30.34	0.99	0.04	36.48		0.41	

and materials mimicking various bone densities ($Z_{eff} > 10$). The tissue-equivalent inserts were only calibrated for ρ_e, while Z_{eff} was calculated based on the parametrization of the electronic cross section (Eq. 4.5) as Z_{eff} varies with photon energy. Z_{min} and Z_{max}, which define the Z domain over which decomposition is valid were $[6.338, 13.582]$ for PCD-CT and $[6.362, 13.562]$ for DECT.

In practice, the electronic cross sections for each of the elements that appear in the tissue-equivalent material compositions were obtained from the XCOM photon cross section database [134]. Beam spectra were generated in SpekPy [127], previously validated for our x-ray source [140]. Separately, each element's electronic cross section was averaged over the photon spectrum or energy bin spectrum in question, weighted by the relative number of photons of each energy. The effective energy of each energy bin was also calculated by taking the mean energy weighted by the photon spectrum within the bin. Then, a composite electronic cross section over all photon energies was then defined for each tissue-equivalent insert by calculating a weighted sum of the electronic cross sections for the elements that made up the insert, with the percent compositions as the weights for each element (Table 4.1), before taking the weighted average over the same photon spectrum. The theoretical Z_{eff} of each insert was then estimated based on a cubic spline interpolation between the energy weighted electronic cross sections of each of the elements and their atomic number. As the theoretical Z_{eff} varies with energy, the average of the two Z_{eff} values from the two energy ranges was used in the calibration and evaluation of the model, and the reason for the variation between PCD-CT and DECT. [42] showed that theoretical Z_{eff} varies weakly with the photon spectrum and can be considered as a systematic error. Table 4.1 shows the variation between the theoretical Z_{eff} values as the distance from the average (the value following the ±). Additionally, given the small variation in Z_{eff} values, we also consider variation to be a systematic error and that Z_{eff} is independent over the energy range of 24–120 keV.

4.3.7 Energy bin optimization

The PCD of the bench-top system offers six energy thresholds, which enabled a large number of potential energy range options for the low and high energy bins to be used in the decomposition. In order to find the energy ranges that offered the best results, fourteen sets of energy thresholds were chosen to encompass all possible energy ranges of 10 keV and larger between 35 and 120 keV, as seen in Table 4.2. The minimum width of an energy range was 10 keV, as the energy resolution of the detector is ∼8 keV. The tissue-equivalent materials were broken into three groups, as shown in Figure 4.2a–c, as the FOV of the system could not accommodate all of the cylinders in a single scan. The model was still optimized on all twelve materials and water. This resulted in 42 total scans, three at each set of energy thresholds. To minimize the number of CT acquisitions necessary, the summation of counts in adjacent bins was used to obtain larger energy ranges. Each of the scans was reconstructed and normalized according to Section 4.3.3, with the water normalization value being taken as the mean value within the water vial of each scan. An exhaustive search for best set of energy ranges was conducted by pairing each energy range with every other possible range; the starting energy of the higher energy range was restricted to be at least 5 keV above the ending energy of the lower range. For each pair, the CT volume was split in half and the model calibrated on half of the slices and evaluated on the other half. Additionally, at each pair of energy range, the model was tested at K and M values ranging between 2 and 7. Some combinations of energy ranges and K and M values did not converge on values of c and b, or produced negative mean values when evaluated, both were discarded. The performance of each pair of energy ranges, at each value of K and M, was evaluated by computing the average root mean squared percent error (RMSPE) of the tissue-equivalent materials excluding LN-300 Lung for both Z_{eff} and ρ_e. The RMSPE of Z_{eff} and ρ_e for LN-300 Lung was calculated separately, as due to its in-homogeneity it appears as an outlier, and skews the results of the average RMSPE. The equation for RMSPE can be seen below:

$$RMSPE = \sqrt{\frac{1}{n}\sum_{i=1}^{n}\left(\frac{y_i - \hat{y}_i}{y_i}\right)^2} * 100 \tag{4.15}$$

where $\hat{y}_i$ is the measured value of either Z_{eff} or ρ_e , y_i is the corresponding theoretical value, and n is the number of data points in the Z_{eff} or ρ_e sample. The data points for each tissue-equivalent materials were calculated as the mean values within a ∼22 mm diameter ROI within each of the slices of the CT scan. A weighted sum of the four values was computed with weights of 0.4, 0.35, 0.1, and 0.15 for the average Z_{eff} RMSPE, the average ρ_e RMSPE,

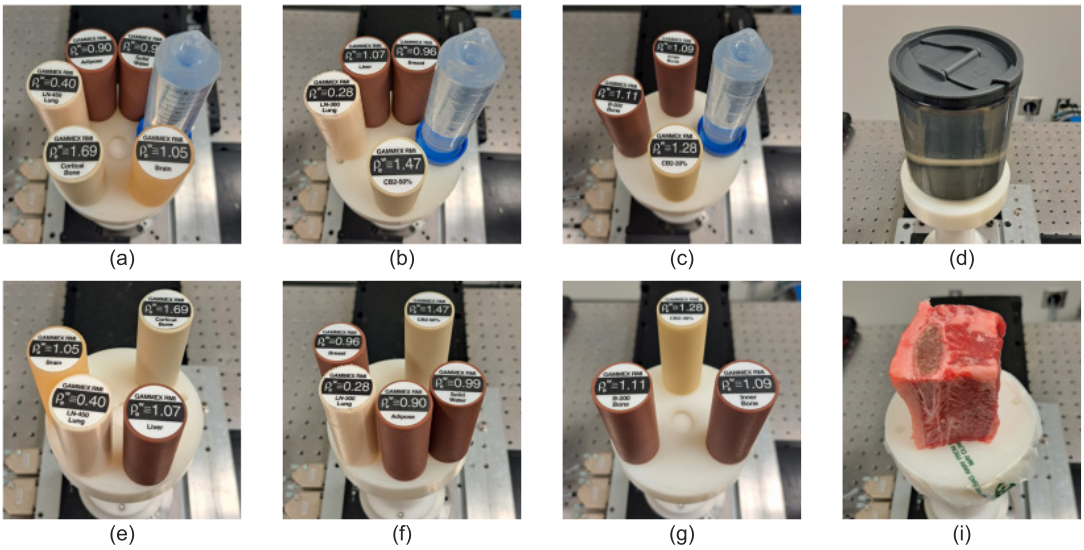

Figure 4.2: (a-c) The optimization tissue-equivalent subsets: (a) Brain, cortical bone, LN-450 lung, adipose, and solid water. (b) CB2-50%, liver, LN-300 lung, and breast. (c) Inner bone, B-200 bone, and CB2-30%. (d–g) The calibration and evaluation cylinder subsets: (d) The water phantom. (e) Cortical bone, brain, LN-450 Lung, and liver. (f) Solid water, adipose, LN-300 Lung, breast, CB2-50%. (g) Inner bone, B-200 bone, and CB2-30%. (i) An *ex-vivo* bovine tissue sample consisting of a short section of rib bone, surrounded by adipose and muscle tissue.

the Z_{eff} RMSPE of LN-300 Lung, and the ρ_e RMSPE of LN-300 Lung, respectively. The weights were chosen in order to minimize each of the four RMSPE values while limiting one of the four from growing too large.

For DECT, all values of K and M between 2 and 7 were used to calibrate and evaluate the model. The values which minimized the sum of the average RMSPE for Z_{eff} and ρ_e were used for further analysis.

4.3.8 Model performance analysis

After optimization, the tissue-equivalent cylinders were scanned at the energy thresholds dictated by the results of the optimization. A water phantom, as well as the inserts (Figure 4.2d–g) were scanned to acquire a data set to be used to calibrate the model. The inserts were again separated into three groups as they were unable to all fit on the rotation stage simultaneously. The entire group of twelve inserts, plus water, was used to calibrate the model. After model calibration, the calibration coefficients were tested by predicting elemental linear attenuation coefficients. Additionally, the CT number predicted by the model

Table 4.2: PCD energy thresholds for the energy range optimization scans.

PCD-CT	**Calibration coefficients**
Scan number	**Thresholds (keV)**
1	30, 45, 55, 65, 75, 120
2	35, 50, 65, 80, 95, 115
3	35, 60, 70, 85, 95, 120
4	35, 45, 70, 80, 90, 100
5	35, 45, 60, 75, 85, 100
6	40, 50, 60, 80, 95, 105
7	40, 55, 70, 85, 95, 115
8	40, 65, 75, 85, 95, 105
9	40, 50, 70, 85, 105, 120
10	40, 50, 75, 90, 105, 115
11	50, 60, 70, 90, 100, 110
12	55, 80, 90, 100, 110, 120
13	55, 65, 75, 85, 100, 120
14	55, 65, 75, 85, 100, 120

for each of the tissue equivalent materials was compared to the average CT number found experimentally. The residual HU was found by subtracting the experimental CT number from the predicted value. An additional set of the same scans was taken to obtain a data set to be used to evaluate the model, using all of the inserts and the water phantom. The values of K and M used in the model were also defined during the optimization. Once the Z_{eff} and ρ_e maps of the evaluation data set were extracted, the accuracy of the Z_{eff} and ρ_e values for each material was evaluated and compared to the calculated values. Mean Z_{eff} and ρ_e values were calculated from a 21 mm ROI within each cylinder over all slices without significant ring artifacts, and the RMSPE of each cylinder was evaluated using the mean value within the cylinder's ROI from each slice as data points, referred to as the ROI points. To compute the absolute error relative to water, the difference between the theoretical values and the ROI points was divided by the corresponding Z_{eff} or ρ_e of water. The mean and standard deviation of the results were then computed. The total mean of Z_{eff} and ρ_e for each material was also evaluated as the mean of all voxels within the ROIs from each of the slices, with the variation of Z_{eff} and ρ_e computed as the standard deviation of the voxels defined by the ROIs in the same slices. Additionally, to evaluate the noise between PCD-CT and DECT, the standard deviation of the voxels within the water insert were evaluated in the low and high energy CT images and the resulting Z_{eff} and ρ_e maps for each method. The model was also tested by scanning a 10 cm high-density polyethylene phantom containing

an approximately 10 mm diameter piece of pure aluminium to extract the atomic number and relative electron density.

4.3.9 *Ex-vivo* bovine tissue samples

An *ex-vivo* bovine tissue sample and was stored at 4°C in a refrigerator until it was scanned with PCD-CT and DECT. The same acquisition parameters as defined by the results of the optimization of the tissue-equivalent inserts were used in both cases. The time between the samples removal from the refrigerator and the end of scanning was approximately two hours. The bovine sample consisted of fat, muscle, and bone and was approximately 75 mm in height and 45 and 60 mm in length and width, respectively (Figure 4.2i). One acquisition was acquired with the bovine sample alone for both PCD-CT and DECT and another acquisition was conducted for PCD-CT after the same sample was injected with 0.3 ml of 50 mg/ml $AuCl_3$ (GG3CS-25.4-100 Lot AUY03-7077, Nanopartz Inc, Loveland, CO) into the muscle and fat portion to mimic a contrast-enhanced CT scan.

4.3.10 *Ex-vivo* tissue data analysis

The Z_{eff} and ρ_e maps for the short rib scans were extracted after the stoichiometric calibration was computed on the values from all of the tissue-equivalent material cylinders. The Z_{eff} and ρ_e values of adipose, muscle, spongiosa (or inner bone), and cortical bone were compared to reference values. The reference material values were calculated from the mass densities and elemental compositions of human tissues referenced from ICRP50 as tabulated in [42]. The measured *ex-vivo* tissue sample's Z_{eff} and ρ_e values found after material decomposition were calculated by placing ROIs in the conventional CT image within areas containing only the specific material. The mean and standard deviation of the voxels defined by the ROIs in all slices without significant ring artifacts were then calculated and compared to the reference value.

4.3.11 K-edge subtraction

Gold K-edge images were reconstructed using the K-edge decomposition method described by Zhang *et al* (2020) [60]. The K-edge subtraction algorithm used the two energy ranges of the sinogram surrounding the K-edge of gold (80.7 keV), as one of the energy thresholds was placed placed at 81 keV. Once reconstructed, the signal of a reference 50 mg/ml $AuCl_3$ gold sample and water were used to normalize K-edge image signal linearly between 0 and 50

mg/ml of Au. As the injected gold in the short rib was 50 mg/ml, signal would not exceed that level.

4.4 Results

4.4.1 Energy bin optimization

We found that the energy ranges of 35–50 keV and 65–95 keV gave the best balance of minimizing the average RMSPE of Z_{eff} and ρ_e for all materials (excluding LN-300 Lung) and the RMSPE of LN-300 Lung itself. K and M values of 5 also gave us the best results for PCD-CT. For DECT, we obtained the best results given K and M values of 2 and 3, respectively. The RMSPE values for the energy ranges of 35–50 keV and 65–95 keV can be seen in Table 4.3 with all combinations of K and M between 2 and 7. The full list of results for PCD-CT and DECT can be found in the Supplementary Materials. The effective energy for the 80 kVp spectrum with 3 mm Al was 44.9 keV, for the 120 kVp spectrum with 6 mm Al was 58.9 keV, for the 35–50 keV bin with 6 mm Al was 42.7 keV, and for the 65–95 keV bin with 6 mm Al was 76.4 keV.

4.4.2 Calibration verification

Given the best energy ranges of 35–50 keV and 65–95 keV, the energy thresholds for the calibration and evaluation scans were set to 30, 35, 50, 65, 81, and 95 keV. The 81 keV threshold was chosen in order to account for K-edge imaging of gold, and the 65–95 keV bin was created by summing the 65–81 and 81–95 keV bins together. The calibration coefficients determined for PCD-CT and DECT can be seen in Table 4.4. Using the b_m values for both energy ranges for PCD-CT and DECT, the values of the sum $\sum_{m=1}^{M} b_{m,r} Z_{eff}^{m-1}$ from Eq. 4.10 was calculated for elements between 5 and 15, the approximate Z_{eff} range the model is calibrated for. The results can be seen in Fig. 4.3. The calculated values ranged between ∼0.75–1.0 at $Z = 5$ and increased to ∼1.4–2.2 at $Z = 15$. Two examples of the predicted elemental linear attenuation coefficients for oxygen and carbon at the effective energies of the two PCD-CT energy bins and the 80 kVp and 120 kVp spectra can be seen in Figure 4.4. The results of the aluminium extraction can be seen in the Fig. 4.5 and 4.6. The comparison between the predicted and experimental CT number for each of the tissue equivalent materials can be seen in Fig. 4.7. Materials with residual CT numbers over ±10 HU were water in all energy ranges, B-200 Bone in the 35–50 keV energy bin, IB Inner Bone in the 80 kVp and 120 kVp spectra, CB2-50% in the 80 kVp and 120 kVp spectra, and

Table 4.3: The optimization results for K and M values with energy bins of 35–50 keV and 65–95 keV. Mean Z_{eff} and ρ_e RMSPE values encompass all tissue-equivalent inserts excluding LN-300 Lung.

K	**M**	**Mean Z_{eff} RMSPE**	**Mean ρ_e RMSPE**	**LN-300 Lung Z_{eff} RMSPE**	**LN-300 Lung ρ_e RMSPE**
2	2	1.465	2.454	3.247	1.056
2	3	1.465	0.806	3.247	0.836
2	4	1.465	0.875	3.247	0.838
2	5	1.465	1.140	3.247	3.027
2	6	1.465	0.871	3.247	1.112
2	7	1.465	2.925	3.247	47.248
3	2	1.357	2.488	3.343	1.123
3	3	1.357	0.862	3.343	0.860
3	4	1.357	0.935	3.343	0.872
3	5	1.357	1.125	3.343	2.543
3	6	1.357	0.843	3.343	1.212
3	7	1.357	1.671	3.343	4.966
4	2	1.021	3.274	4.979	5.966
4	3	1.021	0.473	4.979	1.117
4	4	1.021	0.514	4.979	1.206
4	5	1.021	1.288	4.979	8.390
4	6	1.021	0.827	4.979	2.545
4	7	1.021	13.008	4.979	2.979
5	2	1.102	2.403	0.535	1.140
5	3	1.102	0.425	0.535	1.420
5	4	1.102	0.470	0.535	1.416
5	5	1.102	0.469	0.535	0.947
5	6	1.102	0.654	0.535	1.431
5	7	1.102	1.535	0.535	1.143
6	2	3.588	3.743	19.058	4.779
6	3	3.588	0.511	19.058	1.982
6	4	3.588	1.943	19.058	2.221
6	5	3.588	3.014	19.058	19.148
6	6	3.588	1.055	19.058	4.859
6	7	3.588	4.256	19.058	3.402
7	2	3.188	3.564	17.457	577.394
7	3	3.188	0.510	17.457	1.901
7	4	3.188	0.590	17.457	8.009
7	6	3.188	1.497	17.457	4.729
7	7	3.188	38.384	17.457	43.952

Table 4.4: The calibration coefficients of the model for PCD-CT and DECT. b_L refers to the calibration coefficients in Eq. 4.10 calculated for the low energy range. b_H are those for the high energy range.

PCD-CT	**Calibration coefficients**
c, $K = 5$	7.80, 51.98, -57.77, -2937.70, 19069.63
b_L, $M = 5$	-3.25, 1.86, -0.31, 0.023, -0.00058
b_H, $M = 5$	0.73, 0.10, -0.017, 0.0014, -0.000031
DECT	**Calibration coefficients**
c, $K = 2$	7.35, 70.68
b_L, $M = 3$	1.00, -0.076, 0.010
b_H, $M = 3$	1.05, -0.062, 0.0074

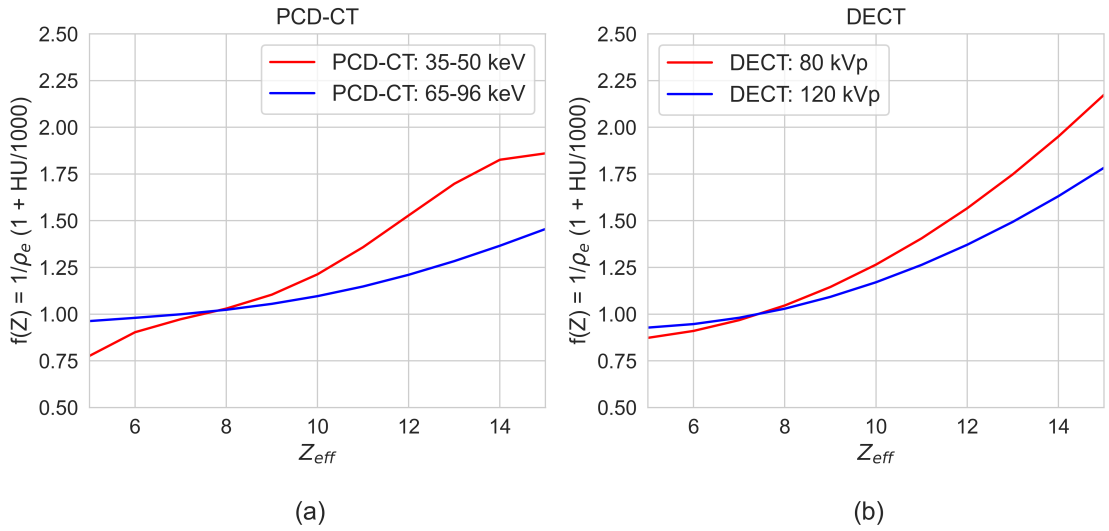

Figure 4.3: Calibration results for elements between 5 and 15 based on the bm coefficients from Table 4.4 and calculating the sum in the Eq. 4.10. (a) The results for PCD-CT. (b) The results for DECT.

Cortical Bone in the 80 kVp spectrum.

4.4.3 Method evaluation with known tissue-equivalent materials

The results of the decomposition of Z_{eff} and ρ_e from the 12 tissue equivalent cylinders and water can be seen in the resulting images in Figure 4.8 for PCD-CT and Figure 4.9 for DECT. Both figures show a conventional CT image with the CB3-50%, AP6 Adipose, LN-300 Lung, Solid Water, and BR-12 Breast and the resulting Z_{eff} and ρ_e maps.

Table 4.5 shows the RMSPE of each of the cylinders and Table 4.6 shows the error of

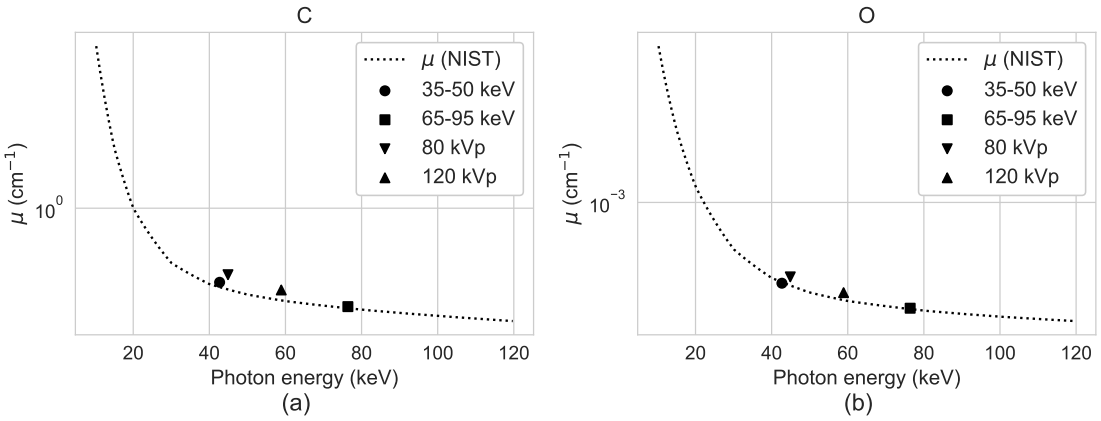

Figure 4.4: Predicted linear attenuation coefficient at the effective energies of the energy bins for PCD-CT and spectra for DECT. (a) Carbon. (b) Oxygen.

on the materials relative to water. Figure 4.10 shows the voxel-wise mean and standard deviation of both Z_{eff} and ρ_e each of the various tissue-equivalent materials plotted as ρ_e vs. Z_{eff}, for both PCD-CT and DECT.

Table 4.7 demonstrates the noise in the low and high energy CT images for PCD-CT and DECT as well as the noise in the Z_{eff} and ρ_e maps for each method.

4.4.4 *Ex-vivo* tissue sample

The decomposition images of the *ex-vivo* tissue sample can be seen in Figure 4.11 for PCD-CT and Figure 4.12 for DECT. The conventional CT image and the Z_{eff} and ρ_e maps are presented in both figures. The mean and standard deviation of Z_{eff} and ρ_e within ROIs of cortical bone, adipose, muscle, and inner bone (spongiosa) are shown for both PCD-CT and DECT in Table 4.8.

4.4.5 K-edge imaging

In addition to material decomposition, PCD-CT offers high-Z contrast material extraction and quantification, as demonstrated in Figure 4.13. In the conventional CT image (Figure 4.13a) the gold solution is indistinguishable from the inner bone (Figure 4.13b). However, gold is extracted in the K-edge subtraction image (Figure 4.13c).

Table 4.5: RMSPE of individual tissue equivalent materials.

	$\mathbf{Z_{eff}}$		$\rho_\mathbf{e}$	
Material	**PCD-CT**	**DECT**	**PCD-CT**	**DECT**
Lung (LN-300)	0.70%	5.46%	4.57%	13.93%
Lung (LN-450)	0.59%	3.06%	0.52%	2.26%
AP6 Adipose	0.94%	0.41%	0.10%	0.11%
BR-12 Breast	0.89%	1.33%	0.33%	0.71%
Water	1.45%	4.00%	1.83%	0.29%
Solid Water	0.86%	1.14%	0.20%	1.02%
BRN-SR2 Brain	0.70%	0.20%	0.14%	0.41%
LV1 Liver	0.37%	1.63%	0.61%	1.17%
IB Inner Bone	0.58%	0.49%	0.13%	0.84%
B-200 Bone Mineral	0.92%	0.91%	0.16%	0.77%
CB2-30% $CaCO_3$	0.32%	0.95%	0.09%	1.32%
CB2-50% $CaCO_3$	0.72%	1.16%	0.52%	0.20%
SB3 Cortical Bone	0.81%	2.21%	0.17%	2.67%

Table 4.6: Absolute error relative to water of individual tissue equivalent materials.

	$\mathbf{Z_{eff}}$		$\rho_\mathbf{e}$	
Material	**PCD-CT**	**DECT**	**PCD-CT**	**DECT**
Lung (LN-300)	0.63% ± 0.32%	5.49% ± 0.55%	1.23% ± 0.36%	3.89% ± 0.35%
Lung (LN-450)	0.53% ± 0.26%	3.02% ± 0.54%	0.19% ± 0.15%	1.02% ± 0.24%
AP6 Adipose	0.76% ± 0.79%	0.33% ± 0.14%	0.07% ± 0.05%	0.10% ± 0.05%
BR-12 Breast	0.79% ± 0.16%	1.18% ± 0.17%	0.30% ± 0.09%	0.67% ± 0.10%
Water	1.42% ± 0.26%	3.99% ± 0.28%	1.83% ± 0.09%	0.26% ± 0.12%
Solid Water	0.86% ± 0.12%	1.10% ± 0.14%	0.18% ± 0.08%	1.01% ± 0.07%
BRN-SR2 Brain	0.55% ± 0.18%	0.11% ± 0.10%	0.12% ± 0.07%	0.44% ± 0.06%
LV1 Liver	0.35% ± 0.15%	1.60% ± 0.12%	0.65% ± 0.08%	1.26% ± 0.04%
IB Inner Bone	0.80% ± 0.11%	0.66% ± 0.22%	0.12% ± 0.08%	0.92% ± 0.17%
B-200 Bone Mineral	1.25% ± 0.11%	1.17% ± 0.24%	0.15% ± 0.09%	0.81% ± 0.24%
CB2-30% $CaCO_3$	0.45% ± 0.10%	1.35% ± 0.22%	0.09% ± 0.07%	1.66% ± 0.26%
CB2-50% $CaCO_3$	1.15% ± 0.22%	1.89% ± 0.26%	0.73% ± 0.21%	0.22% ± 0.20%
SB3 Cortical Bone	1.40% ± 0.30%	3.88% ± 0.19%	0.25% ± 0.15%	4.50% ± 0.19%

Table 4.7: The noise in the low and high energy CT images and Z_{eff} and ρ_e maps for PCD-CT and DECT.

Image noise	**PCD-CT**	**DECT**
Low energy CT	17 HU	19 HU
High energy CT	20 HU	13 HU
Z_{eff} map	0.567	0.556
ρ_e map	0.031	0.032

Table 4.8: Effective atomic numbers and relative electron densities extracted from *Ex-vivo* bovine tissue sample. Mean and standard deviation are displayed with the corresponding ICRP human tissue values [141], calculated from their elemental compositions [129] as detailed in Section 4.3.6.

Material	**Adipose**	**Muscle**	**Inner bone (spongiosa)**	**Cortical bone**
PCD-CT Effective Z (ICRP)	6.41 ± 0.51 (6.636)	7.74 ± 0.51 (7.751)	10.60 ± 0.51 (10.391)	13.39 ± 0.72 (13.666)
DECT Effective Z (ICRP)	6.56 ± 0.66 (6.659)	7.72 ± 0.67 (7.760)	10.36 ± 3.24 (10.407)	12.94 ± 1.44 (13.653)
PCD-CT Relative electron density (ICRP)	0.95 ± 0.03 (0.951)	1.05 ± 0.03 (1.04)	1.15 ± 0.06 (1.15)	1.60 ± 0.05 (1.781)
DECT Relative electron density (ICRP)	0.95 ± 0.03 (0.951)	1.06 ± 0.04 (1.04)	1.16 ± 0.27 (1.15)	1.68 ± 0.20 (1.781)

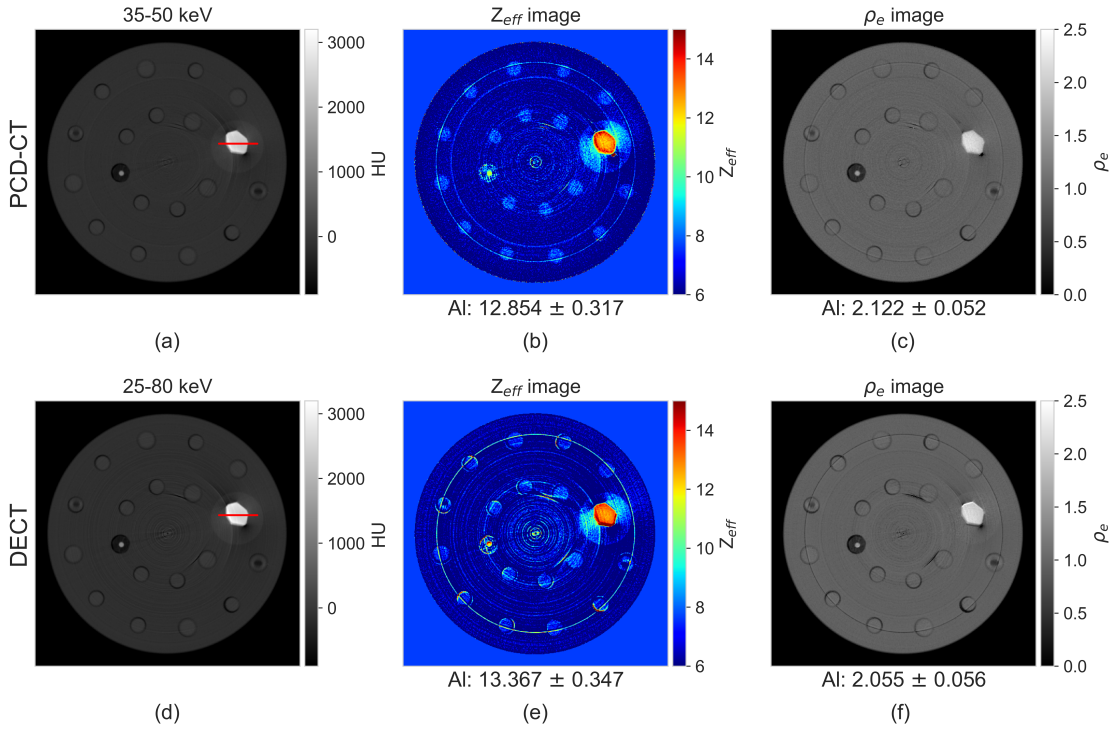

Figure 4.5: The 10 cm high-density polyethylene phantom containing a 10-mm diameter piece of aluminium. (a–c) PCD-CT images: (a) the 35-50 keV bin with a profile drawn through the Al, (b) the Z_{eff} map, and (c) the ρ_e map. (d–f) DECT images: (d) the 25-80 keV bin with a profile drawn through the Al, (e) the Z_{eff} map, and (f) the ρ_e map. The Z_{eff} and ρ_e maps show the mean and standard deviation of the extracted values. The atomic number of Al is 13 and the relative electron density is 2.344, calculated values for PCD-CT and DECT are shown below each figure. Excessive beam hardening negatively affects the Z_{eff} maps for both PCD-CT and DECT.

4.5 Discussion

The ability for the decomposition method to accurately segment materials based on Z_{eff} and ρ_e was successfully demonstrated with a set of calibration tissue-equivalent materials along with an *ex-vivo* bovine tissue sample. The mean RMSPE values for Z_{eff} and ρ_e for PCD-CT were 0.76% and 0.72%, respectively, and 1.77% and 1.98% for DECT. One potential explanation for the better performance of the PCD-CT model compared to DECT model can be seen in Fig. 4.3. Over the entire Z_{eff} range that the PCD-CT or DECT models are calibrated for, the difference in the values for the low and high energy range is larger for PCD-CT, meaning material analysis is easier. For both data sets, however, a number of shortcomings exist that could lead to the the decomposed data not matching the theoretical

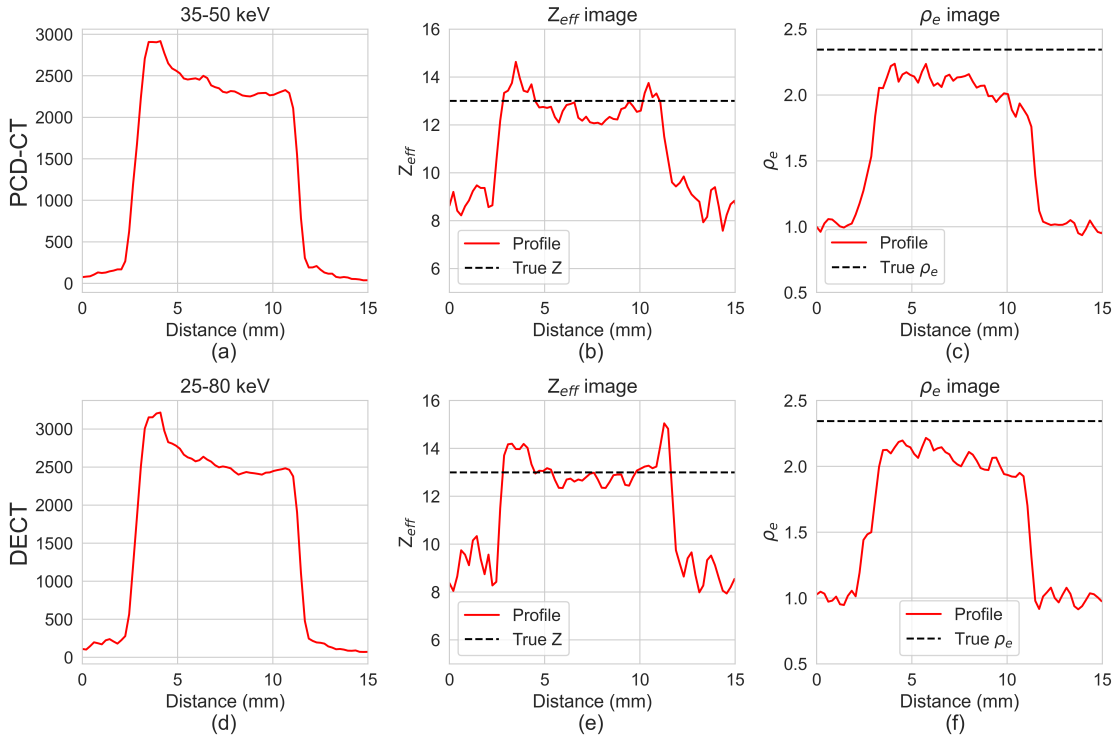

Figure 4.6: The image signal for the profile seen in Supplementary Figure 1 in (a–c) PCD-CT images: (a) the 35–50 keV bin, (b) the Z_{eff} map, and (c) the ρ_e map. (d–f) DECT images: (d) the 25–80 keV bin, (e) the Z_{eff} map, and (f) the ρ_e map. The Z_{eff} and ρ_e maps show the mean and standard deviation of the extracted values.

values. Due to the fact that the phantom was an older model, the manufacturer did not have the composition data for the specific batch of tissue-equivalent inserts. The density and ρ_e specifications were included with the phantom, so the predicted ρ_e was accurate. The manufacturer did provide an elemental composition table for the current makeup of the various inserts with their density and ρ_e. For the materials whose ρ_e did not quite match with the manufacturer-provided table, the closest data was found in the literature. As the calculation for the theoretical Z_{eff} values depends significantly on the elemental makeup of the inserts, this introduced uncertainty. However, as seen in Fig. 4.7, the experimental CT number for the various tissue-equivalent materials was generally within 10 HU of the CT number predicted by the model for all energy bins or spectra, excluding some outliers. This indicates that the composition of the materials in Table 4.1 is close to the real composition for those that were found in the literature. The material that showed the highest consistent residual CT number across both energy bins and both DECT spectra was, in fact, water. Given that the composition of water is well defined, and that the materials whose compo-

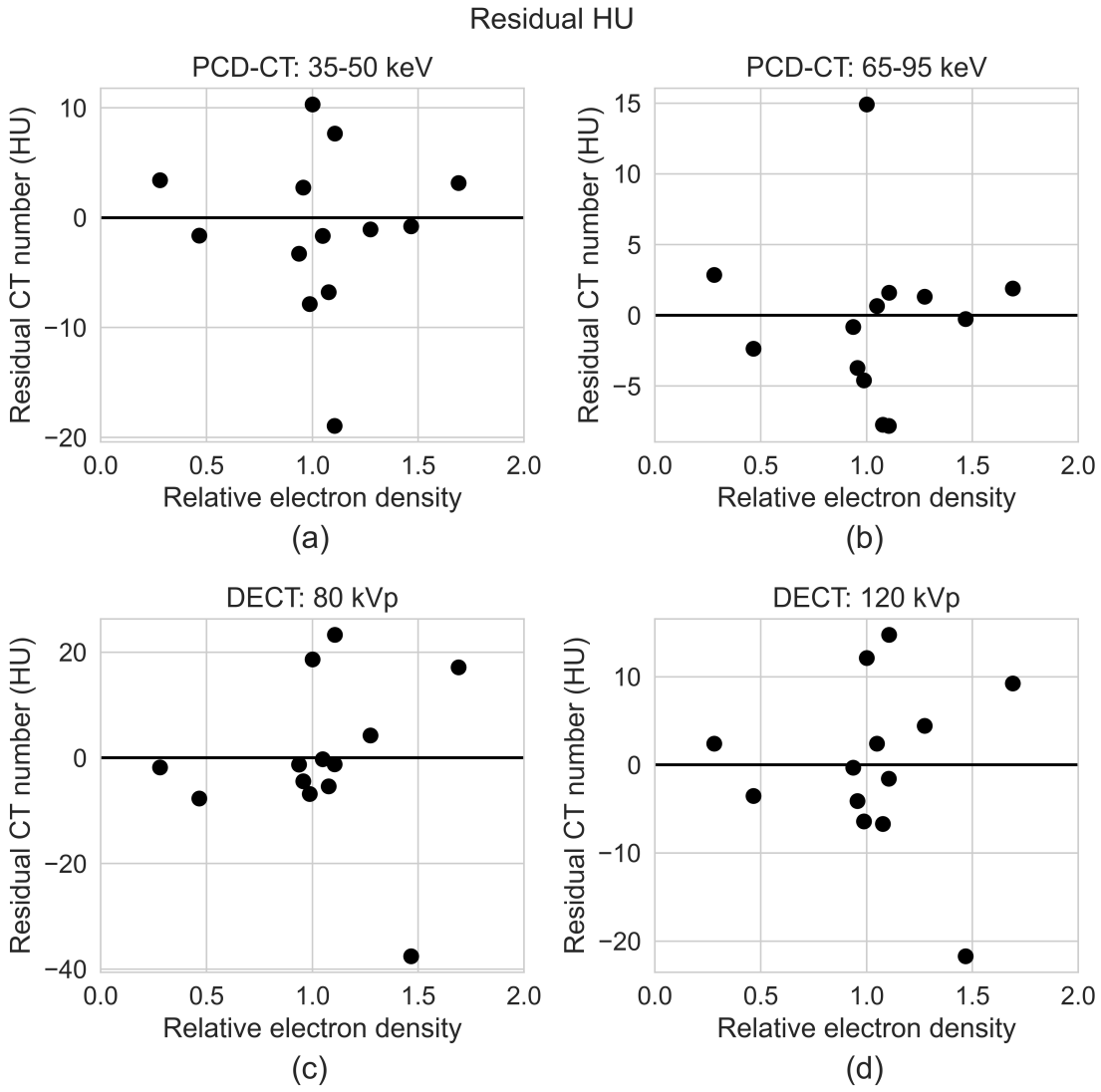

Figure 4.7: The residual CT number for the tissue-equivalent materials plotted against their relative electron density. The residual CT number is the experimental CT number subtracted from the CT number predicted by the model. (a) the 35–50 keV bin for PCD-CT, (b) the 65–95 keV bin for PCD-CT, (c) the 80 kVp spectrum for DECT, and (d) the 120 kVp spectrum for DECT.

sitions were found in the literature did not deviate over all energy bins and spectra, the deviation was likely not due entirely from erroneous compositions. In fact, LN-450 Lung, whose density deviated the most from the density found in the literature, still demonstrated similar accuracy when compared with other inserts for the PCD-CT data.

Next, there was also uncertainty in the beam weighting of the electronic cross sections

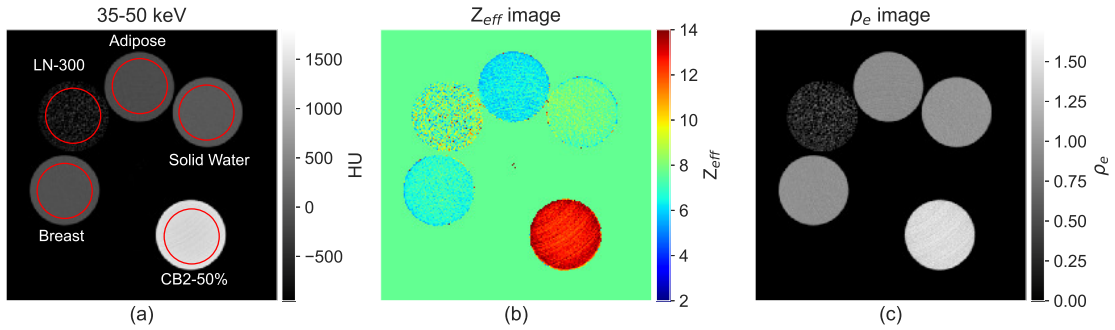

Figure 4.8: PCD-CT images of the second evaluation subset of tissue equivalent materials and water. (a) 35-50 keV CT image with labeled materials and ROIs depicted in red. (b) Effective atomic number image. (c) Relative electron density image.

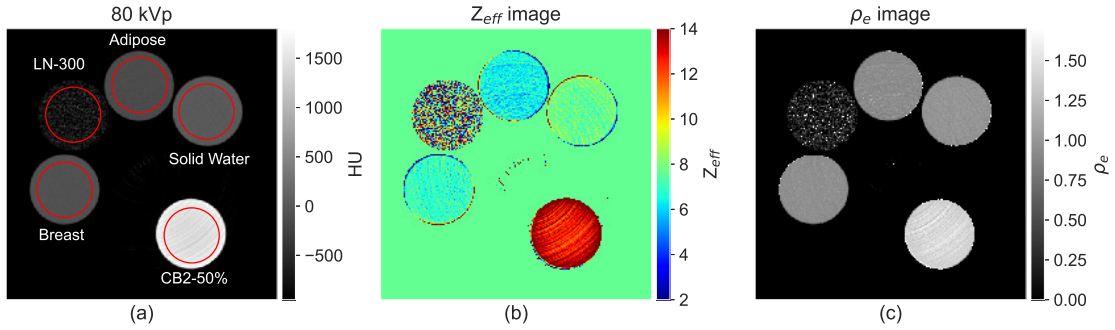

Figure 4.9: DECT images of the second evaluation subset of tissue equivalent materials and water. (a) 80 kVp CT image with labeled materials and ROIs depicted in red. (b) Effective atomic number image. (c) Relative electron density image.

in the calculation of the predicted Z_{eff} values. The spectra used in the calculations were the x-ray tube spectra, but as we were using a PCD, which suffers from effects such as charge-sharing and pulse pileup [11], in addition to having a non-finite energy resolution, the number of x-rays in a given bin may not match the actual number of x-rays produced by the x-ray tube in that energy range. For the PCD-CT data, we also restricted the energy ranges to contain energies 35 keV and above, which could impact the optimization negatively. This is due to the fact that many soft tissues have larger differences in attenuation in the low energy range, and thus lead to a more accurate decomposition. However, our PCD does suffer from large differences in pixel response at energies below 30 keV, so in order to reduce image noise, the lowest energy threshold in the optimization was restricted to 35 keV. Error could still have been introduced in the DECT data, as it encompassed all energies from 24

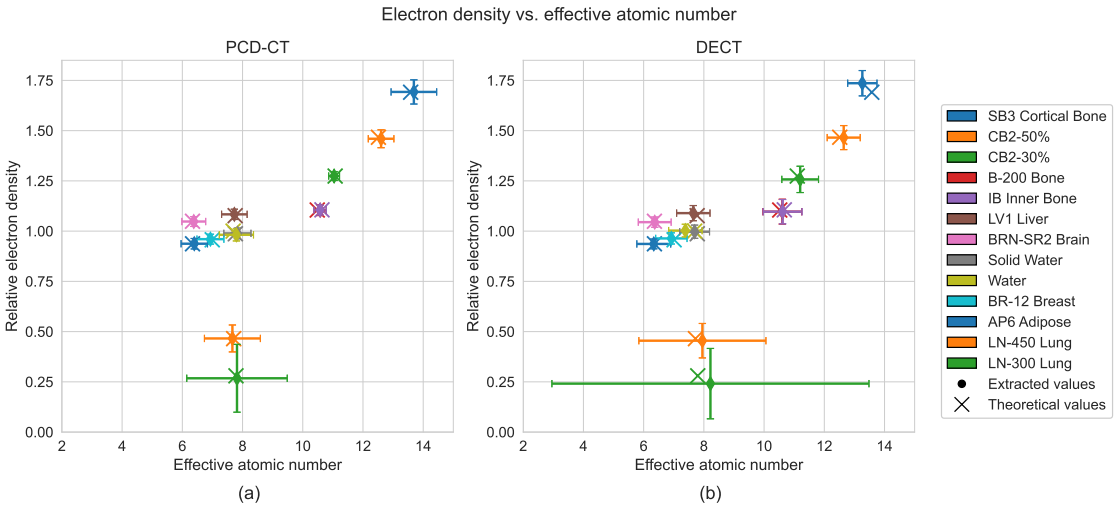

Figure 4.10: Effective atomic number versus relative electron density for all the tissue equivalent materials and water. Crosses designate the theoretical values, and diamonds show the extracted values, with error bars showing the standard deviation within the ROI for each cylinder. (a) PCD-CT. (b) DECT.

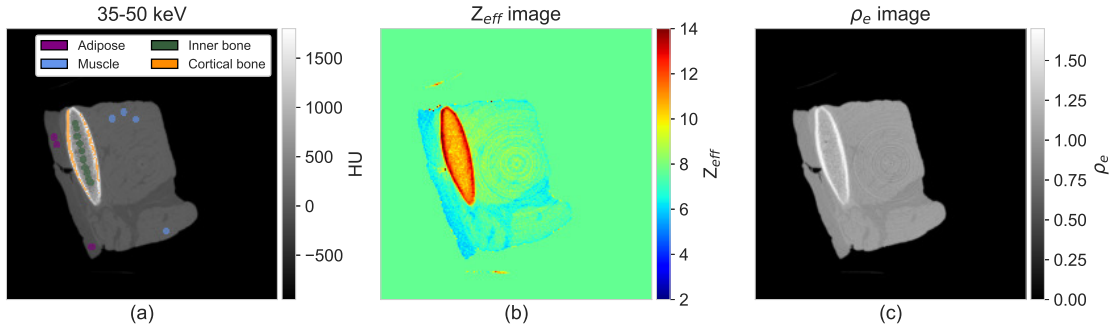

Figure 4.11: PCD-CT images of an *ex-vivo* tissue sample. (a) 35-50 keV CT image with the color-coded tissue-specific ROIs. (b) Effective atomic number image. (c) Relative electron density image.

keV (the electronic noise threshold) to the peak beam energy. This could be evident in the increased ring artifacts seen in the DECT images (Figures 4.9 and 4.12) when compared with the PCD-CT images (Figures 4.8 and 4.11). This introduced the potential for error in CT number for the DECT data, as seen with the higher residual CT numbers for the two DECT spectra (Fig. 4.7), and increased the noise within the cylinders when compared with the PCD-CT data.

These properties and shortcomings of the PCD were also demonstrated in the prediction

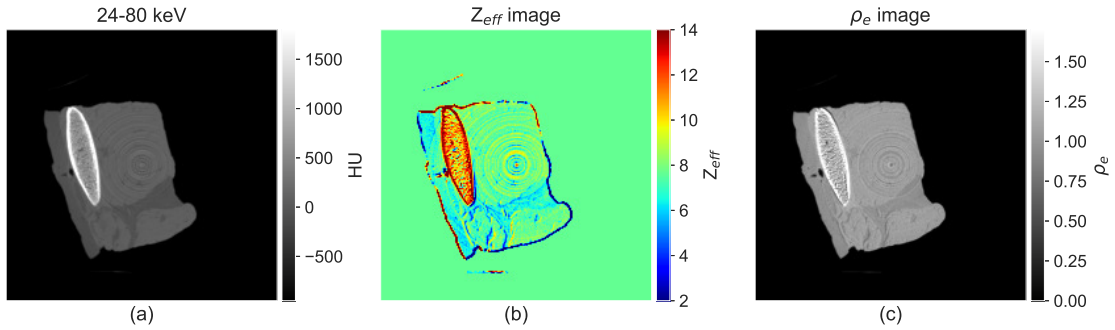

Figure 4.12: DECT images of an *ex-vivo* tissue sample. (a) 80 kVp CT image with the color-coded tissue-specific ROIs. (b) Effective atomic number image. (c) Relative electron density image.

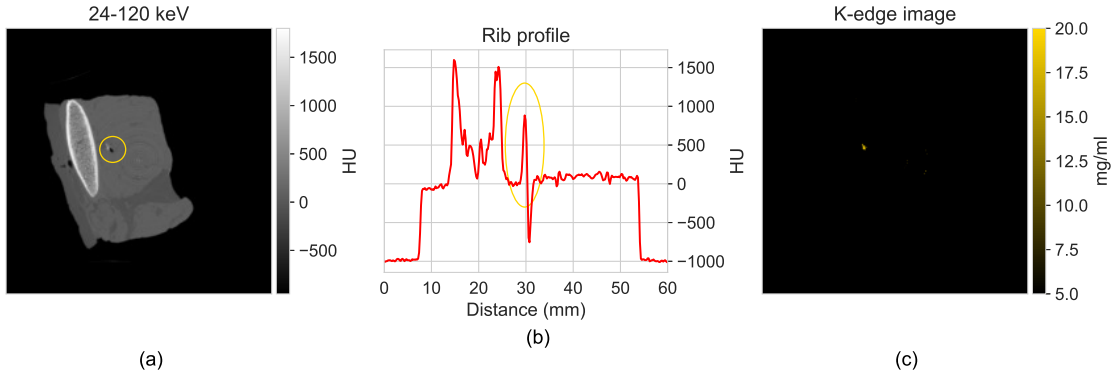

Figure 4.13: K-edge imaging for gold identification in an *ex-vivo* tissue sample. (a) 24-120 keV CT image, gold circled. (b) Profile drawn across the rib, shown as the red line in (a), gold signal circled. (c) K-edge subtraction image of gold.

of the linear attenuation coefficients of carbon and oxygen (Fig. 4.4) at the effective beam energies for both PCD-CT bins and both DECT spectra. Though the model successfully predicted the linear attenuation coefficients of carbon and oxygen (Fig. 4.4), closely for PCD-CT, the predictions of the linear attenuation coefficients at the effective beam energies of the 80 kVp beam and the 120 kVp beam were further from the true values. This is likely due to the inclusion of the detections in the PCD below 30 keV, which include more spurious counts and are subject to more noise than other energies. The effective energies were calculated using the beam spectra calculated in Spekpy, which did not take into account the spectra the detector records, which were distorted by charge-sharing and pileup. The PCD-CT linear attenuation values were more accurate as the two energy bins suffer less from noise introduced by the detector in the energy range below 30 keV and thus the effective beam energies were

more accurate. The performance of the model was also demonstrated in the decomposition of the aluminum (Fig. 4.5, 4.6), which was not a calibration material. Although the Z value was reconstructed accurately, beam hardening was seen in the CT images and especially in the Z_{eff} maps. ρ_e was underestimated for both PCD-CT and DECT, though it was outside of the calibration values for ρ_e, which contributed to the effect.

A potential shortcoming of the bin optimization for PCD-CT was the inclusion of the water vial in the insert scans. As these were cone-beam acquisitions, the water vial was used to normalize the reconstructions to CT number. The placement of the water vial in the same scan as the inserts could have lead to beam hardening artifacts from the bone-equivalent inserts in the water vial within the reconstructed images. Artifacts would affect the normalization and thus the correct calculation of CT number. However, each of the scans was examined qualitatively and the slices chosen in which to calculate the normalization value were free from artifacts. The choice to include the water vial in the other tissue-equivalent insert scans was to reduce to the total number of optimization scans that were necessary. For the calibration and evaluation scans, the separate water phantom was scanned in order to reduce the possibility of beam hardening artifacts.

PCD-CT outperformed DECT overall. Though DECT demonstrated slightly better RMSPE and relative error values for some of tissue-equivalent materials, such as AP6 Adipose and BRN-SR2 Brain, DECT did not offer better results for both Z_{eff} and ρ_e for a single insert. Figure 4.10 demonstrates how the PCD-CT data agreed better with the predicted values than DECT did, with mean values which were closer to the predicted values. The RMSPE and relative errors for Z_{eff} and ρ_e were calculated from the mean values in each slice in order to mitigate the effect the ring artifacts had the results. The DECT images also suffered from mis-registration, which is obvious in areas immediately surrounding the cylinders and the *ex-vivo* bovine tissue sample in the Z_{eff} images (Figures 4.9b and 4.12b). Each of the 80 kVp DECT scans was approximately half of a degree out of rotation with the corresponding 120 kVP scan, as shifting the sinogram one projection along the angle space in either the positive or negative resulted in larger rings surrounding the objects in the Z_{eff} images. This was largely mitigated for the calculated Z_{eff} and ρ_e values for tissue-equivalent cylinders since the ROIs avoided the edges of the inserts, and excluding the two lung-mimicking materials, the inserts were homogeneous. The results for the two lung materials demonstrated how mis-registration can be a detriment in DECT due to the various pores within the material being misaligned. However, even when excluding the lung samples, PCD-CT demonstrated mean RMSPE values for Z_{eff} and ρ_e of 0.78% and 0.39%, respectively, compared with 1.30% and 0.87% for DECT.

For the *ex-vivo* bovine tissue sample, our method was not able to offer results which were as accurate for all of the real tissue types as those that were found for the electron density inserts.Adipose, muscle, and inner bone were accurately determined, with relative errors for Z_{eff} below 2.9% for both PCD-CT and DECT, and errors of 2% or less for ρ_e. Cortical bone deviated much more significantly for both methods. There are a few likely sources which contributed to the differences between the predicted and measured values. First, the tissue sample is bovine, which may offer slightly different tissue compositions compared to the measured human tissue compositions from the ICRP. Additionally, the types of bone measured as spongiosa and cortical bone (Figures 4.11 and 4.12)in the rib may not actually represent the type of bone that was defined for the ICRP values. The areas adipose and muscle are more obvious in the images and as a result the decomposed values more accurate as well.

Gold chloride was successfully segmented within the bovine tissue sample with K-edge subtraction imaging demonstrating the ability of PCD-CT to extract high-Z contrast materials in images while performing Z_{eff} and ρ_e decomposition. K-edge subtraction results in material specific and quantifiable material maps, which can, as demonstrated in this study, be produced from the same set of energy bin data as was used for material decomposition.

One of the major benefits of PCD-CT in regard to material decomposition is that PCD-CT is able to acquire the requisite energy data for material decomposition without the need for a separate DECT system. With PCD-CT, multi-energy scans can be acquired on the same system that acquires conventional CT data. Additionally, more than two sets of energy data can be acquired, which offers the potential to decompose data into more than just two maps [56], as done in this study with Z_{eff} and ρ_e. The fact that the PCD-CT spectral data is already co-registered also makes projection-based decomposition methods more easily feasible than many DECT systems where co-registration can be more complicated, as demonstrated in this study. Projection-based decomposition methods avoid errors that can be introduced by the reconstruction process in image-based methods, as the decomposition is done in the raw data space and reconstructed afterwards [142]. Our lab is currently investigating projection-based methods in addition to image-based methods, as the one detailed in this study.

Dual source PCD-CT has been demonstrated to provide lower noise values compared to dual source EID-CT in both conventional [143, 144] and spectral mode [145, 146]. A large part of this reduction in dose with the dual-source PCD-CT system is due to the improved contrast-to-noise ratio with PCDs compared to EIDs because of the reduction in electronic noise and the lower statistical noise [147]. This noise reduction with PCDs enables

an equivalent signal-to-noise ratio (SNR) and CNR to be achieved at a lower dose compared with EIDs. In this work we compared a dual-source PCD-CT with a single-source PCD-CT. In addition to lower mean RMSPE values, PCD-CT provided similar noise in the water vial compared to DECT (Table 4.7), with only half the dose. The DECT images suffered from increased ring artifacts which affected the tissue-equivalent material results. The similar level of noise with less dose can be explained by a better spectral separation between low and high energy images with low/high energies of 42.7/76.4 keV and 44.9/58.9 keV for PCD and DECT, respectively. This spectral separation could be improved for the DECT but would necessitate a high source voltage that is not available in our facility. A fair comparison of the dose efficiency could then be performed.

If we compare other DECT methods decomposing Z_{eff} and ρ_e maps to that of our method reproducing [42] in PCD-CT, we find better results with the PCD-CT data described here. For reference, with PCD-CT we obtain mean RMSPE values of 0.76% and 0.72% for Z_{eff} and ρ_e, respectively, and mean relative errors of 0.84% and 0.46%, respectively. With our DECT scans we obtained mean RMSPE values of 1.77% and 1.98%, respectively, and mean absolute relative errors of 1.69% and 1.07%.[95] found mean errors on ρ_e of 1.01%., using a linear relationship of ρ_e and the difference in CT number in a DECT scan. [96] showed average Z_{eff} RMSPE values of 5.1%, and [103] demonstrated an RSMPE on average Z_{eff} of 2.9% [101] obtained relative errors of 1.7% and 0.4% for Z_{eff} and ρ_e, respectively, achieving better results for ρ_e than using our method with PCD-CT. And finally, [42] found RMSPE values of 3.58% and 0.60% for Z_{eff} and ρ_e, respectively, which still outperforms our adaptation in respect to ρ_e. More recently, these methods have also been applied experimentally in clinical settings for the purpose of evaluating whether DECT could better predict the stopping power ratio (SPR) for proton therapies. Using a dual-layer DECT (DL-DECT) system, [148] adapted their previous method to obtain RMSPE values of 1.0% for ρ_e and 2.9% for Z_{eff}, and from there obtain a RMSPE of less than 1% for SPR. [149]also investigated DL-DECT for SPR calculations at the Heidelberg Ion Beam Therapy Center demonstrated similar values to [148]with reported relative errors on the order of 1% to 2% for both ρ_e and Z_{eff}. Given these values, our PCD-CT method offers decomposition results which are comparable to DL-DECT solutions in the clinic.

However, there are currently still a number of drawbacks with PCD-CT when compared to DECT. There is currently only a single PCD-CT scanner that has been cleared by the Food and Drug Administration for clinical scanning [3], though many others are nearing clinical implementation as well [4, 5, 6, 7, 8]. However, DECT systems are more readily available in the clinic, in addition to being well integrated into clinical workflows. Ideally, the spectral

separation between two energy bins of a PCD would be total but is often not total due to inherent properties of PCDs, as mentioned above. As such, the incident beam spectrum is not accurately captured by the detector and thus spectral distortions are introduced. To mitigate these distortions in the captured spectrum detector energy response models are needed [150] and can be difficult to define [31]. As such not every DECT method, if the specific beam spectra are used in the decomposition, may lend itself as easily to PCD-CT translation. However, PCDs are currently the subject of intense interest for clinical CT applications, and many workarounds and corrections for the issues of PCDs, such as charge-sharing and pulse pileup, are being investigated [151, 2, 152, 153]. As such, PCD-CT has potential as a replacement for both SECT and DECT in clinical use.

4.6 Conclusion

In this study we demonstrated that a PCD-CT bench-top system is able to extract effective atomic number (Z_{eff}) and relative electron density (ρ_e) using two energy bins from a single acquisition, replicating a DECT stoichiometric material decomposition method. Z_{eff} and ρ_e were accurately determined for known tissue-mimicking materials with an average RMSPE of 0.76% and 0.72%, respectively, compared to RMSPE of 1.77% and 1.98%, respectively, for DECT. Tissue types within an *ex-vivo* tissue sample demonstrated values within two standard deviations of known human tissue values. In addition, the original method was extended to include material discrimination of high-atomic number contrast agents with K-edge subtraction, demonstrated with gold injected into an *ex-vivo* tissue sample. As such, PCD-CT offers DECT material decomposition capabilities, with additional high-Z contrast agent extraction, along with conventional SECT capacity as well, making it an attractive option for clinical use.

Chapter 5

Multi-contrast K-edge imaging on a bench-top photon-counting CT system: Acquisition parameter study

The following work was published in the *Journal of Instrumentation* in 2020 and can be found at the following DOI: 10.1088/1748-0221/15/10/P10029.

5.1 Summary

Photon-counting computed tomography (PCCT) shows promise for medical imaging in regards to material separation and imaging of multiple contrast agents. However, many PCCT setups are under development and are not optimized for specific contrast agents or use cases. Here, we demonstrate how experimental system parameters may be varied in order to enhance performance and we propose a set of recommendations to achieve this based on contrast agent. A table-top PCCT system with a cadmium zinc telluride (CZT) detector capable of separating six energy bins was used to image multiple contrast agents in a small phantom. The contrast agents were separated and the concentration was quantified using K-edge subtraction. To increase system performance, we investigated three parameters: beam filter type and thickness, projection acquisition time, and energy bin width. The results from the parameters were compared based on PCCT signal and contrast to noise ratio (CNR) or noise in K-edge images. The concentrations of the contrast agents were quantified in K-edge images and compared to known concentrations. The bench-top PCCT system was able to successfully quantify the contrast agents through K-edge subtraction. Decreasing projection acquisition time showed a decrease in K-edge CNR. However, it did not scale as the square root of time. Filter type and bin width demonstrated a dependence on the specific contrast agent. The presented bench-top system demonstrated the ability to separate contrast agents

using K-edge subtraction and accurately determine contrast concentration in K-edge images. Specific parameters for future use will be chosen based on contrast agent.

5.2 Introduction

Computed tomography (CT), first described by Hounsfield and others [33, 154, 155], has been widely used for research [156, 157, 158] and in clinical imaging [159] since the first CT scanner was built [160]. While conventional CT offers many benefits such as high spatial resolution and fast imaging time, one drawback is its inability to distinguish between materials with similar attenuation curves, such as those with effective atomic numbers (Z) that are close to one another. Energy selective CT, or multi-energy CT, was first proposed in the 1970's [34], allows for material decomposition while still offering the benefits of conventional CT. Energy selective CT functions by utilizing multiple beams with different energies, or a single beam with detectors able to separate a single beam into two or more energy spectra to obtain energy information from the detected x-rays. The most widely used type of energy selective CT is dual energy CT (DECT), in which the object being imaged is typically scanned with two beams of different energies. The two beams result in different images, which can be exploited to separate similar materials. Clinically, DECT is used to distinguish materials based on their energy attenuation dependencies. Using DECT, materials such as bone and iodine (a common CT contrast agent) can be separated [161] or the amount of injected contrast can be quantified. For example, in order to determine the composition of kidney stones [162], DECT can be used to quantify the concentration of iodine present in the image. A number of algorithms and methods have been developed to accomplish such material decomposition and quantification. Bazalova *et al* demonstrate how materials can be separated by converting the measured Hounsfield units (HU) into effective atomic number (Z) and and the corresponding electron density by iteratively solving for Z [92]. Mendonca *et al* provide an algorithm and show how multiple materials can be distinguished through the identification of multiple linear attenuation coefficient triplets [163].

With the advent of high-flux photon-counting detectors (PCDs) [104, 105, 106], research into the uses of multi-energy CT has been underway. Conventional CT and DECT utilize energy integrating detectors (EIDs), which detect x-rays by measuring the total energy deposited in the detector without accounting for the individual energy deposited by each x-ray. PCDs allow for the spectral binning of x-rays into predefined energy ranges by measuring the pulse height of every interaction in the semiconducting layer of the detector [11]. Imaging modalities like positron-emission tomography (PET) rely on energy discriminating detectors

to detect 511 keV photons with high resolution, but those detectors operate at much lower flux rates than the beams produced by CT scanners [164]. With the development of high-flux PCDs, photon-counting CT (PCCT) is possible, in which only one beam energy is necessary. A number of groups are even working towards full-body clinical PCCT scanning [165, 166, 167].

The PCDs used for PCCT normally have a number of energy thresholds which determine the edges of the energy ranges, or bins, that individual x-rays are placed into. These energy thresholds are tunable, which allows for the specific energy ranges to be isolated or for the energy threshold to be placed at specific energies corresponding to the K-edge of a contrast material. The K-edge of an element is characterized by a large increase in the attenuation of photons with energies above the K-edge. This is because x-rays with energies above the K-edge are able to eject electrons in the K-shell of the atoms of that element. Placement of a threshold at a K-edge gives the ability to take advantage of this increase in attenuation to distinguish high-Z contrast materials from the background using K-edge subtraction. K-edge subtraction is accomplished by the acquisition of a higher energy image above the K-edge and a lower energy image below the K-edge and subtracting the lower from the higher. A detailed description of the algorithm can be found elsewhere [60]. In the two images, the signal from the background will be effectively constant because the attenuation properties of the background vary only slightly over the energy range around the K-edge. However, the difference in attenuation of the contrast material above and below the K-edge is large due to the increase in photoelectric absorption. This results in leftover signal only in areas containing the contrast material. K-edge subtraction has been used with mono-energetic x-rays [59, 168] to acquire the two images above and below the K-edge as well as with PCCT systems [169, 60].

PCCT is actively being researched for use in areas of preclinical imaging research such as cancer treatment [58] and the imaging and separation of contrast agents [56, 57, 63, 117, 170] as well for use clinically [171, 172, 173, 11]. In both the clinic and other areas it is necessary to develop protocols which offer the best results based on the work or research being performed. For example, in small animal research, the imaging procedure needs to be optimized in order to have an imaging time that reduces movement artifacts and stress to the animals as well as keeping radiation dose to the animals at a minimum. However, reducing imaging time too drastically can have detrimental effects on image quality. In the clinic, dose and imaging time also need to be kept low in order to reduce patient motion, discomfort, and future risk of cancer while also keeping image quality high enough for accurate diagnosis or treatment planning.

One current area of research using PCCT is imaging of multiple contrast agents [63, 57, 170]. Depending on the number of energy thresholds available, PCCT offers the ability to accomplish this using K-edge subtraction. The potential benefit this offers is to distinguish multiple tissues or processes in one scan, thereby reducing dose and allowing for the possibility of studying how different processes may interact *in vivo*. However, the PCCT system used must be optimized for the best results depending on the desired image quality and contrast agent(s) used. In this work we demonstrate the experimental variation of a few parameters on a bench-top PCCT system to obtain the best results as measured by the resulting signal and K-edge contrast-to-noise ratio (CNR). The adjusted parameters were filter type and thickness, projection acquisition time, and energy bin width due to their effect on image quality in previous research [174, 175, 176]. A set of practices was developed to choose the correct parameters in our system based on the contrast agent.

5.3 Materials and methods

5.3.1 Phantoms and imaging setup

The imaging setup and phantoms used in this study are shown in figure 5.1. The imaging setup consisted of an x-ray tube, rotation stage, various linear motion stages, the phantom containing the various contrast agents, and a cadmium zinc telluride (CZT) detector. The x-ray tube was an XRS-160 (Comet Technologies, San Jose, CA) mounted on two linear motion stages (Newport Corporation, Irvine, CA) allowing it move vertically as well as away from and towards the detector. The CZT detector module (Redlen Technologies, Saanichton, BC, Canada) consisted of the 8×24 mm^2 sensor (shown as the Active Area in figure 5.1a) and the housing with the hardware and cooling system. The sensor is 2 mm thick with a 330 μm pixel pitch and is capable of operating at 250 Mcps/mm^2 without polarization [126]. The high-flux detector operates in non-paralyzable mode and the pile-up effects are smaller than 2% with the parameters used here [115]. The detector also has 6 energy thresholds that can be tuned by the user. To calibrate the thresholds, the central energy threshold was swept over the entire energy range twice to obtain the spectra of Co-57 and Am-241, both of which have a distinct energy peak. Each pixel was then calibrated based on their response. The CZT detector was mounted on two linear motion stages letting it move both vertically and parallel to the plane of the detector. The rotation stage (Newport Corporation, Irvine, CA) was itself mounted on a motion stage between the tube and the detector which allowed for motion parallel to the plane of the detector as well.

The phantom (figure 5.1d), was 3D printed from solid polylactic acid (PLA) with a den-

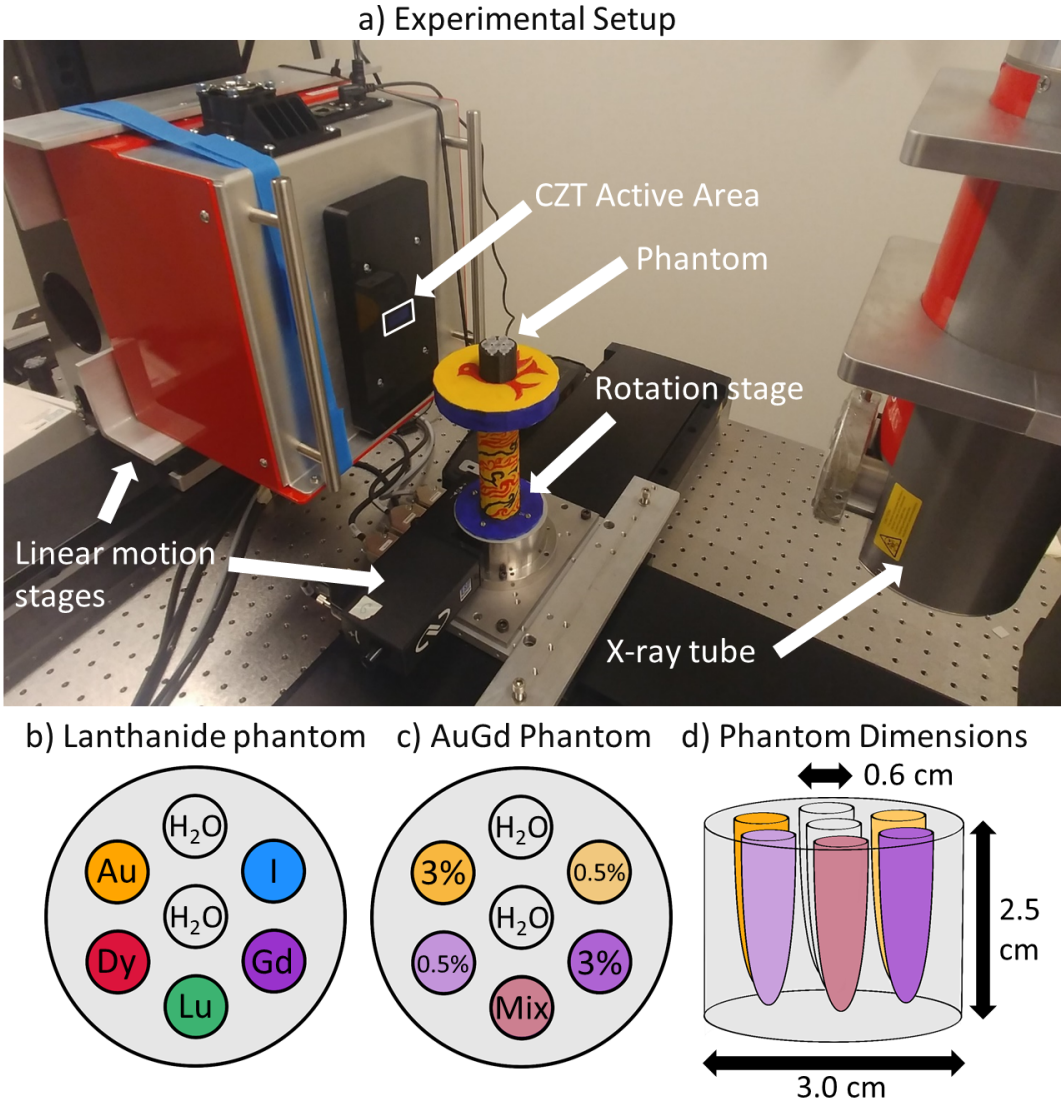

Figure 5.1: *Experimental setup.* a) Experimental setup showing the x-ray tube, detector, phantom, and movement stages. b) Contrast material layout for the three Lanthanide phantoms, one for each concentration of 5%, 3%, and 1% of all contrast materials. c) Layout for the AuGd phantom showing % concentration in each vial with Au (orange) and Gd (violet). Mix contained 0.5% concentration of both materials. d) The phantom dimensions.

sity of 1.25 g/cm^3 (3D Hubs, Victoria, BC, Canada). The phantom has seven holes with a diameter of 0.6 cm which fit Fisherbrand 0.2 ml PCR tubes (Fisher Scientific, Nepean, ON, Canada). These tubes (or vials) contained pure water or water-based solutions of gold, gadolinium, dysprosium, lutetium, or iodine of various concentrations. Four phantom configurations were used in the study, three of which followed the layout shown in figure 5.1b, (called the Lanthanide phantoms), with concentrations of 5%, 3%, or 1% for all materials in that particular phantom. The fourth phantom, hereby refered to as the AuGd Phantom, is shown in figure 5.1c, with gold and gadolinium concentrations and with the mixture vial consisting of 0.5% concentrations of both materials. The concentrations were chosen in order to be sure they were visible with the current bench-top system. The gold solutions were synthesized from gold (III) chloride (GG3CS-25.4-100 Lot AUY03-7077, Nanopartz Inc, Loveland, CO). The iodine solutions used the iodine-based Omnipaque 300 (iohexol, GE Health-care, Princeton, NJ). Gadolinium, dysprosium, and lutetium chloride hexahydrate salts (Sigma-Aldrich, Oakville, ON) were used to synthesize the remaining solutions by dissolving the salts of the specific element in water to obtain a 5% concentration by weight. This stock was then diluted as necessary. The purities of the salts were 99.99% for $LuCl_3$, 99.9% for $DyCl_3$, and 99.999% for $GdCl_3$. The plots of each contrast agent's linear attenuation coefficient (at 5% concentration) with respect to x-ray energy can be seen in figure 5.2a.

5.3.2 Data acquisition

Filter type and thickness, projection acquisition time, and bin width were examined with different phantoms and setup parameters. All images were acquired with a cone-beam geometry with the phantom at isocentre, located 32 cm from the x-ray source and 11 cm from the detector [177]. The CZT detector was connected to a high-speed photon counting Application Specific Integrated Circuit (ASIC), operating at rates up to 62.5 Mcps per channel. The ASIC allowed photons incident on the detector to be sorted into six energy bins with the thresholds set by the user and varied in this study between the different acquisitions. The sixth energy bin was used for overflow counts of the detector in all scans.

Each phantom was scanned by acquiring 180 projection images in 2 degree intervals over a 360° rotation about the isocentre. Three separate 360° rotations were performed for each phantom in order to image the entire phantom body. Between each rotation, the detector was translated 13.5 mm parallel to the detector plane to image the full phantom with the small-area detector. The projections from each rotation were then combined to produce the entire projection data set of the full phantom.

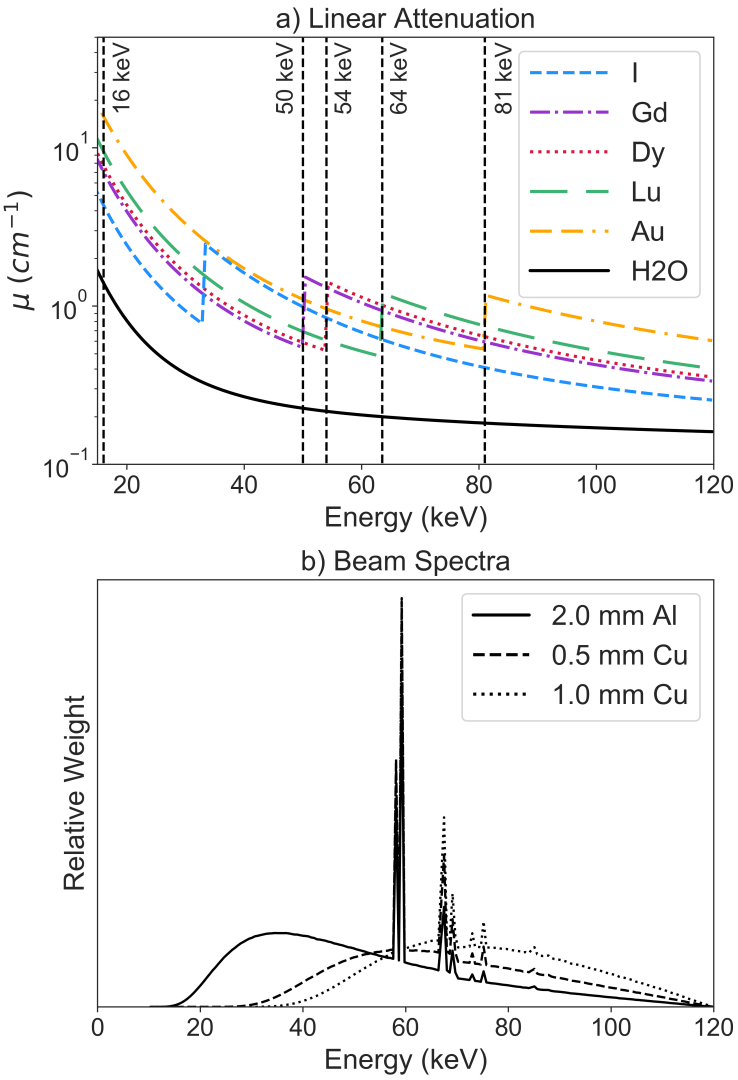

Figure 5.2: *Linear attenuation coefficients and beam spectra.* a) Semi-log plot of the linear attenuation coefficients of water and all contrast agents (5% concentrations) included in the study, over the relevant energy range. b) Relative number of photons with respect to energy of the three filtered beam spectra. Each spectra was scaled by the tube current used for that filtration.

All acquisitions were captured with a tube voltage of 120 kVp using the small focal spot (1.0 mm). The tube current varied between different setups, and is detailed in each of the evaluated parameter subsections below. Unless specified otherwise, one projection image was captured over 1 second every two degrees, and the phantom was rotated at a speed of 1.48 °/s to accommodate for the time to transmit the data from each projection. This resulted in an imaging time of approximately 4 minutes per rotation and ∼12 minutes total.

Filter selection

Three different filter setups were investigated for this study: 2.0 mm Al, 0.5 mm Cu, and 1.0 mm Cu. In order to obtain similar noise levels in the final images using each filter, the tube current was varied to acquire a similar total number of photons in the airscan when compared with the total number when using a 1.0 mA tube current with 2.0 mm Al filtration. This yielded tube currents of 2.25 mA and 4.75 mA for 0.5 mm Cu and 1.0 mm Cu, respectively. The spectra for each beam filtration can be seen in figure 5.2b. The unfiltered spectrum was calculated using a validated EGSnrc Monte Carlo model and then filtered according to Beer's Law. The three filters were chosen due to the use of aluminum and copper in other CT and PCCT studies [175, 167, 117, 165, 174] and to cover a lower, middle, and higher weighted energy spectrum.

All three Lanthanide phantoms were scanned using the tube currents listed above. Bin thresholds were set to 16, 50, 54, 64, 81, and 120 keV to accommodate the K-edges of gadolinium (50.2 keV), dysprosium (53.8 keV), lutetium (63.3 keV), and gold (80.7 keV). This translated to bins with energy ranges of 16–50 keV, 50–54 keV, 54–64 keV, 64–81 keV, and 81–120 keV.

Bin width selection

In order to facilitate the modification of bin width, only two contrast agents were investigated, placed in the AuGd phantom. 0.5 mm Cu filtration and a tube current of 2.25 mA were used for image acquisitions as it offered a compromise between the other two filters detailed above. The energy thresholds were shifted to create different bin widths on either side of the K-edge of the two contrast materials. The two energy thresholds that remained the same were those set at 50 keV and 81 keV, corresponding to the K-edges of gadolinium and gold. Four different scans were taken of the AuGd phantom corresponding to bin widths of 5, 8, 10, and 14 keV for gadolinium and bin widths of 5, 10, 14, and 20 keV for gold.

Projection time selection

Three different times were investigated: 1 s, 0.5 s, and 0.1 s. While 1 s acquisitions gives adequate image quality, lower acquisition times were explored to examine image quality at lower imaging doses. For all three options, 0.5 mm Cu filtration was used along with a tube current of 2.25 mA. The 3% Lanthanide phantom was used, with identical energy thresholds as those used for filter selection, except that the lowest threshold was moved from 16 keV to 35 keV to exclude the lower energy photons which are most affected by charge sharing.

For the projection acquisition, 1800 0.1 s projections were collected while the phantom was rotated 360° at a speed of 0.471°/s. 180 projections were used for image reconstruction with every ten projections summed together for 1 s acquisition, every other five acquisitions summed for 0.5 s acquisitions, and every tenth acquisition was used for 0.1 s acquisitions. The imaging time per rotation was approximately 12.5 minutes for a total imaging time of 37.5 minutes.

5.3.3 Dose

The dose to the phantom was calculated at each filter and tube current setup with 1 s projection acquisitions by simulating a cylindrical water phantom in TOPAS [178] as described by Dunning *et al* [177]. For both 2 mm Al and 1 mm Cu filtration, with their corresponding tube currents, the dose to the phantom was 333 mGy. For 0.5 mm Cu and 2.25 mA tube current, the dose was 250 mGy.

5.3.4 Image reconstruction and analysis

PCCT image reconstruction

All images were reconstructed using MATLAB (The Mathworks, Natick, MA) and analyzed using Python. Projections were created by converting the count data from the detector using the following equation:

$$p_n = -ln\Big(\frac{I_n}{I_{0,n}}\Big); \quad n = 1, 2, 3, ..., 7 \tag{5.1}$$

where I is the intensity of the beam including the phantom and I_0 is the intensity of the beam in air. I_0 was obtained from an airscan taken at each corresponding detector translation in order to normalize the count data (I) to the flat field. The index number n corresponds to the index number of each of the six energy bins and the full count data bin ($n = 7$).

The CT images from each of the corrected projection data sets were reconstructed using the Feldkamp-Davis-Kress algorithm [20] with a Hamming filter.

K-edge images

K-edge images were created by subtracting the CT image of the energy bin below each respective K-edge from the CT image of the energy bin above the K-edge. For example, to create the K-edge image of gadolinium using the AuGd phantom and 5 keV bin widths, the image of the 45–50 keV bin would be subtracted from the 50–55 keV bin.

Image analysis

Analysis of the CT images was done by first normalizing all of the voxels to Hounsfield units (HU) by applying the following equation to each voxel:

$$HU = 1000 * \frac{\mu - \mu_{water}}{\mu_{water}}, \tag{5.2}$$

where μ is the signal in each voxel and μ_{water} is the average signal in the water vial. The water vial signal was obtained separately for each filter choice and used for all subsequent images taken with the same parameters. To obtain signal for each of the contrast agents at the various concentrations in each of the phantoms, a region of interest (ROI) encompassing only the inside of each vial was drawn and the mean value of the voxels within the ROI was taken to get the average signal (μ_{ROI}) and the standard deviation of the voxel values (σ_{ROI}) was calculated to evaluate the error bars.

Analysis of the K-edge images was done in two ways. First was to calculate the CNR of each contrast agent in its respective K-edge image and the error (CNR_{err}) using the following equations:

$$CNR = \frac{\mu_{ROI} - \mu_{phantom}}{\sigma_{phantom}}, \qquad CNR_{err} = \frac{\sqrt{\sigma_{ROI}^2 + \sigma_{phantom}^2}}{\sigma_{phantom}}, \tag{5.3}$$

where $\mu_{phantom}$ and $\sigma_{phantom}$ are the mean and standard deviation of the phantom body, respectively.

Second, to calculate the concentration associated with the measured K-edge signal, the average signal from the ROI of the contrast material at 5% was measured in one set of images from one acquisition at each filter choice and used for image normalization in all phantoms

for subsequent acquisitions with the same parameters. Then, the average signal was taken in an ROI to find the measured concentration.

5.4 Results

5.4.1 Filter selection

Examples of the CT images analyzed for this study are shown in figure 5.3. Figure 5.4a–d show the results of the filter selection for various concentrations of each of the contrast agents. The corresponding CT images from which the data was analyzed can be seen in figure 5.3a–d. Figure 5.4a and b show CT signal as HU vs. contrast concentration for all contrast elements with 0.5 mm Cu filtration. A linear signal response with contrast concentration is seen, with the slope of the line decreasing with increasing Z for the lowest energy bin (figure 5.4a) and the slope increasing with increasing Z for the highest energy bin (figure 5.4b). Figure 5.4c shows the linear relationship of signal with concentration for dysprosium with each filter in the 16–50 keV bin, in which the slope of the lines decreases from 1.0 mm Cu, to 0.5 mm Cu, and finally to 2.0 mm Al. Figure 5.4d demonstrates the same lines as figure 5.4c but for gold in the 16–50 keV bin, with the slopes of the lines reversing their order from those shown in figure 5.4c.

Figure 5.5 depicts K-edge images using the three filters for dysprosium (a–c) and gold (d–f), both at 3% concentration. For dysprosium, an increase in noise is seen for increasing filtration from 2.0 mm Al to 0.5 mm Cu and finally to 1.0 mm Cu. For gold the opposite is true, with noise decreasing with softer filtration. Table 5.1 shows the K-edge CNR for all four contrast agents with each filter type.

Table 5.1: K-edge CNR by contrast agent (3%) and filter type.

Filter type	Contrast agent			
	Gd ($Z = 64$)	Dy ($Z = 66$)	Lu ($Z = 71$)	Au ($Z = 79$)
2.0 mm Al	3.5 ± 1.4	10.6 ± 1.3	19.9 ± 1.3	12.6 ± 1.3
0.5 mm Cu	8.8 ± 1.4	7.9 ± 1.3	19.0 ± 1.4	15.8 ± 1.3
1.0 mm Cu	5.6 ± 1.5	4.2 ± 1.4	13.5 ± 1.4	14.9 ± 1.4

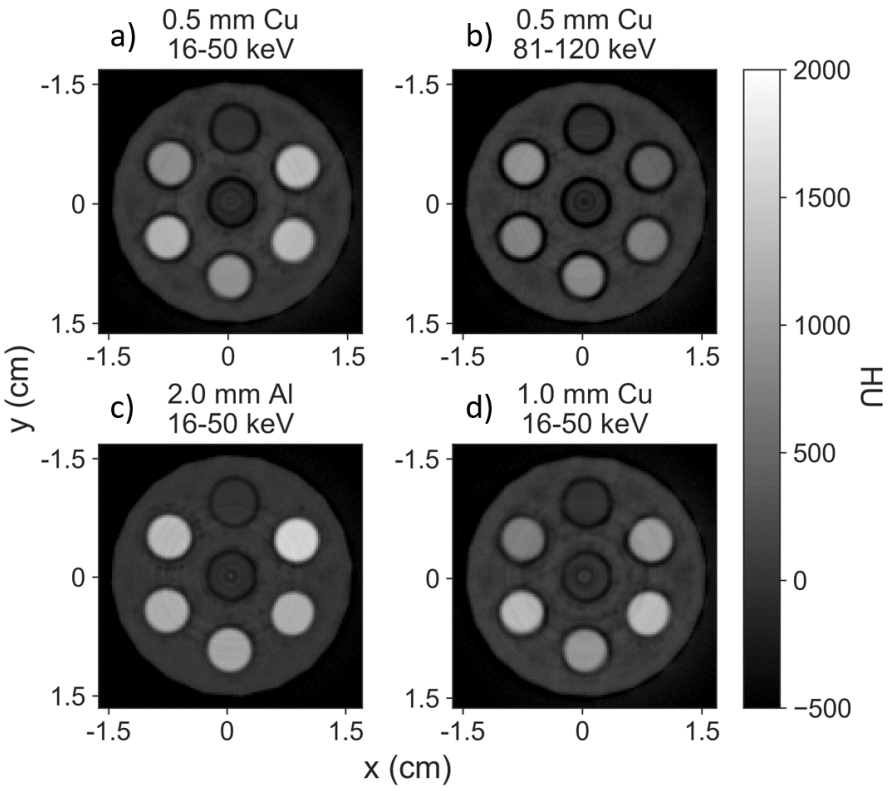

Figure 5.3: *CT images from filter selection.* a) A CT slice showing the 3% lanthanide phantom with 0.5 mm Cu filtration in the 16–50 keV energy bin. b) The same CT slice of the same phantom with 0.5 mm Cu filtration in the 81–120 keV energy bin. c) A similar slice of the same phantom with 2.0 mm Al filtration in the 16–50 keV energy bin. d) A similar slice with 1.0 mm Cu filtration in the 16–50 keV energy bin.

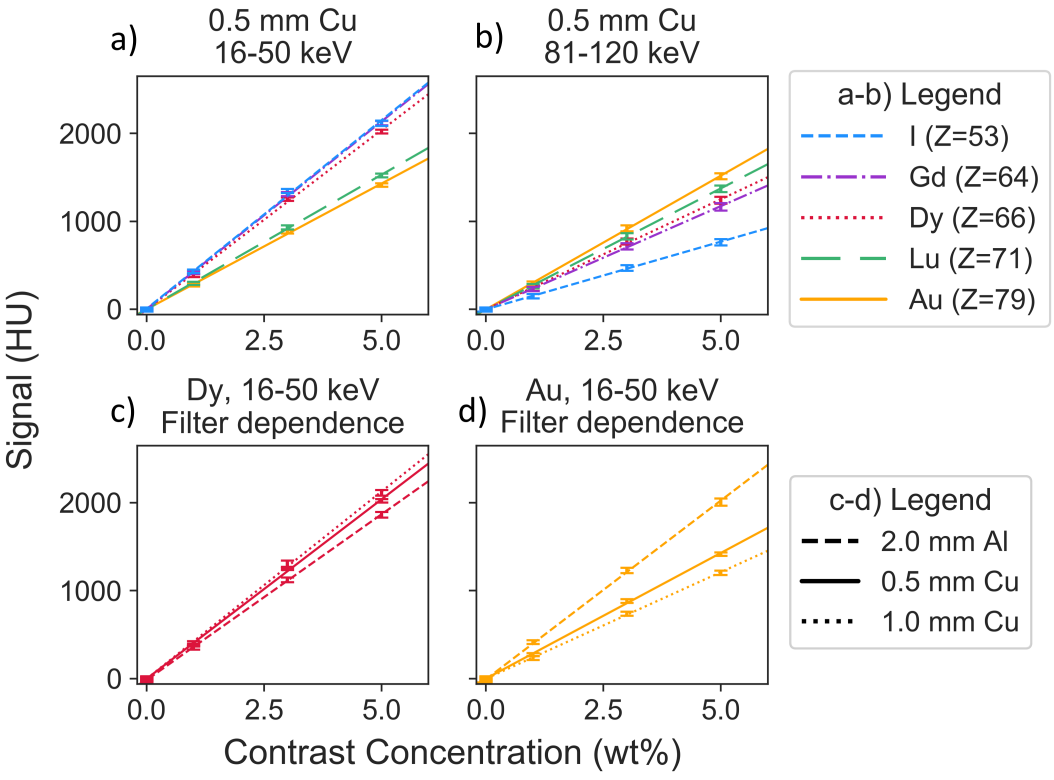

Figure 5.4: *Filter selection.* a) Signal from all contrast agents at 1%, 3%, and 5% concentrations demonstrating a linear relationship. Energy range of 16–50 keV with 0.5 mm Cu filtration. b) The same components as in a), instead showing the signal in the energy range 81–120 keV. c) Gadolinium signal at all 3 concentrations demonstrating the effect of three different filters in the 16–50 keV energy range. d) The same setup as in c) with gold replacing gadolinium as the contrast agent.

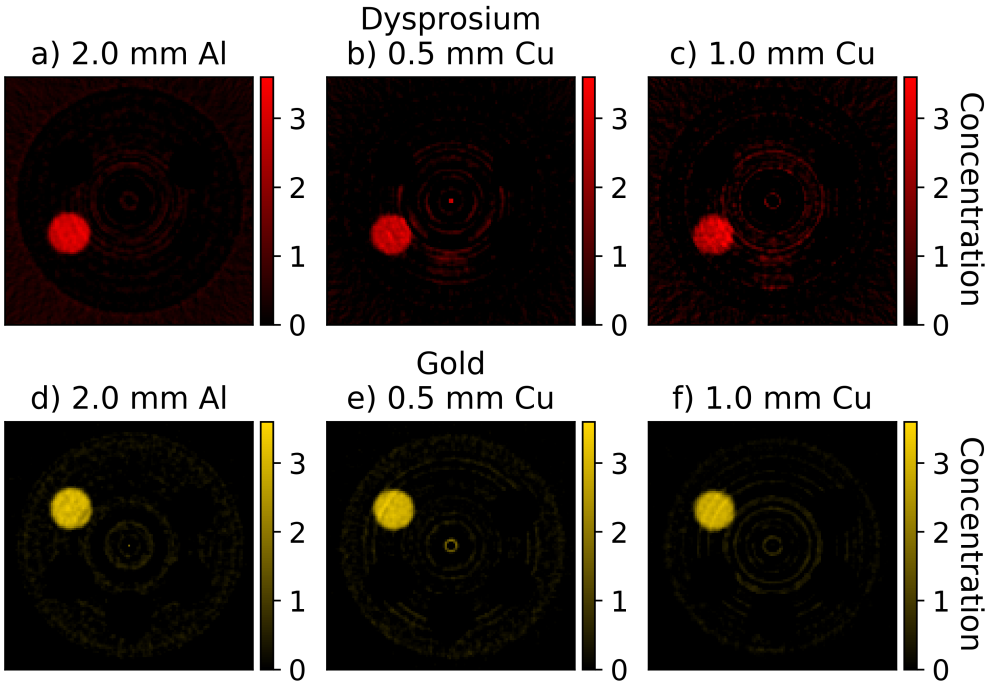

Figure 5.5: *K-edge images with different filters.* a–c) K-edge images of 3% dysprosium with the different filters: a) 2.0 mm Al, b) 0.5 mm Cu, and c) 1.0 mm Cu. d–f) K-edge images of 3% gold with the different filters: d) 2.0 mm Al, e) 0.5 mm Cu, and f) 1.0 mm Cu.

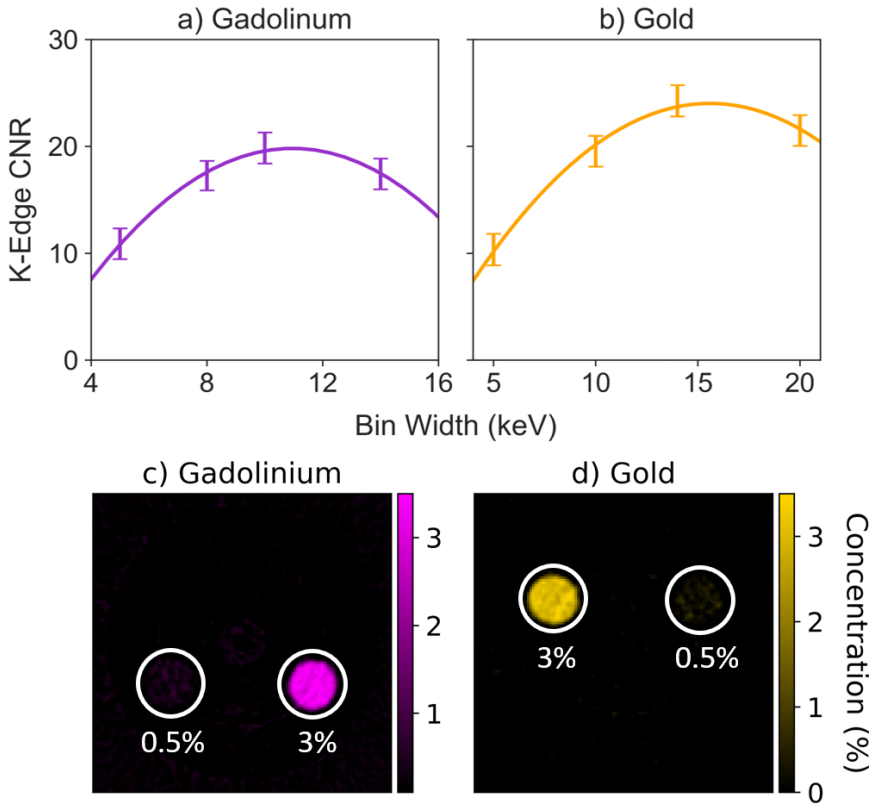

Figure 5.6: *Bin selection.* a) K-edge CNR curve for gadolinium. b) K-edge CNR curve for gold. c) K-edge image of gadolinium reconstructed with 10 keV bin widths. d) K-edge image of gold reconstructed with 14 keV bin widths.

5.4.2 Bin width selection

Figure 5.6a and 5.6b demonstrate how bin width affects the CNR of gadolinium and gold K-edge images, respectively. The data was fit with a quadratic curve to show how the K-edge CNR would likely behave over the range of bin width data that was collected. The ideal bin width must be found for every contrast material separately, as the bin width that results in the highest K-edge CNR can vary, as demonstrated. For gadolinium, peak K-edge CNR was achieved with a bin width of 10.7 keV, and for gold, the optimal bin width was 15.8 keV. The resulting K-edge images reconstructed using the data closest to these peaks (10 keV for gadolinium and 14 keV for gold) are shown in figure 5.6c–d. The 3% vial of each contrast can be seen clearly. However, the 0.5% vials were not visible, with CNR values under 4. The mixed vial was not resolved in either image.

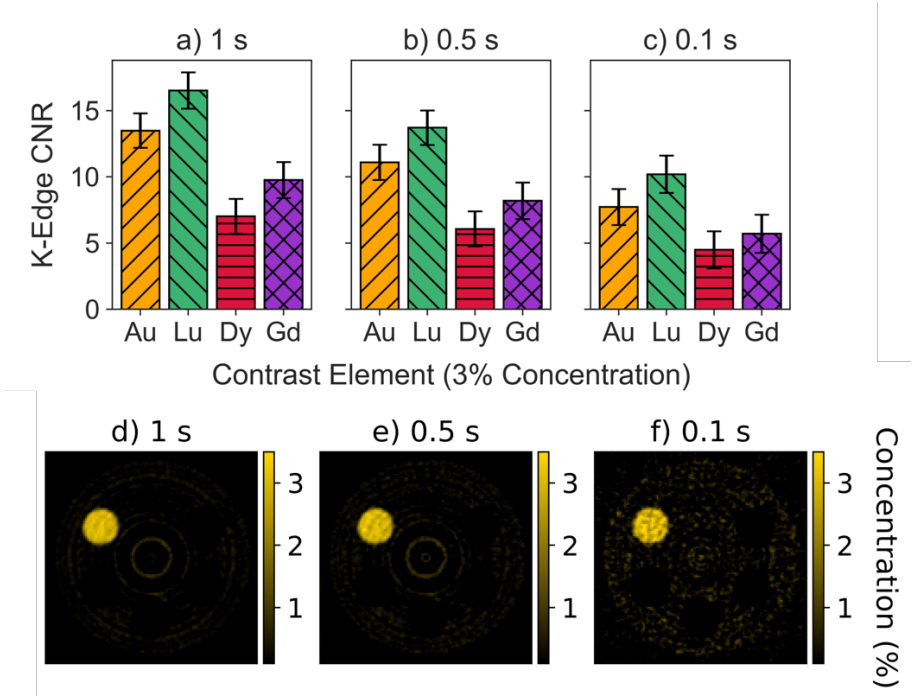

Figure 5.7: *Projection time selection.)* a–c) K-edge CNR of Au, Lu, Dy, and Gd with a) 1 s acquisitions, b) 0.5 s acquisitions, c) 0.1 s acquisitions. d–f) K-edge images of gold at d) 1 s acquisitions, e) 0.5 s acquisitions, f) 0.1 s acquisitions.

5.4.3 Projection time selection

The K-edge CNR for the various contrast elements for the three projection times used in this study are shown in bar plots in figure 5.7a–c. The relationship seen between CNR and imaging time is not what is expected, which is that CNR should increase proportionally to the square root of dose, or time. Figure 5.7d–f shows the resultant K-edge images of gold at each of the three acquisition times. The noise increased with decreasing projection acquisition time.

5.4.4 Reconstructed concentration

Figure 5.8 shows the reconstructed concentration in the K-edge images of each of the contrast elements true concentration, i.e 0, 1, 3, and 5%. All reconstructed concentrations are accurate within the error bars when compared the true concentration. The trend of the error bar size is consistent between the contrast agents at each concentration, with a larger error for the two lower Z contrast agents (gadolinium and dysprosium) than the error for the higher

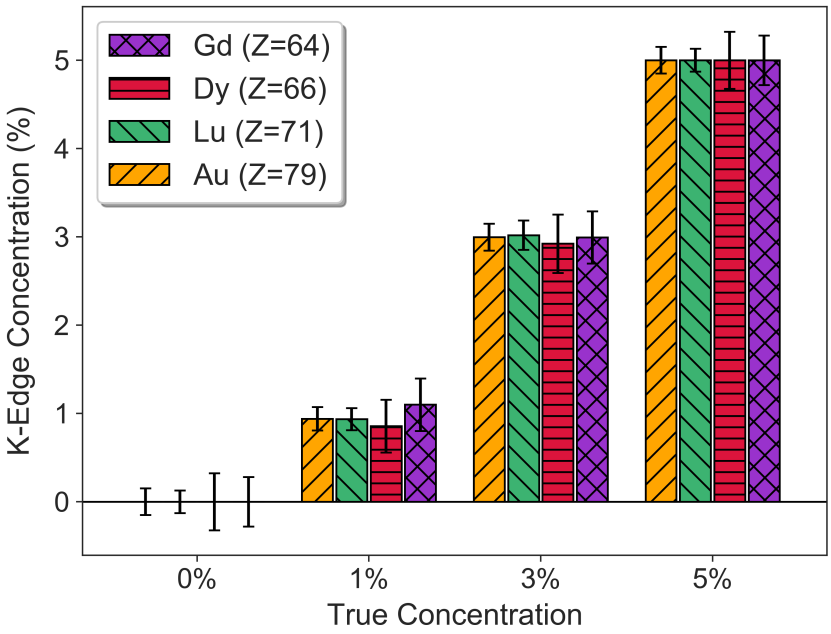

Figure 5.8: *Reconstructed contrast concentration.* Bar graph depicting the reconstructed concentration vs. the actual concentration for four contrast agents: Au, Lu, Dy, and Gd. The values were normalized to the mean value in each of the 5% vials.

Z contrast agents (lutetium and gold). The largest percent difference of the 1% and 3% concentrations for the four contrast agents were 0.15%, 0.13%, 0.32% and 0.30% for gold, lutetium, dysprosium, and gadolinium, respectively.

5.5 Discussion

First, we consider the contrast signal response as a function of contrast concentration seen in figure 5.4a–b. There, we see an increase in signal as Z of the contrast material increases, demonstrated by the increase in slope. This is due to the increase in attenuation coefficient that occurs as Z increases, as shown in figure 5.2a. In figure 5.2a, in the energy range from 81–120 keV, we see that the order of the attenuation coefficients follows the order of the signal in figure 5.4b. If Eq. 5.2 is examined, the signal (HU) at a specific energy will be higher the larger the difference is between the contrast material's linear attenuation coefficient and the linear attenuation coefficient for water. For an actual signal value, one would need to take the average attenuation of both the contrast and water, weighted by the relative number of x-rays of each energy in the relevant energy range. For the energy range from 81–120 keV,

the order of the average linear attenuation coefficients is obvious, following an increase in atomic number. However, the order of attenuation coefficients in the lower energy ranges differ from what we expect, as seen in the 16–50 keV bin shown in figure 5.4a. This difference is likely caused by degradation of the energy data via a number of factors such as the energy resolution of the detector (∼8 keV), charge sharing between detector elements [179, 180], scattering, and fluorescent x-rays [181]. Errors due to the energy resolution of the detector would affect the data by binning x-rays inaccurately because the energy of x-ray was within the energy resolution of the threshold and was binned on the opposite side of said threshold. Of these factors charge sharing likely distorted the energy data the most. Based on the analytical model by Iniewski *et al.*, and extrapolating between pixel pitches of 250 and 500 μm, the expected percentage of events that suffer from charge sharing is approximately 32% [113], with the lower energies being most affected. A charge sharing correction algorithm is currently under development by our collaborators. Initial results indicate, that while true counts in energy bins can be estimated accurately, resulting in reduced bias (i.e. a more accurate contrast concentration determination), noise increases and CNR decreases as a result [150]. Ongoing work is aimed towards optimizing the bias and image noise. As a result, these preliminary corrections have not been applied here. However, with or without these corrections, it is imperative to choose the energy bin that offers the highest signal in order to best show the contrast agent when displaying CT images or to choose the bin that offers the best contrast with the other materials present.

In terms of filter selection for CT signal, shown for dysprosium and gold in figure 5.4c–d, dysprosium (figure 5.4c) showed a small filter dependence, while gold signal (figure 5.4d) had a comparatively large dependence. The order of the how the filtration affected the signal was also opposite between the two. Theoretically, based on the spectra (figure 5.2b), the order of the filters in the 16–50 keV bin should follow the order that gold demonstrated due to the higher number of lower energy photons that less filtration offers. This discrepancy was also likely due to effects in the lower energy range such as charge sharing.

In figure 5.5, K-edge images for dysprosium (a–c) and gold (d–f) can be seen for each of the three filters used in this study. Image noise increased with harder filtration for dysprosium and decreased with harder filtration for gold. This noise trend can also be seen in table 5.1, where the K-edge CNR increased with harder filtration for contrast agents with atomic numbers below 71, while CNR decreased for contrast agents with Z-values above 71. The total number of x-ray counts was maintained over the different filters in order to keep the full spectrum image noise constant for a set imaging time. As a result, the counts in each of the different energy bins varied according to the spectra in figure 5.2b. Constant full spectrum

image noise is desirable because the anatomical information gained from conventional CT images is necessary to localize the contrast agents. With this restriction, filter choice makes a difference on the detectability of different contrast agents based on their effective atomic number due to the relative number of counts in the two bins used to construct the K-edge images of each contrast agent. Therefore, for contrast agents with Z-values below 71, 2.0 mm Al offers the best results of the three filters tested. For those equal to or above 71, 0.5 mm Cu gives the highest K-edge CNR. One exception, based on this data, is that 0.5 mm Cu gave better CNR than 2.0 mm Al for Gd. The likely cause of this inconsistency is again the distortion in counts due to charge sharing. Since the lower energy bin used in the K-edge subtraction for Gd had a relatively higher flux with 2.0 mm Al, this could result in more charge sharing, increasing the noise in that energy bin. Additionally, the K-edge CNR with 1.0 mm Cu decreased for higher-Z contrast agents, the opposite of what should happen with higher counts. Looking at the K-edge images for gold (figure 5.5d–f), there was a reduction in the background image noise, however the ring artifacts became more prominent, which raised the overall image noise. This was due to pixel non-uniformity that was not completely corrected by the flat field correction.

The energy bin selection shows the necessity of setting the ideal bin widths in order to maximize CNR to best separate and localize contrast agents. Meng *et al.* [182] stated that to get the best contrast resolution, the signal to noise ratio (SNR) must be maximized, and developed an algorithm to accomplish this. The first contributing factor to SNR in K-edge images would be the signal, which is determined by difference in the average linear attenuation coefficient of the contrast agent in the bin above the K-edge and the bin below it. The second factor affecting K-edge SNR is, of course, noise. Theoretically, this is determined by the number of x-rays falling in each of the two bins on either side of the K-edge. According to Poisson statistics, the relative noise is equal to the square root of the average number of photons over the average number of photons. So, if photon flux is constant, adjusting the bin width results in a different number of photons that would fall in that energy range. Ideally, in terms of the signal, the smallest bin size possible would be best to get the largest difference in linear attenuation and thus the most signal in the K-edge image. However, this results in a very small number of x-rays, increasing the noise significantly. Thus, a balance between the two must be found to maximize the SNR. The differences in the bin width that maximizes gadolinium CNR versus gold CNR can likely be explained by the relative difference in x-ray fluence in the bins around the respective K-edges. The x-ray spectrum filtered with 0.5 mm Cu had more x-rays around the K-edge of gadolinium (50.2 keV) than around the K-edge of gold (80.7 keV), as shown in figure 5.2b. This results in the need to

have a wider bin for gold, relative to that for gadolinium in order to increase the counts and reduce the noise to maximize CNR. According to figure 5.6a–b, the bin widths that would result in peak CNR for gadolinium and gold would be 10.7 keV and 15.8 keV, respectively, as determined by the quadratic fit. In addition to reducing noise, the wider optimal bins are also likely a result of the ∼8 keV resolution of the detector. Bin widths smaller than 8 keV are likely comprised of fewer counts than what truly falls within that energy range. These optimal bin widths of 10.7 and 15.8 keV are approximately 20% of the K-edge energy of the respective contrast agent. Using 20% of the K-edge energy results in bin width values of 10.0 keV for gadolinium and 16.1 keV for gold. This gives a good rule-of-thumb for setting the bin widths for these contrast agents, with the 20% values falling within 1 keV of the peak value determined from the quadratic fit.

The effect of lowering the projection acquisition time would have on K-edge CNR was also investigated for the various contrast materials. Lowering the projection acquisition time is desirable in order to keep the dose, as well as imaging time, as low as possible. Figure 5.7a–c shows this effect on K-edge CNR and figure 5.7d–f demonstrates how the noise increases with decreasing time. At 3% concentration, all contrast agents were visible even at 0.1 s projection acquisitions. However, for some agents (i.e. dysprosium), no concentrations lower than 3% would likely be resolved in K-edge images using 0.1 s acquisitions. The Rose Criterion [22] states that features with SNR values of less than 5 are not readily resolved, so concentrations of dysprosium lower than 3% would fall below a CNR of 5. Note that bin width could be chosen to raise the CNR if fewer contrast agents needed to be separated or more energy thresholds were available. In addition, theoretically, CNR should increase according to the square root of image acquisition time. This is not case in our system. From 0.1s to 1.0s, CNR should increase by a factor of 3.2, while the data only shows an increase of ∼1.7 times on average over all of the contrast agents. This relationship is not as expected, which is likely due to non-uniform pixel response. The relative differences in pixel responses remain constant with an increasing number of counts and thus with increasing projection time. So while increasing the projection time decreases the noise according to Poisson statistics, the near-constant non-uniform pixel response plays a major role in increasing the noise and thus depressing CNR. Unfortunately, attempting to account this using a flat field correction, as done according to equation 5.1, does not fully correct the non-uniform pixel response. This could be due in part to the relative difference in charge-sharing counts between the flat field and phantom images. For small animal studies or for other uses more research needs to be done in order to determine typical concentrations of contrast agents found in tissues in order to optimize the projection acquisition in terms of what CNRs would be measurable to

keep the dose as low as reasonably possible. For future use of the bench-top PCCT system as is, the particular application will need to be considered in order to determine how long projection acquisition times should be.

Finally, the PCCT system was able to reliably determine the real concentration of the various contrast agents. Accurate determination of concentration is necessary for further use of spectral CT in small animal studies and in the clinic as it allows for the tracking of the exact amount of contrast agent or other high-Z material in various tissues. This allows for researchers investigating new therapies and imaging agents to accurately predict toxicities and the effects of their materials without *ex vivo* analysis, lowering the number of animals necessary for studies and thus lowering study costs.

5.6 Conclusions

It has been demonstrated here how parameters in an experimental PCCT bench-top system can be varied to determine the configuration that offers the best imaging performance for a certain contrast agent. The PCCT system was also able to separate four different contrast agents in a range of Z-values (64–79) at varying concentrations using K-edge subtraction, even without ideal parameter selection. Possible further improvement of results could be obtained through algorithmic correction of the various mechanisms of energy data distortion, such as charge sharing. Work on charge sharing corrections for this detector are currently underway, though the results are mixed, and the algorithm was not applied here. For future use, filter type and thickness will be considered based on Z-value of the contrast agent. The 2.0 mm Al filter will be used for contrast agents with atomic numbers of less than 71, and 0.5 mm Cu used for contrast agents with Z-values of 71 and above. For energy bin width, 20% of the contrast's K-edge energy will be used for gadolinium and gold, and verified for other contrast agents before use. Projection acquisition time will need be considered in context of the imaging task, i.e. what the limiting dose to the animal or patient is, or the desired image quality. This study demonstrates how parameters in a bench-top system can be evaluated in order to obtain the best image quality possible.

Chapter 6

Metal artifact correction in photon-counting detector computed tomography: metal trace replacement using high-energy data

The following work was published in *Medical Physics* in 2022 and can be found at the following DOI: 10.1002/mp.16049

6.1 Summary

Background: Metal artifacts have been an outstanding issue in computed tomography (CT) since its first uses in the clinic and continue to interfere. Metal artifact reduction (MAR) methods continue to be proposed and photon-counting detectors (PCDs) have recently been the subject of research towards this purpose. PCDs offer the ability to distinguish the energy of incident x-rays and sort them in a set number of energy bins. High-energy data captured using PCDs have been shown to reduce metal artifacts in reconstructions due to reduced beam hardening.

Purpose: High energy reconstructions using PCD-CT have their drawbacks, such as reduced image contrast and increased noise. Here, we demonstrate a MAR algorithm, trace replacement MAR (TRMAR), in which the data corrupted by metal artifacts in full energy spectrum projections is corrected using the high energy data captured during the same scan. The resulting reconstructions offer similar metal artifact reduction to that seen in high energy reconstructions, but with improved image quality.

Methods: Experimental data was collected using a bench-top PCD-CT system with a cadmium zinc telluride PCD. Simulations were performed to determine the optimal high energy threshold and to test TRMAR in simulations using the XCAT phantom and a biological sample. For experiments a 100-mm diameter cylindrical phantom containing vials of water,

two screws, various densities of Ca(ClO4)2, and a spatial resolution phantom was imaged with and without the screws. The screws were segmented in the initial reconstruction and forward projected to identify them in the sinogram space in order to perform TRMAR. The resulting reconstructions were compared to the control and to reconstructions corrected using normalized metal artifact reduction (NMAR). Additionally, a beef short rib was imaged with and without metal to provide a more realistic phantom.

Results: XCAT simulations showed a reduction in the streak artifact from -978 HU in uncorrected images to -10 HU with TRMAR. The magnitude of the metal artifact in uncorrected images of the 100-mm phantom was -442 HU, compared to the desired -81 HU with no metal. TRMAR reduced the magnitude of the artifact to -142 HU, with NMAR reducing the magnitude to -96 HU. Relative image noise was reduced from 176% in the high energy image to 56% using TRMAR. Density quantification was better with NMAR, with the Ca(ClO4)2 vial affected most by metal artifacts showing 0.8% error compared to 2.1% with TRMAR. Small features were preserved to a greater extent with TRMAR, with the limiting spatial frequency at 20% of the MTF fully maintained at 1.31 lp/mm, while with NMAR it was reduced to 1.22 lp/mm. Images of the beef short rib showed better delineation of the shape of the metal using TRMAR.

Conclusions: NMAR offers slightly better performance compared to TRMAR in streak reduction and image quality metrics. However, TRMAR is less susceptible to metal segmentation errors and can closely approximate the reduction in the streak metal artifact seen in NMAR at 1/3 the computation time. With the recent introduction of PCD-CT into the clinic, TRMAR offers notable potential for fast, effective MAR.

6.2 Introduction

Metal artifacts have plagued images in computed tomography (CT) almost since its inception [183, 184]. As the name implies, metal artifacts are a result of the presence of high-density materials within the patient, and consist mostly of metal implants such as hip protheses, surgical materials like screws and clips, and dental fillings. Metal artifacts manifest in several ways such as large dark bands between two metal objects and thin, light or dark streaks originating from the metal object(s). These artifacts are due to one or a combination of effects such as beam hardening, scattering, noise, and nonlinear partial volume effects [66, 23]. Metal artifacts can severely damage image quality, especially in close proximity to the metal objects, which reduces the images' reliability for diagnosis or radiation treatment planning [185, 186].

Methods for metal artifact reduction (MAR) have been developed routinely since CT has been in use clinically, starting with Lewitt and Bates in 1978, with serious increases in method development in recent years [187, 67]. There are many techniques for MAR such as improving the data acquisition process, or through algorithms that reduce metal artifacts. MAR methods fall into a number of categories, namely, projection completion, iterative models, and more recently, deep learning models. Additionally, beam hardening correction methods can be applied to reduce metal artifacts, as beam hardening is the main cause of metal artifacts [188, 189, 190, 191]. In projection completion, the data that are affected by the metal are either corrected or replaced through interpolation or corrected using various inpainting methods [186, 187, 192, 193, 194, 195, 196, 197, 198, 199, 200]. However, inpainting does have its drawbacks; new artifacts can be introduced [193, 197, 201, 202, 203] and precise segmentation of the metal is needed [184, 204], though is often difficult to achieve with irregular-shaped objects. Iterative MAR correction models operate by using prior physics knowledge and measurement and imaging statistics and then utilizing iterative reconstruction methods to approach the best solution [205, 206, 207, 208, 209, 210, 211]. However, iterative methods usually require extensive computation time due to their iterative nature. More recently, deep learning has been applied to the problem of metal artifacts in CT images [212, 213, 214, 215]. While these methods demonstrate good results, the drawback is that they are supervised learning methods, and require labeled datasets of images with metal artifacts and the same images with corrected or no metal artifacts as a target. One solution to this is unsupervised learning, which has been implemented for MAR more recently [216, 217].

Additionally, a number of recent studies have investigated how photon-counting detectors (PCDs), used in place of the conventional energy-integrating detectors (EIDs), could improve aspects of MAR [70, 71, 218], including better assessment of bone health immediately around metal implants [219] as well as better detection of implant failure when compared to current imaging methods [220]. PCDs are direct-conversion detectors that can distinguish the energy of each incident x-ray and bin them into a number of predetermined energy ranges. This results in a separate projection set for each energy bin consisting of mainly x-rays from that energy range. This is beneficial because metal artifacts are less prevalent at higher energies. For example, by using dual energy CT to synthesize virtual monoenergetic images (VMIs) metal artifacts were greatly reduced at VMIs with higher energies [72, 73]. Using PCDs, Rajendran *et al.* showed that beam hardening and metal artifacts decreased in CT images of various metallic structures when using energy ranges from 50–80 keV or 60–80 keV with an 80 kVp tube voltage [70]. Additionally, better MAR results have been seen using PCDs compared to EIDs when reconstructions used only data above a threshold energy of 70–75

keV [71, 218].

However, one downside of utilizing only high-energy x-rays for image reconstruction is the reduction in contrast within the resulting images. Additionally, image noise is likely to increase since fewer photons are being utilized during reconstruction. Here, we propose a hybrid correction method of inpainting in the high image quality energy bins of a PCD by replacing the data affected by the metal with data from a higher energy bin where the metal artifacts are less prevalent. This will allow for MAR while maintaining the desired contrast and noise. Compared with recently developed MAR methods, such as with deep learning, our method requires no training and can reduce metal artifacts on a case-by-case basis regardless of whether the specific metal distribution has been included in the training data. We use a bench-top PCD-CT system with a six-bin PCD and demonstrate how the proposed method is able to reduce metal artifacts in phantom images while maintaining image quality and compare it to normalized metal artifact reduction (NMAR) [197]. We termed the new method trace replacement metal artifact reduction (TRMAR).

6.3 Materials and Methods

6.3.1 MAR Algorithms

The first step in TRMAR outlined in Fig. 6.1 is to identify the corrupted data in the original sinogram. First, an uncorrected CT image is reconstructed and then metal is segmented in a high energy bin using thresholding. The algorithm allows for the selection of the appropriate threshold value based on the uncorrected images. Here, the center of the images was excluded from metal thresholding due to the presence of ring artifacts. Then, a number of iterations of binary dilation to apply to account for any errors in thresholding are applied. From there, the metal-only image is forward projected using Siddon's method [221] to obtain the location of the metal traces in the original sinogram. Once the metal traces have been identified in the sinogram, a mask can be created of the metal traces from which the original sinograms can be manipulated. Using the mask, the metal trace data in the original sinogram are replaced with the equivalent data from a high-energy bin from the PCD. The corrected sinogram is then reconstructed with reduced metal artifacts. The full algorithm takes approximately 7 s to produce a corrected image.

We use a modified version of the normalized metal artifact reduction (NMAR) [197] for comparison with TRMAR (also depicted in Fig. 6.1). In brief, the metal is segmented in the uncorrected full energy CT in the same way as detailed for TRMAR, with the user selecting the desired threshold and number of binary dilation iterations. The metal traces in the

original sinogram are replaced through linear interpolation and then reconstructed. Linear interpolation is done along each row of the sinogram (as oriented in Fig. 6.1). From the linear interpolated image, a prior image is computed using thresholding, assigning areas determined to be air to -999 HU (to avoid computational errors), areas with soft-tissue-like properties to a soft-tissue like HU value, and areas determined to be bone left as is. The metal can be assigned to any value, here we use the value for soft-tissue. A prior sinogram is created through forward projection and multiplied pixel wise with the original sinogram to obtain a normalized sinogram. In the normalized sinogram, the metal traces are linearly interpolated and then the newly interpolated sinogram is denormalized via the prior sinogram to obtain the corrected sinogram. Then, the final corrected NMAR image is reconstructed. NMAR takes 21 seconds to fully produce a corrected image.

6.3.2 Experiments

PCD-CT bench-top system

The bench-top setup can be seen in Fig. 6.2a, showing the x-ray tube (MXR 160/22, Comet Technologies, San Jose, CA), phantom, and PCD (Redlen Technologies, Saanichton, BC, Canada). The PCD and x-ray tube were both mounted on vertical motion stages and the phantom was mounted on a rotation stage (Newport Corporation, Irving, CA). The two vertical motion stages and the rotation stage were all mounted on separate horizontal motion stages (Newport Corporation, Irving, CA). For all CT acquisitions, the source to detector distance was 578 mm and the source to isocenter distance was 322 mm and the center of the phantom was placed at the isocenter of the imaging system.

The PCD consisted of two 8×95 mm2 modules aligned end to end to create an 8×190 mm2 detector, which yields a 106 mm field of view with 4.5 mm Z-coverage at isocenter. The detector crystal was 2 mm thick cadmium zinc telluride (CZT) bonded to an Application Specific Integrated Circuit (ASIC) offering a pixel pitch of 330 µm. The detector was capable of operation at 250 Mcps/mm2 without polarization [126].

Phantom

The phantom (Fig. 6.2b) was a 100-mm diameter, 30-mm thick cylinder machined from high density polyethylene (HDPE) and contained insets for eight 0.6 ml Eppendorf tubes (6.3 mm diameter, 29 mm height) and ten 0.2 ml Eppendorf tubes (5.5 mm diameter, 20 mm height) that could be filled with contrast agents. Also housed in the 100 mm phantom was a 22 mm diameter, 2 mm thick acrylic spatial resolution piece that contained six 4×4

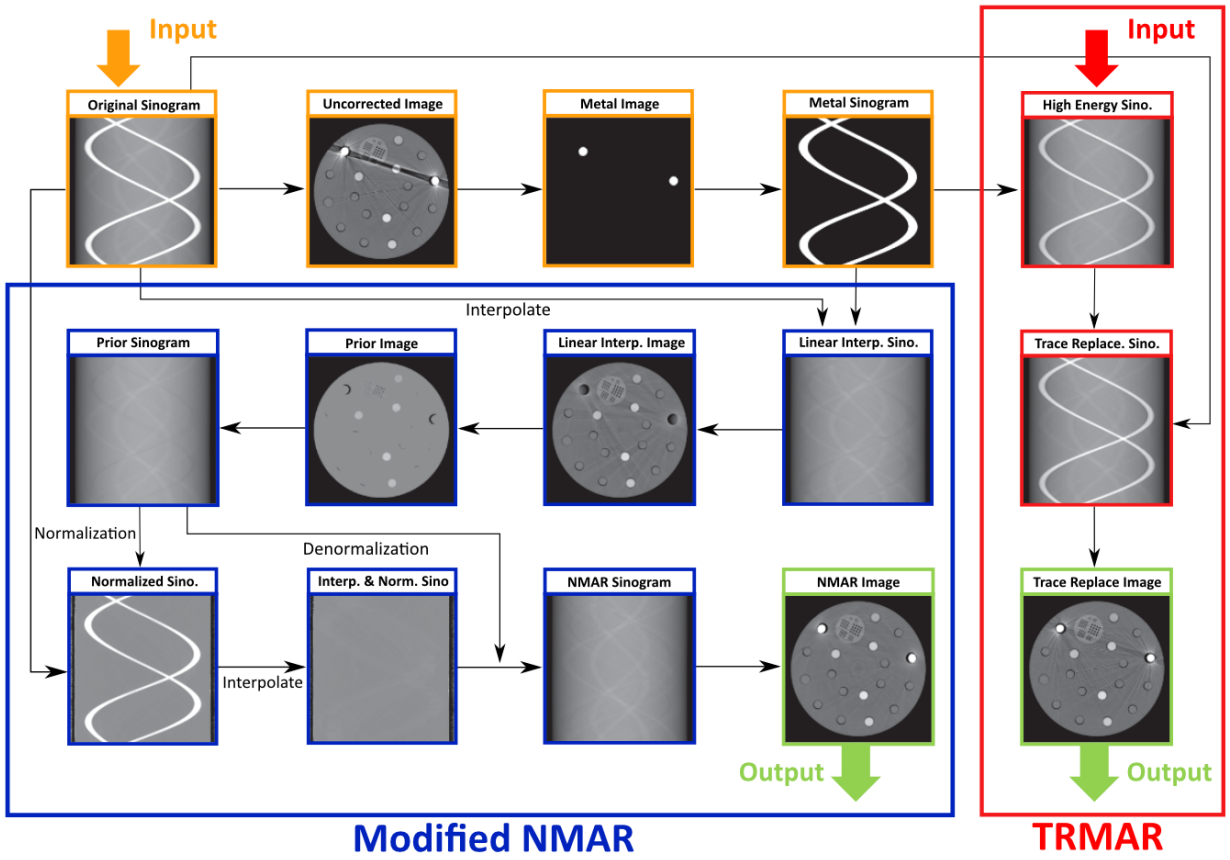

Figure 6.1: Scheme of TRMAR and modified NMAR. First, a metal image is created through thresholding, from which the metal segments are forward projected. For TRMAR, the metal corrupted data in the original sinogram is replaced with the equivalent data from a high energy bin and then reconstructed. For modified NMAR, the metal segments are linearly interpolated to create a linear-interpolated-corrected image. From the corrected image, a prior image is synthesized through thresholding and forward projected into a prior sinogram. The original sinogram is normalized with the prior sinogram and then corrected through linear interpolation, denormalized, and reconstructed into the NMAR corrected image.

arrays of precisely sized holes drilled through the acrylic (Fig. 6.2b). The hole diameters and spacings were 1, 0.75, 0.66, 0.5, 0.33, and 0.25 mm. In the phantom layout used in this study, as seen in Fig. 6.2b, five of 0.6 ml vials contained various concentrations of $Ca(ClO_4)_2$, a bone analog, to provide areas of contrast with the larger phantom. $Ca(ClO_4)_2$ solutions were synthesized by dissolving calcium perchlorate tetrahydrate (Sigma Aldrich, Oakville, ON, 99% pure) in water. The densities of the solutions were 1.47, 1.37, 1.33, 1.31, and 1.19 g/cm^3. The rest of the vials contained only water. Two phantom layouts were used in the study; in one layout, two of the 0.6 ml water vials were replaced with A2-70 stainless steel

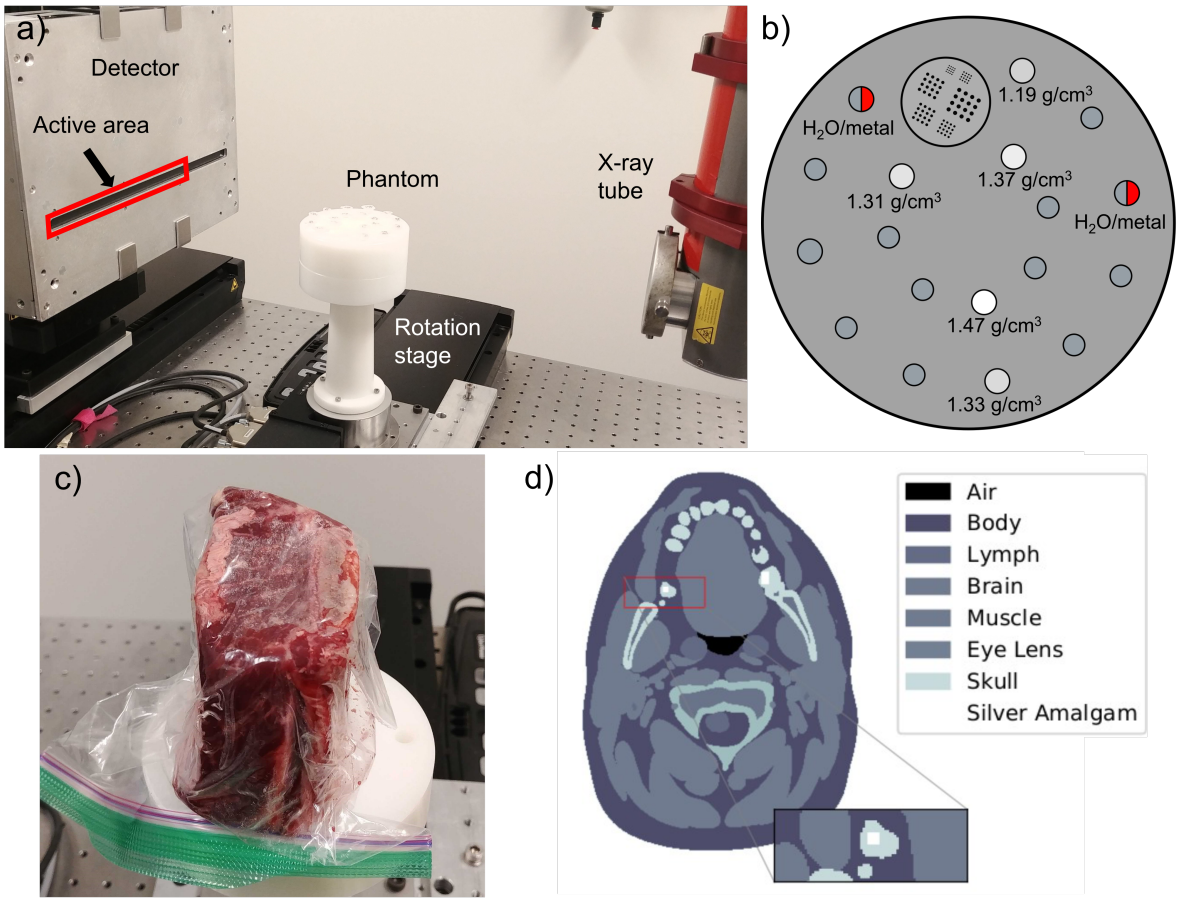

Figure 6.2: a) Bench-top photon-counting detector CT (PCD-CT) setup. b) The phantom layout showing spatial resolution piece (upper middle) and the various $Ca(ClO_4)_2$ densities. The vials that are half red represent the differences between the non-metal and metal acquisitions; in the metal acquisition screws replaced the water vials at the half-red vial locations. c) An image of the beef short rib on the rotation stage. d) A schematic of the XCAT head phantom showing the various tissue types and materials present.

Allen bolts. The bolts were 16 mm in height (10 mm threading height, 6 mm head height) with 5 mm diameter and a 9.5 mm diameter head. When inserted into the phantom, only the threading sat below the top of the phantom.

Beef short rib

In order to image a specimen that was more realistic than the 100-mm phantom, a beef short rib was imaged with and without two small steel screws (Fig. 6.2c). Imaging was performed under the same parameters as the 100-mm phantom. The short rib was approximately 80

mm long, parallel to the bone and the cross section was 70 mm by 60 mm. The two steel screws were 8 mm long, with a 3 mm diameter thread, and 5 mm diameter head. After imaging the short rib without the screws, small cuts were made in the short rib in which to insert the screws, immediately followed by imaging the short rib again.

Image acquisition

Two separate scans were acquired for both the 100-mm phantom and the beef short rib, one with the metal screws and one with the water vials in place of the screws. All scans were acquired with a 120 kVp tube potential using the small (1 mm) x-ray focal spot. In all scans the beam was collimated to 172.5 mm horizontal and 17.25 mm vertical coverage at isocenter. Two additional scans of the phantom with and without metal were acquired with the beam collimated to 276 mm horizontal and 103.5 mm vertical coverage at isocenter in order to evaluate the effect of increased scatter. The 100-mm phantom was rotated at 2 degrees per second for a total imaging time of 180 s per scan. 720 projection frames were acquired with a 0.25 s imaging time per frame. For the beef short rib, an imaging time of 360 s was used with 0.5 s per projection for 720 projections.

The image sets with and without the metal screws in place were acquired at detector thresholds of 30, 50, 70, 100, 110, 120 keV. The beam was filtered with 1 mm of Cu to harden the incident beam spectrum and a tube current of 5 mA was used in order to compensate for the filtration thickness. The filtration and tube current were chosen to achieve a higher number of counts in the 100-110 keV bin, and thus less noise. The portion of the filtered spectra separated into each energy bin can be seen in Fig. 6.3a-e along with the full spectra (Fig. 6.3f).

Image reconstruction

Projection images of each bin n were corrected for air using the following equation:

$$p_n = -ln\left(\frac{I_n}{I_0}\right); \quad n = 1, 2, 3, \ldots 6 \tag{6.1}$$

where I is the number of counts in the projection image and $I0$ is the number of counts in a flat field scan. n corresponds the detector bin number, though any combination of bins could be reconstructed by adding the counts from the appropriate bins before conducting the flat field correction. The flat field scan was acquired for 60 s and scaled appropriately for the time of each projection image. Before undergoing the flat field correction, pixels with non-uniform response were identified and corrected using nearest neighbors' interpolation.

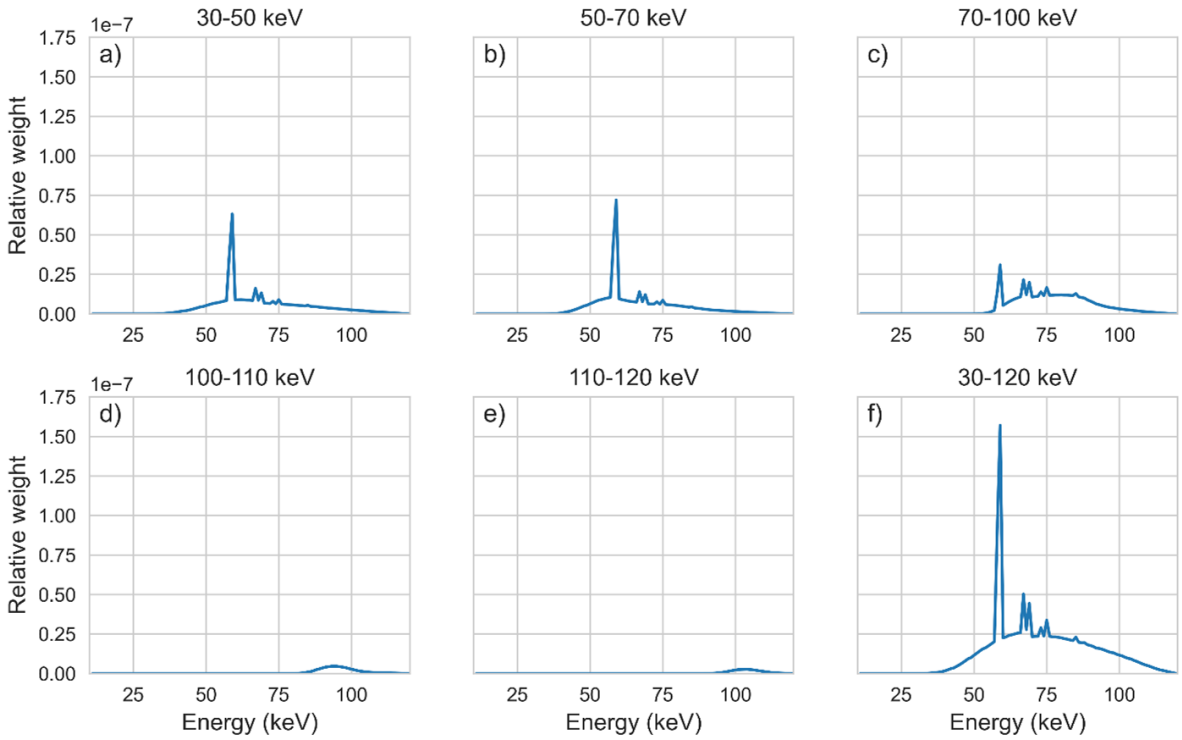

Figure 6.3: Plots of the portion of the incident 120 kVp spectra filtered with 1 mm Cu that is acquired in each energy bin: a) Bin 1, b) Bin 2, c) Bin 3, d) Bin 4, e) Bin 5, and f) the full energy range.

Additionally, an in-house ring artifact correction method was applied to the sinogram before reconstruction. Briefly, a uniform cylindrical water phantom was imaged in a single projection. It was then corrected for air using the flat field correction (Eq. 6.1). The profiles across each row of data were fit with a 6-degree polynomial and the ratio was found between the water phantom data and the fitted data for each pixel. The CT data was then multiplied by the ratio array to further correct for the remaining pixel non-uniformity.

Once the corrected sinogram was obtained, CT images were reconstructed using the Feldkamp-Davis-Kress (FDK) algorithm48 with a Hamming filter, implemented in the TIGRE package [128] for Python. The CT data sets were reconstructed in 24 slices of 512×512 pixels with a corresponding image size of 105×105 mm^2. All reconstructed images were normalized to HU using the following equation:

$$HU = 1000\left(\frac{\mu - \mu_{water}}{\mu_{water}}\right) \tag{6.2}$$

where μ is the un-normalized image signal, μ_{water} is the mean signal within the water vials,

and μ_{air} is the mean signal within the air surrounding the phantom. All images throughout the study are displayed with a window (W) and level (L) of 1300 HU and 150 HU, respectively.

TRMAR images were reconstructed using the 100–110 keV bin as the high energy bin and the 30–120 keV bin as the full energy bin. The metal was segmented in the 100–110 keV bin and the threshold was set to 2000 HU and no binary dilation was employed. For the beef short rib, the metal traces were normalized by a factor of 1.10 to offer a smooth transition between the attenuation signal in the high energy metal traces and the signal of the full energy sinogram. NMAR images were reconstructed using the 30–120 keV bin and the metal was segmented in the same bin using a threshold of 2000 HU and two iterations of binary dilation.

Streak artifact magnitude

The magnitude of the main streak artifact in the 100-mm phantom was evaluated by means of a region of interest (ROI) seen in red in Fig. 6.7b. This ROI was chosen because it encompasses the streak artifact without being overtly affected by other objects and/or artifacts within the image. The mean and the standard deviation of the ROI HU value was calculated for ten slices. The artifact magnitude was compared to the HU value of the same area in the non-metal images.

Image quality

Image quality in the 100-mm phantom images was measured in the phantom body only; it excluded the area with the streak artifact, all the vials, and the spatial resolution piece. A box and whisker plot was calculated for each energy bin and the various MAR methods. The standard deviation of the signal within the phantom body divided by the mean signal within the phantom body for ten slices for each set of data was reported as image noise. The mean signal within the phantom body was between -37 HU and -100 HU depending on the energy range of the bin.

Density quantification

The density of each of the five $Ca(ClO_4)_2$ vials in the 100-mm phantom was measured as by applying a linear fit to the real vial densities versus the mean HU value in each of the five vials in the non-metal images. Then the image densities of the vials in uncorrected, TRMAR, and NMAR images were calculated by applying the linear fit to the mean HU values from

the five vials in each image, respectively. The mean values were taken in 10 slices in each of the image types and the standard deviation of the mean values was calculated as the error.

Small features

The preservation of the modulation within the patterns on the spatial resolution piece in the 100-mm phantom were measured by drawing profiles parallel and perpendicular to the streak artifact over the four rows and columns of each of the five largest patterns in the resolution piece. In addition, the profiles were interpolated to smooth them, and the peaks and valleys were identified in each of the interpolated profiles and the mean peak difference was calculated. From there, the zero-frequency modulation was found as the difference between the spatial resolution piece and air and the modulation of each of the five patterns was calculated as the ratio of the peak differences in the profiles and the zero-frequency modulation. All profiles and calculations were done on six slices and the standard deviation between the slices was used as the error. Using linear interpolation, the modulation transfer function (MTF) was plotted and the limiting spatial frequency at 20% of the MTF was found for metal-free, uncorrected metal, TRMAR, and NMAR images.

Dose

The phantom dose was calculated by simulating a cylindrical water phantom in TOPAS as described by Dunning *et al.* [178, 177]. With the imaging parameters detailed in the image acquisition section, the dose to the 100-mm phantom was 153 mGy and the dose to the short rib was 306 mGy.

6.3.3 Simulations

Scatter to primary ratio optimization

CT imaging simulations were performed to assess the minimum photon energy threshold used in TRMAR. This was achieved through simulation of the scatter to primary ratio (SPR) in the detector for the projection in which the beam is attenuated by both screws. SPR was seen to correlate with metal artifacts in the reconstruction, thus the lower energy threshold for the TRMAR was based on SPR evaluation. Specifically, an $SPR = 1.0$ was chosen as the threshold to ensure that the photons used in the TRMAR are mostly primary, which resulted in greatly reduced metal artifacts.

CT simulations were performed using the Fastcat hybrid Monte Carlo (MC) code [222,

223]. Fastcat combines MC scatter and detector response functions with GPU ray tracing to produce fast and accurate CBCT images. To mimic the experimental setup, a 330-μm pixel pitch 2-mm thick CZT detector and a 100-mm diameter, 30-mm high polyethylene phantom were simulated with 6-mm inserts of Teflon, Delrin, and acrylic to mimic the inserts found in the phantom. Since the exact composition of the metal screws used in the experimental data acquisition was unknown, the metal screws were approximated as iron alone in simulations for simplicity. Additionally, SPR was assessed in a Fastcat projection image in the region of the phantom where the two screws aligned for monoenergetic simulations between 30 and 110 keV. Scatter was defined as any particle hitting the detector that had interacted in the phantom. SPR was also assessed in the situation with only one screw.

All simulations were run on a Linux desktop with 8 Intel Skylake cores (Intel Corp., Santa Clara, CA, USA) and a Nvidia GeForce RTX 2070 GPU (Nvidia Corp., Santa Clara, CA, USA). CT simulations took on average 10 seconds for the monoenergetic simulations and 60 seconds for full poly-energetic simulations. Though the incident beams in the monoenergetic simulations were comprised of x-ray of only that specific energy, the resulting polyenergetic scatter from the phantom itself was still detected and used for image reconstruction. The poly-energetic simulations consisted of a 120 kVp x-ray source filtered by 1 mm of copper simulated analytically by Fastcat. Additionally, focal spot blurring was applied for a 1 mm focal spot. 720 projections were acquired for each simulation and the images were reconstructed using the FDK method with a Hamming filter. CT images were reconstructed with 512×512 voxels with an image size of 105×105 mm^2. In the relevant MC simulations performed in TOPAS [178], the particle range cutoffs were set to 0.05 mm and no variance reduction techniques were used.

XCAT phantom

Fastcat simulations were also performed using the head of the anthropomorphic XCAT phantom [24], containing two silver amalgam dental fillings (Fig. 6.2d). 110 keV monoenergetic images and 120 kVp images filtered with 1 mm of copper were both simulated. Using the 110 keV monoenergetic simulations, TRMAR was applied to the 120 kVp simulated images using a 2000 HU threshold without any dilation. Additionally, a normalization factor of 1.15 was multiplied to the high energy metal traces for TRMAR in order to provide a smooth transition between high energy metal traces and the rest of the full energy sinogram. This was due to the sharp difference in bone attenuation in the 120 kVp simulation and 110 keV simulation. NMAR was applied to the 120 kVp simulated images with a 10000 HU threshold

and no binary dilation. Threshold and dilation values were found iteratively. The magnitude of the streak artifact was measured by placing an ROI within the streak artifact and calculating the mean and standard deviation of the pixels within the ROI.

6.4 Results

6.4.1 Simulations

CT simulation results of the 100-mm phantom are summarized in Fig. 6.4. The 120 kVp reconstruction (Fig. 6.4a) shows good agreement with the experimental results presented in Fig. 6.7b. The scatter simulation results (Fig. 6.4b and c) confirmed the increase of primary radiation reaching the detector with increasing energy and that SPR = 1.0 at 102.5 keV. The monoenergetic CT images presented in Fig. 6.4d confirm this pattern with the metal artifacts being prominent for energies of <100 keV. At 100 keV and 110 keV, the metal artifacts started to subside, and as a result and given that clinical scans are often performed with 120 kVp beams, 100 keV was chosen as the lower energy threshold for the high energy bin in TRMAR. For the case of only one screw, SPR was equal to 1.0 at approximately 80 keV (Fig. 6.5).

Simulated images of the XCAT head phantom for the 120 kVp beam and the 110 keV monoenergetic beam are shown in Fig. 6.6a-b. As previously demonstrated in Fig. 6.4d, the metal artifact is significantly reduced in the 110 keV monoenergetic images of the XCAT phantom (Fig. 6.6b). The TRMAR and NMAR images can be seen in Fig. 6.6c and d, respectively. All images in Fig. 6.6 also show the magnitude of the metal artifact, where the actual value of the same area in slices without metal artifacts was 32 ± 4 HU.

6.4.2 Experimental measurements

Reconstructions of the 100-mm diameter phantom with and without the screws can be seen in Fig. 6.7a and b, respectively. The dark streak artifact is seen in the image containing the screws, obscuring a portion of the spatial resolution piece and one of the $Ca(ClO_4)_2$ vials. The high-energy (100-110 keV) bin reconstruction is shown in Fig. 6.7c with a notable reduction in the magnitude of the streak artifact.

Metal artifact reduction with TRMAR

The results in the 100-mm phantom from both TRMAR and NMAR methods can be seen in Fig. 6.8. The noise texture in the phantom body from the 30-120 keV bin without metal

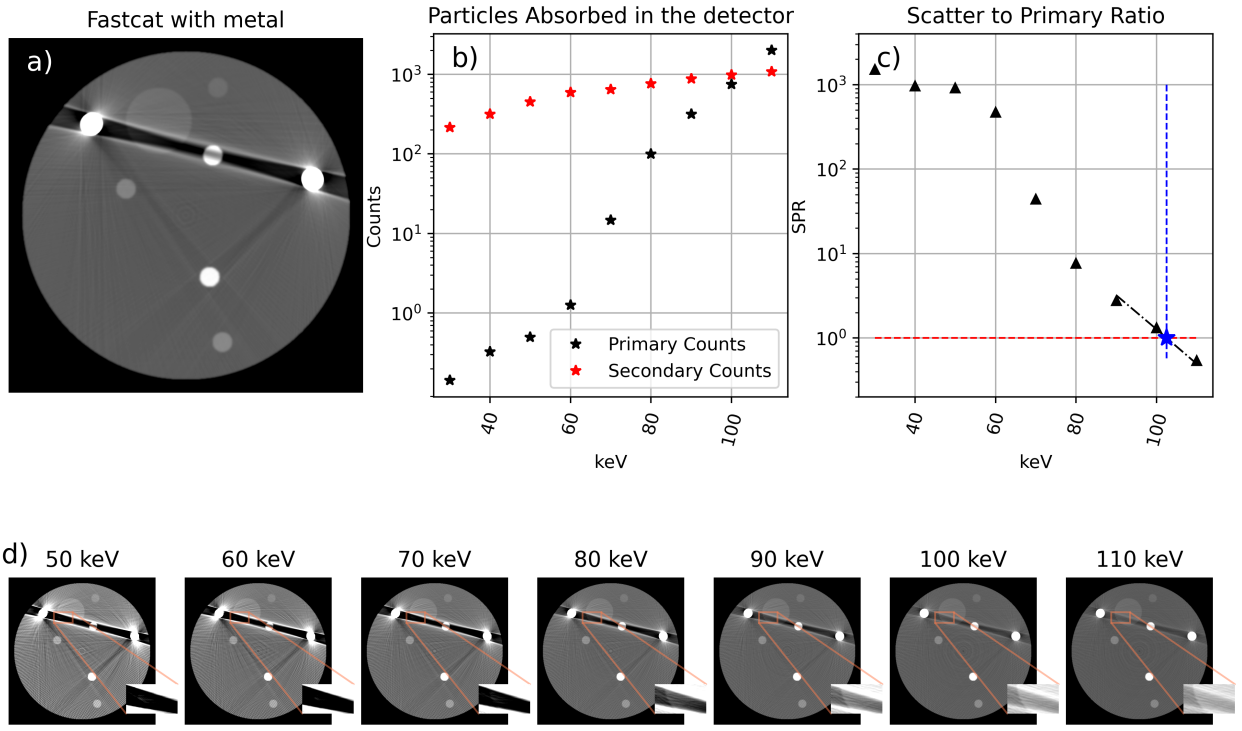

Figure 6.4: a) Fastcat image of phantom with metal inserts produced with the 120 kVp beam. b) A plot of the relative number of primary and secondary particles arriving at the detector in the area where the two metal screws align. c) The corresponding scatter to primary ratio. The blue star indicates an SPR of one. d) CT reconstructions of monoenergetic simulations of the phantom at energies between 50 and 110 keV with W/L = [1300/150 HU] and an inset image of the artifact area with W/L = [-800/0 HU].

(Fig. 6.8a) was maintained in the TRMAR images (Fig. 6.8b), though there are smaller artifacts still present. Additionally, the amount of reduction seen in the streak artifact in the high energy image (Fig. 6.7c) was maintained with TRMAR. In the modified NMAR image (Fig. 6.8c), a large reduction in the streak artifact was also seen, as well as the removal of many of the smaller, thin artifacts. However, other artifacts were introduced due to the interpolation process, which is common for linear interpolation methods [67, 201, 202]. These artifacts can be seen in the three insets in Fig. 6.8c (white arrows), and occur at the edges of water and $Ca(ClO_4)_2$ vials where there is a small amount of air between the phantom and the vial. They are also obvious in the spatial resolution piece, where bands of higher HU run in line with the direction of the holes. There is also some loss in the sharp edges of the holes in the spatial resolution piece.

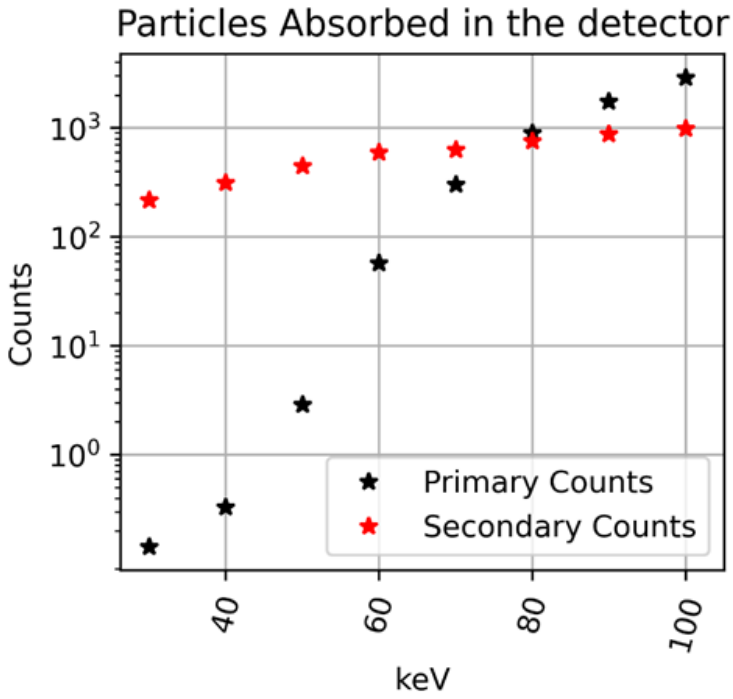

Figure 6.5: A plot of the relative number of primary and secondary particles arriving at the detector in the area in the case where there is one metal screw in the 10-cm polyethylene phantom.

Streak artifact quantification

Fig. 6.9a displays the magnitude of the streak artifact as calculated using the ROI shown in Fig. 6.7b. The mean phantom CT number in the 30-120 keV bin with no metal was -81 HU. The CT number decreases with the introduction of the metal. Using the high energy bin alone (100-110 keV), the streak artifact was markedly reduced. With TRMAR, we were able to reduce the effect of the streak artifact to almost the same extent as the high energy image, but slightly better results were seen using NMAR.

Additionally, the 100-mm phantom was scanned with a larger collimator to evaluate the effect of scatter and SPR experimentally. In the uncorrected image with the larger collimator the streak artifact demonstrated a signal of -567 $\pm$ 66 HU compared to -442 $\pm$ 105 HU with the smaller collimator. After correction with TRMAR, the streak signal was -237 $\pm$ 44 HU with the larger collimator compared to -142 $\pm$ 51 HU with the smaller. The same areas in the images without metal were -80 $\pm$ 12 HU and -84 $\pm$ 14 HU for the smaller and larger collimators, respectively. All images can be seen in Fig 6.10.

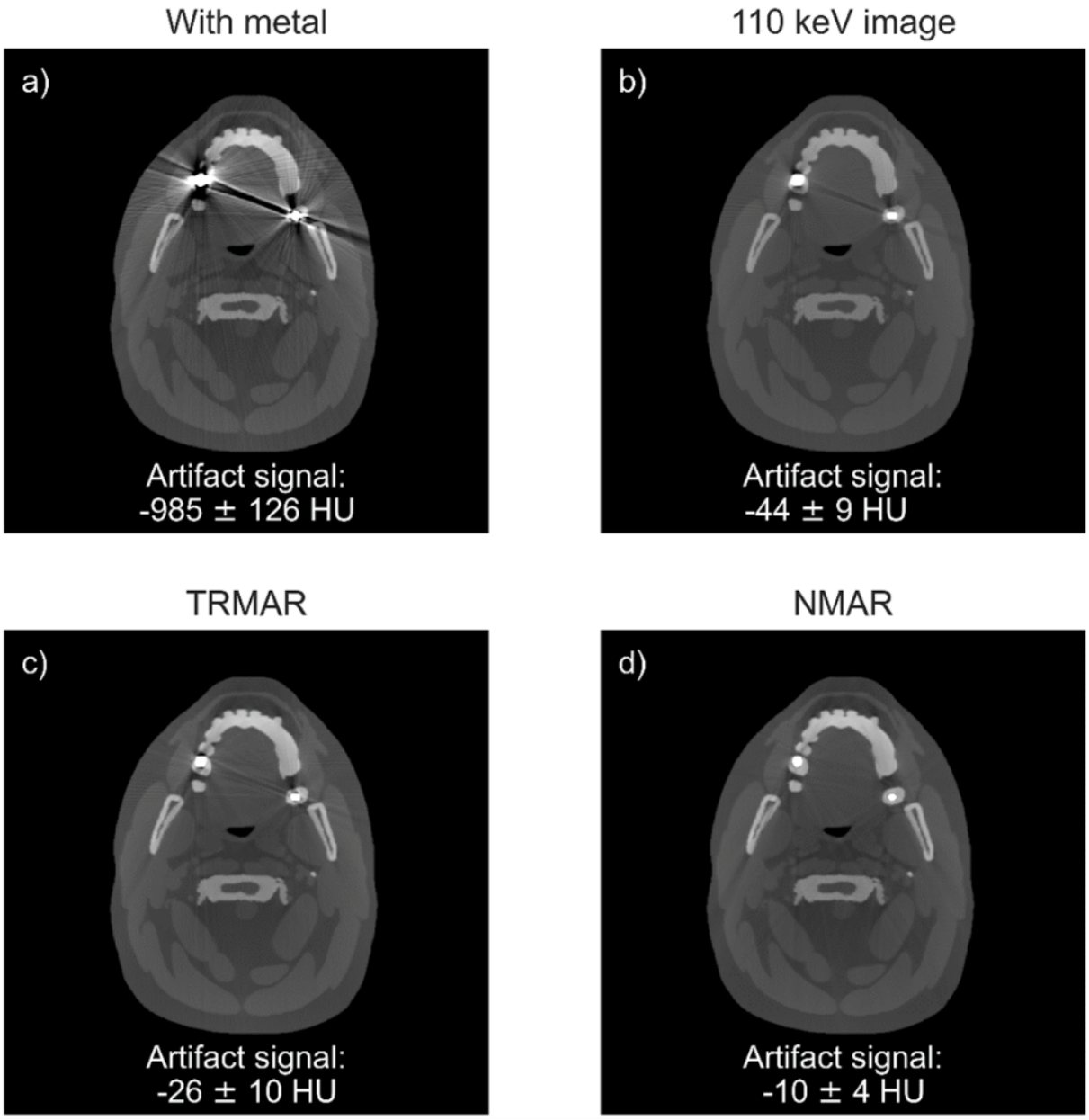

Figure 6.6: Simulated Fastcat images of the XCAT head phantom a) using a 120 kVp beam, b) using a 110 keV monoenergetic beam, c) using TRMAR with the metal traces from the 110 keV monoenergetic images, and d) using NMAR.

Density accuracy

Fig. 6.9b depicts the effect that the two metal artifact reduction techniques had on quantifying the density of the contrast vials. Both TRMAR and NMAR corrected the density in the 1.37 g/cm^3 vial, which was the vial bisected by the streak artifact, though NMAR was more

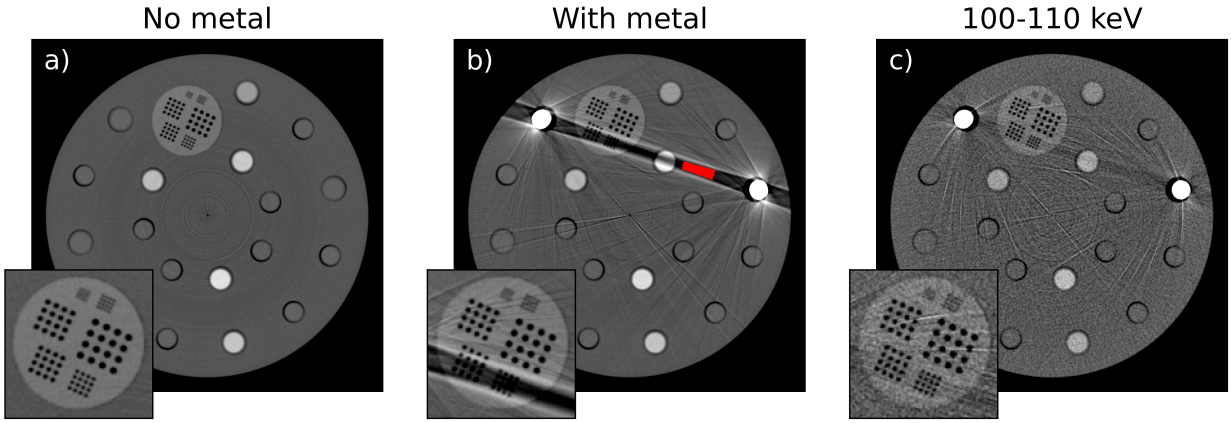

Figure 6.7: CT reconstructions using the 30–120 keV bin of the two phantoms layouts: a) without metal and b) with metal. c) The 100–110 keV bin showing reduced metal artifacts. The red overlap in the images is the ROI used for the artifact magnitude measurement. W/L = [1300/150 HU].

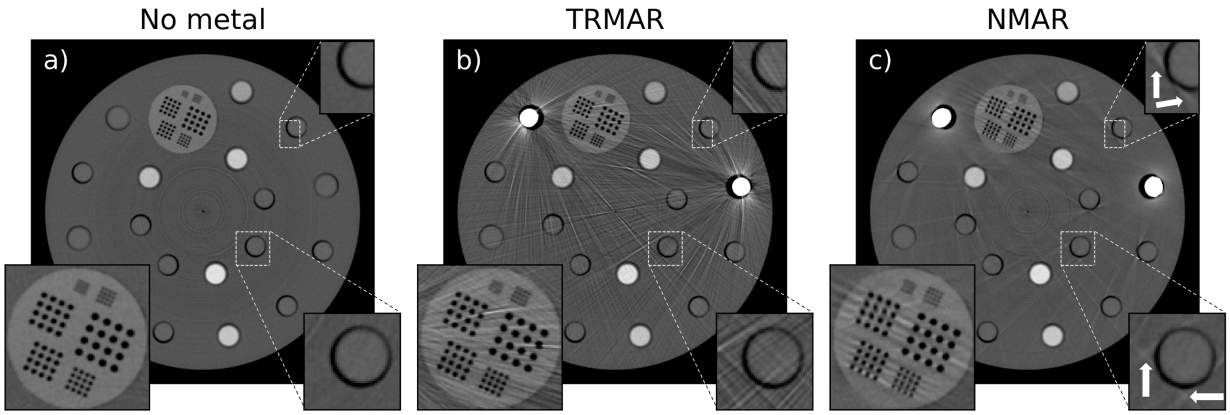

Figure 6.8: CT reconstructions a) without metal b) with the 100–110 keV TRMAR in the 30-120 keV energy bin and c) NMAR in the 30–120 keV energy bin. Inserts show areas with introduced artifacts in NMAR (white arrows). W/L = [1300/150 HU].

accurate. NMAR also offered more accurate density values for the other vials which were less affected by the streak artifact. TRMAR slightly underestimated the non-metal image density and demonstrated similar values to the uncorrected metal image densities for the four vials that were relatively unaffected by the streak artifact. However, for both TRMAR and NMAR the error on the image density values encompassed the mean density found in the non-metal images. The mean absolute error on the density value for all vials for TRMAR was 0.018 $\pm$ 0.002 g/cm^3 and 0.0016 $\pm$ 0.0008 g/cm^3 for NMAR.

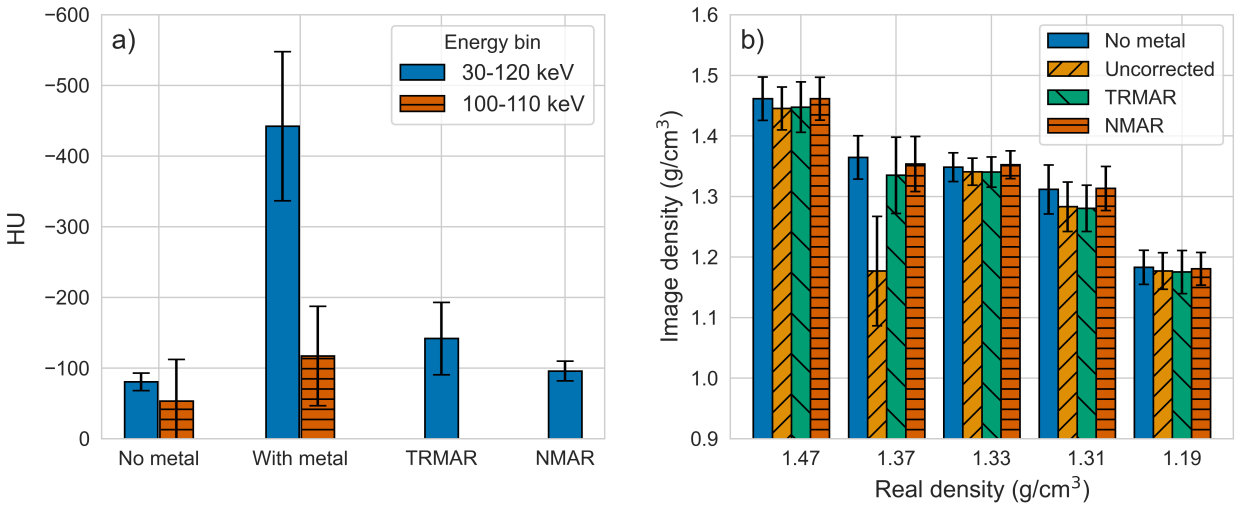

Figure 6.9: a) The main streak artifact magnitude in the CT images containing no metal, the images containing metal (middle), and the three correction methods. b) Quantitative accuracy of the density of the five bone analogue vials in the no-metal, uncorrected, TRMAR, and NMAR images.

Image quality

In addition to the main streak artifact, the metal also produced other smaller artifacts, which were quantified via the relative image noise, as shown in Fig. 6.11. The relative noise increased in both the 30-120 keV and 100-110 keV images when metal was introduced (Fig. 6.11b). The noise levels in the MAR methods were not reduced compared to the relative noise seen in images without metal artifacts, although they were reduced compared to the uncorrected metal images. The 100-110 keV TRMAR demonstrated a 4.4% decrease in relative noise compared to the 30-120 keV image with metal artifacts. The NMAR images demonstrated a larger reduction of 29.2%, with a relative mean noise close to that of the metal-free images.

MTF measurements

Fig. 6.13a shows the MTF for the profiles drawn perpendicular to the streak artifact and Fig. 6.13b show the profiles drawn parallel to the streak artifact for metal-free, uncorrected metal, TRMAR, and NMAR images, respectively. Fig. 6.12a-d shows the spatial resolution piece for same image types and Fig. 6.12e-h shows an example of the profile that is drawn in the images in Fig. 6.12a-d after interpolation. 6.1 shows the limiting spatial frequency at 20% of the MTF in each of the profile directions for metal-free, uncorrected, TRMAR,

Table 6.1: Limiting spatial frequency.

	Limiting spatial frequency (lp/mm)			
Profile direction	No metal	With metal	TRMAR	NMAR
Perpendicular	1.35	1.21	1.35	1.15
Parallel	1.27	1.27	1.27	1.29
Mean	1.31	1.24	1.31	1.22

and NMAR images. The mean limiting frequency for both perpendicular and parallel is also listed. In both cases TRMAR outperformed NMAR, but especially so in the direction perpendicular to the streak artifact.

Beef short rib images

The images of the beef short rib with and without metal, as well as the MAR images, can be seen in Fig. 6.14. A closeup inset of the upper screw can be seen in all the images containing the screws showing that the physical shape of the screws in best visualized in the 100-110 keV bin (Fig. 6.14c), with the delineation maintained in the TRMAR image (Fig. 6.14d). To obtain the best MAR results in NMAR, two iterations of binary dilation were applied, which distorted the shape of the screws and the air pockets that existed in some areas around the screw (white arrows in Fig. 6.14c and e). Distortions in the shape of air pockets further away from the screws were also observed and can be seen in the lower image insets, with some of the smaller air pockets almost lost in the NMAR images. Additionally, the results of applying no dilation to NMAR metal segmentation can be seen in Fig. 6.14f where the metal artifacts are still present, though to a lesser extent than seen in the uncorrected metal image (Fig. 6.14b).

6.5 Discussion

6.5.1 Scatter to primary ratio

Here, a MAR algorithm (TRMAR) was presented exploiting PCD-CT's ability to bin photons based on their energy when incident on the PCD. The artifact reduction provided by TRMAR was based on the reduced beam hardening seen at higher x-ray energies, which can be distinguished with PCD-CT. For the experiments conducted as part of the study, it was found, based on simulations performed in Fastcat, that energies above 100 keV would provide the best MAR. This high energy lower threshold was chosen based on the simulation results

that demonstrated that the SPR reached 1.0 just above 100 keV, meaning that there was an equal amount of primary to secondary x-rays incident on the detector at the location in which the two metal screws overlapped. An SPR of 1.0 is not sufficient by itself to generate a good CT image in terms of MAR and is specific to the case of the 100-mm diameter phantom. However, the rationale is that energy bins above the 100 keV threshold at which SPR would equal 1.0 would have SPRs much less than one, due to the fact that the SPR is decreasing exponentially, as seen in Fig. 6.4c, leading to more primary photons. Simulations with a higher number of primary photons would mean that there was more penetration through the metal. Beam hardening would not occur in monoenergetic simulations if only monoenergetic x-rays are detected. However, metal artifacts are still seen, which are due to polyenergetic scatter generated within the phantom by the monoenergetic beam. The presence of more primary photons leading to reduced metal artifacts can be seen in the monoenergetic 100 keV and 110 keV simulation images (Fig. 6.4d). For larger objects, the threshold of 100 keV corresponding to an SPR of 1.0 would not hold, though MAR should still be observed. This can be seen in the simulated CT images of the XCAT head phantom at 110 keV (Fig. 6.6b), which still demonstrated significant MAR though the diameter of the head was much larger than the 100-mm diameter phantom. The XCAT head phantom simulates a 50th percentile man, whose head has a circumference of 585 mm, which corresponds to a diameter of roughly 180 mm. As such, TRMAR also demonstrated a similar reduction in the streak artifact seen in the XCAT images (Fig. 6.4c). To further support the fact TRMAR could still be used with a lower high energy threshold, MAR reduction was still seen in the 100-mm in the 70-100 keV bin and with TRMAR using the 70-100 keV bin (Fig. 6.15b, c). In addition, clinical CT scanners often have a higher peak tube voltage of 140 kVp, which would allow a higher energy threshold to be used for full-body imaging. This would allow for lower noise in the high energy bin, or the increase of the high energy bin range, which would further reduce beam hardening. In our experiments, we were limited to 120 kVp due to room shielding. Also, clinical scanners often include an anti-scatter grid, which would lower the threshold at which an SPR = 1.0 could be achieved. Since metal artifacts were reduced more as the energy was increased in simulation past the SPR = 1.0 energy value, we would expect to see reduced metal artifacts at the same energy if an anti-scatter grid were added.

All of the simulation images did suffer from some additional artifacts not seen in experimental data, especially in the monoenergetic reconstructions (Fig. 6.4d). They appeared as linear patterns called Moiré patterns [66] and were due to a number of causes. Moiré patterns are interference patterns caused when two similar patterns are overlaid with one another, but with a slight offset, such as a small rotation. This, of course, occurs during

reconstruction in CT, as similar backprojections are overlaid with one another with only a slight rotational offset. They are especially prevalent in simulations, and in particular here, due to view under-sampling [66], high-spatial resolution, and idealized data acquisition with perfect sample rotation. Combined, these factors lead to the patterns seen in the simulation images (Fig. 6.4a, d). The severity of the patterns was also correlated with the severity of metal artifacts. These patterns can also occur in experimental data, though are not as prevalent, partly likely due to the imperfect sample rotation resulting in Moire pattern smearing.

6.5.2 XCAT phantom

In order to evaluate the performance of TRMAR initially, the algorithm was first applied to simulations of the XCAT head phantom (Fig. 6.6c) and compared with NMAR, which was applied on the same images (Fig. 6.6d). In this case, as the metal fillings were embedded in the teeth, the segmented metal traces showed a slight border in the projection space that contained bone. When the metal traces were replaced with the high energy metal traces, a sharp edge was seen between the bone attenuation in the 120 kVp sinogram and bone attenuation in the 110 keV traces. This led to a dark ring appearing around the fillings, causing significant artifacts. This was mitigated by normalizing the high-energy metal traces, which reduced the ring. In the case of the XCAT images, TRMAR performed similarly to NMAR with negligible differences in the measured magnitude of the streak artifact. However, the dark artifacts directly above and below the fillings in the 110 keV monoenergetic image (Fig. 6.6b) were also seen in the TRMAR image (Fig. 6.6c), but not in the NMAR image (Fig. 6.6d). Overall, NMAR offers a slightly fewer artifacts in the XCAT simulations compared to TRMAR, on which the streak artifact can still be visualized, and smaller artifacts can also still be seen.

6.5.3 Experiments

The 100-110 keV bin was used as the high energy bin for the experimental verification of TRMAR. This energy range was chosen not only due to it containing energies above the SPR threshold dictated by the Fastcat simulations, but also because previous work has demonstrated the benefits of smaller bins for MAR using PCDs [219]. The 30-120 keV energy range used for the metal-free, uncorrected, and NMAR images, as well as the base of the TRMAR images. X-rays below 30 keV were excluded as they include a disproportionate amount of noise due to charge sharing [118, 113], and they are largely attenuated by the 1

mm Cu filtration. Additionally, an extensive proportion of x-rays below 30 keV would be attenuated by the phantom.

Streak artifact

The 100-mm phantom images for both methods of MAR were evaluated based on a number of criteria, the first, like the XCAT images, being the magnitude of the streak artifact between the metal. In this case, NMAR offered HU values closest to the metal-free images by a small margin. In NMAR, by interpolating along each row in all the normalized sinogram slices, the signal on either side of the metal traces is largely composed of the phantom (with a slight amount of air around the metal itself). This results in signal within the metal traces closely resembling the phantom signal. However, the metal traces within the sinogram are not only surrounded by the phantom, but the metal also crosses the traces of other objects within the phantom, such as the spatial resolution piece, which leads to some non-uniformities within the interpolated traces. This introduces other artifacts which can be seen in the reconstructed NMAR images (Fig. 6.8c, white arrows). For the 100-110 keV image and the TRMAR images, the metal traces still showed attenuation by the metal, though to a lesser extent than the full energy range. Therefore, the TRMAR images still suffered from beam hardening and scattering. However, the streak artifact was smaller in magnitude resulting from the reduced effects of beam hardening. TRMAR with the 100-110 keV traces reduces the magnitude of the streak artifact to a lesser extent than NMAR, but does not introduce additional artifacts to the images. However, NMAR still outperforms TRMAR to a small extent in terms of streak artifact reduction.

Additionally, the initial simulations showed a lower SPR was correlated with reduced metal artifacts. Experimentally, this was tested by widening the collimation of the beam and scanning the same phantom with and without metal in order to evaluate the effect on the streak artifact. In both images that were uncorrected, and images corrected using TRMAR, the streak artifact signal was greater in the presence of more scatter with the widened collimator under otherwise identical conditions. As the conditions were identical except for the collimation, any significant difference in counts in the projection images would be due to a change in scattered detections, supporting the correlation between increased metal artifacts and increased SPR.

Density quantification

The 1.37 g/cm^3 $Ca(ClO_4)_2$ vial was the only contrast tube significantly affected by the metal artifacts, as it was bisected by the streak artifact. In that vial, NMAR offered the best correction as the streak artifact was reduced almost completely while TRMAR still showed a residual artifact. However, TRMAR was still able to greatly increase the accuracy of the vial density due to the reduction in the streak artifact to within the margin of error on the value found in the non-metal images. Even including the 1.37 g/cm^3 $Ca(ClO_4)_2$ vial, TRMAR was able to correct the density, on average, to within 0.018 g/cm^3. NMAR still offered better results however, being able to correct the density to within 0.0016 g/cm^3.

Image quality

The smaller streaking artifacts seen in the 100-mm phantom and short rib images are common in CT images containing metal and were measured here via the relative image noise in the phantom body. These small artifacts can be due to a number of factors, including beam hardening, scatter, and Poisson noise. The edges of the metal can also create streaks as a result of undersampling, motion, and cone beam artifacts [23]. Here, these artifacts were not due to motion, as we were using a phantom with the metal screws fixed in place. Undersampling was also likely not the source as additional data with double the number of projections was acquired with no changes in the small streaking artifacts. Many of these small artifacts appeared as thinner versions of the streak artifact, which occurred between the two metal screws with higher attenuation. Unfortunately, our prototype PCD detector suffers from considerable pixel non-uniformity which leads to ring artifacts that are not completely mitigated by flat-field and other tested ring artifact correction methods. Consequently, ring artifacts can make it appear that an area has higher attenuation than expected, and many of the small artifacts occur between a screw and a ring artifact. The non-uniform responding pixels also appear to potentially interact with the metal artifacts, cause the blooming signal around the metal to sweep along the path of the ring artifacts, as in Fig. 6.14c. Two especially noticeable streaking artifacts occur through the central pixels of every image with metal artifacts, whether corrected using a MAR method or not. The centers of these images have noticeable ring artifacts, supporting this hypothesis. Additionally, these artifacts were non-existent in the NMAR data, where the metal signal from the screws was completely replaced, and the small streaking artifacts were not present. Overall, NMAR was more successful at improving image quality visually as well as quantitively. However, TRMAR still warrants further investigation since fewer artifacts would be likely to occur in a clinical

system due to reduced ring artifacts as further improvements in PCD technology are made.

6.5.4 TRMAR benefits

The first benefit of TRMAR over NMAR is in the preservation of small features. 6.1 demonstrates that the limiting spatial frequency is preserved with TRMAR compared to even the metal-free image, while the limiting spatial frequency is reduced for NMAR. The MTFs for both TRMAR and NMAR can be seen in Fig. 6.13. For NMAR, the major factor affecting the reduction in the ability to distinguish small details is the introduction of new artifacts, which can be prominently seen in Fig. 6.12d in the direction parallel to the streak artifact. The artifacts are especially prevalent in the 0.75 mm array (the array with the red line profile), where they run not only parallel, but diagonal as well. These diagonal artifacts significantly reduce the NMAR MTF at that point (0.66 lp/mm). The example profile (Fig. 6.12h) also demonstrates this fact. The beef short rib images also bolster the benefits of TRMAR over NMAR regarding small detail preservation.

The second major benefit with TRMAR is the process of segmenting the metal in the reconstructed CT image. The segmentation needs to be much more exact for NMAR and often requires iterations of binary dilation to encompass artifacts that occur around the physical edges of the metal objects. This results in distortion of the metal object's appearance in the final NMAR image (Fig. 6.8c, Fig. 6.14e). However, if the binary dilation is not applied, metal artifacts can be left uncorrected (Fig. 6.14f). Alternatively, TRMAR is much more forgiving in terms of segmentation as the data is an exact replacement, only at a higher energy. Thus, even if the object is overestimated in the segmentation, the excess data is still replaced with real data, though from a higher energy range. This is not without issues however, as can be seen in the XCAT images (Fig. 6.6c, d) when the metal is completely enveloped in bone. Then, when the data is replaced with the data from the high energy bin, the bone appears to have much lower attenuation that expected, which could cause artifacts, if the edges of the replaced data are not normalized. In the case of the XCAT data, NMAR is slightly easier to segment and the metal is not excessively distorted, though that could be due to their more uniform shape. Underestimation of the edges of metal is not ideal in either TRMAR or NMAR as it will result in the edges of the metal not being corrected. All that aside, the segmentation for TRMAR is more forgiving than for NMAR, especially since the metal can be segmented in the higher energy bin with PCD-CT, resulting in better delineation of the metal object before forward projection.

And finally, the last benefit of TRMAR over NMAR is that it can correct images in

approximately 1/3 of the time because there are fewer reconstructions to compute.

6.5.5 Future work

The clinical applicability of TRMAR is not fully assessed in this study, as it is limited to a simulations and scans with a bench-top PCD-CT system which is only able to accommodate small objects.

Future research will include scanning objects at higher tube voltages, such as 140 kVp, implementing an anti-scatter grid to improve SPR, and scanning larger objects. These steps are unfortunately not feasible with our present setup, however, in the near future our table-top system will be equipped with a new, larger PCD, which will enable the scanning of larger objects. The new PCD will also contain higher quality CZT, which should mitigate some of the pixel response non-uniformity and improve image quality. The installation of an anti-scatter grid is also planned for the new detector.

In the meantime, next steps are to implement TRMAR in combination with NMAR or another MAR methods to see if better artifact reduction can be obtained than either method alone. Anhaus et al recently showed that iterative metal artifact reduction (iMAR) could be combined with virtual monoenergetic images with a clinical PCD-CT scanner to obtain better metal artifact reduction [224]. It is possible similar results could be obtained by first applying TRMAR to obtain a reduced artifact image, and then an additional method could be applied to further improve the results.

6.6 Conclusion

In this study, we demonstrated that PCD-CT can greatly reduce metal artifacts between two metal objects in simulations and in phantom experiments by excluding low energy data. Additionally, we introduced the trace-replacement mental artifact reduction (TRMAR) method, which allowed us to replicate the reduction of the metal artifact seen in high energy reconstructions made possible with PCD-CT while maintaining the contrast and image quality of the original image. With TRMAR, the projection data affected by the metal (the metal traces) are replaced with the data from a high energy range. We compared TRMAR with a commonly used MAR method, NMAR, though NMAR offered slightly better results in terms of streak artifact reduction, contrast quantification, and image quality. However, TRMAR outperformed NMAR when it came to conserving small details and better preserving the shape of the metal objects and was able to correct images in approximately 1/3 of the time. Based on these results PCD-CT demonstrates notable future options in fast, accurate metal

artifact reduction with both high-energy reconstructions and TRMAR.

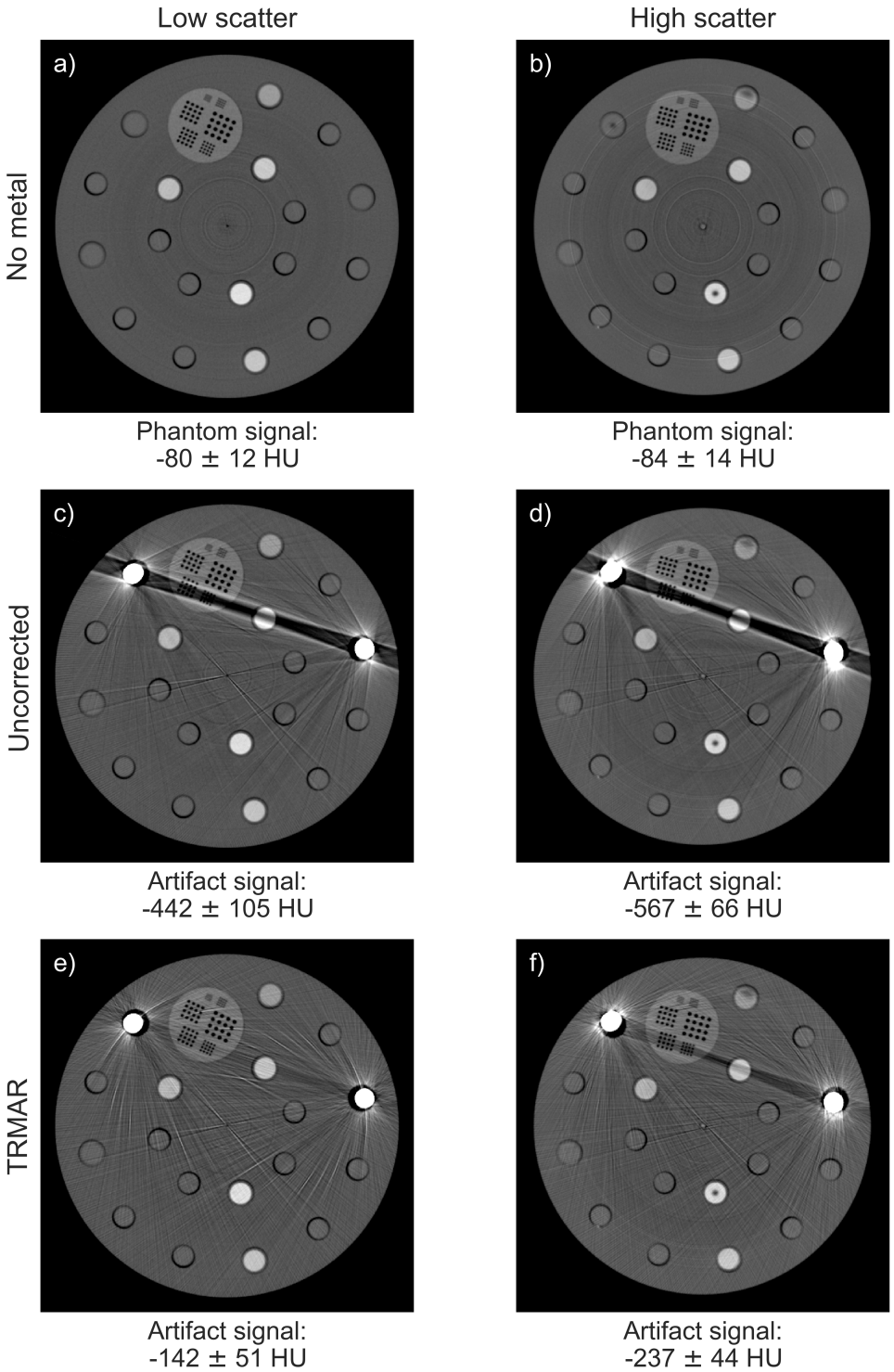

Figure 6.10: CT images demonstrating the effect of scatter on metal artifacts. a–b) CT images with no metal. c–d) CT images with uncorrected metal artifacts. e–f) CT images corrected with TRMAR. a), c), and e) show images with tighter collimation and less scatter. b), d), and f) show images with wider collimation and more scatter.

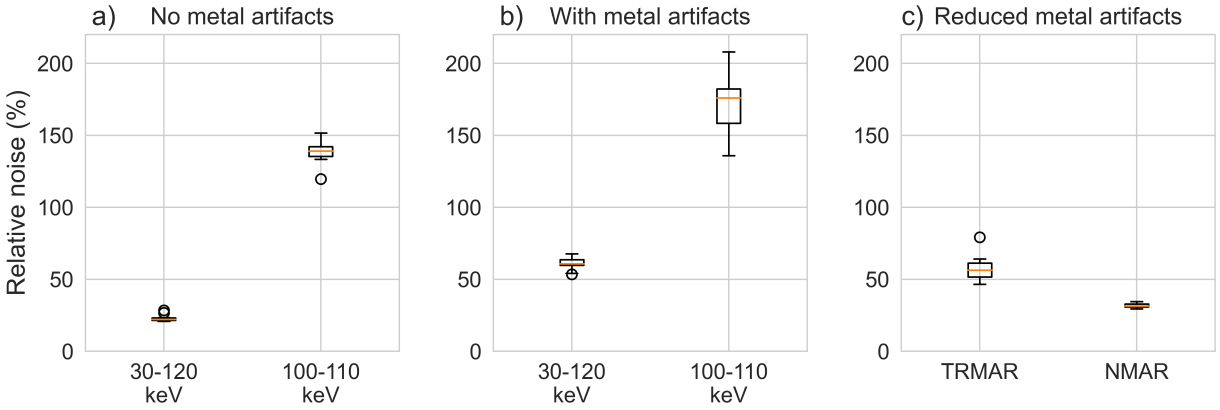

Figure 6.11: Relative noise in the phantom body in the images a) with no metal artifacts, b) with uncorrected metal, and c) with three correction methods. For each bar, the orange line corresponds to the median value in each data set. The boxes extended from the lower to the upper quartile of the relative noise values, with the whiskers extending 1.5 times the interquartile range.

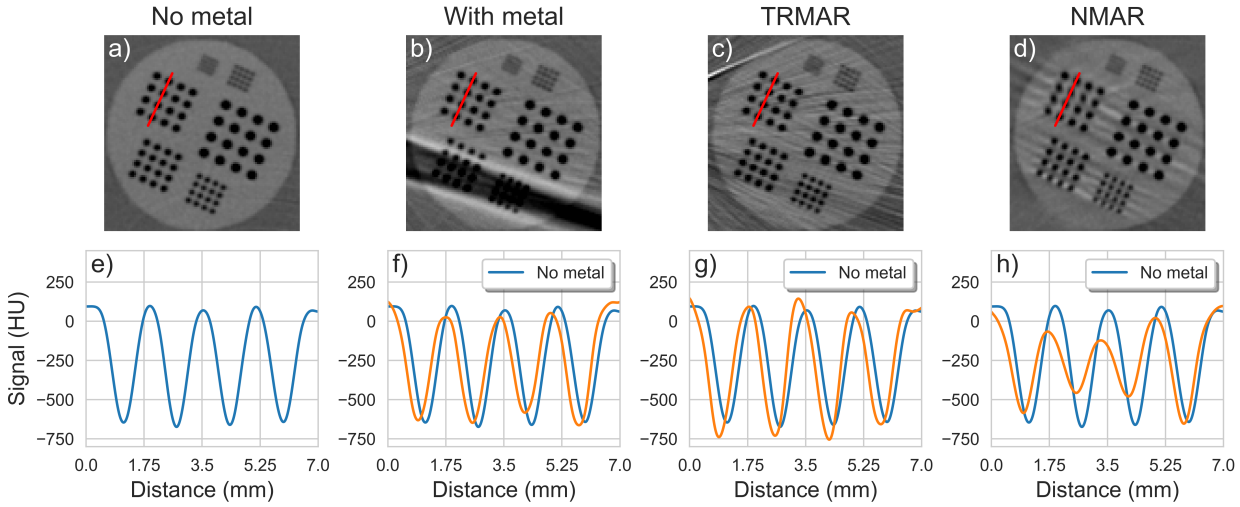

Figure 6.12: The spatial resolution piece with a profile (in red) drawn across the 0.75 mm array perpendicular to the streak artifact in a) the non-metal image, b) the 30-120 keV image with uncorrected metal, c) the 30-120 keV image with 100-110 keV TRMAR, and d) the 30-120 keV image corrected using NMAR. W/L = [1300/150 HU]. e-h) The interpolation of the profiles drawn in a-d), respectively.

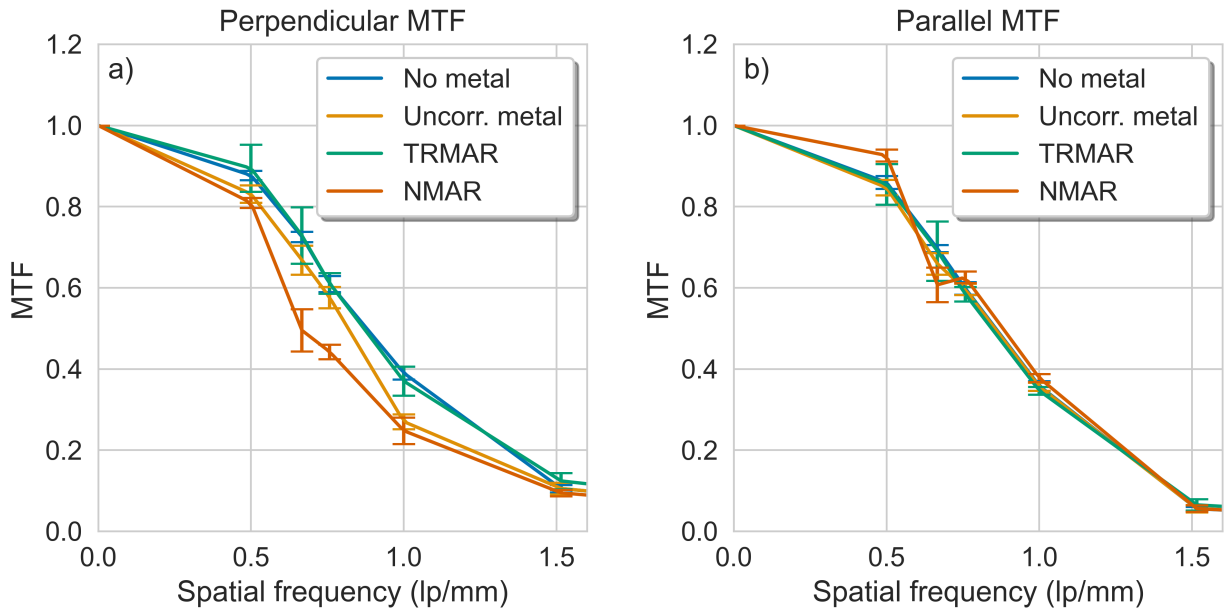

Figure 6.13: The MTF for the metal-free, uncorrected metal, TRMAR, and NMAR images for a) the profiles drawn perpendicular to the streak artifact (see Fig. 6.12a-d) and b) the profiles drawn parallel to the streak artifact.

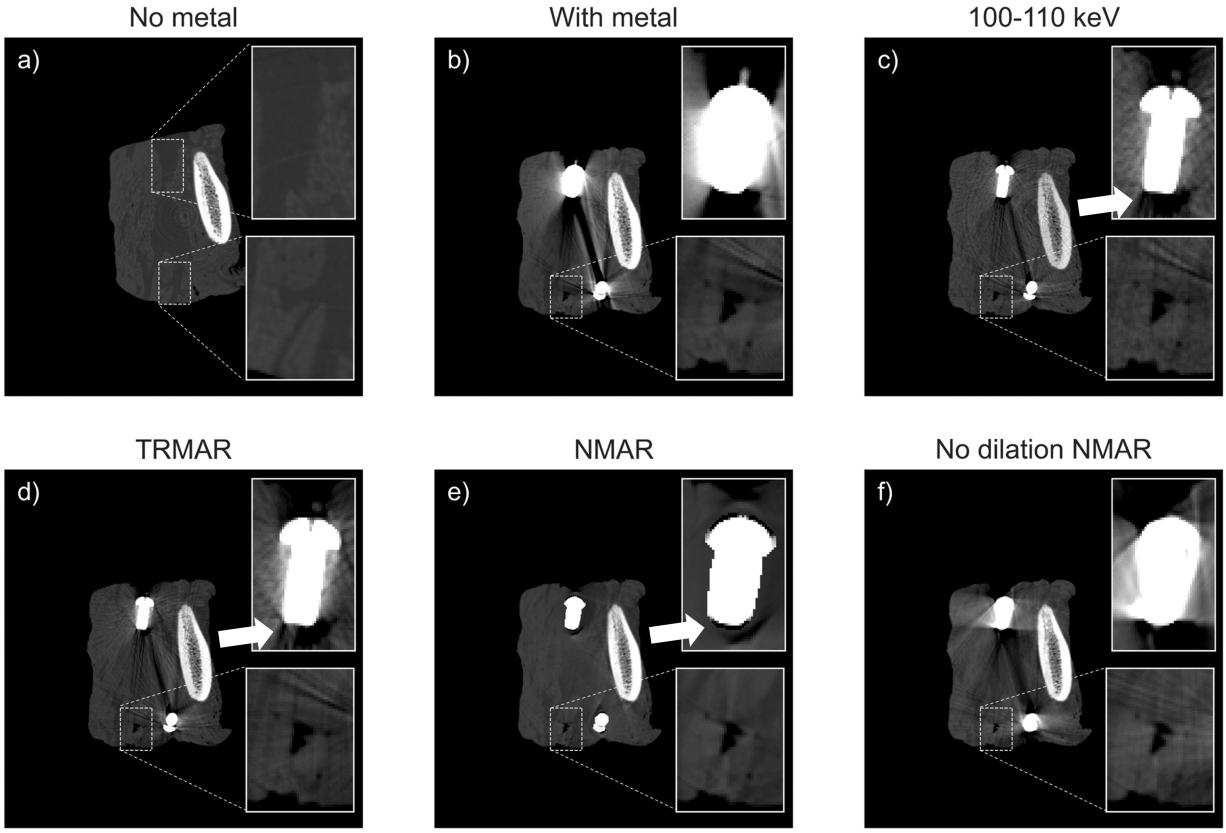

Figure 6.14: CT images of a beef short rib in a) the 30-120 keV bin no embedded, b) the 30-120 keV bin with uncorrected metal, c) the 100-110 keV bin with metal, d) the 30-120 keV bin corrected using TRMAR, e) the 30-120 keV bin corrected using NMAR, and f) the 30-120 keV bin corrected using NMAR with no dilation applied to the segmented metal. Inserts in b-f) show closeups of the two screws. W/L = [1800/500 HU].

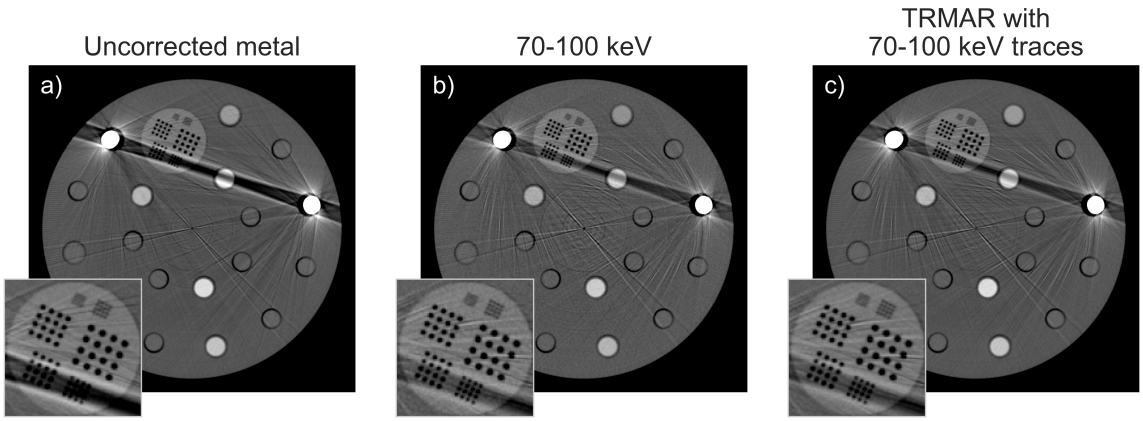

Figure 6.15: CT reconstructions a) with uncorrected metal in the 30–120 keV bin. b) with uncorrected metal in the 70-100 keV bin, and c) using trace replacement with 70–100 keV metal traces in the 30–120 keV image. W/L = [1300/150 HU].

Chapter 7

The feasibility of accurate stent visualization with photon-counting detector CT and K-edge imaging

The following work was published in *IEEE Transactions on Radiation and Plasma Medical Sciences* in 2023 and can be found at the following DOI: 10.1109/TRPMS.2023.3287566

7.1 Summary

CT stent imaging suffers from blooming and metal artifacts, reducing the diagnostic quality of images in the areas around stents. Photon-counting detectors (PCDs) have been shown to reduce these artifacts. Two clinical scanners, a GE Optima 580 and Discovery IQ, were compared to a bench-top PCD-CT system for stent imaging with three stents: Medtronic Protégé, Cordis Precise, and Cordis S.M.A.R.T. Control. The apparent strut thickness, lumen diameter, and lumen attenuation of the stents were evaluated in reconstructed images. K-edge images were also reconstructed to demonstrate more accurate delineation of the tantalum radiopaque markers. PCD-CT offered lower percent differences for strut thickness for all three stents ($p < 0.001$) and for lumen diameter for the Protégé and Precise stents ($p < 0.01$). The lumen attenuation was more accurate with PCD-CT as well ($p < 0.01$), excluding the comparisons between the Optima 580 and PCD-CT for the Protégé and Precise stents. The PCD-CT system was better able to delineate stents, specifically strut thickness. The stents were more easily distinguished in PCD-CT images and in 3D volume renderings than the clinical systems. The tantalum radiopaque markers were clearly visible in K-edge images due to reduced metal artifacts.

7.2 Introduction

CT angiography (CTA) is a common imaging assessment used to diagnose vascular diseases and monitor potential complications before and after treatment [225]. Vascular issues such as stenoses can often be treated with the implantation of a stent, which can prevent the blood vessel from narrowing. However, monitoring of the area in which the stent is implanted can be hindered due to the stent itself. Stents are usually manufactured from various metals, which cause metal artifacts [184, 23], especially blooming artifacts, due to their high atomic number and density. These artifacts can reduce the diagnostic value of CTA scans [226] and need to be mitigated as much as possible. The artifacts obscure the visualization of the stent lumen, which needs to be examined in order to assess whether or not there are any blockages which have developed within the stent. Stent imaging with CT is especially problematic with stents with lumen diameters under 3 mm [227] , as the lumen covers a smaller area and visualization is more readily impaired by artifacts. A number of CT advances are currently approaching the point where they could be used in the clinic to address some of the issues of stent imaging, including ultra-high-resolution (UHR) CT and photon-counting detector (PCD) CT [228].

PCDs are direct-conversion x-ray detectors, which are able to distinguish the energy of incident x-ray and bin them within specific energy ranges. As PCDs have been developed which are able to handle higher flux rates, research has been ongoing to investigate replacing conventional energy-integrating detectors (EIDs) in conventional CT scanners to investigate the benefits PCDs could offer [9, 11, 1, 69, 2]. To date this has resulted in one PCD system being approved for clinical use [3], with others currently under development [107, 7, 4]. The benefits offered by PCDs include reduced metal and blooming artifacts as well as increased spatial resolution[69, 2], among others, which could offer gains for CTA for imaging stents. A number of previous studies have investigated the comparison between PCD-CT and EID-CT for stent imaging including lumen visualization, lumen attenuation, lumen diameter, and the apparent size of stent struts [80, 79, 81, 78, 82, 111, 229]. PCD-CT also offers the potential for K-edge imaging of high-atomic number contrast agents [118, 117, 60], such as iodine and gadolinium, as well stents containing proportions of high-atomic number elements [78]. Additionally, the first comparisons with in-human data of the two modalities have been published [227, 230].

In this study we evaluate the performance of a prototype bench-top PCD-CT system against two conventional clinical CT systems by imaging several larger ($> 5mm$ diameter) carotid artery stents. Though the stents are larger than those that are currently the most

difficult to image, it provides a baseline comparison between our bench-top PCD-CT system and every-day clinical systems. We evaluate the apparent lumen diameter, lumen attenuation and noise, and visualize and quantify the size of radiopaque markers with K-edge subtraction imaging. We also demonstrate that our bench-top system provides the smallest measured apparent strut thickness compared with previous studies.

7.3 Materials and Methods

7.3.1 Imaging Systems

Three different CT systems were used to image stents in this study: a GE Optima 580 radiation therapy simulator, a GE Discovery IQ scanner (both GE Healthcare, Chicago, IL), and a prototype bench-top PCD-CT scanner. All three scanners can be seen in Fig. 7.1a–c. The bench-top PCD-CT system consisted of a Comet MXR 160/22 x-ray tube (Comet Technologies, San Jose, CA), rotation and motion stages (Newport Corporation, Irving, CA), and a state-of-the-art flat panel PCD (Redlen Technologies, Saanichton, BC, Canada). The source to isocenter distance was set to 322 mm with a source to detector distance of 578 mm. The PCD consisted of 2 mm thick cadmium zinc telluride (CZT) crystal with a 330μm pixel pitch and an active area of 8×190 mm^2, which gives a 106 mm field of view with 4.5 mm Z-coverage at isocenter [25]. The PCD is capable of the energy discrimination with binning of up to six energy bins and can operate without polarization at counts rates up to 650 Mcps/mm^2 [115, 125].

7.3.2 Stents and Imaging Phantom

Three nitinol stents were imaged in this study: a Medtronic Protégé stent (Medtronic plc, Minneapolis, MN), a Cordis Precise stent, and a Cordis S.M.A.R.T. Control stent (both Cordis, Santa Clara, CA). Strut thicknesses were measured using a microscope with a 4X objective and found to be 0.186 mm, 0.238 mm, and 0.177 mm, respectively. All other physical dimensions were measured with calipers. The lumen diameters of the stents were 5.82 mm, 5.71 mm, and 5.84 mm, respectively. The two Cordis stents also had tantalum radiopaque markers. All stents were inserted into plastic straws to mimic being compressed *in vivo*, inserted into a custom 100-mm diameter, 30-mm thick high-density polyethylene phantom (Fig. 7.1d, e), and filled with water. In addition to the stents, the phantom held 6.3 mm and 5.5 mm diameter Eppendorf tubes filled with water.

7.3.3 Data Acquisition

Acquisition and reconstruction parameters for all systems can be found in Table 7.1. PCD-CT and HR PCD-CT were reconstructed from the same data set, with differing reconstruction parameters. For the PCD-CT acquisitions, the energy thresholds were set to 35, 52, 67, 81, 95, and 120 keV. This created energy bins with ranges between each threshold pair, with the addition of a bin summing counts from all other energy ranges, 35-120 keV.

7.3.4 Image Reconstruction

Clinical CT images were reconstructed using filtered back projection with the BONEPLUS kernel. PCD-CT images were reconstructed bin-wise using the Feldkamp-David-Kress algorithm [20] with a Shepp-Logan filter implemented in the TIGRE package for Python [128]. Once reconstructed, the PCD-CT images were normalized bin-wise to Hounsfield units (HU) utilizing Eq. 7.1:

$$HU = 1000 * (\frac{\mu - \mu_w}{\mu_w}) \tag{7.1}$$

in which μ is the attenuation values in the un-normalized image and μ_w is mean signal within the water-containing Eppendorf tubes within the un-normalized image. PCD-CT and HR PCD-CT were reconstructed from the same projection data set. PCD-CT images were reconstructed in order to mimic the reconstructed clinical CT images as closely as possible in terms of pixel size and slice thickness, while HR PCD-CT offered the standard in-house reconstruction parameters.

7.3.5 K-edge Image Reconstruction

K-edge subtraction images of tantalum were reconstructed using the K-edge decomposition algorithm (KDA) described by Zhang *et al* [60]. Briefly, Ta-specific sinograms were acquired according to the following equation:

$$D_K(\mathbf{r}) = \frac{\hat{\mu}_{bg,U} \cdot T_L - \hat{\mu}_{bg,L} \cdot T_U}{\hat{\mu}_{K,L} \cdot \hat{\mu}_{bg,U} - \hat{\mu}_{K,U} \cdot \hat{\mu}_{bg,L}} \tag{7.2}$$

where D_K refers to the material-specific sinogram, $\hat{\mu}_{bg}$ is average the mass attenuation coefficient of the background, $\hat{\mu}_K$ is the average mass attenuation coefficient of the K-edge material, T_L is the sinogram of the lower bin, and T_U is the sinogram of the upper bin. The subscripts U and L refer to the upper and lower bin, respectively. So $\hat{\mu}_{bg,L}$ would be the average mass attenuation coefficient of the background within the energy range of the lower

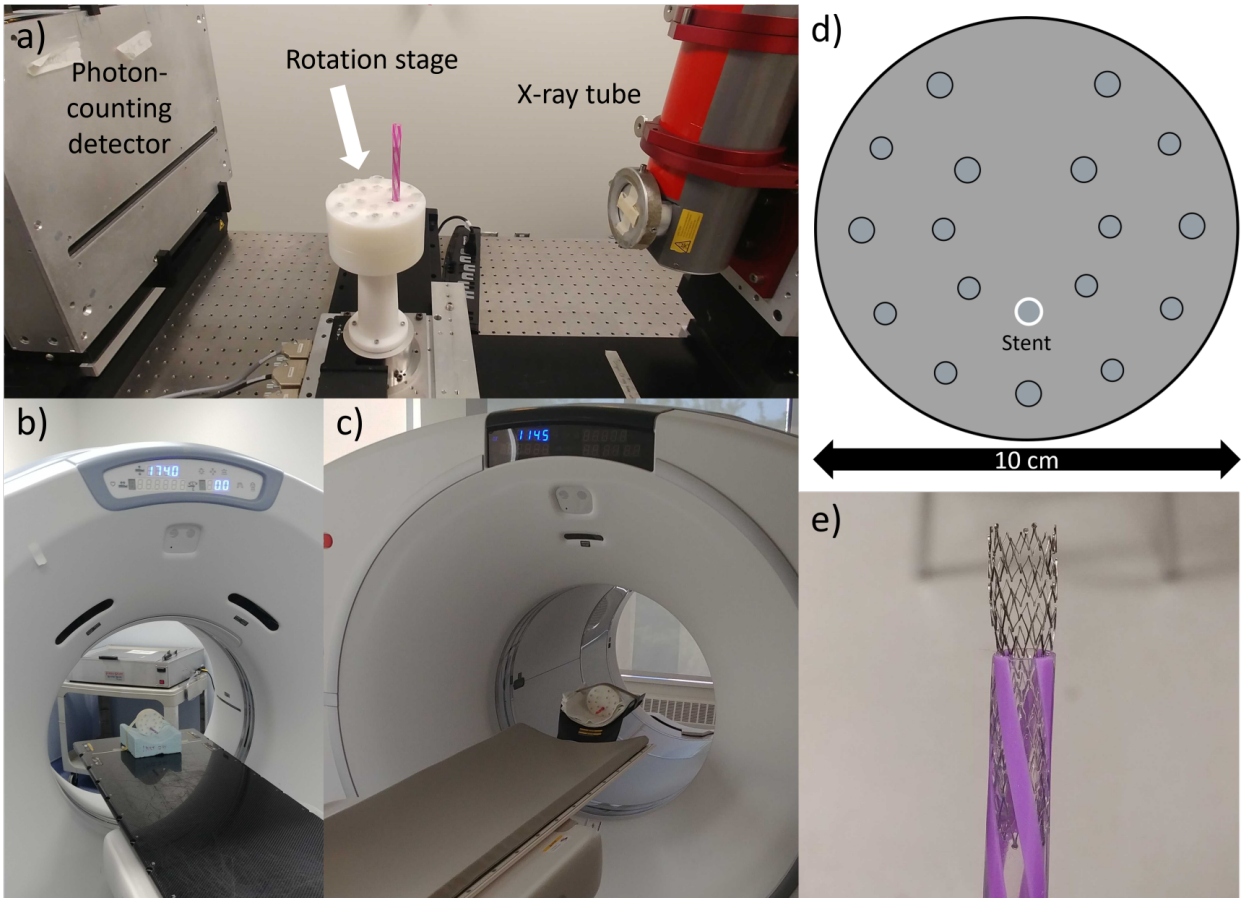

Figure 7.1: Setup images of the a) GE Optima 580, b) GE Discovery IQ, and c) the bench-top PCD-CT system. d) Phantom layout. e) Image the Cordis Precise stent inside the straw.

bin. To reconstruct the Ta-specific sinogram the 67-81 keV and the 81-97 keV ranges were used for the lower and upper bins, respectively. Once the Ta-specific sinogram was found, the K-edge images were reconstructed with the FDK algorithm and a Shepp-Logan filter.

7.3.6 Dose

CTDIvol (CT Dose Index) values were collected from the clinical CT scanners and measured on the PCD-CT system with the CTDI head phantom and 100-mm CTDI probe.

7.3.7 Conventional CT Image Analysis

CT images were analyzed in a number of ways. For both PCD-CT resolution image types, the 35-120 keV CT images were analyzed in order to provide the closest comparison to the clinical images. First, 3-dimensional (3D) volume renderings of the stents were created in

Table 7.1: CT image acquisition and reconstruction parameters.

Parameter	**GE Optima 580**	**GE Discovery IQ**	**PCD-CT**	**HR PCD-CT**
Collimation	16 × 0.625mm	16 × 0.625mm	24 × 0.184mm	24 × 0.184mm
Tube Voltage (kV)	120	120	120	120
Tube Current (mA)	180	180	1	1
Rotation Time (s)	1.0	1.0	180	180
Helical Pitch	0.5625	0.5626	0.5626	0.5626
Beam Filter	HEAD FILTER*	HEAD FILTER*	6 mm Al	6 mm Al
Focal Spot Size (mm)	0.7	0.7	∼0.4**	∼0.4**
Source to Detector Distance (mm)	1063	949	578	578
Source to Axis Distance (mm)	606	541	322	322
Reconstruction Filter/Kernel	BONEPLUS***	BONEPLUS***	Shepp-Logan	Shepp-Logan
Reconstructed FOV (cm)	15.3	12.7	10.5	10.5
Reconstructed Pixel size (mm)	0.299	0.248	0.248	0.205
Slice Thickness (mm)	0.625	0.625	0.625	0.208
MTF 10% (lp/mm)	1.16	1.16	1.29	1.33

*HEAD FILTER is the filtration used from head
scans in GE CT systems.
**The PCD-CT x-ray tube focal spot was measured using the EN 12543 convention, the approximate IEC 60336 size is shown.
***BONEPLUS is a GE proprietary reconstruction kernel.
PCD-CT = photon-counting detector CT
HR PCD-CT = high-resolution PCD-CT
MTF = modulation transfer function
FOV = field of view

3D Slicer and segmented using a lower threshold of 1750 HU. Second, the lumen attenuation was determined. A circular region-of-interest (ROI) between 3.5 and 3.7 mm in diameter was delineated within the stent and the mean and variance within the ROI was calculated for a minimum of seven slices. The lumen diameter and the strut thickness were evaluated by measuring their apparent values in the CT images. The center of the stent was first found using the Hough Gradient method [231], and fine-tuned manually. Line profiles were then interpolated from the center through individual struts and the full-width-half-maximum (FWHM) of the peak formed from the strut's signal was found. The lumen radius was calculated as the mean distance from the center of the stent to the closer FWHM point. The strut thickness was calculated as the FWHM of the peak itself. Finally, the modulation transfer function (MTF) was calculated in all image sets based on the method detailed by Takenaga *et al* [232]. Briefly, the center and radius of the 100 mm diameter phantom was found using the Hough method and fine-tuned manually. A normalized image was then calculated based on the equation:

$$I_N(i,j) = \frac{I(i,j) - \overline{I_{BG}}}{\overline{I_{phantom}} - \overline{I_{BG}}} \tag{7.3}$$

in which I_N is the normalized image, I is the original image, i and j are the row and column numbers for individual pixels, $\overline{I_{BG}}$ is the mean signal outside of the phantom, and $\overline{I_{phantom}}$ is the mean signal within the phantom. The signal of each pixel within 5 mm inside and outside of the edge of the phantom was plotted against its distance from the center of the circle, creating an over-sampled edge spread function (ESF). The over-sampled ESF was fitted using least-squares to the equation:

$$ESF(x) = \frac{a}{1 + exp[-b(x-c)]} + d \tag{7.4}$$

where x is the distance from the center of the circle. a, b, c, and d were initially set to 1, -1, $r_{phantom}$, and 0, respectively. $r_{phantom}$ is the radius of the phantom. The ESF was then differentiated to find the line spread function (LSF), and the Fast Fourier Transform applied to the LSF to find the MTF.

7.3.8 K-edge Image Analysis

The Ta marker size for the Cordis Precise and S.M.A.R.T. Control stents was compared between clinical system images, the two PCD-CT method images, and the two resulting K-edge images from both PCD-CT methods. The size of the markers was measured by drawing

a single profile through each Ta marker in the slice in which they appeared largest. The size of each marker was measured as the FWHM of the profile, in the same manner as the width of the individual struts in the conventional CT images. The diameter of the Ta markers were measured using calipers at ∼0.75 mm, though the tantalum is pressed into the nitinol disks that make up the marker structure, so that actual size of the tantalum itself will be somewhat smaller.

7.3.9 Statistical Analysis

Normality of the quantitative variables were assessed via the Shapiro-Wilk test. All data, excluding the Ta marker data, were found to be non-normal and thus displayed as the median and interquartile range (IQR). The Wilcoxon rank-sum test was used to compare the variables. Given the Ta marker data had limited data points, it was reported as the mean and minimum and maximum values.

7.4 Results

7.4.1 Qualitative Evaluation

Fig. 7.2 demonstrates representative CT slices from the GE Optima 580 (Fig. 7.2a, e, i), GE Discovery IQ (Fig. 7.2b, f, j), PCD-CT (Fig. 7.2c, g, k), and HR PCD-CT (Fig. 7.2d, h, l) for the Medtronic Protégé, Cordis Precise, and Cordis S.M.A.R.T Control stents, respectively. The CT images for both PCD-CT options were reconstructed using the 35-120 keV bin. The lumen of the stents appears larger in PCD-CT and HR PCD-CT images compared to both GE scanners, and the struts are easily delineated in PCD-CT, whereas they are not as easily separated in the GE CT images.

The 3D stent volume renderings created for all four image sets are shown in Fig. 7.3. The most accurate representation of the stents was produced by HR PCD-CT (Fig. 7.3d, h, l). Individual struts and the greater pattern of the stents were visible and easily recognizable. PCD-CT (Fig. 7.3c, g, k) offered less accurate representations, although individual struts could be distinguished and the pattern could still be recognized in some areas of the stents when comparing them to the HR PCD-CT renderings. Neither of the clinical scanners offered the same strut delineation or greater pattern recognizability (Fig. 7.3a–b, e–f, i–j) and appeared largely as solid cylinders with the occasional window into the interior lumen.

In addition to better visualization of the stent structure in PCD-CT compared to clinical CT, radiopaque markers can also be better defined through the use of the energy information

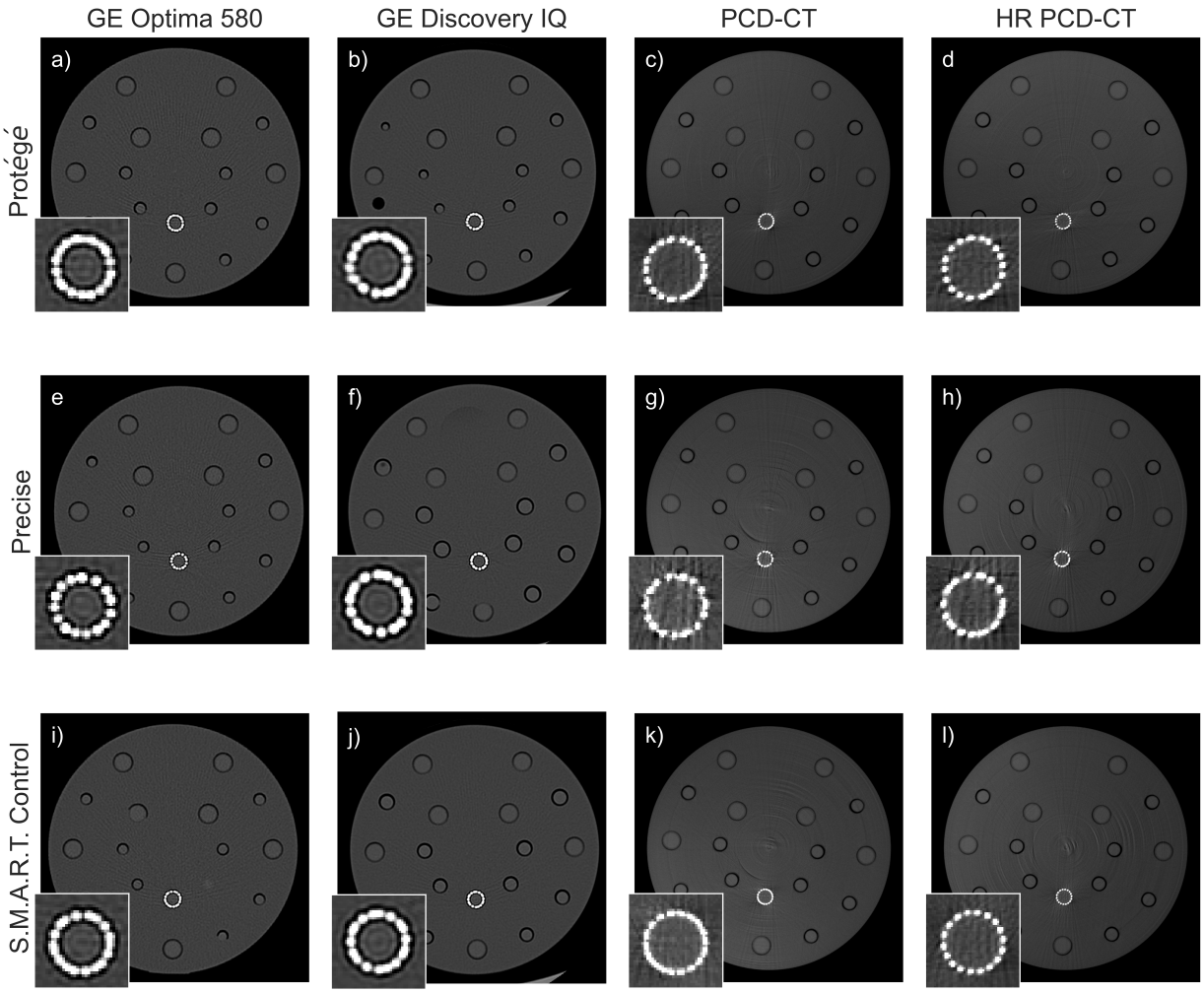

Figure 7.2: CT images of the plastic phantom with close-ups of the stents. Scans of a)–d) the Medtronic Protégé stent, e)–h) the Cordis Precise stent, and i)–l) the Cordis S.M.A.R.T. Control stent with each of the four imaging methods. W/L = [2100/450].

that is inherent to PCD-CT. Fig. 7.4 shows the radiopaque markers on the Cordis S.M.A.R.T Control stent in images from both the GE Discovery IQ (Fig. 7.4a) and PCD-CT (Fig. 7.4b). Metal and blooming artifacts can be seen in both, although they are more prevalent in the PCD-CT image than in the HR PCD-CT image. Using K-edge subtraction imaging, a Ta-specific image could be created (Fig. 7.4c), which mitigated many of the metal and blooming artifacts. The Ta-specific image could be viewed alone or as an overlay to the PCD-CT image (Fig. 7.4d) in order to better register the markers within the phantom.

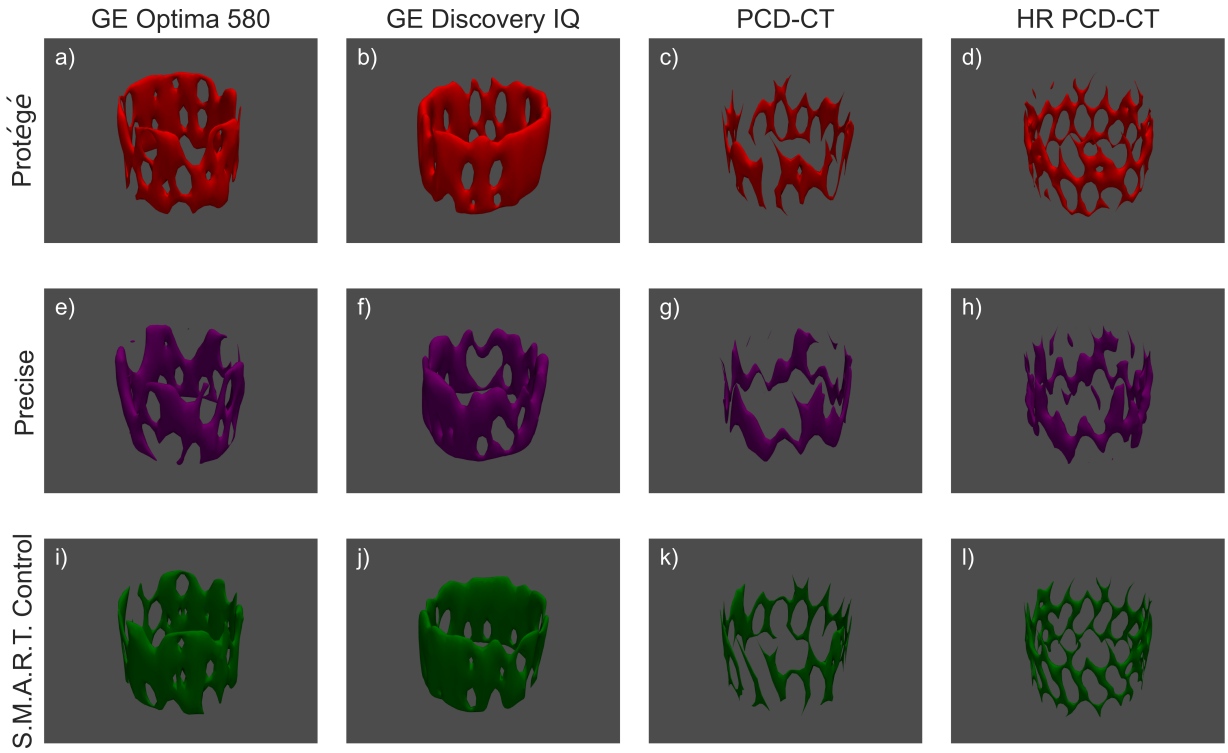

Figure 7.3: 3D volume renderings of all three stents. Volume renderings created from scans of a)–d) the Medtronic Protégé stent, e)–h) the Cordis Precise stent, and i)–l) the Cordis S.M.A.R.T. Control stent with each of the four imaging methods.

7.4.2 Quantitative Evaluation

Fig. 7.5 shows boxplots of the median and IQR for strut thickness and lumen diameter. For all three stents, PCD-CT and HR PCD-CT demonstrated strut thicknesses closer to the true thicknesses than either clinical scanner ($p < 0.001$) (Fig. 7.5a–c). PCD-CT and HR PCD-CT also demonstrated values closer to the true value for the lumen diameter than either clinical scanner for the Medtronic Protégé and Cordis Precise stents ($p < 0.01$). The lumen diameter results were not significantly different for the Cordis S.M.A.R.T. Control stent when comparing the clinical scanners to the PCD-CT system ($p > 0.01$).

Table 7.2 shows the absolute difference of lumen attenuation from water (0 HU). The median HU value fell closer to zero with PCD-CT and HR PCD-CT than the clinical scanners ($p < 0.01$). The only comparisons between HU data that were not significantly different were between the GE Optima 580 and PCD-CT for the Protégé and Precise stents ($p = 0.065$ and $p = 0.042$, respectively). However, the IQRs for all the stents were smaller with the clinical scanners than either PCD-CT method.

Table 7.2: Absolute difference of lumen attenuation.

	Medtronic Protégé (**median**; IQR)	**Cordis Precise** (**median**; IQR)	**Cordis S.M.A.R.T. Control** (**median**; IQR)
Optima 580	**-14 HU**; -61–41HU	**-10 HU**; -66–44 HU	**-5 HU**; -66–43 HU
Discovery IQ	**-15 HU**; -56–25 HU	**-23 HU**; -71–21 HU	**-22 HU**; -64–21 HU
PCD-CT	**-4 HU**; -63–64 HU	**-5 HU**; -86–88 HU	**4 HU**; -59–63 HU
HR PCD-CT	**2 HU**; -52–65 HU	**5 HU**; -82–104 HU	**12 HU**; -49–79 HU

Lumen attenuation is presented as the median absolute difference and IQR from 0 HU, the expected mean attenuation of water.

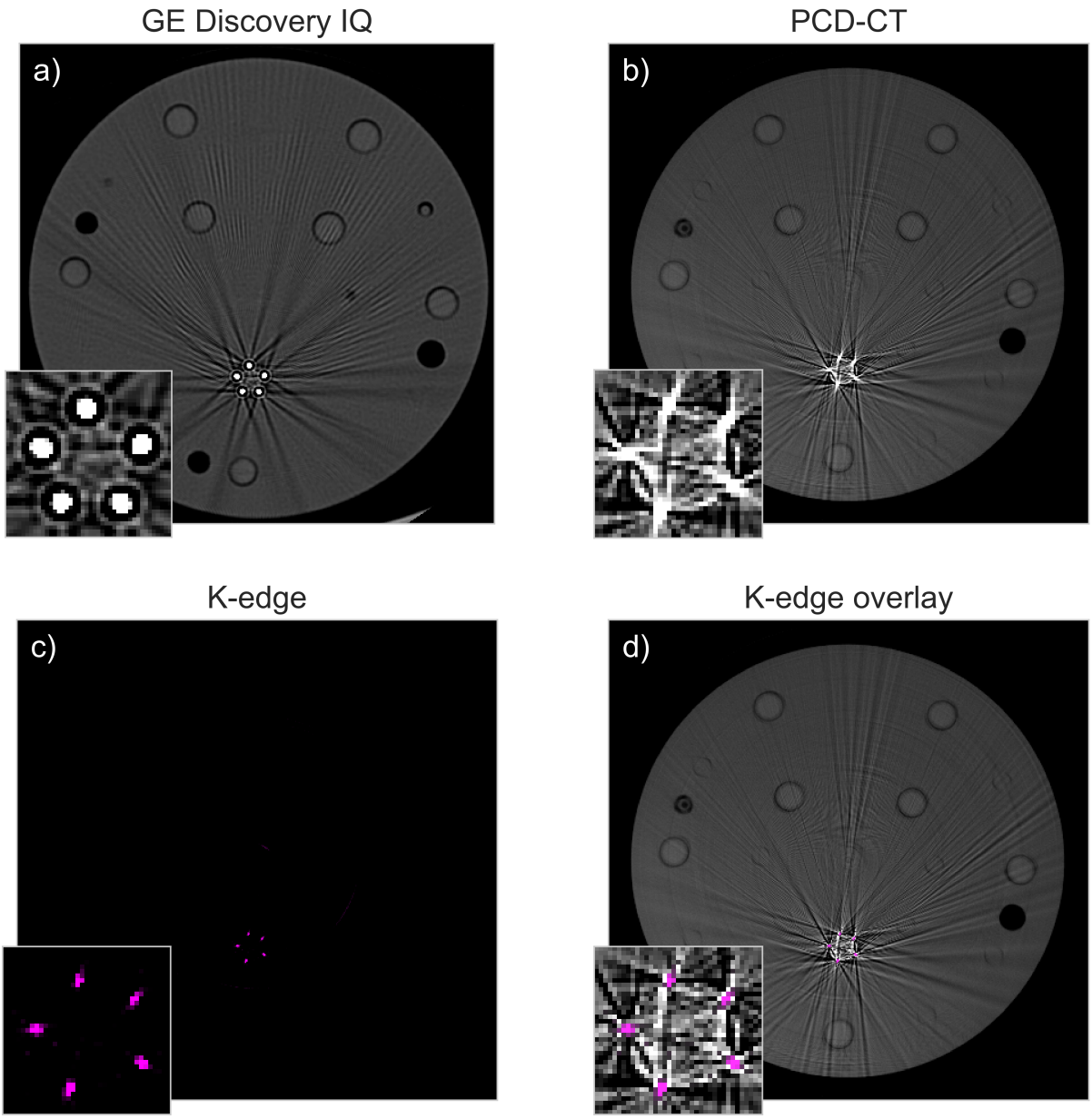

Figure 7.4: K-edge subtraction of radiopaque markers of the Cordis S.M.A.R.T. Control stent. CT image acquired with the a) GE Discovery IQ and b) PCD-CT. c) Ta K-edge decomposition image. d) PCD-CT image with the Ta K-edge image overlaid on top of it. W/L = [2100/450].

Fig. 7.6 shows the Ta marker size tangential to the edge of the circle made by the stent; perpendicular to the most prevalent metal artifacts in the PCD-CT image (Fig. 7.4b). Both the PCD-CT and HR PCD-CT demonstrate smaller diameters than the measured diameter of the nitinol and tantalum together, while the clinical systems show larger values. The K-

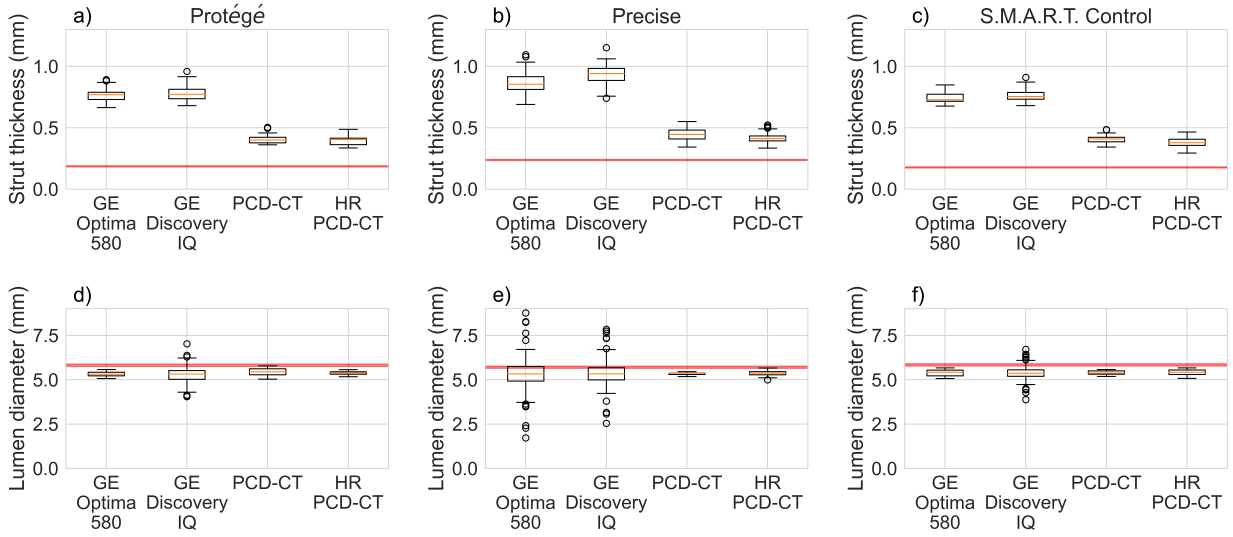

Figure 7.5: Measured stent dimensions. The shaded red bands across the entirety of each plot indicate the true dimensions. Orange lines within the boxes indicate median values, and the boxes indicate interquartile range. a)–c) The measured strut thickness for the a) Medtronic Protégé, b) Cordis Precise, and c) Cordis S.M.A.R.T Control stents with the four image sets. d)–f) The measured lumen diameter for the d) Medtronic Protégé, e) Cordis Precise, and f) Cordis S.M.A.R.T Control stents with the four image sets.

edge measurements are similar for the Precise stent, but smaller for the S.M.A.R.T. Control.

The 10% value of the MTF for each system can be seen in Table 7.1. The reported CTDI_{vol} values for the Optima 580 and the Discovery IQ were 28.60 mGy and 62.16 mGy, respectively. The measured CTDI_{vol} for the PCD-CT setup was 93.30 mGy.

7.5 Discussion

We evaluated the performance of our bench-top PCD-CT scanner with respect to two clinical EID-CT scanners for stent imaging. Quantitatively, we found that the apparent strut thickness was closest to the physical measurement using PCD-CT and HR PCD-CT for all stents. To our knowledge, we also demonstrated the smallest measured apparent strut thickness. The significant improvement in the measurement of the strut thickness with PCD-CT can be largely attributed to the higher inherent spatial resolution of PCDs compared with the EIDs on the clinical scanners. The PCD has a detector pixel pitch of 0.33 mm, which is likely smaller than the EID detectors, allowing for less partial volume effects in the projections. This allowed for reduced blooming artifacts in the reconstructions, even though the PCD-CT and clinical CT scans were reconstructed with nearly identical voxel sizes, which

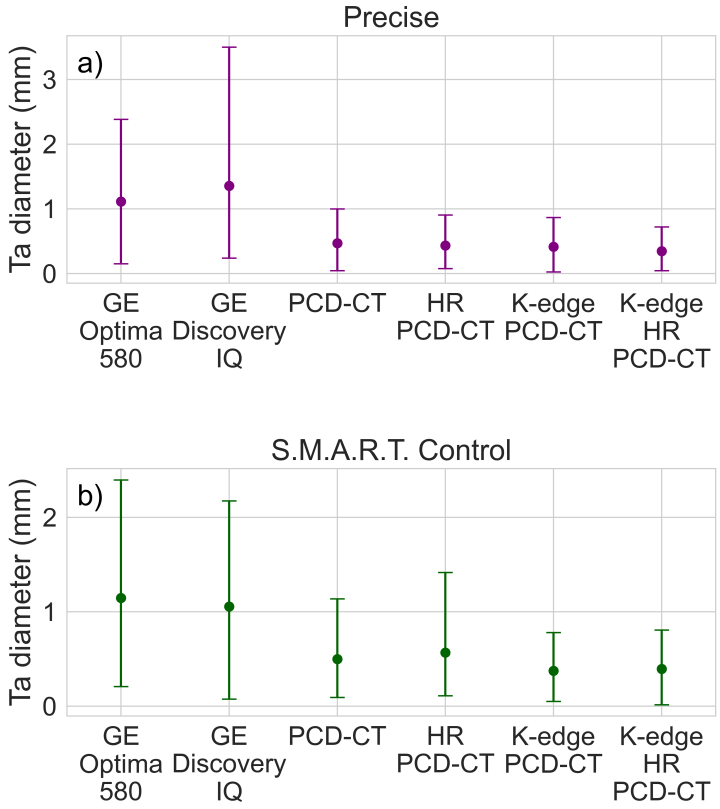

Figure 7.6: Measured tantalum marker diameter for a) the Cordis Precise stent and b) the Cordis S.M.A.R.T. Control stent.

should ensure fewer differences in terms of partial volume effects in the reconstructed images. With HR PCD-CT, which had a smaller voxel size compared to the other three image sets, there were even better results in terms of apparent strut thickness, demonstrating that partial volume effects do have some effect on the blooming artifacts. With smaller stents it would be crucial to reconstruct at a higher resolution. The two PCD-CT methods also benefited from a smaller focal spot size, which would cause less focal spot blurring, as well as smaller source to axis and source to detector distances, leading to less object magnification over multiple pixels.

For lumen diameter (Fig. 7.5d–f), there was little variation in the measurements, due in part to the large lumen diameter. The lumen edges were more visible in the PCD-CT and HR PCD-CT images, though this was likely due to the BONEPLUS kernel creating dark undershoots around the individual struts.

Median lumen attenuation (Table 7.2) was more accurate for PCD-CT and HR PCD-CT compared to the two clinical scanners, though again the differences were small. A more

accurate representation of what would be seen *in vivo* would be if there was contrast within the stent lumen. This would make the stent structures less visible as the attenuation would be higher within the lumen and could have some effect on the noise within the lumen. However, in this simpler case, we were also concerned with the accuracy of the signal to the expected value of 0 HU as well as the noise that was inherent to the stent. In respect to the noise, the IQR of the lumen attenuation is larger for both PCD-CT methods, indicating higher image noise within the lumen diameter. The higher noise can be attributed mostly to the high degree of non-conforming pixels whose signal deviations are not fully mitigated by flat-field corrections. We also notice that these pixels, especially those that create ring artifacts, can lead to additional metal artifact streaks between the metal and artificially high signal areas within the ring artifacts [25]. And we see residual metal artifact streaks within the PCD-CT images. For HR PCD-CT, the increase in noise over PCD-CT was also due to the smaller slice thickness, which resulted in reduced counts per voxel, and thus higher noise. The dose we saw with PCD-CT was also higher than either clinical scanner, in fact it was three times as high as the dose recorded by the Optima 580. This is due in large part to the source to axis distance differences between the scanners. If the dose was scaled accordingly, we would record $CTDI_{vol}$ values of 90.67 mGy and 175.47 mGy for the Optima 580 and Discovery IQ, respectively, which compare well to the 93.30 mGy for the PCD-CT system.

Qualitatively, the best results were seen with HR PCD-CT, which offered the best 3D volume rendering of the stents and subtly reduced blooming artifacts when compared to PCD-CT. However, both PCD-CT methods outperformed the EID-CT scanners, offering much better delineation of individual struts in CT images as well as better 3D volume rendering of the stents. In addition, PCD-CT offers the ability to visualize the radiopaque markers with K-edge subtraction imaging, allowing the marker location and shape to be more accurately determined (Fig. 7.4C, D). The measured Ta sizes showed the best results with the K-edge images, as they mitigated the majority of the metal artifacts seen in the conventional images (Fig. 7.4a, b). A large difference was seen between the sizes measured in the K-edge images compared to the clinical systems, while less of a difference was seen between the the K-edge and conventional PCD-CT images. The main reason for this being that the thickness of the Ta markers was measured along the short axis of the markers (Fig. 7.4c) in order to avoid the excessive metal artifacts which occurred along the longer axis in the conventional PCD-CT images (Fig. 7.4b). One benefit of Ta-specific images for clinical imaging would be the reduction of metal artifacts around the markers, leading to less obfuscation of the stent lumen.

There are a number of limitations to our study. First, neither clinical scanner would be utilized for coronary CT angiography as they would not supply the necessary resolution to image the small stents utilized in coronary arteries. However, the stents used in this study are carotid artery stents and were used mainly as a comparison to evaluate the performance of our prototype bench-top PCD-CT system. The clinical scanners also used the BONEPLUS kernel which had some dark undershoots are the stent struts, which affected the lumen visibility in images. Both clinical scanners had x-ray focal spots which were larger than the PCD-CT system's focal spot and had larger source to detector and source to axis distances. However, the PCD-CT system is not equipped with an anti-scatter grid, which would serve to limit the noise in reconstructed images and has a prototype detector, which is still being developed. With that said, the bench-top PCD-CT system outperformed the current, clinical EID scanners in terms measuring apparent strut thickness.

In regard to the future clinical possibilities with this PCD technology, the prospects are promising. The superior collimation and resolution of the PCD-CT methods is due almost exclusively to the detector itself. Unlike with an EID, PCDs require no septa between pixels in the detector; there is relatively little spread of the electrons produced in the PCD crystal when compared with the potential light spread in EIDs. The minimal spread of electrons is due to the high bias voltage applied and the fact that the anodes are pixelated. The collimation in the PCD-CT methods is due to the size of the individual rows of the detector and the geometry of the setup. Given that the detector specifications should remain the same when implemented in a clinical system, the collimation would be approximately 24×0.188 mm with a geometry comparable to the clinical systems studied here. Clinical results could even be further improved with the use of proprietary kernels and other, more sophisticated reconstruction methods.

7.6 Conclusion

PCD-CT offered better stent visualization than current clinical CT scanners including more accurate quantification of apparent strut thickness due to the increased spatial resolution offered by photon-counting detectors. Additionally, the energy information of PCDs could be used to visualize radiopaque markers without metal artifacts in tantalum-specific K-edge images.

Chapter 8

Conclusions

The development of PCD-CT is a significant advancement in the realm of medical imaging, building on traditional CT. PCD-CT offers improvements in spatial resolution and contrast-to-noise ratios, which is pivotal for more accurate disease diagnosis and efficient radiotherapy treatment planning. Despite these advancements, PCD-CT faces challenges in clinical adoption, including overcoming technical limitations such as charge-sharing and pulse pileup in PCDs. However, as PCD-CT is beginning to be integrated into clinical practice it offers the potential to significantly improve patient care.

This thesis presents an in-depth analysis of several applications for PCD-CT. This work represents the initial first step in the applications studied. Proof-of-concept was successfully demonstrated on a bench-top system for material decomposition, multi-contrast imaging, metal artifact reduction, and high resolution imaging. Through this work, the bench-top PCD-CT system demonstrates the usefulness of systems with flexibility to examine multiple potential aspects of PCD-CT efficiently and effectively. Further demonstrations of these applications on clinical systems are ongoing in the greater field.

Altogether, PCD-CT offers a significant step forward in CT imaging. While energy information can be obtained with DECT systems and ultra-high resolution EID-CT systems are available, PCD-CT marries the benefits of both into a single system. Even operating without energy information, PCD-CT will offer better image quality in terms of better contrast due to equal energy weighting of x-rays, better spatial resolution, and lower image noise, especially at low doses or x-ray fluxes, which is especially important for larger patients and pediatric patients. Utilizing the energy information opens up many other avenues in which PCD-CT can offer similar diagnostic information to other imaging modalities such as magnetic resonance imaging (MRI), which can help speed up patient diagnosis and treatment as extra scans can be reduced.

8.1 Summary

Chapters 1 introduced PCD-CT and its potential clinical implications. Chapter 2 explained the physics of matter and x-ray interactions and their subsequent downstream effects, x-ray generation for imaging, x-ray detectors, and the CT imaging process, image quality metrics, and image artifacts. Chapter 3 presented the principles of PCD-CT and offered a high-level overview of the bench-top PCD-CT system along with a high-level introduction into the four applications of PCD-CT that were explored in this thesis and a background of the applications in CT and PCD-CT.

Chapter 4 examined a DECT material decomposition method for extracting Z_{eff} and ρ_e and adapted it to use two energy bins with PCD-CT. The stoichiometric material decomposition model operates through calibration with a set of tissue equivalent materials with known Z_{eff} and ρ_e. Two models were optimized: one model using two energy bins for PCD-CT and the other model using two separate scans at two beam energies from DECT. Both models were optimized for parameters determining the degree of accuracy of the polynomial expansions and the PCD-CT model was also optimized for the energy ranges. An initial scan of the electron density inserts from an electron density calibration phantom with known Z_{eff} and ρ_e was acquired for both models in order to calibrate them, followed by a subsequent scan of the inserts for model evaluation. Additionally an *ex-vivo* tissue sample was scanned to evaluate the accuracy of the model in real tissue. K-edge imaging was also applied in order to separate a gold contrast agent from the tissue sample in PCD-CT.

Chapter 5 investigated imaging of multiple contrast agents in a single scan with PCD-CT and examined the effect system parameters such as filter type, energy bin width, and projection time had on the image quality and CNR. The study successfully demonstrated the ability of the PCCT system to differentiate and quantify these agents using K-edge subtraction. The ideal parameters varied between contrast agents and for best results in the clinic separate protocols should be developed based on the specific contrast agent.

Chapter 6 described a novel metal artifact reduction method, TRMAR. A phantom model was used in order to represent a ground truth scan without metal artifacts. TRMAR uses the metal trace information in the projection space to replace the metal-corrupted data in the full spectrum images with the high-energy metal traces in order to retain the image quality of the full spectrum image but with reduced metal artifacts. Images reconstructed using a high-energy bin with 100–110 keV x-rays were shown to reduce metal artifacts compared to full 120 kVp spectrum images, though with reduced contrast and higher noise.

Chapter 7 demonstrated the high-resolution abilities of PCD-CT by imaging three stents.

The stents were scanned with the bench-top PCD-CT system as well as two clinical GE CT scanners. Even in PCD-CT images with resolution comparable to the clinical systems, PCD-CT outperformed the clinical systems in reducing blooming artifacts and reconstructing a more accurate view of the stents. Our PCD-CT system at its highest resolution further outperformed the initial results.

8.2 Future Work

For multi-contrast imaging we demonstrated that gadolinium (K-edge energy = 50.2 keV) and dysprosium (K-edge energy = 53.8 keV) were distinguishable from one another using K-edge imaging, even given a K-edge separation of 3.6 keV. While impressive, dysprosium is not currently a clinically available contrast agent. Two clinical relevant CT contrast agents are iodine (K-edge energy = 33.2 keV), which is the most common CT contrast agent and barium (K-edge energy = 37.4 keV) in the form of barium sulphate [44]. Although the K-edge of iodine is considered to be outside or at the edge of the diagnostic energy range due to few x-rays with energies between ∼30 and ∼40 keV reaching the detector either due to beam filtration or attenuation within the patient. This would make the separation of the two contrast agents with K-edge subtraction impossible due to the lack of counts in the energy bins below the K-edge of barium (37.4 keV). And the dose necessary to get a sufficient number of counts below 33 keV would be prohibitive. However, we are planning on conducting a phantom study to investigate whether these contrast agents could be separated and demonstrate how much exposure would be necessary to obtain sufficient counts in the low energy bins to conduct K-edge subtraction imaging. Additionally, for our PCD, these bins are also at the high end of the energy range in which we see high pixel count noise and fluctuations, so gauging whether this is feasible with our system is also of technical interest.

Additionally, while the bench-top PCD-CT system is versatile it is lacking when it comes to the size of phantoms and subjects we can scan. At the moment, we would be able to do mouse studies, however, the z-coverage of flat panel detector (Fig. 2.15) is only 4.4 mm at isocenter, meaning there would be an extended scan time to get a full view of the entire mouse, even with helical scanning. However, the XCITE lab is currently installing a new radiotherapy system (the SITKA system, which has been developed by our lab) which will feature two robots which will be capable of non-coplanar kV radiotherapy and provide cone-beam imaging. We are in the early stages of considering making the flat panel detector removable so we could move between an EID and a PCD. We have a close relationship with Redlen Technologies, the manufacturer of our current PCD, and have co-written several

grants with them, so both parties are excited by this new opportunity. When we obtain a larger flat panel PCD for the SITKA system, we will be able to conduct superb comparison studies, as the system geometry and parameters will remain exactly the same between EID and PCD scans. Additionally, we will be treating veterinary patients with SITKA, so this could provide opportunities to compare EID and PCD radiotherapy treatment planning. Our adapted material decomposition method could be utilized to provide accurate tissue segmentation for such studies. The system would also be ideal for other imaging studies, such as metal artifact reduction, though prostheses are likely not as common in the veterinary clinic.

Finally, we are also receiving a new, small PCD from Redlen as part of a grant we received in which the ASIC hardware has been upgraded. Both Redlen and our lab are interested in studying whether image quality has improved with the new hardware and what effect it might have on charge-sharing and other shortcomings of PCDs. One area we hope to study is how the ASIC upgrade has affected non-conforming pixels in the low-energy range and how this might affect ring artifacts.

Bibliography

[1] Thomas Flohr, Martin Petersilka, Andre Henning, Stefan Ulzheimer, Jiri Ferda, and Bernhard Schmidt. Photon-counting CT review. *Phys. Med.*, 79(October):126–136, 11 2020.

[2] Scott S. Hsieh, Shuai Leng, Kishore Rajendran, Shengzhen Tao, and Cynthia H. McCollough. Photon Counting CT: Clinical Applications and Future Developments. *IEEE Transactions on Radiation and Plasma Medical Sciences*, 5(4):441–452, 7 2021.

[3] Kishore Rajendran, Martin Petersilka, André Henning, Elisabeth R. Shanblatt, Bernhard Schmidt, Thomas G. Flohr, Andrea Ferrero, Francis Baffour, Felix E. Diehn, Lifeng Yu, Prabhakar Rajiah, Joel G. Fletcher, Shuai Leng, and Cynthia H. McCollough. First Clinical Photon-counting Detector CT System: Technical Evaluation. *Radiology*, 303:130–138, 4 2022.

[4] Salim A. Si-Mohamed, Sara Boccalini, Marjorie Villien, Yoad Yagil, Klaus Erhard, Loic Boussel, and Philippe C Douek. First Experience With a Whole-Body Spectral Photon-Counting CT Clinical Prototype. *Investigative Radiology*, 58(7), Jul 2023.

[5] Avinash K. Nehra, Kishore Rajendran, Francis I. Baffour, Achille Mileto, Prabhakar Shantha Rajiah, Kelly K. Horst, Akitoshi Inoue, Tucker F. Johnson, Felix E. Diehn, Katrina N. Glazebrook, Jamison E. Thorne, Nikkole M. Weber, Elisabeth R. Shanblatt, Hao Gong, Lifeng Yu, Shuai Leng, Cynthia H. McCollough, and Joel G. Fletcher. Seeing More with Less: Clinical Benefits of Photon-counting Detector CT. *Radiographics : a review publication of the Radiological Society of North America, Inc*, 43(5):e220158, 5 2023.

[6] Kai Higashigaito, Victor Mergen, Matthias Eberhard, Lisa Jungblut, Monika Hebeisen, Susan Rätzer, Bettina Zanini, Adrian Kobe, Katharina Martini, André Euler, and Hatem Alkadhi. CT Angiography of the Aorta Using Photon-counting Detector CT

with Reduced Contrast Media Volume. *Radiology: Cardiothoracic Imaging*, 5(1), 2 2023.

[7] Xiaohui Zhan, Ruoqiao Zhang, Xiaofeng Niu, Ilmar Hein, Brent Budden, Shuoxing Wu, Nicolay Markov, Cameron Clarke, Yi Qiang, Hiroki Taguchi, Keiichi Nomura, Yoshihisa Muramatsu, Zhou Yu, Tatsushi Kobayashi, Richard Thompson, Hiroaki Miyazaki, and Hiroaki Nakai. Comprehensive evaluations of a prototype full field-of-view photon counting CT system through phantom studies. *Physics in Medicine & Biology*, 68(17):175007, 8 2023.

[8] Francis I. Baffour, Katrina N. Glazebrook, Andrea Ferrero, Shuai Leng, Cynthia H. McCollough, Joel G. Fletcher, and Kishore Rajendran. Photon-Counting Detector CT for Musculoskeletal Imaging: A Clinical Perspective. *American Journal of Roentgenology*, 220(4):551–561, 4 2023.

[9] Shuai Leng, Michael Bruesewitz, Shengzhen Tao, Kishore Rajendran, Ahmed F Halaweish, Norbert G Campeau, Joel G Fletcher, and Cynthia H McCollough. Photon-counting Detector CT: System Design and Clinical Applications of an Emerging Technology. *RadioGraphics*, 39(3):729–743, 5 2019.

[10] Judith van der Bie, Marcel van Straten, Ronald Booij, Daniel Bos, Marcel L. Dijkshoorn, Alexander Hirsch, Simran P. Sharma, Edwin H.G. Oei, and Ricardo P.J. Budde. Photon-counting CT: Review of initial clinical results. *European Journal of Radiology*, 163(April):110829, 2023.

[11] Martin J. Willemink, Mats Persson, Amir Pourmorteza, Norbert J. Pelc, and Dominik Fleischmann. Photon-counting CT: Technical principles and clinical prospects. *Radiology*, 289(2):293–312, Nov 2018.

[12] Harold Elford Johns and John Robert Cunningham. *Physics of Radiology*. Charles C Thomas, 4 edition, 1983.

[13] Lise Meitner. Über die β-Strahl-Spektra und ihren Zusammenhang mit der γ-Strahlung. *Zeitschrift für Physik*, 11(1):35–54, 1922.

[14] P Auger. Sur les rayons beta secondaries produits dans gaz par des rayons X. *C.R.A.S.*, 177:169–171, 1923.

[15] O. Klein and Y. Nishina. The scattering of light by free electrons according to Dirac's new relativistic dynamics [2]. *Nature*, 122(3072):398–399, 1928.

[16] Jerrold T Bushberg and John M Boone. *The Essential Physics of Medical Imaging*. Lippincott Williams & Wilkins, 2011.

[17] Yuko Nakamura, Toru Higaki, Shota Kondo, Ikuo Kawashita, Isao Takahashi, and Kazuo Awai. An introduction to photon-counting detector CT (PCD CT) for radiologists. *Japanese Journal of Radiology*, 41(3):266–282, 2023.

[18] J. O'Connell, S. Kundu, M. Saidaminov, and M. Bazalova-Carter. Next generation high resolution perovskite direct conversion detector: Monte Carlo design optimisation and virtual clinical trial. *Physics in Medicine and Biology*, 68(2), 2023.

[19] Johann Radon. On the determination of functions from their integral values along certain manifolds. *IEEE Transactions on Medical Imaging*, MI-5(4):170–176, 1986.

[20] Lee A Feldkamp, L C Davis, and James W Kress. Practical cone-beam algorithm. *J. Opt. Soc. Am. A.*, 1(6):612–619, Feb 1984.

[21] Katsuyuki Taguchi, Ira Blevis, and Krzysztof Iniewski. *Spectral, Phonton Counting Computed Tomography*. CRC Press, Boca Raton, FL, 1 edition, 2021.

[22] A. Rose and Lucien Biberman. Vision: Human and Electronic. *Physics Today*, 28(12):49, 1975.

[23] F. Edward Boas and Dominik Fleischmann. CT artifacts: Causes and reduction techniques. *Imaging in Medicine*, 4(2):229–240, 2012.

[24] W. P. Segars, G. Sturgeon, S. Mendonca, Jason Grimes, and B. M.W. Tsui. 4D XCAT phantom for multimodality imaging research. *Medical Physics*, 37(9):4902–4915, Sep 2010.

[25] Devon Richtsmeier, Jericho O'Connell, Pierre Antoine Rodesch, Kris Iniewski, and Magdalena Bazalova-Carter. Metal artifact correction in photon-counting detector computed tomography: metal trace replacement using high-energy data. *Medical Physics*, Sep 2022.

[26] Glenn F. Knoll. *Radiation Measurement and Detection*. Wiley, Hoboken, NJ, 4 edition, 2010.

[27] Jürgen Giersch, Daniel Niederlöhner, and Gisela Anton. The influence of energy weighting on X-ray imaging quality. *Nucl. Instrum. Methods Phys. Res. A.*, 531(1-2):68–74, 2004.

[28] Taly Gilat Schmidt. Optimal "image-based" weighting for energy-resolved CT. *Medical Physics*, 36(7):3018–3027, 2009.

[29] Taly Gilat Schmidt. CT energy weighting in the presence of scatter and limited energy resolution. *Medical Physics*, 37(3):1056–1067, Mar 2010.

[30] J. Nguyen, P. A. Rodesch, D. Richtsmeier, K. Iniewski, and M. Bazalova-Carter. Optimization of a CZT photon counting detector for contaminant detection. *Journal of Instrumentation*, 16(11), 2021.

[31] Pierre-Antoine Rodesch, Devon Richtsmeier, Elmaddin Guliyev, Kris Iniewski, and Magdalena Bazalova-Carter. Comparison of threshold energy calibrations of a photon-counting detector and impact on CT reconstruction. *IEEE Transactions on Radiation and Plasma Medical Sciences*, 7:263–272, 2023.

[32] P.-A. Rodesch, D. Richtsmeier, K. Iniewski, and M. Bazalova-Carter. Photon-counting detector spectral calibration enabling iodine quantification for spectral CT. In *2023 IEEE Nuclear Science Symposium, Medical Imaging Conference and International Symposium on Room-Temperature Semiconductor Detectors*, pages 1–2. Institute of Electrical and Electronics Engineers (IEEE), dec 2023.

[33] G. N. Hounsfield. Computerized transverse axial scanning (tomography): I. Description of system. *British Journal of Radiology*, 46:1016–1022, 1973.

[34] Robert E. Alvarez and Albert MacOvski. Energy-selective reconstructions in X-ray computerised tomography. *Physics in Medicine & Biology*, 21:733–744, 1976.

[35] R A Rutherford, B R Pullan, and I Isherwood. Measurement of effective atomic number and electron density using an EMI scanner. *Neuroradiology*, 11:15–21, 1976.

[36] E. Roessl and R. Proksa. K-edge imaging in x-ray computed tomography using multi-bin photon counting detectors. *Physics in Medicine & Biology*, 52:4679–4696, 8 2007.

[37] J. P. Schlomka, E. Roessl, R. Dorscheid, S. Dill, G. Martens, T. Istel, C. Bäumer, C. Herrmann, R. Steadman, G. Zeitler, A. Livne, and R. Proksa. Experimental feasibility of multi-energy photon-counting K-edge imaging in pre-clinical computed tomography. *Physics in Medicine & Biology*, 53:4031–4047, 2008.

[38] Cherry Kim, Wooil Kim, Sung Joon Park, Young Hen Lee, Sung Ho Hwang, Hwan Seok Yong, Yu Whan Oh, Eun Young Kang, and Ki Yeol Lee. Application of dual-energy

spectral computed tomography to thoracic oncology imaging. *Korean Journal of Radiology*, 21(7):838–850, 2020.

[39] Aaron D Sodickson, Abhishek Keraliya, Bryan Czakowski, Andrew Primak, Jeremy Wortman, and Jennifer W Uyeda. Dual energy CT in clinical routine: how it works and how it adds value. *Emergency Radiology*, 28(1):103–117, 2021.

[40] Giuseppe V Toia, Achille Mileto, Carolyn L Wang, and Dushyant V. Sahani. Quantitative dual-energy CT techniques in the abdomen. *Abdominal Radiology*, 47(9):3003–3018, 2022.

[41] Ana P Borges, Célia Antunes, and Luís Curvo-Semedo. Pros and Cons of Dual-Energy CT Systems: "One Does Not Fit All". *Tomography*, 9(1):195–216, 2023.

[42] Alexandra E. Bourque, Jean François Carrier, and Hugo Bouchard. A stoichiometric calibration method for dual energy computed tomography. *Physics in Medicine & Biology*, 59:2059–2088, 4 2014.

[43] Smithuis, Robin. CT contrast injection and protocols, 2014.

[44] Hrvoje Lusic and Mark W. Grinstaff. X-ray-computed tomography contrast agents. *Chemical Reviews*, 113(3):1641–1666, 2013.

[45] Priyanka Singh, Santosh Pandit, V.R.S.S. Mokkapati, Abhroop Garg, Vaishnavi Ravikumar, and Ivan Mijakovic. Gold Nanoparticles in Diagnostics and Therapeutics for Human Cancer. *International Journal of Molecular Sciences*, 19(7):1979, Jul 2018.

[46] Nikolai Khlebtsov and Lev Dykman. Biodistribution and toxicity of engineered gold nanoparticles: a review of in vitro and in vivo studies. *Chemical Society reviews*, 40(3):1647–1671, 2011.

[47] Kyle Bromma and Devika B. Chithrani. Advances in Gold Nanoparticle-Based Combined Cancer Therapy. *Nanomaterials*, 10(9):1671, 2020.

[48] A. K. Khan, R. Rashid, G. Murtaza, and A. Zahra. Gold nanoparticles: Synthesis and applications in drug delivery. *Tropical Journal of Pharmaceutical Research*, 13(7):1169–1177, 2014.

[49] Sarah D. Brown, Paola Nativo, Jo Ann Smith, David Stirling, Paul R. Edwards, Balaji Venugopal, David J. Flint, Jane A. Plumb, Duncan Graham, and Nial J. Wheate. Gold nanoparticles for the improved anticancer drug delivery of the active component of oxaliplatin. *Journal of the American Chemical Society*, 132(13):4678–4684, 2010.

[50] Feng Wang, Yu Cai Wang, Shuang Dou, Meng Hua Xiong, Tian Meng Sun, and Jun Wang. Doxorubicin-tethered responsive gold nanoparticles facilitate intracellular drug delivery for overcoming multidrug resistance in cancer cells. *ACS Nano*, 5(5):3679–3692, 2011.

[51] Simmyung Yook, Zhongli Cai, Yijie Lu, Mitchell A Winnik, Jean-Philippe Pignol, and Raymond M Reilly. Intratumorally Injected 177Lu-Labeled Gold Nanoparticles: Gold Nanoseed Brachytherapy with Application for Neoadjuvant Treatment of Locally Advanced Breast Cancer. *Journal of nuclear medicine : official publication, Society of Nuclear Medicine*, 57(6):936–42, Jun 2016.

[52] James F. Hainfeld, F. Avraham Dilmanian, Daniel N. Slatkin, and Henry M. Smilowitz. Radiotherapy enhancement with gold nanoparticles. *Journal of Pharmacy and Pharmacology*, 60(8):977–985, Aug 2008.

[53] Karl T. Butterworth, Stephen J. McMahon, Fred J. Currell, and Kevin M. Prise. Physical basis and biological mechanisms of gold nanoparticle radiosensitization. *Nanoscale*, 4(16):4830, Jul 2012.

[54] Matthew M. Mahan and Amber L. Doiron. Gold Nanoparticles as X-Ray, CT, and Multimodal Imaging Contrast Agents: Formulation, Targeting, and Methodology. *J. Nanomat.*, 2018:1–15, 3 2018.

[55] Oshra Betzer, Nisim Perets, Ariel Angel, Menachem Motiei, Tamar Sadan, Gal Yadid, Daniel Offen, and Rachela Popovtzer. In Vivo Neuroimaging of Exosomes Using Gold Nanoparticles. *ACS Nano*, 11(11):10883–10893, Nov 2017.

[56] Salim Si-Mohamed, David P. Cormode, Daniel Bar-Ness, Monica Sigovan, Pratap C. Naha, Jean-Baptiste Langlois, Lara Chalabreysse, Philippe Coulon, Ira Blevis, Ewald Roessl, Klaus Erhard, Loic Boussel, and Philippe Douek. Evaluation of spectral photon counting computed tomography K-edge imaging for determination of gold nanoparticle biodistribution in vivo. *Nanoscale*, 9(46):18246, 2017.

[57] David P. Cormode, Salim Si-Mohamed, Daniel Bar-Ness, Monica Sigovan, Pratap C. Naha, Joelle Balegamire, Franck Lavenne, Philippe Coulon, Ewald Roessl, Matthias Bartels, Michal Rokni, Ira Blevis, Loic Boussel, and Philippe Douek. Multicolor spectral photon-counting computed tomography: in vivo dual contrast imaging with a high count rate scanner. *Sci. Rep.*, 7:4784, 12 2017.

[58] Mahdieh Moghiseh, Chiara Lowe, John G. Lewis, Dhiraj Kumar, Anthony Butler, Nigel Anderson, Aamir Raja, and Alessandro Bombonati. Spectral Photon-Counting Molecular Imaging for Quantification of Monoclonal Antibody-Conjugated Gold Nanoparticles Targeted to Lymphoma and Breast Cancer: An in Vitro Study. *Contrast Media and Molecular Imaging*, 2018, 2018.

[59] A. Sarnelli, A. Taibi, A. Tuffanelli, G. Baldazzi, D. Bollini, A. E. Cabal Rodriquez, M. Gombia, F. Prino, L. Ramello, E. Tomassi, and M. Gambaccini. K-edge digital subtraction imaging based on a dichromatic and compact x-ray source. *Physics in Medicine and Biology*, 49(14):3291, 2004.

[60] Zhidu Zhang, Jinming Hu, Xiaomei Zhang, Qiong Xu, Mohan Li, Cunfeng Wei, Long Wei, and Zhe Wang. Experimental research of the energy bins for K-edge imaging using a photon counting detector: a phantom and mice study. *Radiation Detection Technology and Methods*, 4(3), 2020.

[61] Laura Schöckel, Gregor Jost, Peter Seidensticker, Philipp Lengsfeld, Petra Palkowitsch, and Hubertus Pietsch. Developments in X-Ray Contrast Media and the Potential Impact on Computed Tomography. *Investigative Radiology*, 55(9):592–597, 2020.

[62] Naim Aslan, Burhan Ceylan, Mümin Mehmet Koç, and Fehim Findik. Metallic nanoparticles as X-Ray computed tomography (CT) contrast agents: A review. *Journal of Molecular Structure*, 1219:128599, 2020.

[63] Rolf Symons, Bernhard Krauss, Pooyan Sahbaee, Tyler E. Cork, Manu N. Lakshmanan, David A. Bluemke, and Amir Pourmorteza. Photon-counting CT for simultaneous imaging of multiple contrast agents in the abdomen: An in vivo study. *Medical Physics*, 44(10):5120, 2017.

[64] Salim Si-Mohamed, Valérie Tatard-Leitman, Alexis Laugerette, Monica Sigovan, Daniela Pfeiffer, Ernst J Rummeny, Philippe Coulon, Yoad Yagil, Philippe Douek, Loic Boussel, and Peter B Noël. Spectral Photon-Counting Computed Tomography

(SPCCT): in-vivo single-acquisition multi-phase liver imaging with a dual contrast agent protocol. *Scientific Reports*, 9(1), 2019.

[65] Tianmeng Sun, Yu Shrike Zhang, Bo Pang, Dong Choon Hyun, Miaoxin Yang, and Younan Xia. Engineered Nanoparticles for Drug Delivery in Cancer Therapy. *Angewandte Chemie International Edition*, 53(46):12320–12364, Oct 2014.

[66] B. De Man, J. Nuyts, P. Dupont, G. Marchal, and P. Suetens. Metal streak artifacts in X-ray computed tomography: a simulation study. *IEEE Nuclear Science Symposium and Medical Imaging Conference*, 3:1860–1865, 1999.

[67] Lars Gjesteby, Bruno De Man, Yannan Jin, Harald Paganetti, Joost Verburg, Drosoula Giantsoudi, and Ge Wang. Metal Artifact Reduction in CT: Where Are We After Four Decades? *IEEE Access*, 4:5826–5849, 2016.

[68] Sathyathas Puvanasunthararajah, Davide Fontanarosa, Marie Luise Wille, and Saskia M Camps. The application of metal artifact reduction methods on computed tomography scans for radiotherapy applications: A literature review. *Journal of Applied Clinical Medical Physics*, 22(6):198–223, 2021.

[69] Adam S Wang and Norbert J Pelc. Spectral Photon Counting CT: Imaging Algorithms and Performance Assessment. *IEEE Transactions on Radiation and Plasma Medical Sciences*, 5(4):453–464, 7 2021.

[70] K. Rajendran, M. F. Walsh, N. J.A. De Ruiter, A. I. Chernoglazov, R. K. Panta, A. P.H. Butler, P. H. Butler, S. T. Bell, N. G. Anderson, T. B.F. Woodfield, S. J. Tredinnick, J. L. Healy, C. J. Bateman, R. Aamir, R. M.N. Doesburg, P. F. Renaud, S. P. Gieseg, D. J. Smithies, J. L. Mohr, V. B.H. Mandalika, A. M.T. Opie, N. J. Cook, J. P. Ronaldson, S. J. Nik, A. Atharifard, M. Clyne, P. J. Bones, C. Bartneck, R. Grasset, N. Schleich, and M. Billinghurst. Reducing beam hardening effects and metal artefacts in spectral CT using Medipix3RX. *Journal of Instrumentation*, 9(3):P03015, 3 2014.

[71] Wei Zhou, David J. Bartlett, Felix E. Diehn, Katrina N. Glazebrook, Amy L. Kotsenas, Rickey E. Carter, Joel G. Fletcher, Cynthia H. McCollough, and Shuai Leng. Reduction of Metal Artifacts and Improvement in Dose Efficiency Using Photon-Counting Detector Computed Tomography and Tin Filtration. *Investigative Radiology*, 54(4):204–211, 4 2019.

[72] Felix G. Meinel, Bernhard Bischoff, Qiaowei Zhang, Fabian Bamberg, Maximilian F. Reiser, and Thorsten R.C. Johnson. Metal artifact reduction by dual-energy computed tomography using energetic extrapolation: A systematically optimized protocol. *Investigative Radiology*, 47(7):406–414, Jul 2012.

[73] Kai Roman Laukamp, Simon Lennartz, Victor Frederic Neuhaus, Nils Große Hokamp, Robert Rau, Markus Le Blanc, Nuran Abdullayev, Anastasios Mpotsaris, David Maintz, and Jan Borggrefe. Correction to: CT metal artifacts in patients with total hip replacements: for artifact reduction monoenergetic reconstructions and post-processing algorithms are both efficient but not similar (European Radiology, (2018), 28, 11, (4524-4533), 10.1007/s00. *European Radiology*, 29(2):1062, 2019.

[74] Polad M. Shikhaliev. Soft tissue imaging with photon counting spectroscopic CT. *Physics in Medicine & Biology*, 60(6):2453, Mar 2015.

[75] Ann Christin Rößler, Willi Kalender, Daniel Kolditz, Christian Steiding, Veikko Ruth, Caroline Preuss, Sandra Christina Peter, Barbara Brehm, Matthias Hammon, Rüdiger Schulz-Wendtland, and Evelyn Wenkel. Performance of Photon-Counting Breast Computed Tomography, Digital Mammography, and Digital Breast Tomosynthesis in Evaluating Breast Specimens. *Academic Radiology*, 24(2):184–190, feb 2017.

[76] Felix K Kopp, Heiner Daerr, Salim Si-Mohamed, Andreas P Sauter, Sebastian Ehn, Alexander A Fingerle, Bernhard Brendel, Franz Pfeiffer, Ewald Roessl, Ernst J Rummeny, Daniela Pfeiffer, Roland Proksa, Philippe Douek, and Peter B Noël. Evaluation of a preclinical photon-counting CT prototype for pulmonary imaging. *Scientific Reports*, 8(1), 2018.

[77] Shuai Leng, Zhicong Yu, Ahmed Halaweish, Steffen Kappler, Katharina Hahn, Andre Henning, Zhoubo Li, John Lane, David L Levin, Steven Jorgensen, Erik Ritman, and Cynthia McCollough. Dose-efficient ultrahigh-resolution scan mode using a photon counting detector computed tomography system. *Journal of Medical Imaging*, 3(4):043504, 2016.

[78] Monica Sigovan, Salim Si-Mohamed, Daniel Bar-Ness, Julia Mitchell, Jean Baptiste Langlois, Philippe Coulon, Ewald Roessl, Ira Blevis, Michal Rokni, Gilles Rioufol, Philippe Douek, and Loic Boussel. Feasibility of improving vascular imaging in the presence of metallic stents using spectral photon counting CT and K-edge imaging. *Sci. Rep.*, 9(1):1–9, Dec 2019.

[79] Jochen Von Spiczak, Manoj Mannil, Benjamin Peters, Tilman Hickethier, Matthias Baer, André Henning, Bernhard Schmidt, Thomas Flohr, Robert Manka, David Maintz, and Hatem Alkadhi. Photon Counting Computed Tomography with Dedicated Sharp Convolution Kernels: Tapping the Potential of a New Technology for Stent Imaging. *Investigative Radiology*, 53(8):486–494, Aug 2018.

[80] Manoj Mannil, Tilman Hickethier, Jochen Von Spiczak, Matthias Baer, André Henning, Madeleine Hertel, Bernhard Schmidt, Thomas Flohr, David Maintz, and Hatem Alkadhi. Photon-Counting CT: High-Resolution Imaging of Coronary Stents. *Invest. Radiol.*, 53(3):143–149, Mar 2018.

[81] Rolf Symons, Yves De Bruecker, John Roosen, Laurent Van Camp, Tyler E. Cork, Steffen Kappler, Stefan Ulzheimer, Veit Sandfort, David A. Bluemke, and Amir Pourmorteza. Quarter-millimeter spectral coronary stent imaging with photon-counting CT: Initial experience. *Journal of Cardiovascular Computed Tomography*, 12(6):509–515, Oct 2018.

[82] Grischa Bratke, Tilman Hickethier, Daniel Bar-Ness, Alexander Christian Bunck, David Maintz, Gregor Pahn, Philippe Coulon, Salim Si-Mohamed, Philippe Douek, and Monica Sigovan. Spectral Photon-Counting Computed Tomography for Coronary Stent Imaging: Evaluation of the Potential Clinical Impact for the Delineation of In-Stent Restenosis. *Invest. Radiol.*, 55(2):61–67, Feb 2020.

[83] Rolf Symons, Veit Sandfort, Marissa Mallek, Stefan Ulzheimer, and Amir Pourmorteza. Coronary artery calcium scoring with photon-counting CT: first in vivo human experience. *International Journal of Cardiovascular Imaging*, 35(4):733–739, 2019.

[84] Matthias Eberhard, Victor Mergen, Kai Higashigaito, Thomas Allmendinger, Robert Manka, Thomas Flohr, Bernhard Schmidt, Andre Euler, and Hatem Alkadhi. Coronary calcium scoring with first generation dual-source photon-counting ct—first evidence from phantom and in-vivo scans. *Diagnostics*, 11(9):1708, 2021.

[85] Tilman Emrich, Gilberto Aquino, U. Joseph Schoepf, Franziska M. Braun, Franka Risch, Stefanie J. Bette, Piotr Woznicki, Josua A. Decker, Jim O'Doherty, Verena Brandt, Thomas Allmendinger, Tristan Nowak, Bernhard Schmidt, Thomas Flohr, Thomas J. Kroencke, Christian Scheurig-Muenkler, Akos Varga-Szemes, and Florian Schwarz. Coronary Computed Tomography Angiography-Based Calcium Scoring: In Vitro and in Vivo Validation of a Novel Virtual Noniodine Reconstruction Algorithm

on a Clinical, First-Generation Dual-Source Photon Counting-Detector System. *Investigative Radiology*, 57(8):536–543, aug 2022.

[86] Roy P. Marcus, Joel G. Fletcher, Andrea Ferrero, Shuai Leng, Ahmed F. Halaweish, Ralf Gutjahr, Terri J. Vrtiska, Mike L. Wells, Felicity T. Enders, and Cynthia H. McCollough. Detection and Characterization of Renal Stones by Using Photon-Counting–based CT. *https://doi.org/10.1148/radiol.2018180126*, 289(2):436–442, aug 2018.

[87] Moritz H. Albrecht, Thomas J. Vogl, Simon S. Martin, John W. Nance, Taylor M. Duguay, Julian L. Wichmann, Carlo N. de Cecco, Akos Varga-Szemes, Marly van Assen, Christian Tesche, and U. Joseph Schoepf. Review of clinical applications for virtual monoenergetic dual-energy CT. *Radiology*, 293:260–271, 9 2019.

[88] Wouter Van Elmpt, Guillaume Landry, Marco Das, and Frank Verhaegen. Dual energy CT in radiotherapy: Current applications and future outlook. *Radiotherapy and Oncology.*, 119:137–144, 4 2016.

[89] Hyun Woo Goo and Jin Mo Goo. Dual-energy CT: New horizon in medical imaging, 2017.

[90] Masami Torikoshi, Takanori Tsunoo, Makoto Sasaki, Masahiro Endo, Yutaka Noda, Yumiko Ohno, Toshiyuki Kohno, Kazuyuki Hyodo, Kentaro Uesugi, and Naoto Yagi. Electron density measurement with dual-energy x-ray CT using synchrotron radiation. *Physics in Medicine & Biology*, 48:673–685, 2003.

[91] T. Tsunoo, M. Torikoshi, Y. Ohno, M. Endo, M. Natsuhori, T. Kakizaki, N. Yamada, N. Ito, N. Yagi, and K. Uesugi. Measurement of electron density and effective atomic number using dual-energy x-ray CT. *IEEE Nuclear Science Symposium Conference Record*, 6:3764–3768, 2004.

[92] Magdalena Bazalova, Jean François Carrier, Luc Beaulieu, and Frank Verhaegen. Dual-energy CT-based material extraction for tissue segmentation in Monte Carlo dose calculations. *Physics in Medicine & Biology*, 53:2439–2456, 2008.

[93] Magdalena Bazalova, Jean François Carrier, Luc Beaulieu, and Frank Verhaegen. Tissue segmentation in Monte Carlo treatment planning: A simulation study using dual-energy CT images. *Radiotherapy and Oncology*, 86:93–98, 1 2008.

[94] Masatoshi Saito. Potential of dual-energy subtraction for converting CT numbers to electron density based on a single linear relationship. *Medical Physics*, 39:2021–2030, 2012.

[95] Masayoshi Tsukihara, Yoshiyuki Noto, Takahide Hayakawa, and Masatoshi Saito. Conversion of the energy-subtracted CT number to electron density based on a single linear relationship: An experimental verification using a clinical dual-source CT scanner. *Physics in Medicine & Biology*, 58:135–144, 2013.

[96] Guillaume Landry, Joao Seco, Mathieu Gaudreault, and Frank Verhaegen. Deriving effective atomic numbers from DECT based on a parameterization of the ratio of high and low linear attenuation coefficients. *Physics in Medicine & Biology*, 58:6851–6866, 2013.

[97] Guillaume Landry, Brigitte Reniers, Lars Murrer, Ludy Lutgens, Esther Bloemen-Van Gurp, Jean Philippe Pignol, Brian Keller, Luc Beaulieu, and Frank Verhaegen. Sensitivity of low energy brachytherapy Monte Carlo dose calculations to uncertainties in human tissue composition. *Medical Physics*, 37:5188–5198, 2010.

[98] Guillaume Landry, Patrick V Granton, Brigitte Reniers, Michel C. Öllers, Luc Beaulieu, Joachim E Wildberger, and Frank Verhaegen. Simulation study on potential accuracy gains from dual energy CT tissue segmentation for low-energy brachytherapy Monte Carlo dose calculations. *Physics in Medicine & Biology*, 56:6257–6278, 2011.

[99] S. Mashouf, E. Lechtman, P. Lai, B. M. Keller, A. Karotki, D. J. Beachey, and J. P. Pignol. Dose heterogeneity correction for low-energy brachytherapy sources using dual-energy CT images. *Physics in Medicine & Biology*, 59:5305–5316, 2014.

[100] Nora Hünemohr, Bernhard Krauss, Julien Dinkel, Clarissa Gillmann, Benjamin Ackermann, Oliver Jäkel, and Steffen Greilich. Ion range estimation by using dual energy computed tomography. *Zeitschrift fur Medizinische Physik*, 23:300–313, 12 2013.

[101] Nora Hünemohr, Bernhard Krauss, Christoph Tremmel, Benjamin Ackermann, Oliver Jäkel, and Steffen Greilich. Experimental verification of ion stopping power prediction from dual energy CT data in tissue surrogates. *Physics in Medicine & Biology*, 59:83–96, 12 2014a.

[102] Nora Hünemohr, Harald Paganetti, Steffen Greilich, Oliver Jäkel, and Joao Seco. Tissue decomposition from dual energy CT data for MC based dose calculation in particle therapy. *Medical Physics*, 41:061714, 2014b.

[103] Masatoshi Saito and Shota Sagara. A simple formulation for deriving effective atomic numbers via electron density calibration from dual-energy CT data in the human body. *Medical Physics*, 44:2293–2303, 6 2017.

[104] P. Fischer and A. Helmich. A photon counting pixel chip with energy windowing. *IEEE Transactions on Nuclear Science*, 47:881–884, 2000.

[105] M. Lindner, L. Blanquart, P. Fischer, H. Krüger, and N. Wermes. Medical X-ray imaging with energy windowing. *Nuclear Instruments and Methods in Physics Research, Section A: Accelerators, Spectrometers, Detectors and Associated Equipment*, 465(1):229, 2001.

[106] Jan S Iwanczyk, Einar Nygård, Oded Meirav, Jerry Arenson, William C Barber, Neal E Hartsough, Nail Malakhov, Jan C Wessel, Einar Nygård, Nail Malakhov, Neal E Hartsough, and Jan C Wessel. Photon-Counting Energy-Dispersive Detector Arrays for X-Ray Imaging. *IEEE Transactions on Nuclear Science*, 56:59–96, 2009.

[107] Joakim da Silva, Fredrik Grönberg, Björn Cederström, Mats Persson, Martin Sjölin, Zlatan Alagic, Robert Bujila, and Mats Danielsson. Resolution characterization of a silicon-based, photon-counting computed tomography prototype capable of patient scanning. *Journal of Medical Imaging*, 6(04):1, 10 2019.

[108] Katsuyuki Taguchi. Energy-sensitive photon counting detector-based x-ray computed tomography. *Radiological Physics and Technology*, 10(1):8–22, 3 2017.

[109] Xinhui Duan, Jia Wang, Shuai Leng, Bernhard Schmidt, Thomas Allmendinger, Katharine Grant, Thomas Flohr, and Cynthia H. McCollough. Electronic noise in CT detectors: Impact on image noise and artifacts. *Am. J. Roentgenol.*, 201(4):626–632, 2013.

[110] Ralf Gutjahr, Ahmed F Halaweish, Zhicong Yu, Shuai Leng, Lifeng Yu, Zhoubo Li, Steven M Jorgensen, Erik L Ritman, Steffen Kappler, and Cynthia H. McCollough. Human imaging with photon counting-based computed tomography at clinical dose levels: Contrast-to-noise ratio and cadaver studies. *Investig. Radiol.*, 51(7):421–429, 2016.

[111] Jayasai R. Rajagopal, Faraz Farhadi, Justin Solomon, Pooyan Sahbaee, Babak Saboury, William F. Pritchard, Elizabeth C. Jones, and Ehsan Samei. Comparison of Low Dose Performance of Photon-Counting and Energy Integrating CT. *Acad. Radiol.*, 28(12):1754–1760, 2021.

[112] Polad M. Shikhaliev. Projection x-ray imaging with photon energy weighting: Experimental evaluation with a prototype detector. *Physics in Medicine & Biology*, 54(16):4971–4992, Jul 2009b.

[113] Kris Iniewski, Henry Chen, Glenn Bindley, Irfan Kuvvetli, and Carl Budtz-Jørgensen. Modeling charge-sharing effects in pixellated CZT detectors. *IEEE Nuclear Science Symposium Conference Record*, 6:4608–4611, 2007.

[114] Katsuyuki Taguchi, Christoph Polster, W. Paul Segars, Nafi Aygun, and Karl Stierstorfer. Model-based pulse pileup and charge sharing compensation for photon counting detectors: A simulation study. *Medical Physics*, 49(8):5038–5051, 2022.

[115] Kris Iniewski, Conny Hansson, Elmaddin Guliyev, Georgios Prekas, and Michael Ayukawa. Performance Characteristics of 250+ Mcps/mm^2 CZT Detector Module for Spectral Computed Tomography. In *5th Workshop on Medical Applications of Spectroscopic X-ray Detectors, CERN, Geneva.*, 2019a.

[116] Katsuyuki Taguchi and Scott S. Hsieh. Charge sharing correction for photon counting detectors with coincidence counters. In *Medical Imaging 2023: Physics of Medical Imaging*, volume 12463, page 124630F. SPIE, Apr 2023.

[117] Chelsea A. S. Dunning, Jericho O'Connell, Spencer M. Robinson, Kevin J. Murphy, Adriaan L. Frencken, Frank C. J. M. van Veggel, Kris Iniewski, and Magdalena Bazalova-Carter. Photon-counting computed tomography of lanthanide contrast agents with a high-flux 330-μm-pitch cadmium zinc telluride detector in a table-top system. *Journal of Medical Imaging*, 7(03):1, Jun 2020.

[118] Devon Richtsmeier, Chelsea A.S. S. Dunning, Kris Iniewski, and Magdalena Bazalova-Carter. Multi-contrast K-edge imaging on a bench-top photon-counting CT system: acquisition parameter study. *Journal of Instrumentation*, 15(10), Oct 2020.

[119] F. A. Dilmanian, X. Y. Wu, E. C. Parsons, B. Ren, J. Kress, T. M. Button, L. D. Chapman, J. A. Coderre, F. Giron, D. Greenberg, D. J. Krus, Z. Liang, S. Marcovici,

M. J. Petersen, C. T. Roque, M. Shleifer, D. N. Slatkin, W. C. Thomlinson, K. Yamamoto, and Z. Zhong. Single- and dual-energy CT with monochromatic synchrotron x-rays. *Physics in Medicine and Biology*, 42(2):371–387, 1997.

[120] Z. Zhong, D. Chapman, R. Menk, J. Richardson, S. Theophanis, and W. Thomlinson. Monochromatic energy-subtraction radiography using a rotating anode source and a bent Laue monochromator. *Physics in Medicine & Biology*, 42(9):1751–1762, 1997.

[121] H. Elleaume, A. M. Charvet, S. Corde, F. Estève, and J. F. Le Bas. Performance of computed tomography for contrast agent concentration measurements with monochromatic x-ray beams: Comparison of K-edge versus temporal subtraction. *Physics in Medicine and Biology*, 47(18):3369–3385, 2002.

[122] Megan C Jacobsen, Sara L Thrower, Rachel B Ger, Shuai Leng, Laurence E Court, Kristy K Brock, Eric P Tamm, Erik N.K. Cressman, Dianna D Cody, and Rick R Layman. Multi-energy computed tomography and material quantification: Current barriers and opportunities for advancement. *Medical Physics*, 47(8):3752–3771, 2020.

[123] Matthijs Ferdinand Kruis. Improving radiation physics, tumor visualisation, and treatment quantification in radiotherapy with spectral or dual-energy CT. *J. Appl. Clin. Med. Phys.*, 23(1):23, 2022.

[124] Yahya Alivov, Pavlo Baturin, Huy Q. Le, Justin Ducote, and Sabee Molloi. Optimization of K-edge imaging for vulnerable plaques using gold nanoparticles and energy resolved photon counting detectors: A simulation study. *Physics in Medicine & Biology*, 59:135–152, 2014.

[125] Kris Iniewski, Matthew C Veale, and Magdalena Bazalova-Carter. High-flux CZT for new Frontiers in computed tomography (CT), non-destructive testing (NDT) and high-energy physics. In *IEEE Nuclear Science Symposium and Medical Imaging Conference*, 2019b.

[126] K. Iniewski. CZT sensors for Computed Tomography: From crystal growth to image quality. *Journal of Instrumentation*, 11, Dec 2016.

[127] Gavin Poludniowski, Artur Omar, Robert Bujila, and Pedro Andreo. Technical Note: SpekPy v2.0—a software toolkit for modeling x-ray tube spectra. *Medical Physics*, 48(7):3630–3637, 2021.

[128] Ander Biguri, Manjit Dosanjh, Steven Hancock, and Manuchehr Soleimani. TIGRE: A MATLAB-GPU toolbox for CBCT image reconstruction. *Biomedical Physics and Engineering Express*, 2:055010, 9 2016.

[129] Uwe Schneider, Eros Pedroni, and Antony Lomax. The calibration of CT Hounsfield units for radiotherapy treatment planning. *Physics in Medicine & Biology*, 41(1):111–124, Jan 1996.

[130] Daphne F. Jackson and D. J. Hawkes. X-ray attenuation coefficients of elements and mixtures. *Physics Reports*, 70:169–233, 1981.

[131] W.V. Mayneord. The significance of the roentgen. *Acta Int Union Against Cancer*, 2:271, 1937.

[132] F. W. Spiers. Effective Atomic Number and Energy Absorption in Tissues. *British Journal of Radiology*, 19(218):52–63, Feb 1946.

[133] D R White. An analysis of the Z-dependence of photon and electron interactions. *Phys. Med. Biol.*, 22(2):219–228, 1977.

[134] M J Berger, J H Hubbell, S M Seltzer, J Chang, J S Coursey, R Sukumar, and D S Zucker. XCOM: photon cross sections database. *NIST Standard Reference Database*, 8:87–3597, 1998.

[135] Brendan J. Kirby, J. R. Davis, J. A. Grand, and Michael J. Morgan. Extracting material parameters from x-ray attenuation: A CT feasibility study using kilovoltage synchrotron x-rays incident upon low atomic number absorbers. *Physics in Medicine & Biology*, 48(20):3389–3409, 2003.

[136] Steward M Midgley. A parameterization scheme for the x-ray linear attenuation coefficient and energy absorption coefficient. *Physics in Medicine & Biology*, 49(2):307–325, 2004.

[137] Thorsten R C Johnson. *Dual energy CT in clinical practice*. Springer, Heidelberg, 1st edition, 2011.

[138] Akash Mehta, Daniel Arrington, Prabhakar Ramachandran, Ryan Motley, Venkatakrishnan Seshadri, Darcie Anderson, Margot Lehman, and Ben Perrett. Investigation of computed tomography numbers on multiple imaging systems using single and multi-slice methods. *J. Med. Phys.*, 48(1):26, 2023.

[139] Takayuki Higuchi and Akihiro Haga. X-ray energy spectrum estimation based on a virtual computed tomography system. *Biomedical Physics and Engineering Express*, 9(2):025002, 1 2023.

[140] N. Clements, D. Richtsmeier, A. Hart, and M. Bazalova-Carter. Multi-contrast CT imaging using a high energy resolution CdTe detector and a CZT photon-counting detector. *Journal of Instrumentation*, 17(1):P01004, Jan 2022.

[141] W S Snyder, M Cook, E Nasset, L Karhausen, and I Tipton. Report of the task group on reference man. *Report Prepared for International Commission on Radiological Protection*, pages 46–57, 1975.

[142] Fuminari Tatsugami, Toru Higaki, Yuko Nakamura, Yukiko Honda, and Kazuo Awai. Dual-energy CT: minimal essentials for radiologists. *Japanese Journal of Radiology*, 40(6):547–559, 2022.

[143] Robin Wrazidlo, Lukas Walder, Arne Estler, Ralf Gutjahr, Bernhard Schmidt, Sebastian Faby, Jan Fritz, Konstantin Nikolaou, Marius Horger, and Florian Hagen. Radiation Dose Reduction in Contrast-Enhanced Abdominal CT: Comparison of Photon-Counting Detector CT with 2nd Generation Dual-Source Dual-Energy CT in an oncologic cohort. *Academic Radiology*, 30(5):855–862, 2023.

[144] Moritz T. Winkelmann, Florian Hagen, Lucie Le-Yannou, Jakob Weiss, Philipp Riffel, Ralf Gutjahr, Sebastian Faby, Konstantin Nikolaou, and Marius Horger. Myeloma bone disease imaging on a 1st-generation clinical photon-counting detector CT vs. 2nd-generation dual-source dual-energy CT. *European Radiology*, 33(4):2415–2425, 2023.

[145] Ronald Booij, Niels R. van der Werf, Marcel L. Dijkshoorn, Aad van der Lugt, and Marcel van Straten. Assessment of Iodine Contrast-To-Noise Ratio in Virtual Monoenergetic Images Reconstructed from Dual-Source Energy-Integrating CT and Photon-Counting CT Data. *Diagnostics*, 12(6), 2022.

[146] Leening P. Liu, Nadav Shapira, Andrew A. Chen, Russell T. Shinohara, Pooyan Sahbaee, Mitchell Schnall, Harold I. Litt, and Peter B. Noël. First-generation clinical dual-source photon-counting CT: ultra-low-dose quantitative spectral imaging. *Eur. Radiol.*, 32(12):8579–8587, 2022.

[147] Mats Danielsson, Mats Persson, and Martin Sjölin. Photon-counting x-ray detectors for CT. *Physics in Medicine & Biology*, 66(3):3–4, 2021.

[148] Guillaume Landry, Fabian Dörringer, Salim Si-Mohamed, Philippe Douek, Juan F.P.J. Abascal, Françoise Peyrin, Isabel P Almeida, Frank Verhaegen, Ilaria Rinaldi, Katia Parodi, and Simon Rit. Technical Note: Relative proton stopping power estimation from virtual monoenergetic images reconstructed from dual-layer computed tomography. *Medical Physics*, 46:1821–1828, 2019.

[149] Friderike K. Faller, Stewart Mein, Benjamin Ackermann, Jürgen Debus, Wolfram Stiller, and Andrea Mairani. Pre-clinical evaluation of dual-layer spectral computed tomography-based stopping power prediction for particle therapy planning at the Heidelberg Ion Beam Therapy Center. *Physics in Medicine and Biology*, 65(9):0–14, 2020.

[150] Jesse Tanguay, Jinwoo Kim, Ho Kyung Kim, Kris Iniewski, and Ian A. Cunningham. Frequency-dependent signal and noise in spectroscopic x-ray imaging. *Medical Physics*, 47(7):2881–2901, 2020.

[151] Scott S. Hsieh. Coincidence Counters for Charge Sharing Compensation in Spectroscopic Photon Counting Detectors. *IEEE Trans. Med. Imaging*, 39(3):678–687, 2020.

[152] Cale E Lewis and Mini Das. Energy-sensitive scatter estimation and correction for spectral x-ray imaging with photon-counting detectors. *Journal of Instrumentation*, 17(12):P12004, 12 2022.

[153] Katsuyuki Taguchi. Multi-energy inter-pixel coincidence counters for charge sharing correction and compensation in photon counting detectors. *Medical Physics*, 47(5):2085–2098, 2020.

[154] A. M. Cormack. Representation of a function by its line integrals, with some radiological applications. *Journal of Applied Physics*, 34(9):2722, 1963.

[155] A. M. Cormack. Representation of a function by its line integrals, with some radiological applications. II. *Journal of Applied Physics*, 35(10):2908, 1964.

[156] S. C. Garcea, Y. Wang, and P. J. Withers. X-ray computed tomography of polymer composites. *Composites Science and Technology*, 156:305, 2018.

[157] Michael J. Paulus, Shaun S. Gleason, Stephen J. Kennel, Patricia R. Hunsicker, and Dabney K. Johnson. High resolution X-ray computed tomography: An emerging tool for small animal cancer research. *Neoplasia*, 2(1-2):62, 2000.

[158] Fernanda Mara Aragão Macedo Pereira, Stela Bonadia de Souza Bete, Letícia Rocha Inamassu, Maria Jaqueline Mamprim, and Bruno Cesar Schimming. Anatomy of the skull in the capybara (Hydrochoerus hydrochaeris) using radiography and 3D computed tomography. *Journal of Veterinary Medicine Series C: Anatomia Histologia Embryologia*, 49(3):317, 2020.

[159] Koen Nieman, Matthijs Oudkerk, Benno J. Rensing, Peter Van Ooijen, Arie Munne, Robert Jan Van Geuns, and Pim J. De Feyter. Coronary angiography with multi-slice computed tomography. *Lancet*, 357(9256):599, 2001.

[160] Godfrey N. Hounsfield. Computed medical imaging. *Medical Physics*, 7(4):283, 1980.

[161] Daniel Y. Chong, Erin Angel, Hyun J. Kim, Graham B. Cole, Lousine Boyadzhyan, Christoph Panknin, Ana M. Gomez, Jonathan G. Goldin, Matthew S. Brown, and Michael F. McNitt-Gray. Separation of bone from iodine- and gadolinium-based contrast agents using dual energy CT. In Jiang Hsieh and Ehsan Samei, editors, *Medical Imaging 2008: Physics of Medical Imaging*, volume 6913, page 69134Q, 2008.

[162] Anno Graser, Thorsten R.C. Johnson, Hersh Chandarana, and Michael Macari. Dual energy CT: Preliminary observations and potential clinical applications in the abdomen. *European Radiology*, 19(1):13, 2009.

[163] Paulo R.S. Mendonca, Peter Lamb, and Dushyant V. Sahani. A flexible method for multi-material decomposition of dual-energy CT images. *IEEE Transactions on Medical Imaging*, 33(1):99, 2014.

[164] A. Shukla and Utham Kumar. Positron emission tomography: An overview. *Journal of Medical Physics*, 31(1):13, 2006.

[165] J. Paul Ronaldson, Rafidah Zainon, Nicola Jean Agnes Scott, Steven Paul Gieseg, Anthony P. Butler, Philip H. Butler, and Nigel G. Anderson. Toward quantifying the composition of soft tissues by spectral CT with Medipix3. *Medical Physics*, 39(11):6847, 2012.

[166] Daniela Muenzel, Daniel Bar-Ness, Ewald Roessl, Ira Blevis, Matthias Bartels, Alexander A. Fingerle, Stefan Ruschke, Philippe Coulon, Heiner Daerr, Felix K. Kopp, Bernhard Brendel, Axel Thran, Michal Rokni, Julia Herzen, Loic Boussel, Franz Pfeiffer, Roland Proksa, Ernst J. Rummeny, Philippe Douek, and Peter B. Noël. Spectral Photon-counting cT: Initial Experience with Dual-Contrast Agent K-Edge Colonography. *Radiology*, 283(3):723, 2017.

[167] Mats Persson, Ben Huber, Staffan Karlsson, Xuejin Liu, Han Chen, Cheng Xu, Moa Yveborg, Hans Bornefalk, and Mats Danielsson. Energy-resolved CT imaging with a photon-counting silicon-strip detector. *Physics in Medicine and Biology*, 59(22):3709, 2014.

[168] W. Thomlinson, H. Elleaume, L. Porra, and P. Suortti. K-edge subtraction synchrotron X-ray imaging in bio-medical research. *Physica Medica*, 49(January):58, 2018.

[169] Polad M. Shikhaliev. Photon counting spectral CT: Improved material decomposition with K-edge-filtered x-rays. *Physics in Medicine and Biology*, 57(6):1595, 2012.

[170] Xiaolan Wang, Dirk Meier, Katsuyuki Taguchi, Douglas J. Wagenaar, Bradley E. Patt, and Eric C. Frey. Material separation in x-ray CT with energy resolved photon-counting detectors. *Medical Physics*, 38(3):1534, 2011.

[171] Huanjun Ding, Hao Gao, Bo Zhao, Hyo Min Cho, and Sabee Molloi. A high-resolution photon-counting breast CT system with tensor-framelet based iterative image reconstruction for radiation dose reduction. *Physics in Medicine and Biology*, 59(20):6005, 2014.

[172] Hyo-Min Cho, Huanjun Ding, William C. Barber, Jan S. Iwanczyk, and Sabee Molloi. Microcalcification detectability using a bench-top prototype photon-counting breast CT based on a Si strip detector. *Medical Physics*, 42(7):4401, 2015.

[173] Zhicong Yu, Shuai Leng, Steven M. Jorgensen, Zhoubo Li, Ralf Gutjahr, Baiyu Chen, Ahmed F. Halaweish, Steffen Kappler, Lifeng Yu, Erik L. Ritman, and Cynthia H. McCollough. Evaluation of conventional imaging performance in a research whole-body CT system with a photon-counting detector array. *Physics in Medicine & Biology*, 61(4):1572, 2016.

[174] Ewald Roessl and Roland Proksa. Optimal energy threshold arrangement in photon-counting spectral x-ray imaging. In *IEEE Nuclear Science Symposium Conference*

Record, volume 3, page 1950. Institute of Electrical and Electronics Engineers Inc., 2006.

[175] Liqiang Ren, Muhammad U Ghani, Di Wu, Bin Zheng, Yong Chen, Kai Yang, Xizeng Wu, and Hong Liu. The impact of spectral filtration on image quality in micro-CT system. *Journal of Applied Clinical Medical Physics*, 17(1):301, 2016.

[176] Adam S. Wang and Norbert J. Pelc. Optimal energy thresholds and weights for separating materials using photon counting x-ray detectors with energy discriminating capabilities. In Ehsan Samei and Jiang Hsieh, editors, *Medical Imaging 2009: Physics of Medical Imaging*, volume 7258, page 725821. SPIE, 2009.

[177] Chelsea Amanda Saffron Dunning and Magdalena Bazalova-Carter. Design of a combined X-ray fluorescence Computed Tomography (CT) and photon-counting CT tabletop imaging system. *Journal of Instrumentation*, 15(06), 2020.

[178] J. Perl, J. Shin, J. Schümann, B. Faddegon, and H. Paganetti. TOPAS: An innovative proton Monte Carlo platform for research and clinical applications. *Medical Physics*, 39(11):6818, 2012.

[179] Paurakh L. Rajbhandary, Mats Persson, and Norbert J. Pelc. Detective efficiency of photon counting detectors with spectral degradation and crosstalk. *Medical Physics*, 47(1):27–36, 1 2020.

[180] Cheng Xu, Mats Danielsson, and Hans Bornefalk. Evaluation of energy loss and charge sharing in cadmium telluride detectors for photon-counting computed tomography. *IEEE Transactions on Nuclear Science*, 58(3 PART 1):614–625, 6 2011.

[181] Polad M. Shikhaliev, Shannon G. Fritz, and John W. Chapman. Photon counting multienergy x-ray imaging: Effect of the characteristic x rays on detector performance. *Medical Physics*, 36(11):5107, 2009.

[182] Bo Meng, Wenxiang Cong, Yan Xi, Bruno De Man, and Ge Wang. Energy window optimization for X-Ray K-edge tomographic imaging. *IEEE Transactions on Biomedical Engineering*, 63(8):1623, 2016.

[183] E. Barmeir, B. Dubowitz, and M. Roffman. Computed tomography in the assessment and planning of complicated total hip replacement. *Acta Orthopaedica*, 53(4):597–604, 1982.

[184] W A Kalender, R Hebel, and J Ebersberger. Reduction of CT artifacts caused by metallic implants. *Radiology*, 164(2):576–577, Aug 1987.

[185] Warren Kilby, John Sage, and Vicki Rabett. Tolerance levels for quality assurance of electron density values generated from CT in radiotherapy treatment planning. *Physics in Medicine & Biology*, 47(9):1485, Apr 2002.

[186] Magdalena Bazalova, Luc Beaulieu, Steven Palefsky, and Frank Verhaegen. Correction of CT artifacts and its influence on Monte Carlo dose calculations. *Medical Physics*, 34(6):2119–2132, Jun 2007.

[187] R. M. Lewitt and R. H.T. Bates. Image-reconstruction from projections. III. Projection completion methods (theory). *Optik*, 50(4):189–204, 1978.

[188] Hyoung Suk Park, Dosik Hwang, and Jin Keun Seo. Metal artifact reduction for polychromatic X-ray CT based on a beam-hardening corrector. *IEEE Transactions on Medical Imaging*, 35(2):480–487, 2 2016.

[189] Yanbo Zhang, Xuanqin Mou, and Shaojie Tang. Beam hardening correction for fan-beam CT imaging with multiple materials. In *IEEE Nuclear Science Symposium Conference Record*, pages 3566–3570, 2010.

[190] Hongli Shi, Zhi Yang, and Shuqian Luo. Reduce beam hardening artifacts of polychromatic X-ray computed tomography by an iterative approximation approach. *Journal of X-Ray Science and Technology*, 25(3):417–428, 2017.

[191] Jin Hur, Dongjoon Kim, Yeong Gil Shin, and Ho Lee. Metal artifact reduction method based on a constrained beam-hardening estimator for polychromatic x-ray CT. *Physics in Medicine & Biology*, 66(6):065025, Mar 2021.

[192] Shiying Zhao, Kyongtae T. Bae, Bruce Whiting, and Ge Wang. A wavelet method for metal artifact reduction with multiple metallic objects in the field of view. *Journal of X-Ray Science and Technology*, 10(1-2):67–76, 2002.

[193] Matthieu Bal and Lothar Spies. Metal artifact reduction in CT using tissue-class modeling and adaptive prefiltering. *Medical Physics*, 33(8):2852–2859, Aug 2006.

[194] Xinhui Duan, Li Zhang, Yongshun Xiao, Jianping Cheng, Zhiqiang Chen, and Yuxiang Xing. Metal artifact reduction in CT images sinogram TV inpainting. *IEEE Nuclear Science Symposium Conference Record*, pages 4175–4177, 2008.

[195] Daniel Prell, Yiannis Kyriakou, Marcel Beister, and Willi A. Kalender. A novel forward projection-based metal artifact reduction method for flat-detector computed tomography. *Physics in Medicine & Biology*, 54(21):6575, Oct 2009.

[196] Yinsheng Li, Xudong Bao, Xindao Yin, Yang Chen, Limin Luo, and Wufan Chen. Metal artifact reduction in CT based on adaptive steering filter and nonlocal sinogram inpainting. In *Proceedings - 2010 3rd International Conference on Biomedical Engineering and Informatics, BMEI 2010*, volume 1, pages 380–383. IEEE, oct 2010.

[197] Esther Meyer, Rainer Raupach, Michael Lell, Bernhard Schmidt, and Marc Kachelrieß. Normalized metal artifact reduction (NMAR) in computed tomography. *Medical Physics*, 37(10):5482–5493, Oct 2010.

[198] Hyoung Suk Park, Jae Kyu Choi, Kyung Ran Park, Kyung Sang Kim, Sang Hwy Lee, Jong Chul Ye, and Jin Keun Seo. Metal artifact reduction in CT by identifying missing data hidden in metals. *Journal of X-Ray Science and Technology*, 21(3):357–372, 2013.

[199] Abolfazl Mehranian, Mohammad Reza Ay, Arman Rahmim, and Habib Zaidi. X-ray CT metal artifact reduction using wavelet domain L0 sparse regularization. *IEEE Transactions on Medical Imaging*, 32(9):1707–1722, 2013.

[200] Esther Meyer, Rainer Raupach, Michael Lell, Bernhard Schmidt, and Marc Kachelrieß. Frequency split metal artifact reduction (FSMAR) in computed tomography. *Medical Physics*, 39(4):1904–1916, Mar 2012.

[201] Gary H. Glover and Norbert J. Pelc. An algorithm for the reduction of metal clip artifacts in CT reconstructions. *Medical Physics*, 8(6):799–807, Nov 1981.

[202] Heang K. Tuy. A post-processing algorithm to reduce metallic clip artifacts in CT images. *European Radiology*, 3(2):129–134, Apr 1993.

[203] J. Müller and T. M. Buzug. Spurious structures created by interpolation-based CT metal artifact reduction. In *Medical Imaging 2009: Physics of Medical Imaging*, volume 7258, page 72581Y. SPIE, Mar 2009.

[204] S Tohnak, AJH Mehnert, M Mahoney, and S Crozier. Dental CT metal artefact reduction based on sequential substitution. *Dentomaxillofacial Radiology*, 40(3):184–190, Feb 2011.

[205] B. De Man, J. Nuyts, P. Dupont, G. Marchai, and P. Suetens. Reduction of metal streak artifacts in x-ray computed tomography using a transmission maximum a posteriori algorithm. *IEEE Transactions on Nuclear Science*, 47(3 PART 3):977–981, 2000.

[206] Bruno De Man, Johan Nuyts, Patrick Dupont, Guy Marchal, and Paul Suetens. An iterative maximum-likelihood polychromatic algorithm for CT. *IEEE Transactions on Medical Imaging*, 20(10):999–1008, 2001.

[207] Catherine Lemmens, David Faul, and Johan Nuyts. Suppression of metal artifacts in CT using a reconstruction procedure that combines MAP and projection completion. *IEEE Transactions on Medical Imaging*, 28(2):250–260, Feb 2009.

[208] Jing Wang and Lei Xing. A binary image reconstruction technique for accurate determination of the shape and location of metal objects in x-ray computed tomography. *Journal of X-Ray Science and Technology*, 18(4):403–414, 2010.

[209] Ge Wang, Donald L. Snyder, Joseph A. O'Sullivan, and Michael W. Vannier. Iterative deblurring for CT metal artifact reduction. *IEEE Transactions on Medical Imaging*, 15(5):657–664, 1996.

[210] Ge Wang, Michael W. Vannier, and Ping Chin Cheng. Iterative X-ray Cone-Beam Tomography for Metal Artifact Reduction and Local Region Reconstruction. *Microscopy and Microanalysis*, 5(1):58–65, 1999.

[211] Idris A. Elbakri and Jeffrey A. Fessler. Statistical image reconstruction for polyenergetic X-ray computed tomography. *IEEE Transactions on Medical Imaging*, 21(2):89–99, 2 2002.

[212] Hyoung Suk Park, Sung Min Lee, Hwa Pyung Kim, Jin Keun Seo, and Yong Eun Chung. CT sinogram-consistency learning for metal-induced beam hardening correction. *Medical Physics*, 45(12):5376–5384, Dec 2018.

[213] Hao Shiyu Xu, Hao Dang, and Shiyu Xu. Deep residual learning enabled metal artifact reduction in CT. *https://doi.org/10.1117/12.2293945*, 10573(9):950–955, 3 2018.

[214] Yanbo Zhang and Hengyong Yu. Convolutional Neural Network Based Metal Artifact Reduction in X-Ray Computed Tomography. *IEEE Transactions on Medical Imaging*, 37(6):1370–1381, 2018.

[215] Kailash Kalare, Manish Bajpai, Shubhabrata Sarkar, and Prabhat Munshi. Deep neural network for beam hardening artifacts removal in image reconstruction. *Applied Intelligence*, 52(6):6037–6056, Apr 2022.

[216] Haofu Liao, Wei An Lin, S. Kevin Zhou, and Jiebo Luo. ADN: Artifact Disentanglement Network for Unsupervised Metal Artifact Reduction. *IEEE Transactions on Medical Imaging*, 39(3):634–643, Mar 2020.

[217] Junghyun Lee, Jawook Gu, and Jong Chul Ye. Unsupervised CT Metal Artifact Learning Using Attention-Guided β-CycleGAN. *IEEE Transactions on Medical Imaging*, 40(12):3932–3944, Dec 2021.

[218] T. D. Do, S. Sawall, S. Heinze, T. Reiner, C. H. Ziener, W. Stiller, H. P. Schlemmer, M. Kachelrieß, H. U. Kauczor, and S. Skornitzke. A semi-automated quantitative comparison of metal artifact reduction in photon-counting computed tomography by energy-selective thresholding. *Scientific Reports*, 10(1):1–10, Dec 2020.

[219] Maya Rajeswari Amma, Anthony Butler, Aamir Younus Raja, Benjamin Bamford, Philip H. Butler, Peter Walker, Aysouda Matanaghi, Sikiru A. Adebileje, Nigel Anderson, Marzieh Anjomrouz, Fatemeh Asghariomabad, Ali Atharifard, Stephen T. Bell, Srinidhi Bheesette, Alexander I. Chernoglazov, Tara Dalefield, Niels J. A. de Ruiter, Neryda Duncan, Robert Doesburg, Steven P. Gieseg, Brian Goulter, Steven D. Alexander, Sam Gurney, Joseph Healy, Peter Hilton, Shishir Dahal, Pierre Carbonez, Jérôme Damet, Claire Chambers, Praveenkumar Kanithi, Tracy Kirkbride, Stuart Lansley, Chiara Lowe, V. B. H. Mandalika, Emmanuel Marfo, Mahdieh Moghiseh, David Palmer, Raj Panta, Hannah Prebble, Mohsen Ramyar, Peter Renaud, Nanette Schleich, Emily Searle, Muhammed Shamshad, Jereena Sheeja, Rayhan Uddin, Lieza Vanden Broeke, Vivek V. S., Manoj Wijesooriya, Michael Walsh, Kenzie Baer, Seamus Tredinnick, and Tim Woodfield. Assessment of metal implant induced artefacts using photon counting spectral CT. In Bert Müller and Ge Wang, editors, *Developments in X-Ray Tomography XII*, page 46. SPIE, Sep 2019.

[220] Lawrence Chun Man Lau, Wayne Yuk Wai Lee, Anthony P.H. Butler, Alex I. Chernoglazov, Kwong Yin Chung, Kevin Ki Wai Ho, James Griffith, Philip H. Butler, and Patrick Shu Hang Yung. Multi-energy spectral photon-counting computed tomography (MARS) for detection of arthroplasty implant failure. *Scientific Reports*, 11(1):1–6, 2021.

[221] Robert L. Siddon. Fast calculation of the exact radiological path for a three dimensional CT array, 1985.

[222] Jericho O'Connell and Magdalena Bazalova-Carter. fastCAT: Fast cone beam CT (CBCT) simulation. *Medical Physics*, 48(8):4448–4458, 2021.

[223] Jericho O'Connell, Clayton Lindsay, and Magdalena Bazalova-Carter. Experimental validation of Fastcat kV and MV cone beam CT (CBCT) simulator. *Medical Physics*, 48(11):6869–6880, 11 2021.

[224] Julian A. Anhaus, Simon Schmidt, Philipp Killermann, Andreas Mahnken, and Christian Hofmann. Iterative metal artifact reduction on a clinical photon counting system—technical possibilities and reconstruction selection for optimal results dependent on the metal scenario. *Physics in Medicine & Biology*, 67(11):115018, Jun 2022.

[225] Kanako K. Kumamaru, Bernice E. Hoppel, Richard T. Mather, and Frank J. Rybicki. CT Angiography: Current Technology and Clinical Use. *Radiol. Clin. N. Am.*, 48(2):213–235, Mar 2010.

[226] Olivier Ghekiere, Rodrigo Salgado, Nico Buls, Tim Leiner, Isabelle Mancini, Piet Vanhoenacker, Paul Dendale, and Alain Nchimi. Image quality in coronary CT angiography: Challenges and technical solutions. *British Journal of Radiology*, 90(1072), 2017.

[227] Sara Boccalini, Salim A. Si-Mohamed, Hugo Lacombe, Adja Diaw, Mohammad Varasteh, Pierre Antoine Rodesch, Marjorie Villien, Monica Sigovan, Riham Dessouky, Philippe Coulon, Yoad Yagil, Elias Lahoud, Klaus Erhard, Gilles Rioufol, Gerard Finet, Eric Bonnefoy-Cudraz, Cyrille Bergerot, Loic Boussel, and Philippe C. Douek. First In-Human Results of Computed Tomography Angiography for Coronary Stent Assessment with a Spectral Photon Counting Computed Tomography. *Investigative Radiology*, 57(4):212–221, Aug 2022.

[228] Alan C. Kwan, Amir Pourmorteza, Dan Stutman, David A. Bluemke, and João A.C. Lima. Next-generation hardware advances in CT: Cardiac applications. *Radiology*, 298(1):3–17, Nov 2021.

[229] Bernhard Petritsch, Nils Petri, Andreas M. Weng, Martin Petersilka, Thomas Allmendinger, Thorsten A. Bley, and Tobias Gassenmaier. Photon-Counting Computed

Tomography for Coronary Stent Imaging: In Vitro Evaluation of 28 Coronary Stents. *Invest. Radiol.*, 56(10):653–660, Oct 2021.

[230] Salim A. Si-Mohamed, Sara Boccalini, Hugo Lacombe, Adja Diaw, Mohammad Varasteh, Pierre Antoine Rodesch, Riham Dessouky, Marjorie Villien, Valérie Tatard-Leitman, Thomas Bochaton, Philippe Coulon, Yoad Yagil, Elias Lahoud, Klaus Erhard, Benjamin Riche, Eric Bonnefoy, Gilles Rioufol, Gerard Finet, Cyrille Bergerot, Loic Boussel, Joel Greffier, and Philippe C. Douek. Coronary CT Angiography with Photon-counting CT: First-In-Human Results. *Radiology*, 303(2):303–313, May 2022.

[231] HK Yuen, J. Princen, J. Illingworth, and J. Kittler. Comparative study of Hough Transform methods for circle finding. *Image and Vision Computing*, 8(1):71–77, 1990.

[232] Tomomi Takenaga, Shigehiko Katsuragawa, Makoto Goto, Masahiro Hatemura, Yoshikazu Uchiyama, and Junji Shiraishi. Modulation transfer function measurement of CT images by use of a circular edge method with a logistic curve-fitting technique. *Radiological Physics and Technology*, 8(1):53–59, Jan 2015.